

UNIVERSITY OF OKLAHOMA

GRADUATE COLLEGE

FUNDAMENTAL UNDERSTANDING OF THE INTERFACIAL PHENOMENA  
INVOLVED IN THE CATALYSIS AT THE WATER-OIL INTERFACE OF  
NANOHYBRID-STABILIZED EMULSIONS

A THESIS

SUBMITTED TO THE GRADUATE FACULTY

in partial fulfillment of the requirements for the

Degree of

DOCTOR OF PHILOSOPHY

By

JIMMY ALEXANDER FARIA ALBANESE

Norman, Oklahoma

2012

FUNDAMENTAL UNDERSTANDING OF THE INTERFACIAL PHENOMENA  
INVOLVED IN THE CATALYSIS AT THE WATER-OIL INTERFACE OF  
NANOHYBRID-STABILIZED EMULSIONS

A THESIS APPROVED FOR THE  
SCHOOL OF CHEMICAL, BIOLOGICAL AND MATERIALS  
ENGINEERING

BY

---

Dr. Daniel E. Resasco, Chair

---

Dr. Lance Lobban

---

Dr. Jeffrey H. Harwell

---

Dr. Dimitrios V. Papavassiliou

---

Dr. David A. Sabatini

© Copyright by JIMMY ALEXANDER FARIA ALBANESE 2012  
All Rights Reserved.

## **Dedicatory**

I dedicate this work to my father and mother, Aureliano Faria and Ana Albanese. Because of you, I have been able to reach my dreams and goals in life.

My father, who taught me to work hard for the things you love and to be myself all the time. He showed me that the greatest moments in life are the ones that you share with the people you love. Although he left this world before I could finish my undergraduate studies, I know that he has been always close to me.

My mother, who taught me to be grateful with God for the opportunities that I have had in my life. She always encouraged me to pursue my dreams and to be thankful and patient during the hard times in life.

Mom and Dad I love you and you are my inspiration.

## **Acknowledgements**

I would like to acknowledge my fiancé and best friend, Pilar, who has been the greatest support since the beginning of my Ph.D. She taught me how to balance work with family and friends and I am grateful to have found someone like her to spend the rest of my life with.

I would like to acknowledge my father, mother and sister for their constant support even from the distance, because every time that I felt down I always had them next to me to give me a brighter perspective of the future. You are the fuel that keeps me moving forward. I am proud to be your son and brother.

I would like to acknowledge Dr. Daniel E. Resasco, my mentor and advisor, for his wisdom, advice, and trust all these years. He taught me to love research and he showed me the beauty of developing technologies that can offer solutions for a better world. He has found the perfect balance between rigorous scientific work and personal kindness that is rarely found in the scientific community. To be part of his research group has been an honor and a privilege. I hope that in the future we can continue a prosper relationship inside and outside of the scientific environment.

I would like to acknowledge my childhood friend Francisco Morales and his family for bringing me back to earth every time I come back to Venezuela. They always made me feel like I was one more of the family. They taught me that happiness is not only on what you do for living, but also on sharing with your family and friends the things you love to do.

I would like to acknowledge my friend Jesus for his support during the Ph.D. and his wisdom all these years. He taught me to be grateful to God for the good and bad things that happen in live. He also showed me that sharing time with your family and friends is as important as your work.

I would like to acknowledge Dr. Steven Crossley for his advice at the beginning of my Ph.D. He taught me that teamwork and brainstorming are the most powerful tools in the creation of new concepts. Also, he showed me that no matter how urgent a project can be, safety is always first.

I would like to acknowledge Dr. Walter Alvarez for his support and personal advice during the decision making process at the end of my Ph.D. He shared with me a more holistic view of research and the possible career paths that as a scientist I could have in the future.

I would to acknowledge my fellow students that have been always a great support during these years. They are Phuong, Martina, Stefano, Trung (Hoang), Trung (Pham), Tanate, Air, Quincy, Surapas, Amalia, Santiago, Veronica, Dachuan, Anh, Nok, Xinli, Anirudhan, Kyle, Yanger, Cristian, Felipe, Rattiya, Paula, Miguel, Tu, Wesley, Nick, Matt, and Mohamed.

I would like to acknowledge the funding agencies supported this work (DoE EPSCOR-Grant DE SC0004600, NSF EPSCoR 0814361, DoE DE-FG36GO88064 and the Advanced Energy Consortium) and people that kindly collaborated, G. W. Strout, Dr. Rolf E. Jentoft, Dr. M. Shen, and SouthWest NanoTechnologies Inc.

I would like to acknowledge Dr. J. Miller for his support during the XAS experiments performed in the synchrotron located in the Atomic Photon Source (APS) in Argonne National Laboratories.

## Table of Contents

Acknowledgements .....	iv
List of Tables .....	xvii
List of Figures.....	xxii
Abstract.....	xxxviii
Chapter 1: Catalysis in Nanoparticles-Stabilized Water-Oil Emulsions .....	1
1.1. Introduction .....	1
1.1.1. Stabilization of Water-Oil Emulsions With Particles.....	6
1.1.2. Controlling Parameters in Particle-Stabilized Emulsions .....	7
1.1.2.1. Particle Size .....	7
1.1.2.2. Particle-Particle Interaction .....	8
1.1.2.3. Particle Concentration .....	9
1.1.2.4. Composition of the Organic and Aqueous Phases .....	9
1.1.2.5. Liquid-Liquid-Solid Contact Angle .....	10
1.1.3. Janus Particles .....	12
1.1.4. Transport in Nanoparticles-Stabilized Emulsion Systems .....	13
1.1.5. Nanoparticles-Stabilized Foams .....	16
1.1.5.1. Effect of Particle-Interface Interaction on the Foam Stability .....	17
1.1.5.2. Effect of the Gas-Liquid Interface on Particle-Stabilized Emulsion .....	19
1.2. Experimental Section.....	20
1.2.1. Synthesis of Amphiphilic Nanoparticles .....	20
1.2.1.1. Synthesis of Carbon Nanotubes/Metal Oxide nanohybrids.....	21
1.2.1.1.1. Synthesis of Single-Walled Carbon Nanotubes on SiO <sub>2</sub> (SWCNT/SiO <sub>2</sub> ).....	21



1.2.1.1.2. Synthesis of Single-Walled Carbon Nanotubes on MgO (SWCNT/MgO)....	22
1.2.1.1.3. Synthesis of oxidized-Multi-Walled Carbon Nanotubes (oxi-MWCNT/Al <sub>2</sub> O <sub>3</sub> ) .....	22
1.2.1.1.4. Synthesis of “Onio-like” Carbon/SiO <sub>2</sub> Nanohybrids .....	23
1.2.1.2. Synthesis of Janus nanoparticles .....	23
1.2.2. Preparation of Janus Particles-Stabilized Emulsions .....	24
1.2.3. Preparation of Nanoparticles-Stabilized Foams .....	24
1.2.4. HRTEM Characterization of the Emulsions Stabilized by the Solid Nanohybrids .....	25
1.2.5. XPS Characterization of Nanohybrid Catalysts .....	25
1.2.6. Droplet Size and Emulsion Fraction of Nanoparticles-Emulsions.....	26
1.2.7. Mass Transport in Nanoparticles-Stabilized Emulsions.....	26
1.2.8. Transportation Under Static Conditions.....	27
1.3. Results and Discussion .....	28
1.3.1. Characterization of the CNT/MeO <sub>x</sub> Nanohybrids .....	28
1.3.1.1. HRTEM Characterization of CNT/MeO <sub>x</sub> Nanohybrids .....	28
1.3.1.2. Raman Characterization of CNT/MeO <sub>x</sub> Nanohybrids.....	30
1.3.1.3. XPS Characterization of CNT/MeO <sub>x</sub> Nanohybrids.....	31
1.3.2. CNT/MeO <sub>x</sub> Nanohybrids as Emulsion Stabilizers .....	32
1.3.3. Freeze-fracture HRTEM of Nanohybrids-Stabilized Emulsions .....	35
1.3.4. Janus Nanoparticles as Emulsion Stabilizers .....	36
1.3.4.1. Effect of Janus Nanoparticles Concentration .....	38

1.3.4.2. Semi-Qualitative Study of the Surface Utilization in the Emulsions Stabilized by Janus Nanoparticles .....	41
1.3.5. Nanoparticles-Stabilized Foams .....	44
1.3.5.1. Effect of the Nanoparticles Concentration .....	46
1.3.5.2. Effect of the pH on the Foam Stability .....	47
1.3.5.3. Effect of the Salt Concentration on the Foam Stability .....	49
1.3.6. Mass Transport in Nanohybrids-Stabilized Emulsions .....	49
1.3.7. Mass Transport in Nanohybrids-Stabilized Emulsions .....	51
1.3.7.1. Effect of the type of oil on the transportation.....	53
1.4. Conclusions .....	57
References .....	59
Chapter 2: Nanohybrid Catalysts for Bio-fuels Upgrading in Water-Oil Emulsions.....	66
2.1. Introduction .....	66
2.1.1. Revalorization of Lignocellulosic Biomass.....	70
2.1.2. Lignocellulosic Biomass Structure.....	71
2.1.3. Primary Conversion of Lignocellulosic Biomass.....	73
2.1.3.1. Gasification of Lignocellulosic Biomass.....	74
2.1.3.2. Pyrolysis of Lignocellulosic Biomass .....	75
2.1.3.3. Lignocellulose Hydrolysis and Dehydration .....	77
2.1.3.4. Dehydration of Sugars .....	78
2.1.4. Catalytic Strategies for Conversion of Furfurals to Fuel and Chemical Intermediates .....	81

2.1.4.1. Aldol-condensation of Furans and Ketones .....	82
2.1.4.2. Etherification of Biomass-Derived Furfural.....	84
2.1.4.3. Hydrodeoxygenation of Biomass-Derived Furans .....	85
2.1.4.4. Hydrodeoxygenation of Lignin-Derived Phenolics.....	87
2.1.5. Quantitative Structure and Properties Relationships (QSPR) for Fuel and Chemical Properties Optimization in Biomass Processing .....	89
2.2. Experimental Section.....	91
2.2.1. Catalyst Preparation and Characterization .....	91
2.2.1.1. Aldol-condensation Reaction Catalysts.....	91
2.2.1.1.1. SWCNT/MgO and MWCNT/MgO .....	91
2.2.1.1.2. MWCNT/MgO_Al <sub>2</sub> O <sub>3</sub> .....	92
2.2.1.1.3. MWCNT/Ce <sub>x</sub> Zr <sub>1-x</sub> O <sub>2</sub> , MWCNT/V <sub>2</sub> O <sub>5</sub> , MWCNT/ZnO and MWCNT/TiO <sub>2</sub> .	93
2.2.2. Hydrogenation Reaction Catalysts .....	93
2.2.2.1. Mixture of SWCNT/MgO and Pd/SWCNT .....	93
2.2.2.2. Pd/MWCNT_Al <sub>2</sub> O <sub>3</sub> and Pt/MWCNT_Al <sub>2</sub> O <sub>3</sub> .....	94
2.2.3. Hydrodeoxygenation Reaction Catalysts .....	94
2.2.3.1. Catalyst for the Hydrodeoxygenation of the Aldol-Condensation Products .....	94
2.2.3.2. Catalyst for the Conversion of Synthetic Bio-oils.....	95
2.2.4. Reactions in Particles-Stabilized Emulsion.....	95
2.2.4.1. Aldol-Condensation Reactions .....	97
2.2.4.2. Hydrogenation and Hydrodeoxygenation Reactions.....	98
2.2.4.3. Products Analysis and Quantification .....	98
2.3. Results and Discussion .....	100

2.3.1. Nanohybrid Catalyst Characterization by HRTEM and Raman Spectroscopy ..	100
2.3.1.1. SWCNT/MgO and MWCNT/MgO .....	100
2.3.1.2. MWCNT/MgO, MWCNT/MgO <sub>2</sub> , MWCNT/MgO <sub>2</sub> -Al <sub>2</sub> O <sub>3</sub> , MWCNT/Ce <sub>x</sub> Zr <sub>1-x</sub> O <sub>2</sub> , MWCNT/V <sub>2</sub> O <sub>5</sub> , MWCNT/ZnO and MWCNT/TiO <sub>2</sub> .....	101
2.3.1.3. Mixture of SWCNT/MgO and Pd/SWCNT .....	102
2.3.2. Biofuel Upgrading Reactions at the Water-Oil Interface of Nanoparticles- Stabilized Emulsions .....	103
2.3.2.1. Aldol-Condensation of Furan and Ketones in Emulsion.....	103
2.3.2.1.1. Catalyst Screening for the Aldol-Condensation of Furans and Ketones in Emulsion.....	105
2.3.2.1.2. Products Evolution during Aldol-Condensation of Furans and Ketones in Emulsion.....	107
2.3.2.2. Cascade Aldol-Condensation and Hydrogenation Reactions in Emulsions....	109
2.3.2.3. Conversion of Synthetic Bio-oils in Emulsion.....	113
2.3.2.3.1. Aldol-condensation and Hydrogenation Reactions of Synthetic Bio-oil in Emulsions .....	114
2.3.2.4. Hydrodeoxygenation of Phenolics Molecules in Emulsion .....	117
2.3.2.4.1. Hydrodeoxygenation of Vanillin in Emulsion .....	117
2.3.2.4.2. Hydrodeoxygenation of Synthetic Bio-oil Mixtures in Emulsion.....	120
2.3.3. Molecular Engineering of Fuel Components Derived from Biomass .....	122
2.3.4. Fischer-Tropsch Reaction in Emulsion coupled with Aldol-condensation .....	125
2.4. Conclusions .....	129
References .....	132

Chapter 3: Catalytic Conversion of Sugars to Fuels and Chemicals in Solid-stabilized Emulsions .....	144
3.1. Introduction .....	144
3.2. Experimental Section.....	148
3.2.1. Catalyst Preparation and Characterization .....	148
3.2.1.1. Isomerization Nanohybrid Catalyst (MWCNT- and SWCNT- NaX).....	149
3.2.1.2. Preparation of Sulfonated Multi-Walled Carbon Nanotubes (MWCNT-SO <sub>3</sub> H) .....	149
3.2.1.3. Synthesis of the Hydrogenation Catalysts (Pd-MWCNT-Al <sub>2</sub> O <sub>3</sub> and Ru-MWCNT-Al <sub>2</sub> O <sub>3</sub> ).....	150
3.2.2. Characterization Techniques .....	150
3.2.2.1. Thermogravimetric/Differential Thermal Analysis Coupled with Mass Spectroscopy (TG-DTA-MS).....	150
3.2.2.2. Diffuse Reflectance Infrared Fourier Transformation Spectroscopy (DRIFT).....	151
3.2.2.3. X-ray Photoelectron Spectroscopy (XPS).....	151
3.2.2.4. X-ray Diffraction (XRD).....	152
3.2.2.5. N <sub>2</sub> Physisorption.....	152
3.2.2.6. High-Resolution Transmission Electron Microscopy (HRTEM).....	152
3.2.3. Preparation of Nanohybrid-Stabilized Emulsions .....	152
3.2.4. Reaction Systems.....	153
3.2.4.1. Isomerization-Dehydration of Glucose/Fructose .....	153
3.2.4.2. Hydrogenation of Hydroxymethylfurfural .....	154

3.3. Results and Discussion .....	156
3.3.1. Particle-Stabilized Emulsions.....	156
3.3.2. Nanohybrid Catalyst Characterization .....	158
3.3.2.1. DRIFTS Characterization of the Functionalized MWCNT Catalysts.....	158
3.3.2.2. XPS Characterization of the Functionalized MWCNT Catalysts .....	160
3.3.2.3. TGA Characterization of the Functionalized MWCNT Catalysts .....	162
3.3.2.4. HRTEM the MWCNT-NaX and NaX Catalysts .....	165
3.3.2.5. Raman Characterization of the MWCNT-NaX and NaX Catalysts .....	166
3.3.3. Glucose Isomerization Over Nanohybrid CNT-NaX Catalysts .....	167
3.3.4. Catalyst Regenerability and Reusability .....	174
3.3.5. Hydrodeoxygenation of 5-Hydroxymethylfurfural on Ru or Pd/MWCNT/Al <sub>2</sub> O <sub>3</sub> Nanohybrids .....	177
3.4. Conclusions .....	179
References .....	181
Chapter 4: Phase Selective Conversion at the Liquid-Liquid Interface of Nanoparticle- stabilized Emulsions.....	186
4.1. Introduction .....	186
4.2. Experimental Section.....	193
4.2.1. Synthesis of Janus Catalyst Nanoparticles .....	193
4.2.2. Nanoparticles Characterization Techniques .....	195
4.2.3. X-Ray Absorption Near de Edge (XANES) and Extended X-Ray Absorption Fine Structure (EXAFS) Characterization of hydrophobized Pt/NaX .....	195

4.2.4. Preparation of Nanoparticles-Stabilized Emulsions .....	196
4.2.5. Catalytic Conversion of Aqueous- and Organic- Soluble Aldehydes in Nanoparticles-Stabilized Emulsions.....	197
4.2.5.1. Hydrogenation of Glutaraldehyde and Benzaldehyde and Octanal.....	197
4.3. Results and Discussion .....	199
4.3.1. Characterization of Janus-Stabilized Emulsions and Pd/Janus Catalyst .....	199
4.3.1.1. HRTEM Characterization.....	199
4.3.1.1.1. Janus Catalytic Nanoparticles (5 wt. % Pd/Janus Silica) .....	199
4.3.1.1.2. Nanohybrid Catalysts (5 wt. % SWCNT/SiO <sub>2</sub> ).....	200
4.3.2. Organic-Phase Selective Catalysis on Pd/Janus Catalysts .....	202
4.3.3. Organic-Phase Selective Catalysis on Pd/SWCNT/SiO <sub>2</sub> Nanohybrids.....	208
4.3.4. Aqueous-Phase Selective Catalysis on Pd/SWCNT/SiO <sub>2</sub> Nanohybrids .....	213
4.3.5. Extended X-ray Fine Structure (EXAFS) Characterization of Pt on hydrophobic NaX zeolite Catalyst.....	216
4.3.6. Hydrophobic Catalyst Nanoparticles with Polar-Selective Catalytic Activity...	218
4.4. Conclusions .....	221
References .....	224

Chapter 5: Amphiphilic Nanohybrid Catalysts for Reactions at the Water/Oil Interface in Subsurface Crude Oil Reservoirs .....	227
5.1. Introduction .....	227
5.2. Experimental Section.....	233
5.2.1. Materials .....	233

5.2.2. Reaction Studies .....	234
5.2.3. Catalytic Surface Wettability Modification.....	235
5.3. Results and Discussion .....	236
5.3.1. Interfacially Active Nanohybrids .....	236
5.3.2. Partial Oxidation of Oil Constituents .....	242
5.3.2.1. Catalyst Activity .....	242
5.3.2.2. Density Functional Theory (DFT) Calculations of the Metal-Nanohybrid Catalysts .....	246
5.3.2.3. Changes in Interfacial Tension After Reaction .....	248
5.3.3. Hydrogenation of Polynuclear Aromatics .....	250
5.3.3.1. Catalyst Activity .....	250
5.3.4. Catalytic Surface Wettability Modification.....	255
5.4. Conclusions .....	258
References .....	260

Chapter 6: Catalyst Hydrophobization for Enhanced Hydrothermal Stability in Condensed Hot Water.....	265
6.1. Introduction .....	265
6.2. Experimental section .....	270
6.2.1. Untreated HY Zeolites.....	270
6.2.2. Preparation of Functionalized Zeolites.....	270
6.2.3. Characterization Techniques .....	271
6.2.3.1. Thermogravimetric/Differential Thermal analysis (TG-DTA) .....	271



6.2.3.2. Temperature-Programmed Oxidation (TPO) .....	271
6.2.3.3. Diffuse Reflectance Infrared Fourier Transformation Spectroscopy (DRIFT) and Pyridine Chemisorption .....	272
6.2.3.4. X-ray Diffraction (XRD).....	272
6.2.3.5. N <sub>2</sub> Physisorption .....	273
6.2.3.6. Electron Microscopy Techniques (SEM and HRTEM) .....	273
6.2.4. Preparation of Particle-Stabilized Emulsions .....	273
6.2.5. Reaction System .....	273
6.3. Results and Discussion .....	275
6.3.1. Characterization of Untreated and Functionalized HY Zeolites .....	275
6.3.2. Particles Dispersability and Emulsion Characterization of Untreated and Functionalized HY Zeolites.....	276
6.3.3. DRIFT of Untreated and Functionalized HY Zeolites .....	277
6.3.4. TG-DTA and TPO of Functionalized HY Zeolites .....	279
6.3.5. Pyridine Chemisorption using in-situ DRIFT of Untreated and Functionalized HY Zeolites .....	281
6.3.6. Alcohols Dehydration.....	283
6.3.7. Alkylation of 2-propanol and m-cresol .....	284
6.3.8. Catalyst Regenerability and Reusability .....	289
6.3.9. Characterization of the Zeolites after Reaction .....	290
6.4. Conclusions .....	296
References .....	299

## List of Tables

Table 1.1. Values of fraction of foam formed (% vol) in the foams stabilized by hydrophobic silica particles .....	45
Table 1.2. Stability of foams at different concentrations of hydrophobic silica nanoparticles.....	47
Table 1.3. Values of fraction of foam formed (% vol) in the foams stabilized by hydrophobic silica particles with aqueous solutions with different pH, right after the formation and 24 h later .....	48
Table 1.4. LogP values of the different types of oils used as the organic phase in the emulsion systems studied .....	54
Table 2.1. Product distribution of the Aldol-condensation–hydrogenation reaction of 5-methylfurfural and acetone over 5 wt% Pd/(CNT/MgO). Reaction conditions were 3 hours at 80°C in 250 pounds per square inch (psi) of N <sub>2</sub> and then 1 hour at 100°C in 250 psi of H <sub>2</sub> . (Aq) aqueous phase; (Org) organic phase .....	112
Table 2.2. Composition (mol/l) of the different synthetic bio-oils prepared.....	114
Table 2.3. Total yield, product yield and total carbon balance obtained in the aldol-condensation and hydrogenation reactions of synthetic bio-oils SBO #1 and #2 at 100 °C and 400 psi in a biphasic system of decalin/water with an aqueous/organic ratio = 1.0 .....	115
Table 2.4. Conversion, product yields, selectivity and total carbon balance after 3 h of reaction over 5 wt. % Pd/MWNT_ Al <sub>2</sub> O <sub>3</sub> at 100 °C and 400 psi of H <sub>2</sub> in a biphasic system of decalin/water with an aqueous/organic ratio = 1.0 .....	121

Table 2.5. Summary of the possible reactions taking place in the conversion of furfural (FAL) and hydroxymethylfurfural (HMF), with the respective products and their properties .....	124
Table 3.1. Type of emulsion, average droplet size and emulsion fraction for the nanohybrid-stabilized emulsions. The MWNT-SO <sub>3</sub> H measurements correspond to a water:decalin (1:1) emulsion with a 1mg/ml of particle concentration. For the MWNT-NaX the emulsion consisted on an aqueous solution of sodium chloride (35 wt.%) and tetrahydrofuran (1:1) with 6.7 mg/ml of particles concentration .....	158
Table 3.2. Surface atomic composition from XPS data and density of acid sites of the purified MWCNT (p-MWCNT), oxidized MWCNT (MWCNT-COOH), and sulfonated MWCNT (MWNT-SO <sub>3</sub> H).....	162
Table 3.3. Conversion and product distribution obtained in the dehydration reaction of glucose and fructose at 150 °C, 300 rpm of agitation and 600 psi of N <sub>2</sub> over 50 mg of nanohybrid catalyst (MWNT-SO <sub>3</sub> H), in water:decalin (1:1) emulsion emulsion. Reactant concentration: 10 % vol. in 40 ml of total volume .....	172
Table 3.4. Rate of glucose conversion and fructose selectivity for the commercial NaX zeolite and nanohybrid MWNT-NaX after recycling the catalysts three times .....	175
Table 3.5. Lattice constants and unit cell volumes for the different catalysts before and after 1 h of isomerization reaction of glucose at 383 K, 600 rpm of agitation and 400 psi of N <sub>2</sub> over 200 mg of catalyst. Feed: 10 wt.% of glucose. Reaction volume: 30 ml ...	177
Table 3.6. Conversion of 5-hydroxymethylfurfural and product distribution obtained in the hydrogenation reaction of hydroxymethylfurfural after 2 h of reaction at 150 °C, 300	

rpm of agitation and 600 psi of N <sub>2</sub> over 50mg of nanohybrid catalyst (5% Ru/MWNT/Al <sub>2</sub> O <sub>3</sub> and 5% Pd/MWNT/Al <sub>2</sub> O <sub>3</sub> ), in water:decalin (1:1) emulsion emulsion .....	178
Table 4.1. Phase composition (before and after reaction). Hydrogenation of aldehydes catalyzed by Pd/Janus nanoparticles at the oil/water interface of the emulsion.....	206
Table 4.2. Conversion of benzaldehyde, droplet size and interfacial area in the systems prepared with different particle concentrations .....	208
Table 4.3. C/Si and Pd/Si Intensity ratios obtained from the XPS analysis of the dried Pd/SWCNT/SiO <sub>2</sub> and Pd/SWCNT/SiO <sub>2</sub> in emulsion.....	209
Table 4.4. Product composition (%) obtained in the hydrogenation reactions over two different catalysts; the former composed of a mixture of SWCNT/SiO <sub>2</sub> nanohybrids and Pd deposited on purified SWCNT (Pd present only in the oil phase), and the latter composed of Pd deposited on SWCNT/SiO <sub>2</sub> nanohybrids (Pd present in both phases) .....	212
Table 4.5. Activity of Hydrophilic/Hydrophobic and Amphiphilic catalysts for the glucose Isomerization in aqueous environment. Mass of catalyst 200 mg and 100 °C. Initial glucose concentration 10 wt. % and 600 rpm of agitation.....	220
Table 5.1. Schematic description of the different nanohybrids used as emulsion stabilizer and support of metal clusters .....	237
Table 5.2. Catalysts tested on tetralin partial oxidation .....	243

Table 5.3. Results for the catalyst screening for tetralin oxidation at 80 °C 200 psi. Reaction time: 24 h. O/W ratio 0.5. Total volume: 30 ml. Catalyst weight: 60 mg. Metal loading: 10 wt. %. Air flow 200 sccm. Y is the products yield and S the selectivity. Support: nanohybrid (a) SWNT/silica.....	244
Table 5.4. Comparison of metal loadings for the Cu, Pd on catalysts on nanohybrid (a) SWNT/silica for tetralin oxidation at 80 °C 200 psi.....	244
Table 5.5. Result of the reaction using 10 wt.% Pd catalysts on different supports for tetralin oxidation at 80 °C 200 psi. Reaction time: 24 h. O/W ratio 0.5. Total volume: 30 ml. Catalyst weight: 60 mg. Air flow 200 sccm. S represents the products selectivity	245
Table 5.6. Change in the QSPR molecular descriptors and the viscosity of phenanthrene upon hydrogenation reaction of phenanthrene .....	254
Table 6.1. Alcohol conversion in the 3 h dehydration reactions of 3-pentanol or 2-propanol at 200 °C and 700 psi of He over both untreated and OTS functionalized HY zeolites. Feed: 3-pentanol or 2-propanol with a total molar concentration of 1 M .....	283
Table 6.2. Conversion of m-cresol and product yield obtained in the alkylation reaction of m-cresol and 2-propanol at 200°C and 700 psi of He over untreated and OTS functionalized HY zeolite (Si/Al = 30), in single aqueous phase and in water/decalin emulsion .....	287
Table 6.3. Adsorption constants [in (g of zeolite) <sup>-1</sup> h <sup>-1</sup> ] of m-cresol and 2-propanol on OTS functionalized HY and untreated HY zeolites (Si/Al = 30).....	288
Table 6.4. Data for analysis of the untreated and OTS functionalized HY zeolites (SiO <sub>2</sub> /Al <sub>2</sub> O <sub>3</sub> molar ratio: 60) stability. Reaction conditions: 3h, 200 °C, 700 psig He,	

feed: 2-propanol/m-cresol molar ratio: 3; total molar concentration: 2 M, 500 mg catalyst..... 290

Table 6.5. Specific area ( $S_{BET}$ ), and pore volume of the two HY zeolites (untreated and OTS functionalized) before and after reaction. Alkylation reaction conditions: 3 h at 200 °C and 700 psi of He; feed: 2-propanol/m-cresol molar ratio: 3; total molar concentration: 2 M..... 295

## List of Figures

Figure 1.1. Schematic representation of the reactions involved in Phase-Transfer Catalysis (PTC) .....	2
Figure 1.2. (A) Optical microscopy image of a water-in-oil emulsion formed by sonicating a 1:1 mixture of decalin and water in the presence of 5 % wt. Pd/SWCNT_SiO <sub>2</sub> nanohybrids; (B) The same mixture as in (A) before sonication. It is seen that the nanohybrids preferentially migrate to the interface; (C) TEM image of the 5 % wt. Pd/SWCNT_SiO <sub>2</sub> nanohybrids. Right: Freeze fracture TEM images of the interface in a water-in-oil emulsion droplet stabilized by SWCNT_SiO <sub>2</sub> nanohybrids, together with a general reaction scheme.....	5
Figure 1.3. Illustration of the stabilization of Pickering emulsions based on particle-particle repulsion and rheology modification.....	7
Figure 1.4. Corresponding probable positioning of particles at a curved oil-water interface. For a contact angle $\theta < 90^\circ$ , solid-stabilized aqueous foams or oil-in-water emulsions may form (top). For $\theta > 90^\circ$ , solid-stabilized aerosols or water-in-oil emulsions may form (bottom) .....	11
Figure 1.5. Particle stabilized foam .....	17
Figure 1.6. Particles residing in a droplet–droplet interfilm effecting $P_{cmax}$ for coalescence .....	19
Figure 1.7. Dipole–dipole formation on particles at an interface.....	20
Figure 1.8. Freeze-fracture HRTEM characterization of nanoparticles-stabilized emulsions .....	25
Figure 1.9. Schematic description of the experimental setup used for this study .....	27

Figure 1.10. Schematic description of the transportation from the oil A phase (tetralin, decalin and $\alpha$ -tetralone) to the oil B phase (tetralin) present in the system studied .....	28
Figure 1.11. Scheme of the different nanohybrids used: SWCNT/SiO <sub>2</sub> , “onion-like” carbon/SiO <sub>2</sub> , MWCNT/Al <sub>2</sub> O <sub>3</sub> , and Oxidized MWCNT/Al <sub>2</sub> O <sub>3</sub> .....	29
Figure 1.12. HRTEM of the catalysts composed of 5 % wt. Pd supported on different nanohybrids: a) SWCNT/SiO <sub>2</sub> ; b) “onion-like” carbon/SiO <sub>2</sub> (top: Pd on the nanohybrid; bottom: closer view of the “onion-like” carbon in the nanohybrid); c) MWCNT/Al <sub>2</sub> O <sub>3</sub> ; and d) Oxidized MWCNT/Al <sub>2</sub> O <sub>3</sub> .....	30
Figure 1.13. Raman spectra of the different nanohybrids: a) SWCNT/SiO <sub>2</sub> , b) “onion-like” carbon/SiO <sub>2</sub> , c) MWCNT/Al <sub>2</sub> O <sub>3</sub> and d) Oxidized MWCNT/Al <sub>2</sub> O <sub>3</sub> . .....	31
Figure 1.14. XPS spectra (C 1s) of MWCNT/Al <sub>2</sub> O <sub>3</sub> and Oxidized MWCNT/Al <sub>2</sub> O <sub>3</sub> . ...	32
Figure 1.15. Microscope images of the water/decalin emulsions stabilized with a concentration of 1 % wt. of different nanohybrids: a) SWCNT/SiO <sub>2</sub> ; b) “onion-like” carbon/SiO <sub>2</sub> ; c) MWCNT/Al <sub>2</sub> O <sub>3</sub> ; and d) Oxidized MWCNT/Al <sub>2</sub> O <sub>3</sub> . .....	33
Figure 1.16. Droplet size (left) and emulsion volume fraction (right) and vs. particle concentration for the water/decalin emulsions prepared with different nanohybrids: SWCNT/SiO <sub>2</sub> , “onion-like” carbon/SiO <sub>2</sub> , MWCNT/Al <sub>2</sub> O <sub>3</sub> and Oxidized MWCNT/Al <sub>2</sub> O <sub>3</sub> .....	34
Figure 1.17. Freeze-fracture HRTEM of the nanohybrid-stabilized emulsions.....	36
Figure 1.18. Schematic description of the three phases (oil/emulsion/water) present in an oil-in-water emulsion stabilized by Janus silica-nanoparticles, together with a microscopy image of the emulsion phase.....	37



Figure 1.19. Pictures of some of the emulsions prepared with different Janus particle concentration: from left to right, 0.05, 0.1, 0.15, 0.2, 0.3 and 0.5 % wt. ....	38
Figure 1.20. Microscope images of emulsions prepared with different concentrations of Janus nanoparticles (wt. %): a) 0.05; b) 0.1; c) 0.15; d) 0.2; e) 1; f) 2.....	39
Figure 1.21. Results of % fraction of emulsion and average droplet size in the emulsions prepared with different concentrations of Janus particles .....	40
Figure 1.22. Schematic illustration of the different situations depending on the surface utilization values. a) Surface utilization > 100 %; b) surface utilization = 100 %; c) surface utilization < 100 %.....	43
Figure 1.23. Surface utilization values in the emulsions prepared with different concentrations of Janus particles .....	44
Figure 1.24. Pictures of the foams stabilized by hydrophobic silica nanoparticles, right after their formation and 2 and 24 h later .....	45
Figure 1.25. Stability of foams after 24 hour at different concentrations of hydrophobic silica nanoparticles .....	46
Figure 1.26. Optical microscopy images of the nanoparticles-stabilized foams using different masses of hydrophobic silica particles; a) 10 mg, b) 20 mg, c) 30 mg, d) 50 mg, e) 70 mg, f) 100 mg. The particles were dispersed in 10 ml of DI water and 1 ml of ethanol using 2 minutes of horn sonication .....	47
Figure 1.27. Pictures of the foams stabilized by hydrophobic silica nanoparticles, with aqueous solutions of different pH, right after their formation and 24 h later.....	48
Figure 1.28. Pictures of the foam stabilized by hydrophobic silica nanoparticles, with an aqueous of 8 % wt. NaCl, right after their formation and 24 h later .....	49

Figure 1.29. Amounts of a-tetralone and decalin transported from the emulsion phase (stabilized by 0.5 wt.% of oxidized MWCNT/Al <sub>2</sub> O <sub>3</sub> ) to the upper pure tetralin phase as a function of time under static conditions .....	50
Figure 1.30. Microscope images of the emulsion stabilized by 2 wt.% of oxidized MWCNT/Al <sub>2</sub> O <sub>3</sub> a) right after preparation, and b) after 24 h of adding the free tetralin oil. Microscopy images of the emulsion stabilized by 6 wt.% of oxidized MWCNT/Al <sub>2</sub> O <sub>3</sub> c) right after preparation, and d) after being homogenized with the pure tetralin oil for 24 h by magnetically stirring at 200 rpm .....	51
Figure 1.31. Amounts of a-tetralone and decalin transported from the emulsion phase (stabilized by 0.5 wt.% of oxidized MWCNT/Al <sub>2</sub> O <sub>3</sub> ) to the upper pure tetralin phase as a function of time under energy agitation.....	52
Figure 1.32. Amounts of the different oils transported as a function of time (under energy agitation); the numbers in the parentheses are the logP values of the oils .....	55
Figure 1.33. Amounts of oil transported as a function of the log P of the oils (under static conditions).....	56
Figure 1.34. Amounts of oil transported as a function of the Log P of the oils for different particle systems (under static conditions).....	57
Figure 2.1. Schematic description of the triphasic system (Gas-Liquid-Solid) with a catalytically-reactive emulsion layer showing; a) continuous reactive-separation of the products and reactants based on solubility differences, b) emulsion droplet stabilized by nanohybrids composed of carbon nanotubes and metal oxide support, and c) schematic illustration of the amphiphilic catalyst particle adsorbed at the liquid/liquid interface .	69

Figure 2.2. Schematic representation of the composition of lignocellulosic biomass ...	72
Figure 2.3. Different strategies for primary conversion of lignocellulosic biomass .....	74
Figure 2.4. Reaction scheme for cellulose conversion a) in the absence and b) in the presence of metal ions .....	76
Figure 2.5. Production of furfurals (2-furfuraldehyde and hydroxymethylfurfural) from lignocellulosic biomass .....	79
Figure 2.6. Putative mechanisms of dehydration of fructose and isomerization of glucose in the presence of halides and hexacoordinate chromium (II) complex, respectively.....	80
Figure 2.7. Catalytic pathways for the conversion of furfural .....	81
Figure 2.8. Catalytic pathways for the conversion of hydroxymethylfurfural .....	82
Figure 2.9. Synthetic pathways for the production of 5,5'-oxy(bis-methylene)-2-furaldehyde (OBMF).....	85
Figure 2.10. Proposed reaction pathway for aqueous-phase hydrodeoxygenation of phenolic aromatics to alkanes and methanol over a metal catalyst and with an acid.....	89
Figure 2.11. Semi-continuous batch reactor.....	96
Figure 2.12. Piping and instrumentation diagram of the semi-continuous batch reactor	97
Figure 2.13. Raman spectrum (left) and HRTEM image (right) of the nanohybrids composed of SWCNT and MgO .....	101
Figure 2.14. HRTEM images of some of the nanohybrids used in this study: a) MWCNT/MgO, b) MWCNT/ MgO_Al <sub>2</sub> O <sub>3</sub> , c) MWCNT/ ZnO, and d) MWCNT/ TiO <sub>2</sub> .....	102

Figure 2.15. Left) Raman spectrum of the purified SWCNT, and right) HRTEM image of the catalyst of 10 wt. % Pd on purified SWCNT .....	103
Figure 2.16. Schematic illustration of the aldol-condensation and hydrogenation reactions taking place at the water/oil interface in nanohybrid-stabilized emulsions ..	104
Figure 2.17. Conversion and product yields (%) in the aldol-condensation of furfural and acetone over different nanohybrids for 3 h at 100 °C and 400 psi of N <sub>2</sub> . Feed: total molar concentration (furfural + acetone) of 1.8 M; furfural/acetone ratio of 1.5 .....	106
Figure 2.18. Mechanism of the condensation reactions of furfural and acetone over CNT/MgO nanohybrids.....	107
Figure 2.19. Conversion and product yields (%) in the aldol-condensation of furfural and acetone over MWCNT/MgO nanohybrids at 100 °C and 400 psi of N <sub>2</sub> . Feed: total molar concentration (furfural + acetone) of 1.8 M; furfural/acetone molar ratio of 1:5 .....	108
Figure 2.20. Product yields (%) in the aldol-condensation of furfural and acetone over MWCNT/MgO nanohybrids at 100 °C and 400 psi of N <sub>2</sub> after different number of injections and corresponding 3 h reaction/injection. Feed: total molar concentration (furfural + acetone) of 1.8 M; furfural/acetone molar ratio of 1:5 .....	109
Figure 2.21. Possible reaction paths and products arising from the condensation and direct hydrogenation of 5-methylfurfural and acetone over 5 wt % Pd/CNT/MgO.....	111
Figure 2.22. Aldol-condensation and hydrogenation reactions of SBO #1 and #2 at 100 °C and 400 psi in a biphasic system of decalin/water with an aqueous/organic ratio = 1.0 .....	116

Figure 2.23. Schematic illustration of the reactions taking place at the water/oil interface in the solid-stabilized emulsions .....	117
Figure 2.24. Total weight fraction of the various products as a function of temperature after 30-min reaction in a batch reactor, from gas chromatographic analysis of each phase (combined).....	118
Figure 2.25. Partition of the various products in between the individual aqueous and organic phases after hydrogenation reaction of vanillin over 5 wt. % Pd/SWCNT/SiO <sub>2</sub> .....	119
Figure 2.26. Evolution of products and reactant concentration with the reaction time in the experiments performed with vanillin over 5 wt. % of Palladium supported on SWNT grown on silica oxide at 100 °C .....	120
Figure 2.27. Hydrodeoxygenation reaction of SBO #3 at 100 °C and 400 psi of H <sub>2</sub> over 5 wt. % Pd/MWNT-Al <sub>2</sub> O <sub>3</sub> in a biphasic system of decalin/water with an aqueous/organic ratio = 1.0 .....	121
Figure 2.28. Catalytic strategies for the conversion of furfural to fuel components and chemicals. The possible reaction steps are indicated with lowercase letters and the corresponding catalysts listed in the inset .....	123
Figure 2.29. Process diagram for the conversion of biomass to liquid hydrocarbons based on Fischer-Tropsch synthesis .....	126
Figure 2.30. Process diagram for the conversion of biomass to liquid hydrocarbons based on a modified Fischer-Tropsch synthesis using the nanohybrid-stabilized emulsion .....	127

Figure 2.31. Gas chromatography and mass spectrum (GC-MS) of the decalin phase after 24 h of reaction of CO:H<sub>2</sub> (1:2) 600 psi at 200 °C over 5 % wt. Ru/MWCNT/Al<sub>2</sub>O<sub>3</sub> (250 mg). The catalyst was reduced in a flow reactor in gas phase for 1 h at 500 °C in H<sub>2</sub> ..... 128

Figure 2.32. Gas chromatography and mass spectrum (GC-MS) of the decalin fraction of the emulsion after 24 h of reaction of CO:H<sub>2</sub> (1:2) 600 psi at 200 °C over 5 % wt. Ru/MWCNT/Al<sub>2</sub>O<sub>3</sub> (250 mg) reduced in a gas phase reactor for 1 h at 500 °C in H<sub>2</sub> 129

Figure 3.1. Flow diagram for the conversion of bio-derived saccharides into chemical intermediates and fuels ..... 145

Figure 3.2. Schematic illustration of the reactions taking place at the liquid-liquid interface in the nanohybrid-stabilized emulsions. In the aqueous phase the glucose rapidly isomerizes to fructose on the Lewis acid catalyst (NaX-MWNT) followed by dehydration on the on the Brønsted acid site (MWNT-SO<sub>3</sub>H). Upon formation the hydroxymethylfurfural migrates to the organic phase and reacts on the metal catalyst, either 5% Ru/MWNT/Al<sub>2</sub>O<sub>3</sub> or 5% Pd/MWNT/Al<sub>2</sub>O<sub>3</sub>) to form 2,5-hexadione or g-hydroxyvaleric acid, respectively ..... 147

Figure 3.3. a) Preferential adsorption the nanohybrids at the water-oil interface, b) the same mixture as in a) after horn sonication of the water:decalin with 1 mg/ml of MWNT-SO<sub>3</sub>H for 15 minutes at 25% amplitude, c) optical microscope image of the water/decalin (1:1) emulsion stabilized by MWNT-SO<sub>3</sub>H (1 mg/ml), and d) optical microscope image of the water + sodium chloride (35 wt. %)/tetrahydrofuran (1:1) emulsion stabilized by MWNT-NaX (6.7 mg/ml) ..... 157

Figure 3.4. DRIFT spectra of the purified MWNT (p-MWNT), oxidized MWNT (MWNT-COOH), and sulfonic functionalized MWNT (MWNT-SO <sub>3</sub> H).....	159
Figure 3.5. XPS Spectra in the regions of a) carbon 1s, b) oxygen 1s, and c) sulfur 2p for the MWCNT (p-MWCNT), oxidized MWCNT (MWCNT-COOH), and sulfonated MWCNT (MWNT-SO <sub>3</sub> H).....	161
Figure 3.6. TGA and gas phase composition of the nanohybrids: a) TGA of the purified MWNT (p-MWNT), oxidized MWNT (MWNT-COOH), and sulfonic functionalized MWNT (MWNT-SO <sub>3</sub> H), and MS of the gas phase products for the b) purified MWNT (p-MWNT), c) oxidized MWNT (MWNT-COOH), and d) sulfonic functionalized MWNT (MWNT-SO <sub>3</sub> H) .....	164
Figure 3.7. HRTEM images at different magnifications and the diffraction pattern of the materials before and after the synthesis of carbon nanotubes; a-b) commercial NaX faujasite zeolite, c-d) MWNT-NaX, and e-f) SWNT-NaX .....	166
Figure 3.8. Normalized Raman spectrum of the SWCNT-NaX and MWCNT-NaX nanohybrids .....	167
Figure 3.9. Reaction scheme for the integrated isomerization-dehydration and hydroprocessing of the cellulosic biomass. The process includes; 1) isomerization of the glucose on a weak Lewis acid site, 2) dehydration of the fructose on a Brønsted acid site; 3.1) hydrolysis of the hydroxymethylfurfural on a acid site followed by hydrogenation of the levulinic acid on a metal site to produce g-hydroxyvaleric acid, and 3.2) hydrogenolysis/hydration of the hydroxymethylfurfural to produce 2,5-hexandione.....	168

Figure 3.10. Rate of glucose conversion and fructose formation for the commercial NaX zeolite, nanohybrid MWNT-NaX, and nanohybrid SWNT-NaX. Obtained from the glucose isomerization in aqueous phase at 110 °C, 600 rpm of agitation and 400 psi of N <sub>2</sub> over 200 mg of catalyst. Feed: 10 wt.% of glucose in a total reaction volume of 30 ml.....	169
Figure 3.11. Product distribution form the isomerization reaction of glucose with time in aqueous phase at 110 °C, 600 rpm of agitation and 400 psi of N <sub>2</sub> over NaX-MWNT nanohybrid catalyst (200 mg). Feed: Feed: 10 wt.% of glucose in a total reaction volume of 30 ml.....	170
Figure 3.12. Conversion of glucose and product distribution from the reaction of isomerization-dehydration in single phase and in water (35 wt.% NaCl):tetrahydrofuran emulsion of glucose.....	174
Figure 3.13. X-ray diffraction of the NaX zeolites and MWCN-NaX nanohybrids before and after 1 h of isomerization reaction of glucose at 383 K, 600 rpm of agitation and 400 psi of N <sub>2</sub> over 200 mg of catalyst. Feed: 10 wt.% of glucose. Reaction volume: 30 ml.....	176
Figure 4.1. The Fick's first law of molecular diffusion in a biphasic liquid catalytic system.....	188
Figure 4.2. Schematic illustration of the surface modification (top) observed upon addition of polarity modifiers (ZnSO <sub>4</sub> , Zn <sub>3</sub> (PO <sub>4</sub> ) <sub>2</sub> ) to ruthenium catalyst nanoparticles during the hydrogenation of benzene in liquid phase (bottom).....	190



Figure 4.3. Illustration of the synthetic approach for the preparation of the Janus catalysts using the masking technique.....	194
Figure 4.4. X-Ray transmission cell for EXAFS and XANES characterization of nanoparticles-stabilized emulsions.....	196
Figure 4.5. Schematic illustration of the three phases (oil/emulsion/water) present in the oil-in-water emulsions, together with a picture of a vial with the emulsion system and a microscopy image of the emulsion phase.....	197
Figure 4.6. HRTEM images of the Pd/Janus nanoparticles. a) Pd deposited on the two sides of the Janus nanoparticles; b) Pd selectively deposited on the hydrophobic side	201
Figure 4.7. HRTEM images of 5 wt. % Pd/SWCNT/SiO <sub>2</sub> and Energy Dispersive X-ray spectroscopy (EDS) of the palladium clusters deposited on the pristine SWCNT and silica.....	201
Figure 4.8. HRTEM and DFT calculations of Pd cluster on pristine SWCNT (a and c) and plasma treated SWCNT (b-d) .....	202
Figure 4.9. Aldehyde conversion in a semi-batch reactor at 100 °C. Left: Pd deposited on the two sides of the Janus nanoparticles; Right: Pd selectively deposited on the hydrophobic side .....	204
Figure 4.10. Reaction network and corresponding products for the hydrogenation of glutaraldehyde (top) and benzaldehyde (bottom) catalyzed by Pd.....	205
Figure 4.11. Microscopy image of the oil-in-water emulsion produced with the Janus particles together with an schematic illustration of the hydrogenation reactions taking place at the water/oil interface catalyzed by Pd clusters supported on both sides of the	

Janus nanoparticles. At the beginning of the reaction, glutaraldehyde is present in the aqueous phase and benzaldehyde in the oil phase.....	207
Figure 4.12. Illustration of Pd/SWCNT/SiO <sub>2</sub> before and after emulsion.....	209
Figure 4.13. Conversion of glutaraldehyde and benzaldehyde obtained in the hydrogenation reactions over two different catalysts; the former composed of a mixture of SWCNT/SiO <sub>2</sub> nanohybrids and Pd deposited on purified SWCNT (Pd present only in the oil phase), and the latter composed of Pd deposited on SWCNT/SiO <sub>2</sub> nanohybrids (Pd present in both phases).....	211
Figure 4.14. Evolution of products and reactant concentration with the reaction time in the experiments performed with glutaraldehyde over 5 wt% of Palladium supported on SWCNT grown on silica oxide at 100°C .....	214
Figure 4.15. Possible reaction mechanism of glutaraldehyde etherification over the palladium surface.....	215
Figure 4.16. Pt L <sub>III</sub> DXANES spectra from 11.54 to 11.6 keV of 5 % wt. Pt/NaX in Water, decalin and 5 % wt. Pt/NaX-C18 at 25°C.....	218
Figure 4.17. Polarity-controlled conversion of polar molecules using a) hydrophilic catalysts and b) hydrophobic functionalized zeolites.....	221
Figure 5.1. Experimental procedure for the surface topography characterization before and after catalytic oxidation of physisorbed asphaltenes .....	236
Figure 5.2. Optical microscopy images of the water/decalin emulsions stabilized by different nanohybrids (see Table 1): (a) SWCNT/SiO <sub>2</sub> , (b) MWCNT/Al <sub>2</sub> O <sub>3</sub> , (c)	

Functionalized MWCNT/Al <sub>2</sub> O <sub>3</sub> , (d) Onion carbon/SiO <sub>2</sub> and (e) Janus silica nanoparticles.....	238
Figure 5.3. Schematic representation of the hydrogenation of phenanthrene at the water-oil interface in the nanohybrid-stabilized emulsions. The reactants and intermediate products are only soluble in the organic phase, while the hydrophobic part of the nanohybrids (CNT) contains most of the catalytically active species (Pd clusters).....	240
Figure 5.4. High-resolution TEM images of the catalysts prepared with 5 %wt. Pd supported on different nanohybrids (see Table 1): (a) SWCNT/SiO <sub>2</sub> , (b) MWCNT/Al <sub>2</sub> O <sub>3</sub> (c) Functionalized MWCNT/Al <sub>2</sub> O <sub>3</sub> , (d) Onion carbon/SiO <sub>2</sub> and (e) Janus silica nanoparticles .....	241
Figure 5.5. Representation of the introduction of the catalyst nanoparticles and the gaseous reactant in the wellbore for application in subsurface reservoirs .....	242
Figure 5.6. The models for Pd clusters adsorption on terrace sites (left); and steps sites (right) of MWCNT .....	248
Figure 5.7. Interfacial tension between mixtures of tetralin/tetralone and water determined experimentally (symbols) and using the exponential model proposed by Kim and Burgess (solid line).....	249
Figure 5.8. Conversion and yields of the different products in the hydrogenation of phenanthrene over 5 % wt. Pd on oxidized MWNT/alumina after 24 h of reaction under 900 psi of H <sub>2</sub> and 200 °C.....	251
Figure 5.9. Validation of the QSPR model for the prediction of the viscosity of polyaromatic molecules ( $r^2=0.9817$ ) and mean absolute error (MAE) was 0.26 cp ....	253

Figure 5.10. Schematic representation of the surface wettability modification via catalytic oxidation of the surface physisorbed hydrocarbon molecules .....	256
Figure 5.11. AFM images and 3D surface topography of the clean silicon wafers (a and d), asphaltenes physisorbed before reaction (b and e), and after oxidation (c-f) in hydrogen peroxide (30 wt. %) using 10mg of 10 wt. % Cu/MWCNT/Al <sub>2</sub> O <sub>3</sub> nanohybrids catalyst. The average surface roughness (Ra) of the samples is presented in red color	257
Figure 5.12. Schematic illustration of the water-air-silicon wafer contact angle measured on the clean silicon surface (a), asphaltenes physisorbed before reaction (b), and after oxidation (c) in hydrogen peroxide (30 wt. %) using 10mg of 10 wt. % Cu/MWCNT/Al <sub>2</sub> O <sub>3</sub> nanohybrids catalyst .....	258
Figure 6.1. Mechanisms for acid-catalyzed dealumination (1) and base-catalyzed hydrolysis of siloxane bonds (2).....	267
Figure 6.2. Schematic illustration of the alkylation of m-cresol and 2-propanol taking place at the water/oil interface in emulsions stabilized by functionalized zeolites .....	268
Figure 6.3. a) Distribution of the untreated and OTS functionalized HY zeolite in a biphasic water/decalin system; b) Optical microscopy image of the water/decalin emulsion stabilized by functionalized HY zeolite (Si/Al = 30) .....	277
Figure 6.4. DRIFT spectra of (a) untreated HY zeolite; (b) OTS functionalized HY zeolite; (bs) functionalized zeolite after 3 h treatment in biphasic solvent (water/decalin) at 200 °C; and (bc) functionalized zeolite after calcination in air at 450 °C for 16 h ..	278
Figure 6.5. Thermogravimetric analysis (TG-DTA) of the untreated and OTS functionalized HY zeolite (Si/Al ratio: 30). Left Axis: Weight (%) Right axis:	

Absorbance due to water ( $3735\text{ cm}^{-1}$ ), hydrocarbons, C-H stretching ( $2962\text{ cm}^{-1}$ ), and $\text{CO}_2$ ( $2350\text{ cm}^{-1}$ ). .....	280
Figure 6.6. DRIFT spectra of the pyridine chemisorption experiments at 100C and atmospheric pressure for the different HY zeolites ( $\text{SiO}_2/\text{Al}_2\text{O}_3$ molar ratio: 60). untreated and functionalized HY zeolite; a) untreated HY zeolite, b) functionalized HY zeolite, bp) functionalized HY zeolite after pyridine chemisorption, ap) untreated HY zeolite after pyridine chemisorption. Right: DRIFT spectra of the region around $2900\text{ cm}^{-1}$ of the functionalized HY zeolite after pyridine chemisorption .....	282
Figure 6.7. Conversion of 3-pentanol after 3 h reaction at $200\text{ }^\circ\text{C}$ and 700 psi of He over functionalized HY zeolites with different $\text{SiO}_2/\text{Al}_2\text{O}_3$ molar ratios .....	284
Figure 6.8. Flow diagram for the conversion of biomass into chemical intermediates by alkylation of the phenolic fraction of the bio-oil with the small oxygenates .....	285
Figure 6.9. Conversion of m-cresol as a function of reaction time during alkylation with 2-propanol at $200\text{ }^\circ\text{C}$ and 700 psi in He over two HY zeolites (Si/Al molar ratio: 30). Circles: Untreated; Triangles: OTS functionalized. Feed: 2-propanol/m-cresol molar ratio: 3; total molar concentration: 2 M.....	289
Figure 6.10. Electron microscopy (HRTEM) of the HY zeolites (Si/Al=30). Untreated zeolite, before (a) and after reaction (c); OTS functionalized zeolite, before (b) and after reaction (d).....	292
Figure 6.11. Scanning electron microscopy (SEM). Untreated zeolite: before (a) and after reaction (c); OTS functionalized zeolite: before (b) and after reaction (d).....	293

Figure 6.12. N<sub>2</sub> Adsorption-desorption isotherms of the HY zeolites (Si/Al=30).  
Untreated zeolite, before (a) and after reaction (c); OTS functionalized zeolite, before  
(b) and after reaction (d)..... 294

Figure 6.13. Pore size distribution of the HY zeolites (before (a) and after reaction (c);  
OTS functionalized zeolite, before (b) and after reaction (d)). Left) differential pore  
volume of the micropores (calculated by the DFT method); and Right) desorption  
cumulative pore volume of the mesopores (calculated by the BJH method) ..... 296

## Abstract

The development of reactive-separation processes in which products are separated from the reaction media (i.e. reactants and catalysts) in a single reaction unit is prized by energy and chemicals industries for its simplicity and novelty. A perfect example of this technology is phase transfer catalysis (PTC), in which reactions are carried out in a biphasic mixture of two immiscible solvents; added surfactants such as quaternary ammonium salts enhance interfacial surface area (through emulsification) and facilitate transfers between the phases. This approach is of interest when valuable products can be separated into the other phase, based on their solubility, preventing undesired secondary reactions (e.g. thermal decomposition). Despite these advantages, the application of this technology in industrial scale result is challenging, as the separation of the reaction products from the catalyst or from any reaction solvent is often complex and expensive. In contrast, solid particles are more easily recoverable and have also been shown in many cases to stabilize aqueous-organic emulsions, but these solid-stabilized emulsions have not been widely used in catalytic contexts.

In this contribution, a unique family of catalytic-amphiphilic nanoparticles that catalyze reactions at the liquid-liquid interface of water-oil emulsions is presented. This novel methodology combines the advantages of phase transfer and heterogeneous catalysis: a) increased interfacial area, b) enhanced mass transfer of molecules between the two phases, c) simplified reaction/separation process by using a recoverable solid catalyst instead of surfactant, and d) effective separation of products from the reaction

mixture by differences in the water/oil solubility (avoiding heating that leads to product decomposition).

To this end, the present work will explore the application of this technology in biomass conversion to fuels (upgrading of pyrolysis oil and sugars), Fischer-Tropsch synthesis, and enhancement of oil recovery. Furthermore, by anchoring the metal catalyst selectively on the hydrophobic or hydrophilic side of the Janus particles it has been demonstrated that it is possible to achieve only conversion of the molecules present in the aqueous or organic phase, i.e. “phase-selectivity”. Interestingly, when the hydrophobization of the catalyst was extended to the entire surface the resulting catalyst had an enhanced stability in aqueous environments, while preserving the same emulsification properties. Consequently, hydrophobization of microporous zeolites and metal-oxides catalysts have been successfully employed in the upgrading of bio-fuels in biphasic liquid systems, in which the use of conventional zeolites or metal-oxide catalysts is hindered by fast rates of deactivation due to dissolution into the bulk aqueous phase.



## Chapter 1:

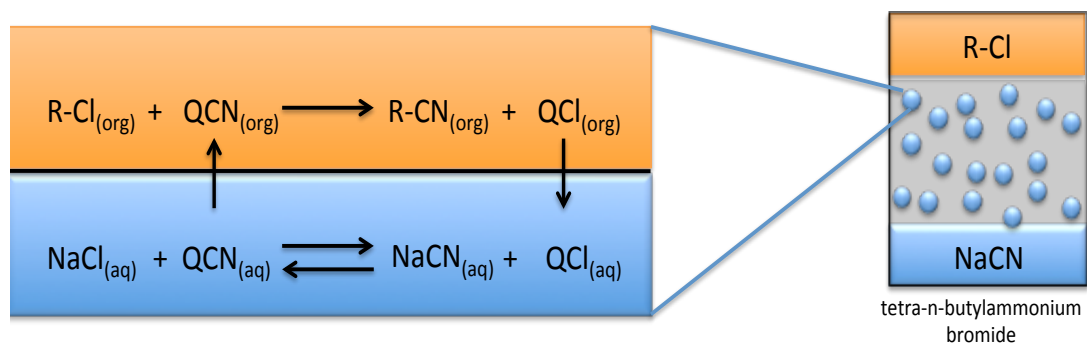
### Catalysis in Nanoparticles-Stabilized Water-Oil Emulsions

#### 1.1. Introduction

In conventional homogenous catalysis substrate molecules and catalysts have to enter in intimate contact. Therefore, it is essential to carry out the chemical reactions in solvents able to dissolve, at least partially, the reacting species and the catalyst. Typically, the organic solvent has to perform several functions: 1) stabilization of the catalyst (water-soluble transition metal complex) and reactants (oil-soluble molecules), 2) promotion of the desirable reaction pathway by changing either the electronic configuration or the stereoselectivity of the catalyst, and 3) acting as an acid or base media [1]. In many cases, these functional requirements severely restrict the selection of the organic solvents that are often toxic, environmentally hazardous and expensive.

An alternative to overcome these problems is the utilization of organic and aqueous phases that decouples the functional requirements of the solvent. Furthermore, if the homogeneous catalyst is replaced by a surface-sensitive complex, like tetra-alkyl-ammonium (TAA) cations, which naturally segregates to the liquid-liquid interface and continuously draws reactive anions from the aqueous phase to the organic phase as lipophilic ion pairs, a significant improvement will be observed in the reaction process (Figure 1.1). This system is widely known as Phase Transfer Catalysis (PTC), which has extensively been studied in the past decades [2-9]. Moreover, the addition of surfactant molecules to the biphasic reaction media promotes the formation of emulsion droplets that increases the interfacial surface area and the mass transfer of molecules

between the phases. The resulting catalytic system retains the chemoselectivity, regioselectivity, and/or enantioselectivity of the catalyst, observed in homogeneous catalysis, as well as reduces the environmental impact and enhances the reactivity, catalyst recovery and product separation.



**Figure 1.1: Schematic representation of the reactions involved in Phase-Transfer Catalysis (PTC).**

Despite these advantages, the application of this technology in industrial scale results challenging, as the separation of the reaction products from the catalyst or from any reaction solvent is often complex and expensive. Such drawback arises because the most common method used for separation, distillation, is not suitable for this process, since at the high temperatures required for the volatilization of the products, the catalyst undergoes through thermal decomposition (usually below 150 °C) even under reduced pressures [10]. Additionally, other conventional processes like chromatography or extraction have been used, but they also lead to catalyst loss [11,12].

Inspired on the concept of reactive-separation in biphasic liquid systems we have developed a unique family of catalytic-amphiphilic nanoparticles capable of stabilize and catalyze reactions at liquid-liquid interfaces in water-oil emulsions. Solid particles are more easily recoverable and have also been shown in many cases to stabilize aqueous-organic emulsions, but these solid-stabilized emulsions have not been widely used in catalytic contexts. Moreover, in cases such as the refining of bio-oils, in which the system is biphasic and contains up to 30% water, the most efficient way of catalyzing reactions is to place the solid catalyst at the liquid/liquid interface and to maximize the extent of interface by creating an emulsion. Otherwise, the catalyst particles will preferentially remain in the heavier phase, such as water. In that case, only the water-soluble molecules will be converted. If further conversion of water-insoluble molecules is wanted, one would need to remove them from the top of the reactor and send them to another reactor with a catalyst operating in the organic phase. Therefore, the concept of solid particles that can simultaneously stabilize an emulsion and catalyze reactions in both phases becomes an attractive proposition.

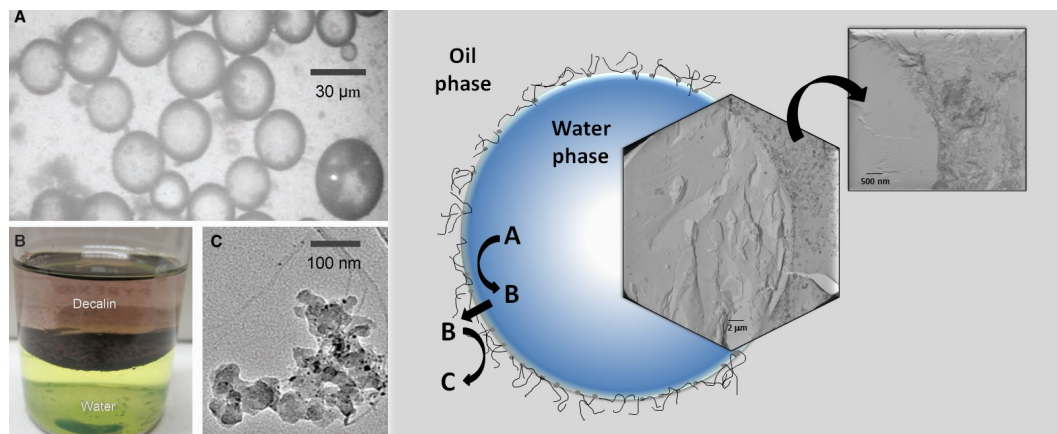
We have recently pointed out that this novel methodology combines the advantages of phase transfer and heterogeneous catalysis [13-15]: a) increased interfacial area, b) enhanced mass transfer of molecules between the two phases, c) simplified reaction/separation process by using a recoverable solid catalyst instead of surfactant, and d) effective separation of products from the reaction mixture by differences in the water/oil solubility (avoiding heating that leads to product decomposition). Such process improvements could have a major impact in the field of biomass conversion to fuels (upgrading of pyrolysis oil and sugars) [16-20], production

of specialty chemicals [21], pharmaceuticals, enhancement of oil recovery, deep desulfurization of fuel oil [22,23], and Fischer-Tropsch synthesis [24,25].

Furthermore, when these particles have a compartmentalized surface that displays different wettabilities (i.e., Janus particles), the stabilization of the emulsions becomes more effective [26-33]. Contrary to homogeneous particles that have uniform wettability and a fixed contact angle, the Janus particles are a more complex system with anisotropic surface chemistry that can exhibit a tailored hydrophilic/hydrophobic balance, and therefore modify the location of the three-phase contact angle. The tuneable surface properties of Janus nanoparticles have attracted attention for applications as diverse as sensing, electronics, photonics, and drug delivery [34-39].

A unique case of Janus particles developed in our research group are the nanohybrids composed of carbon nanotubes (hydrophobic) fused to oxide nanoparticles (hydrophilic), which are able to stabilize emulsions and, when properly functionalized, catalyze reactions at the water/oil interface (i.e., liquid/solid/liquid interfacial catalysis) [4,40]. The amphiphilic character of these nanohybrids makes them segregate naturally to the water/oil interface, thus becoming suitable for the stabilization of emulsions with small droplet sizes with remarkable stability (Figure 1.2).

Furthermore, we have demonstrated that, by anchoring the metal catalyst selectively on the hydrophobic side of the nanohybrids, we have achieved only conversion of the molecules present in the organic phase. We called this phenomenon “phase-selectivity” [4,41,42].



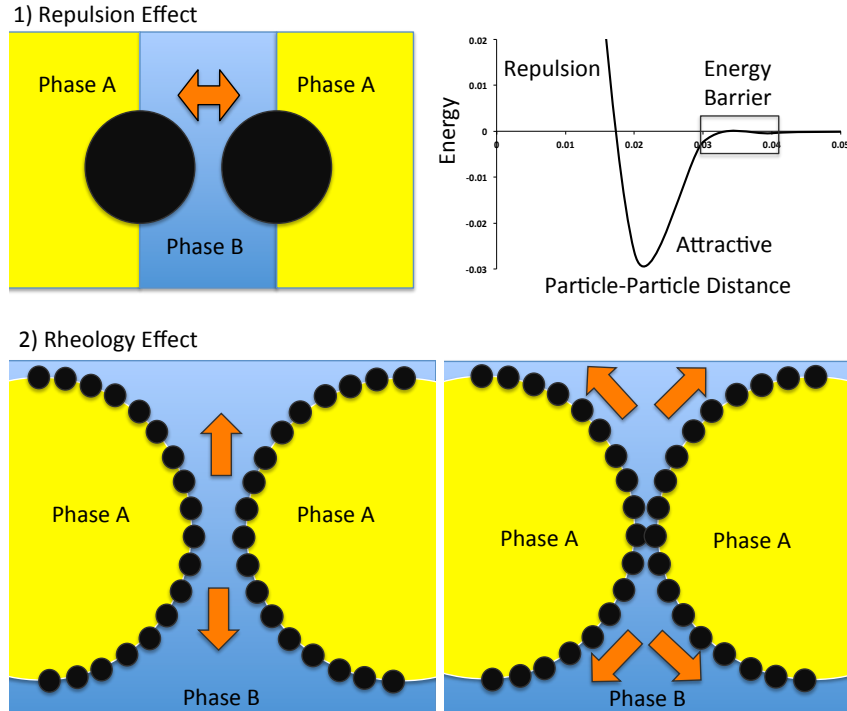
**Figure 1.2: (A) Optical microscopy image of a water-in-oil emulsion formed by sonicating a 1:1 mixture of decalin and water in the presence of 5 % wt. Pd/SWCNT\_SiO<sub>2</sub> nanohybrids; (B) The same mixture as in (A) before sonication. It is seen that the nanohybrids preferentially migrate to the interface; (C) TEM image of the 5 % wt. Pd/SWCNT\_SiO<sub>2</sub> nanohybrids [4]. Right: Freeze fracture TEM images of the interface in a water-in-oil emulsion droplet stabilized by SWCNT\_SiO<sub>2</sub> nanohybrids, together with a general reaction scheme [4].**

While our experimental findings clearly show that these novel systems exhibit remarkable activity and selectivity enhancement, the fundamental reasons behind this phenomenon are not entirely clear. Therefore, the main goal of my research project was to gain a detailed understanding of the interfacial phenomena involved in catalytic reactions occurring at the liquid-liquid interface of water/oil emulsions stabilized by amphiphilic catalyst particles. Furthermore, to explore the application of these nanostructured catalytic materials in two major research areas, upgrading of biomass-derived fuels/chemicals and enhancement of oil recovery (EOR). Typically the complexity of these systems requires the use of expensive and elaborated processing and production schemes, hence the development of technologies that can accomplish multifunctional tasks, as the catalytic nanoparticles in emulsions, offers remarkable

opportunities for energy conversion, chemicals production, and environmental remediation processes.

### *1.1.1. Stabilization of Water-Oil Emulsions With Particles*

The first observation of emulsions stabilized by solid particles was reported by S. U. Pickering in 1907 [43], who noticed that colloidal particles in mixture with water and petroleum can act as emulsifying agents to produce oil-in-water emulsions. In this process, the emulsion formed is a kinetically stable system characterized by 1) the formation of a rigid film of particles, at the liquid-liquid interface, that suppresses the coalescence of the droplets by steric repulsion [44-47], and 2) the modification of the rheological properties (viscosity) of the liquid at the droplet-droplet interface (Figure 1.3), delaying the liquid drainage between coalescing droplets [48,49]. Additionally, other studies suggested that, in order to observe the coalescence of emulsion droplets, it is necessary to displace the particles from the interfacial region to either the organic or aqueous phases. This means that additional energy is required to break the emulsion, providing an energetic barrier for coalescence [50,51]. Furthermore, another possible mechanism by which colloidal particles stabilize emulsions is related to the capillary pressure of the droplet-droplet liquid film, which arises by the deformation of the liquid interface around the adsorbed particles when the liquid is squeezed out of the thin film [52].



**Figure 1.3: Illustration of the stabilization of Pickering emulsions based on particle-particle repulsion and rheology modification.**

In contrast to the regular emulsions stabilized by surfactant molecules, in Pickering emulsions a new set of parameters significantly affects the emulsion stability, such as: 1) particle size, 2) the interaction between particles at the interface, 3) particle concentration, 4) the composition of the organic and aqueous phases, and 5) the contact angle between the water-solid-oil phases. In the following sections a detail description of the above parameters will be reviewed.

### *1.1.2. Controlling Parameters in Particle-Stabilized Emulsions*

#### *1.1.2.1. Particle Size*

According to theoretical calculations and experimental results, stable emulsions

are formed when the particles size is within the range of 0.01 to 1.0 mm, in which is both the flocculation (particles too large) and Brownian motion (particles too small) are prevented in either of the liquid phases [53,54]. Additionally, experimental results from several authors confirm these calculations; e.g. for spherical electrostatic charged latex particles with a control diameter (0.029 - 2.70 mm), the average droplet size (35 - 75 mm) initially increases with increasing particle size and then remains constant, in line with an increase in the sedimentation [55].

#### 1.1.2.2. Particle-Particle Interaction

The stabilization of the emulsion droplets by particles is strongly dependent of the particle-particle interaction. It has been found that when appropriate proportions of water-wetted particles (oil-in-water emulsifiers agents) are mixed with oil-wetted particles (water-in-oil emulsifiers agents), the resulting system is no longer stable and the emulsion droplets coalesce rapidly [2]. This observation suggests that the strength of the rigid film of particles at the water/oil interface depends significantly on the particle-particle interaction, which ultimately affects the emulsion stability. However, when the interaction between particles is larger, then the formation of aggregates is favoured, which decreases the amount of particles at the droplet surface, reducing the stability of the emulsion [56].



#### 1.1.2.3. Particles Concentration

The concentration effect of the insoluble emulsifier agent in Pickering emulsions has been reported in several studies in the literature [57-59]. In general, it is observed that the concentration of particles is directly proportional to the volume fraction and emulsion stability, and inversely proportional to the droplet size. This reduction in the emulsion droplets size results in an increase of the total droplet surface, which enables additional particles to be accommodated at the interface. However, the addition of particles also modifies the rheological properties of the continuous phase [60], i.e. at low concentration of particles at the fluid-fluid interface the viscous coefficients dominate the rheological parameters, while at high concentrations the elastic contribution becomes significant (particle-particle interaction) and, as a result, the fluid at the colloid-laden interface develops a viscoelastic or pseudoplastic behaviour.

#### 1.1.2.4. Composition of the Organic and Aqueous Phases

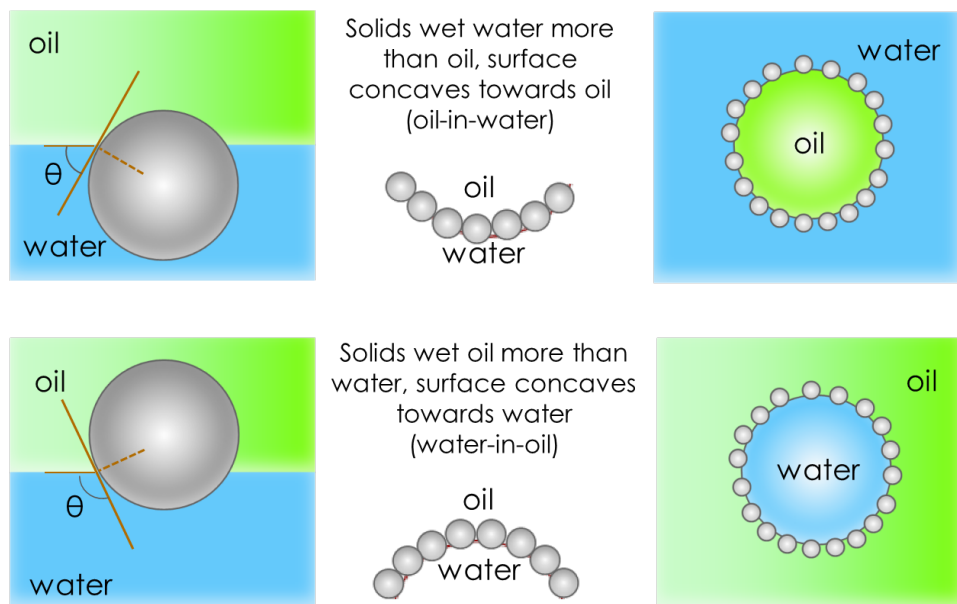
The composition of the organic and aqueous phases in the so-called Pickering emulsions is especially important, as the surface of the particles is sensitive to: 1) the adsorption of surface-active molecules that can change the hydrophilic-lipophilic balance (HLB) or wettability of the particle, and 2) the concentration of ionic species in the aqueous phase that can modify the electrostatics interaction between particles and, in consequence, their state of aggregation. The concentration of asphaltenes and resins is a controlling parameter in the stability of the brine-crude oil emulsions [61-69], as small flocculation of these molecules can form a highly viscous or rigid film at the oil-

water interface that prevents coalescence. Moreover, when colloidal particles are present in such a system, asphaltenes and resins can be adsorbed on the surface of the solid, increasing the hydrophobicity of the particle and facilitating the formation of stable water-in-oil emulsions [70,71]. However, if the pH of the aqueous phase is modified to levels in which the ionization of the polar functional groups of the resinous and asphaltenic material can be ionized, then the charge density of the surface would drastically change, introducing internal electrostatic repulsion in the film and thereby destroying the mechanical properties that give rise to protection against coalescence [72]. Such effect can be also observed when solely colloidal particles stabilize emulsions, e.g. in the stabilization of oil-in-water emulsions by metal oxide particles ( $\text{SiO}_2$ ), where the coalescence is observed when the pH is in the extremes ( $\text{pH} = 0$  and  $\text{pH} = 14$ ) in which the surface silanol groups ( $\text{Si-OH}$ ) are either positively or negatively charged and electrostatic repulsion disrupts the rigid film at the surface of the emulsion droplets [73,74]. On the other hand, in the presence of electrolytes in solution the colloidal particles are covered by charged ions that, at low concentrations, increase the stability of the resulting emulsion by partial flocculation. Nevertheless, higher concentrations of ions enhance the agglomeration of particles, which reduces the ability of the particles to stabilize the fluid-fluid interface [16].

#### 1.1.2.5. Liquid-Liquid-Solid Contact Angle

The three phase contact angle (wettability) of the particles at the liquid-liquid interface is another parameter that significantly influences the stability and the type of

emulsion obtained. It has been observed that for contact angles at the oil-water-solid interface (as measured across the aqueous phase) slightly lower than 90 degrees, the type of emulsion obtained is oil-in-water, and when the contact angles are slightly greater than 90 degrees, the type of emulsion is inverted to water-in-oil (Figure 1.4) [36,75,76]. This wettability of the particle can be modified by either adsorption of surface-active molecules or by functionalization of the particle. The latter is a technique widely used in the hydrophobization of silica oxide ( $\text{SiO}_2$ ), and experimentally involves the silylation of the silanol groups ( $\text{Si-OH}$ ) on the silica oxide, with alkylchlorosilanes or alkylsilazanes [77]. Partially hydrophobized metal oxides nanoparticles with anisotropic surface chemistry are called “Janus particles” or “Janus nanoparticles”.



**Figure 1.4: Corresponding probable positioning of particles at a curved oil-water interface. For a contact angle  $\theta < 90^\circ$ , solid-stabilized aqueous foams or oil-in-water emulsions may form (top). For  $\theta > 90^\circ$ , solid-stabilized aerosols or water-in-oil emulsions may form (bottom). Adapted from ref [32].**

### *1.1.3. Janus Particles*

The term “Janus particles” is referred to compartmentalized solids that display a heterogenic surface and, as the god Janus who had two faces, these particles have two different wettabilities. The term “Janus” particles was coined originally by C. Casagrande et al. to describe glass spherical particles with one hemisphere hydrophilic, and the other one hydrophobic [78,79]. In that case, the amphiphilic beads were synthesized by protecting one hemisphere with a varnish and chemically treating the other with a silane reagent, which resulted in a particle with equal hydrophilic and hydrophobic areas (after dissolving the varnish). Since then and as it was anticipated by De Gennes, on the occasion of his Nobel lecture [80], the surface properties of these particles have become an area of great interest for a variety of applications, such as drug delivery, catalysis, sensing, stabilization of water-oil emulsions and gas-liquid foams.

Differently than the homogeneous particles that have uniform wettability and a fixed contact angle, the Janus particles are a more complex system with asymmetric wettability that can be tuned depending on the HLB of the particle, and therefore modifying the location of the three phase contact angle (Figure 1.4).

When comparing the adsorption of homogeneous particles and Janus particles, it is useful to distinguish between surface activity and amphiphilicity. A surface active species is one which shows a tendency to adsorb at surfaces, whereas an amphiphilic species is one possessing a diblock structure in which the two blocks have different affinities for the solvent(s). Homogeneous particles for which the contact angle with the oil-water interface is around  $90^\circ$  are strongly surface active at this interface but are not

amphiphilic. Janus particles are both surface active and amphiphilic. The amphiphilicity of Janus particles can be tuned through variation of the relative areas of the polar and apolar regions [81].

The dual nature of Janus nanoparticles confers them fascinating properties, such as the capability to form clusters with controlled size and shape, unique surface properties and response to multiple stimuli [82]. Janus nanoparticles can be divided in three groups, depending on the preparation method: by self-assembly, masking or phase separation.

#### *1.1.4. Transport in Nanoparticles-Stabilized Emulsion Systems*

Oil transportation rate from an emulsion phase to a nearby oil phase was systematically investigated by using gas chromatography (GC) and optical microscopy, as techniques to determine the oil concentration in the free oil phase and the emulsion droplet size, respectively. Factors such as the presence of energetic agitation and oil composition were tested. Our results suggest that the agitation can greatly facilitate the transport process, as expected. Besides, the type of oil seems to strongly affect the transportation process. Oils with higher water solubility tend to transport faster. Also, the emulsion droplets undergo significant change in terms of droplet size during the oil transport process under agitated conditions. The above observations were determined to be quite common, regardless of the emulsifier particle type. The implication of these results for the heterogeneous catalysis based on emulsion systems was briefly discussed.

Mass transport phenomena in emulsion systems have been previously explored because of its importance in governing Ostwald ripening processes [83,84]. It has been generally accepted that the solubility of the transferring oil species in the micellar solution [85] and the ratio of the number of oil molecules to that of surfactant molecules [86] can determine the oil transportation rate. However, very limited research efforts have been directed to the understanding of the oil transport phenomena in solid-stabilized emulsion systems (Pickering emulsion) [87,88]. In principle, the transportation of oil in particle-stabilized emulsions should be mechanistically different from that in the surfactant-stabilized emulsions because of the difference in the emulsion stabilization principle and unique behavior of interfacial active particles in emulsions. L. Sacca et al. [87] utilized calorimetry to demonstrate that transfer of water from pure water droplets towards urea droplets in mixed emulsions stabilized by solid particles is slower compared with the emulsions stabilized with nonionic surfactant. More recently, B.P. Binks et al. [88] compared the composition ripening processes for both surfactant-stabilized and particle-stabilized emulsions: by monitoring the emulsion droplet size evolution after mixing two emulsions stabilized by one mobile and one immobile oil, they found that for particle-stabilized emulsion, the final swollen droplet radius for the emulsion containing immobile oil to be proportional to the swelling ratio to the power of 1 while in surfactant-stabilized emulsions to the power of 1/3.

Recently we reported on the stabilization of O/W and W/O emulsions by using carbon nanotubes/silica nanohybrids and the application of these systems for heterogeneous catalytic reactions [42]. Both single-walled (SWCNT) and multi-walled (MWCNT) carbon nanotubes supported on different oxides, silica or alumina, have the

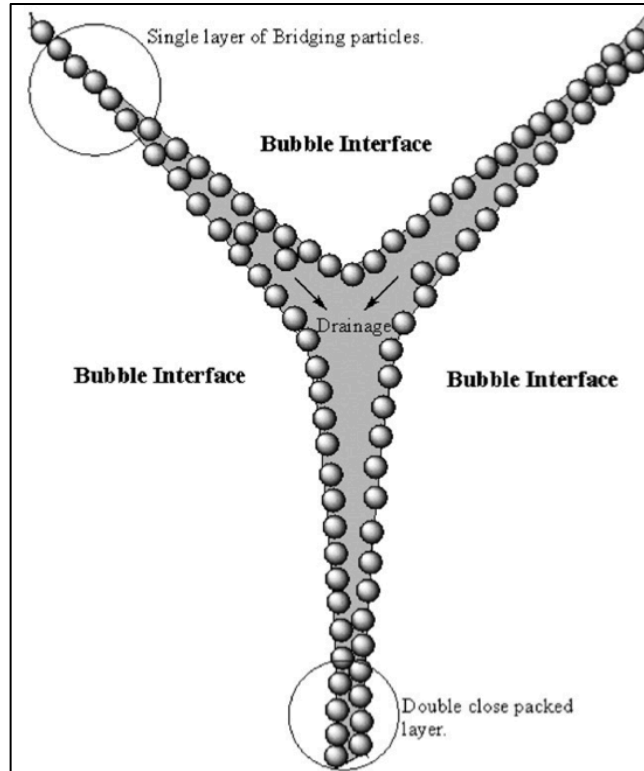
capability to stabilize emulsions due to their amphiphilic character. Furthermore, other types of emulsifier particles, such as Janus silica particles or “onion-like” carbon/silica have been also investigated [42]. The biphasic catalytic reactions can be catalyzed by active species supported on the solid emulsifier particles, rendering much higher interfacial areas and phase reaction selectivity. In our original proposal, the working reaction systems can be made of three phases: oil, emulsion and water. During reaction, the reactants and products could be separated depending on their solubility in water/oil. In some circumstances, the removal of the upper oil phase or bottom water phase might effectively shift the reaction equilibrium. However, the presumption for this strategy is that there should be sufficient transportation of oil from the inner emulsion droplet to the upper free oil phase (in the case of o/w emulsion). Thus, it is very necessary to quantitatively understand this phenomenon. Unfortunately, very scarce literature has been reported on this topic according to the best of our knowledge. In this contribution, we have investigated the transportation rates of different oil compounds from the o/w emulsion droplets to a free oil phase. In order to better quantitatively estimate this oil transportation rate, we rely on the application of a gas chromatography (GC). The effect of the presence of energetic agitation and the oil type were tested. Our results indicate that these two parameters could significantly affect the oil transportation rate from the emulsion phase to the free oil phase.

### *1.1.5. Nanoparticles-Stabilized Foams*

Our research group recently submitted a patent on the stabilization of foams into subsurface reservoirs for enhancement of oil recovery [89]. In this approach amphiphilic nanoparticles are used as foam-stabilizers for the selective delivery of gas phase reactant (e.g. hydrogen, oxygen, ammonia) to the water-oil interface inside the crude oil reservoir. To this end, the present section is intended to briefly describe key parameters involved in the stabilization of foams by nanoparticles. The use of nanoparticles for the stabilization of foams is especially attractive in some industrial applications as they can endure the harsh process conditions (e.g. ultra-stable and environmentally friendly foams for enhancement of oil recovery).

Analogous to the Pickering emulsions the stabilization of foams by particles is related to the formation of a solid film of particles that prevents coalescence (Figure 1.5). Here stabilization of foams by particles is closely related to three main parameters, including; 1) particle-interface interaction, capillary pressure of coalescence, particle-particle interactions, and 2) gas-liquid interface. In foams the particles are located at the liquid-gas interface, in which the hydrophobic part of the particles is facing the gaseous phase, while the hydrophilic part faces liquid phase. In this case the gas bubbles are dispersed in the top of the liquid continuous phase, rather than dispersed in the liquid phase.



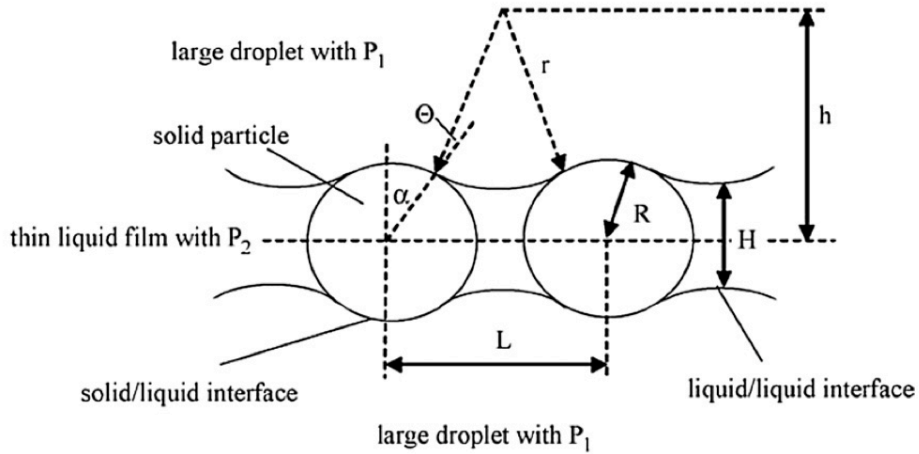


**Figure 1.5: Particle stabilized foam [90].**

#### 1.1.5.1. Effect of Particle-Interface Interaction on the Foam Stability

The extent of the interaction of nanoparticles and the interface in foams is associated to the particle-interface detachment energy and the capillary pressure inside the liquid films between two bubbles. In the first one the contact angle is an indirect measurement of this interaction, i.e. when the nanoparticles have a liquid-gas-solid contact angle close to 90 degrees the energy required to remove the particles from the interface is at the maximum. The best examples of these kinds of solids are the Janus particles, in which the anisotropic surface chemistry dramatically enhances the adsorption energy of the particles. While the contact angle is a theoretical indication that detachment energies and foams stability are related, it has been demonstrated that

higher foams stabilities are obtained when the contact angles are lower than 90 degrees, with values around 70 to 60 degrees. In this case the capillary pressure of the liquid film is the cause of this unpredicted behaviour. Kaptay et al. [91], derived an analysis for a single hexagonal layer of particles between two bubbles. Here particles with a zero contact angle (and radius  $R$ ) that are completely resting in the interfilm, straddled between the two droplets as shown in Figure 1.6. As drainage occurs, the bubbles form a meniscus around the particles causing a decrease in the film thickness ( $H$ ). The curvature of the meniscus is given from an assumed sphere radius ' $R$ ', hence increasing capillary pressure between the bubbles. The capillary pressure increases accordingly ( $P_2$ ), until the maximum pressure for bubbles coalescence is reached. The result from this analysis is that for a given size, shape, concentration, and distribution of particles at the liquid-gas interface the lower the entrainment of the particles towards the inside of the bubbles the larger the volume of liquid to be drained to reach the maximum capillary pressure, hence the more stable the foam. In fact, when the proper detachment energy (contact angle) and capillary pressure are achieved, the stability of the foams is maximized.



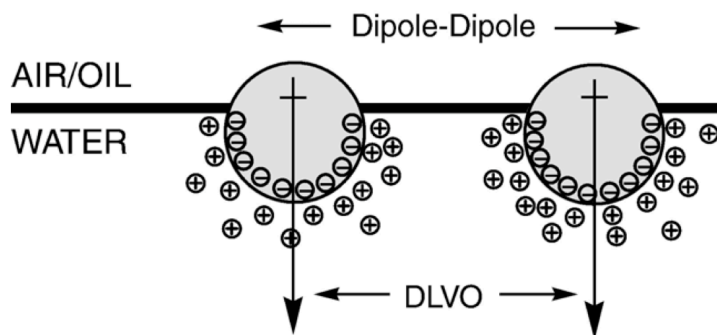
**Figure 1.6: Particles residing in a droplet–droplet interfilm effecting  $P_{cmax}$  for coalescence [91].**

The stability of the liquid film in between the gas bubbles in the foam is also strongly related to the particle-particle interaction. In order to produce the coalescence of foam bubbles film drainage and thinning must occur. Considering the high free energies of the adsorbed particles at the gas-liquid interface, lateral movement along the contact interface is far more likely than the removal or expulsion into the open continuous phase, during film thinning [48,92]. Hence, particle–particle forces such as electric double layer repulsion and dipole–dipole repulsion, as well as van der Waals attraction and capillary forces are of utmost importance to overall stability of foams and emulsions, and may dominate interactions over particle–interface attachment.

#### 1.1.5.2. Effect of the Gas-Liquid Interface on Particle-Stabilized Emulsions

At the gas-liquid interface the particles experience the formation of asymmetrical charge distribution, as the portions of the particles in the aqueous phase

undergo ionization [93,94]. This partial polarization of the particles induces a dipole perpendicular to the interface, which crosses the interface from the gas phase to the liquid phase due to DLVO (Derjaguin and Landau, Verwey and Overbeek theory) interactions caused by the charge neutralization of the counter-ions in the liquid phase and the surface charge of the particles [95]. In highly hydrophilic particles, however, additional ions in the liquid phase effectively screen the charge repulsion between particles at the interface, allowing particle agglomeration, reducing the foam stability. Hence, particles with high hydrophobicity are less prone to the destabilization effects caused by the ions concentration in the liquid phase (Figure 1.7).



**Figure 1.7: Dipole–dipole formation on particles at an interface.**

## 1.2. Experimental Section

### 1.2.1. Synthesis of Amphiphilic Nanoparticles

This section is intended to explain the synthesis of the CNT-metal oxide nanohybrids and Janus nanoparticles. In these two distinct amphiphilic nanoparticles the

catalytically active functionalities were incorporated after the synthesis. Therefore, it will be limited to the preparation of amphiphilic nanoparticles as in the following chapters the catalyst synthesis will be presented.

#### 1.2.1.1. Synthesis of Carbon Nanotubes/Metal Oxide nanohybrids

The CNT-metal oxide nanohybrids were produced based on the CoMoCAT technology developed by our research group for the production of carbon nanotubes by chemical vapour deposition (CVD), in which a reduced CoMo-based catalyst supported on metal oxide particles is fluidized in a reactor at high temperatures with continuous flow of carbon-containing gases (e.g. CO, CH<sub>4</sub>, C<sub>2</sub>H<sub>4</sub>).

##### 1.2.1.1.1. Synthesis of Single-Walled Carbon Nanotubes on SiO<sub>2</sub> (SWCNT/SiO<sub>2</sub>)

Single-walled carbon nanotubes (SWCNT) were grown on Co-Mo/silica oxide following our own CoMoCAT synthesis method. The silica-supported Co-Mo catalyst over which SWNT are grown is synthesized by impregnating appropriate amounts of cobalt nitrate and ammonium heptamolybdate over SiO<sub>2</sub>; the silica used in this case was a HiSil 210 (primary particles  $d < 50$  nm, BET area 135 m<sup>2</sup>/g, from PPG). The total metal loading was 2 % at a Co/Mo molar ratio of 1:3. After reduction in H<sub>2</sub> at 500°C, the catalyst was heated in He flow to 750°C and then exposed to a flow of pure CO for 1 h. The as-produced material was passed through a micro- fluidizer to achieve a

uniform SWNT-silica aggregate size of about 1  $\mu\text{m}$ . The carbon loading in the final product as determined by a total-carbon analyzer was about 7 wt. %.

#### 1.2.1.1.2. Synthesis of Single-Walled Carbon Nanotubes on MgO (SWCNT/MgO)

MgO powder was used as a support for the nanotube growth catalysts (FeMo) instead of silica. These catalyst were prepared by a combustion method in which a solution of the precursors,  $\text{Mg}(\text{NO}_3)_2$ ,  $\text{Fe}(\text{NO}_3)_3 \cdot 9\text{H}_2\text{O}$  and  $(\text{NH}_4)_6\text{Mo}_7\text{O}_{24} \cdot 4\text{H}_2\text{O}$ , was mixed with citric acid (combustible agent), and then it was dried and calcined at  $450^\circ\text{C}$  for 2 h. The total metal loading (Fe and Mo) was 4 % with a molar ratio Fe:Mo of 10:1. In order to produce the nanotubes, this catalyst was reduced in  $\text{H}_2$  at  $500^\circ\text{C}$  for 1 h, then heated in He up to  $800^\circ\text{C}$  and finally exposed to a flow of 7 % of  $\text{CH}_4$  in He at this temperature for 1 h.

#### 1.2.1.1.3. Synthesis of oxidized-Multi-Walled Carbon Nanotubes (oxi-MWCNT/ $\text{Al}_2\text{O}_3$ )

MWCNT/ $\text{Al}_2\text{O}_3$  were obtained from SouthWest NanoTechnologies. Oxidized MWCNT/ $\text{Al}_2\text{O}_3$  were prepared by oxidation of MWCNT/ $\text{Al}_2\text{O}_3$  with nitric acid. 1 g of MWCNT/ $\text{Al}_2\text{O}_3$  was treated with 50 ml of  $\text{HNO}_3$  16 M with stirring for 3 h at  $100^\circ\text{C}$ . The final product was filtered and washed with DI water until neutral pH was reached, and then dried overnight at  $100^\circ\text{C}$ .

#### 1.2.1.1.4. Synthesis of “Onion-like” Carbon/SiO<sub>2</sub> Nanohybrids

The method used to prepare Onion carbon/SiO<sub>2</sub> was as follows. First, silica Aerosil 200 (from Evonik, Degussa) was impregnated with an aqueous solution of Co(NO<sub>3</sub>)<sub>2</sub>·6H<sub>2</sub>O and (NH<sub>4</sub>)<sub>6</sub>Mo<sub>7</sub>O<sub>24</sub>·4H<sub>2</sub>O (provided by Sigma Aldrich), reaching a final metal loading of 2 % wt, with a Co:Mo molar ratio of 1:3. The powder was then calcined in air following this sequence: 1 h at 100 C, 1 h at 200 C, 1 h at 300 C and 2 h at 500 C. After cooling it down, 1 g of this catalyst was placed in a reactor where was first reduced with 300 sccm of H<sub>2</sub> at 500 C for 30 min, then heated up to 700 C in 300 sccm of He, and finally exposed at that temperature to a mixture of 300 sccm of He and 100 sccm of C<sub>2</sub>H<sub>4</sub> for 20 min at 700 C. The final product (Onion carbon/SiO<sub>2</sub>) was then cooled down in helium.

#### 1.2.1.2. Synthesis of Janus Nanoparticles

As shown by Perro et al. [96,97], an emulsion stabilized by silica nanoparticles is first prepared with paraffin wax and water. The silica particles dispersed in a solution of ethanol/water are partially hydrophobized by addition of a surfactant. At 80 C the wax is melted and after sonication a water/wax emulsion is formed. When cooled down to room temperature, the wax droplets solidify and keep the silica nanoparticles trapped at the wax/water interface. The side of the silica particles free of wax is functionalized with aminopropyltriethoxysilane (APTES), which renders this side of the silica particles hydrophobic. Finally, the wax is dissolved with dichloromethane, releasing the Janus silica-nanoparticles, which are collected by centrifugation.

### *1.2.2. Preparation of Janus Particles-Stabilized Emulsions*

In order to prepare the water/oil emulsions stabilized by the different nanohybrids mentioned, DI water and decalin were used as the aqueous and organic phases, respectively. The nanohybrids were first dispersed in the water by sonication with a Horn sonicator (Fisher Scientific 600W, 20 kHz) at 25 % of amplitude for 30 min. Then, a volume of decalin was added and the final mixture was sonicated for 1 h in the same conditions. The water/decalin volume ratio was kept constant and equal to 1 in all cases. The amount of nanohybrids was varied as shown before. A green water-soluble dye (fluorescent Na salt) and a red oil-soluble (Sudan III) were added to the respective phases to help to differentiate the emulsion fraction.

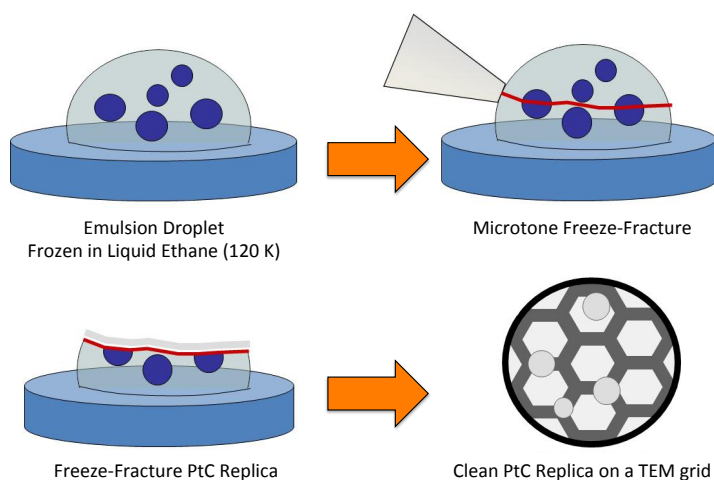
### *1.2.3. Preparation of Nanoparticles-Stabilized Foams*

For the stabilization of the foams hydrophobic particles AEROSIL<sup>®</sup> R972 obtained from Evonik were employed, which are a hydrophobic fumed silica after treated with DDS (Dimethyldichlorosilane) based on a hydrophilic fumed silica with a specific surface area of 130 m<sup>2</sup>/g. The stabilization of foams using hydrophobic nanoparticles was accomplished by dispersing the nanoparticles in an ethanol aqueous solution in the horn sonicator (Fisher Scientific 600W, 20 kHz) at 25 % of amplitude for 30 min. Then, the foam was prepared by introducing air into the aqueous phase using the horn sonicator for 5 minutes. This was accomplished by placing the tip of the sonicator at the water-air interface during the sonicator. A green water-soluble dye (fluorescent Na salt) was added to the aqueous phase.



#### 1.2.4. HRTEM Characterization of the Emulsions Stabilized by the Solid Nanohybrids

HRTEM images were obtained by freezing the emulsions in a bath of liquid ethane cooled to 120 K, in order to vitrify the water inside the emulsion droplet. The samples were then fractured in a vacuum, and then with Pt-C replicas of the surface were created (Figure 1.8). TEM measurements were then obtained on a JEOL JEM-2000FX.



**Figure 1.8: Freeze-fracture HRTEM characterization of nanoparticles-stabilized emulsions.**

#### 1.2.5. XPS Characterization of Nanohybrid Catalysts

XPS spectra were obtained on a Physical Electronics PHI5800 ESCA system, equipped with an  $AlK\alpha$  X-ray anode operated at 350W and 15kV. In this case the XPS spectrum was collected for the particle in dispersion and the nanoparticles-stabilized emulsions. Both were dried in vacuum before analysis until constant pressure was reached.

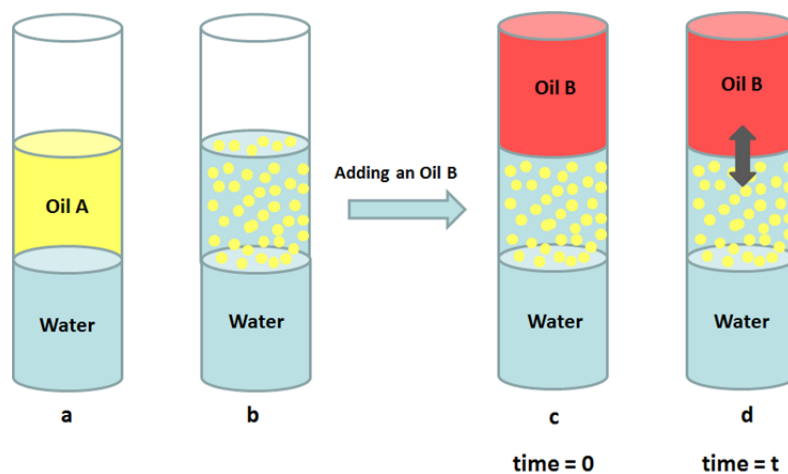
### *1.2.6. Droplet Size and Emulsion Fraction of Nanoparticles-Emulsions*

Once the nanoparticles-stabilized emulsion was prepared the emulsion fraction and droplet size were measured. Typically the emulsion fraction is calculated based on the ratio of emulsion volume and total volume. Then, a sample of the emulsion fraction was characterized by optical microscopy biological (XSP-150, Microscope, Inc) in order to identify the droplet size distribution.

### *1.2.7. Mass Transport in Nanoparticles-Stabilized Emulsions*

The experimental setup for testing the oil transport phenomena in our emulsion system is illustrated in Figure 1.10. Initially, an oil-in-water emulsion stabilized by the oxidized MWCNT/Al<sub>2</sub>O<sub>3</sub> was prepared. By selecting appropriate oil/water ratio and particle concentration, no extra free oil phase could be detected (Figures 1.9 a and b). In this case, we used 4 ml of oil and 12 ml water to prepare the emulsion. The oil phase in this step (Oil A) contained a mixture of equal volumes of different oils. Afterwards, a certain amount (4 ml) of a pure oil (Oil B) was carefully transferred onto the top of this emulsion layer (Figure 1.10c). As driven by the chemical potential difference, the mixed oils in the emulsion phase will migrate to the upper pure oil phase (Figure 1.10d). Thus, by monitoring the composition of the top oil layer as a function of time, we could estimate the speed of transportation of different oils from the emulsion phase to the upper oil phase. In this paper, the amount of oil transported was shown by dividing the respective oil concentration by the maximum oil concentration of that oil in

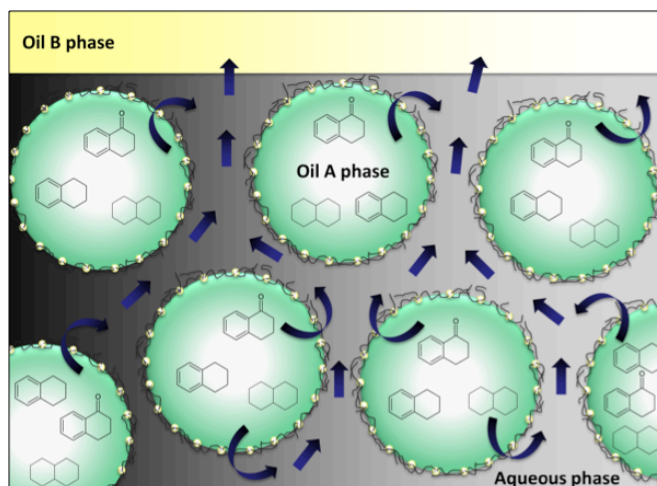
the free oil phase, assuming that eternally all the oils would become homogenous in the whole solution.



**Figure 1.9: Schematic description of the experimental setup used for this study.**

#### *1.2.8. Transportation Under Static Conditions*

First we investigated the oil transport phenomena under static conditions (no energetic agitation). The oil-in-water emulsion from which transportation took place was stabilized by 0.5 wt.% of oxidized MWCNT/Al<sub>2</sub>O<sub>3</sub>, and was made from an oil mixture containing equal amounts of tetralin, decalin, and  $\alpha$ -tetralone. The free oil phase added afterwards only contains pure tetralin. With this system, it was possible to study the transportation of decalin and  $\alpha$ -tetralone to the pure tetralin phase (Figure 1.10).



**Figure 1.10: Schematic description of the transportation from the oil A phase (tetralin, decalin and  $\alpha$ -tetralone) to the oil B phase (tetralin) present in the system studied.**

### 1.3. Results and Discussion

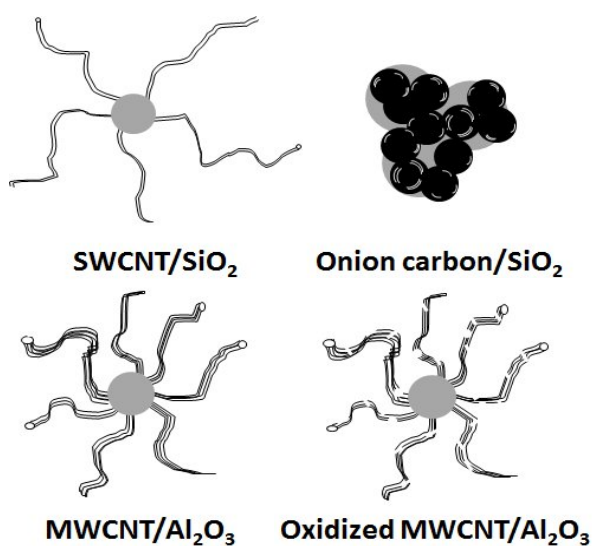
#### 1.3.1. Characterization of the CNT/MeO<sub>x</sub> Nanohybrids

Several techniques were employed to characterize the properties and structure of the CNT/MeO<sub>x</sub> nanohybrids and Janus nanoparticles. They include Raman spectroscopy, high-resolution transmission electron microscopy (HRTEM), and scanning electron microscopy.

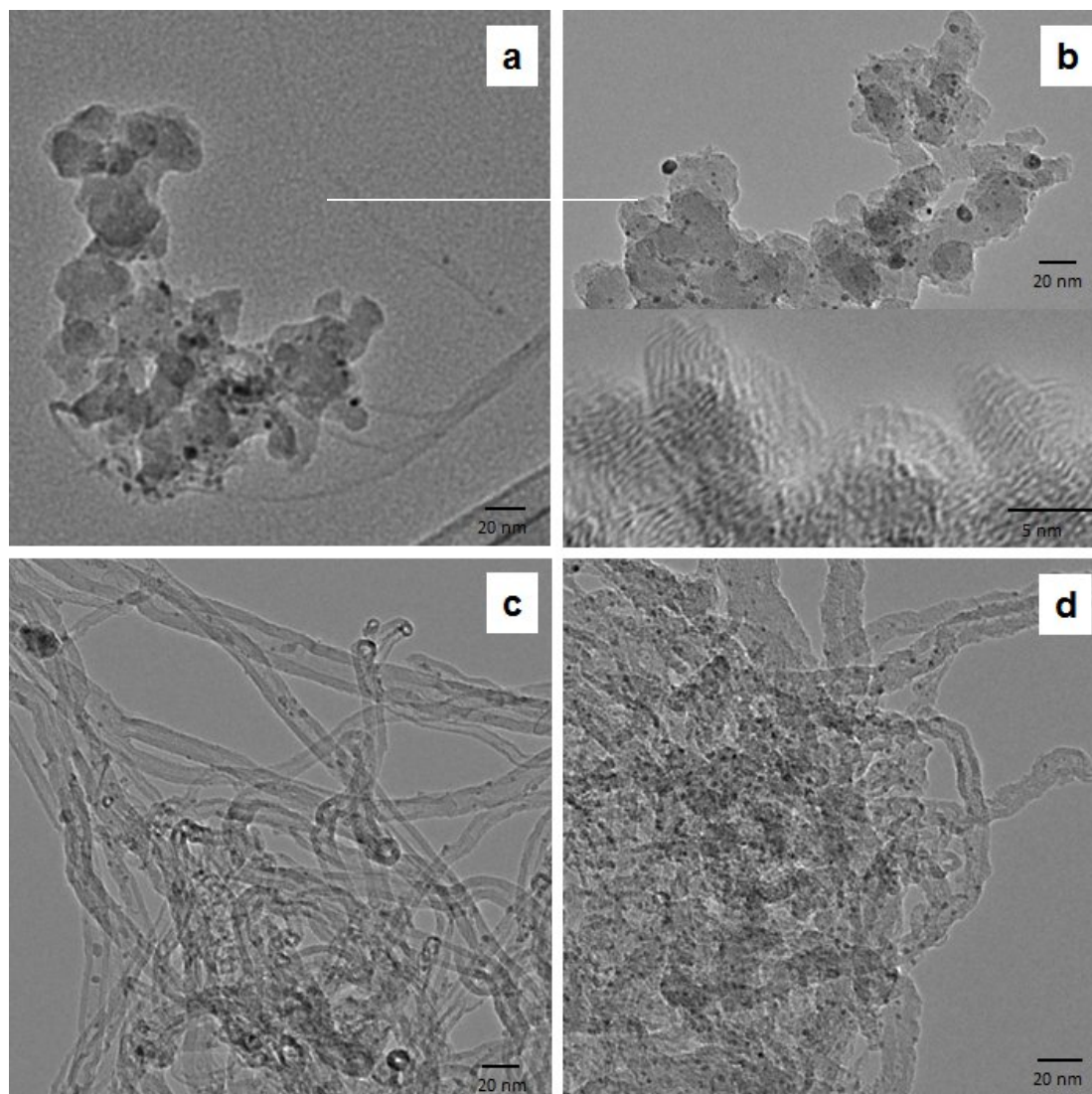
##### 1.3.1.1. HRTEM Characterization of CNT/MeO<sub>x</sub> Nanohybrids

As mentioned above, the core of this study is the comparison of a series of nanohybrids with different carbon structures. Specifically, the nanohybrids chosen for this comparison include SWCNT/SiO<sub>2</sub>, “onion-like” carbon/SiO<sub>2</sub>, MWCNT/Al<sub>2</sub>O<sub>3</sub>, and

nitric-acid-oxidized MWCNT/ $\text{Al}_2\text{O}_3$ . A schematic depiction of the structure of the different nanohybrids is shown in Figure 1.11. High-resolution HRTEM images of the catalysts prepared using these nanohybrids loaded with Pd clusters can be observed in Figure 1.12, illustrating the different morphologies of the nanohybrids. The carbon content is also quite different among the samples. While the carbon content on both SWCNT/ $\text{SiO}_2$  and “onion-like” carbon/ $\text{SiO}_2$  is around 7 %, on the MWCNT/ $\text{Al}_2\text{O}_3$  it is around 30 %.



**Figure 1.11: Scheme of the different nanohybrids used: SWCNT/ $\text{SiO}_2$ , “onion-like” carbon/ $\text{SiO}_2$ , MWCNT/ $\text{Al}_2\text{O}_3$ , and Oxidized MWCNT/ $\text{Al}_2\text{O}_3$ .**

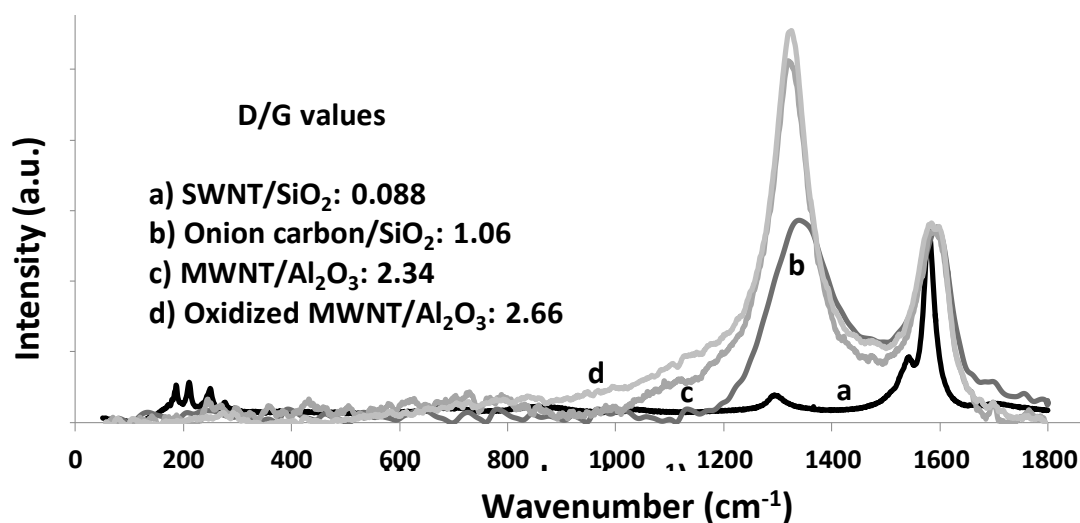


**Figure 1.12: HRTEM of the catalysts composed of 5 % wt. Pd supported on different nanohybrids: a) SWCNT/SiO<sub>2</sub>; b) “onion-like” carbon/SiO<sub>2</sub> (top: Pd on the nanohybrid; bottom: closer view of the “onion-like” carbon in the nanohybrid); c) MWCNT/Al<sub>2</sub>O<sub>3</sub>; and d) Oxidized MWCNT/Al<sub>2</sub>O<sub>3</sub>.**

#### 1.3.1.2. Raman Characterization of CNT/MeO<sub>x</sub> Nanohybrids

Raman spectroscopy has been used to characterize the carbon structure on the various nanohybrids. This technique has been widely employed in evaluating the purity and quality of CNT products. The relative density of defects in different CNT samples

has been typically evaluated in terms of two characteristic bands, the G band, which appears at  $\sim 1590\text{ cm}^{-1}$  is ascribed to  $\text{sp}^2$  ordered carbon, and the D band, which appears around  $1350\text{ cm}^{-1}$ , is commonly ascribed to  $\text{sp}^3$  carbon associated with defects. Figure 1.13 shows the normalized Raman spectra for the different nanohybrids, together with the calculated D/G intensity ratios. The SWCNT/SiO<sub>2</sub> had the smallest D/G ratio (0.09), consistent with a low density of defects. “Onion-like” carbon/SiO<sub>2</sub> have an intermediate value (1.1), while the most defective carbon structures are MWCNT/Al<sub>2</sub>O<sub>3</sub> and Oxidized MWCNT/Al<sub>2</sub>O<sub>3</sub> (D/G ratios of 2.3 and 2.7, respectively). A small, but noticeable change in intensity of the D band is observed upon oxidation.



**Figure 1.13:** Raman spectra of the different nanohybrids: a) SWCNT/SiO<sub>2</sub>, b) “onion-like” carbon/SiO<sub>2</sub>, c) MWCNT/Al<sub>2</sub>O<sub>3</sub> and d) Oxidized MWCNT/Al<sub>2</sub>O<sub>3</sub>.

### 1.3.1.3. XPS Characterization of CNT/MeO<sub>x</sub> Nanohybrids

The effect of the nitric acid oxidation of the MWCNT/Al<sub>2</sub>O<sub>3</sub> has been also evaluated by XPS analysis. Figure 1.14 shows the C(1s) spectra for the

MWCNT/Al<sub>2</sub>O<sub>3</sub>, before and after oxidation. Again, a slight but noticeable difference can be seen in the region of 286 eV, which can be ascribed to the formation of carboxylic groups upon the nitric acid oxidation treatment.

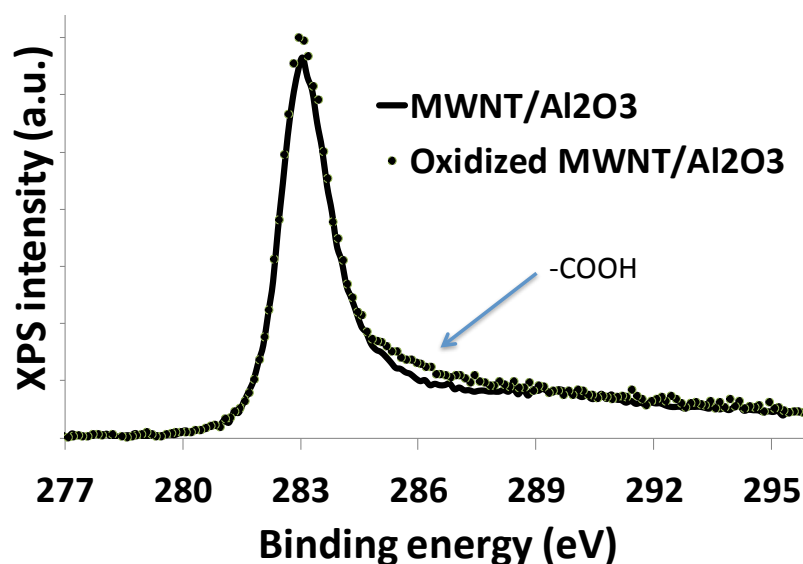


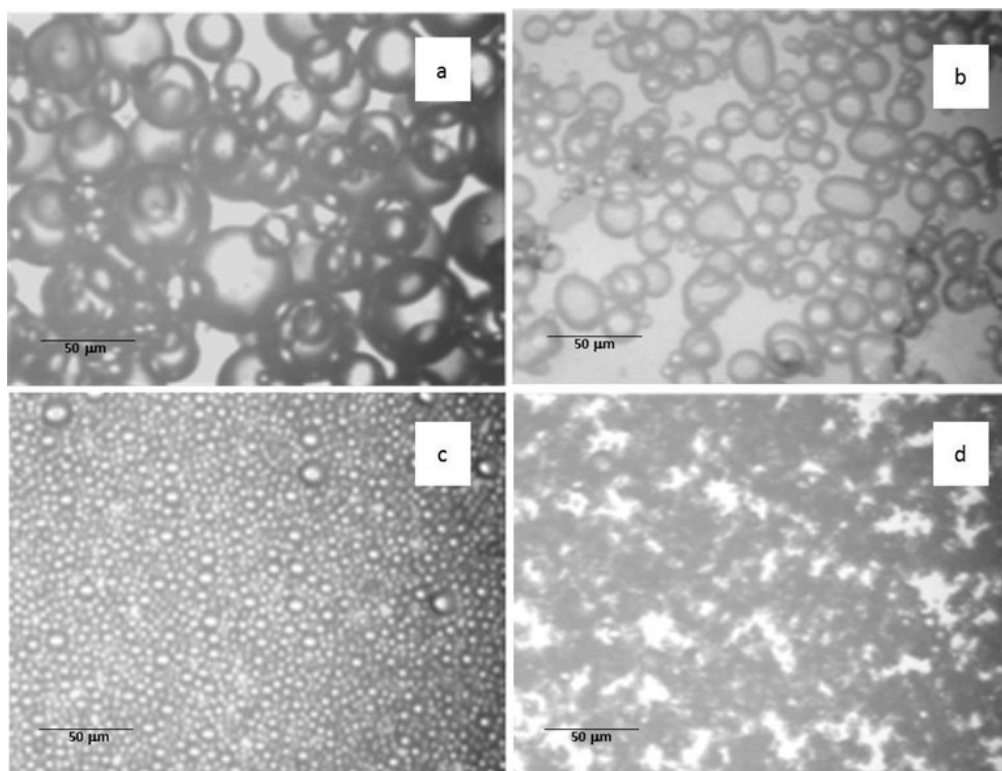
Figure 1.14: XPS spectra (C 1s) of MWCNT/Al<sub>2</sub>O<sub>3</sub> and Oxidized MWCNT/Al<sub>2</sub>O<sub>3</sub>.

### 1.3.2. CNT/MeO<sub>x</sub> Nanohybrids as Emulsion Stabilizers

The ability of the different nanohybrids (SWCNT/SiO<sub>2</sub>, “onion-like” carbon/SiO<sub>2</sub>, MWCNT/Al<sub>2</sub>O<sub>3</sub> and oxidized MWCNT/Al<sub>2</sub>O<sub>3</sub>) to stabilize water/decalin emulsions has been compared. Illustrative microscope images of the different emulsions prepared are shown in Figure 1.15. Clear differences in emulsion characteristics upon changing the type of nanohybrids are evident. Figure 1.16 shows the changes in emulsion volume fraction and the average droplet size obtained with the different nanohybrids analysed. The effect of changing the concentration of nanohybrids was also



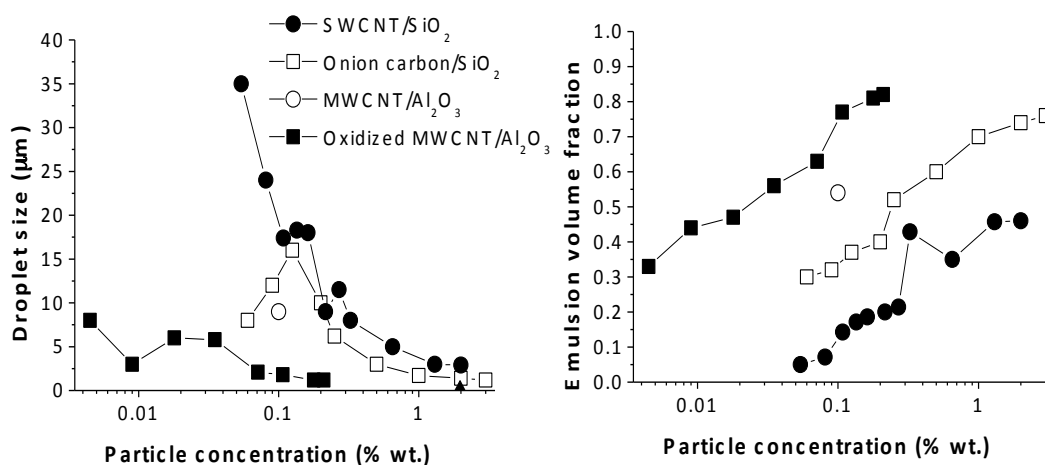
investigated, since we have shown before that the particle concentration strongly affects both the emulsion volume stabilized and the droplet size. In general, for all of the nanohybrids, an increase in particle concentration leads to an increase in the fraction of emulsion stabilized and a decrease in the size of the emulsion droplets.



**Figure 1.15: Microscope images of the water/decalin emulsions stabilized with a concentration of 1 % wt. of different nanohybrids: a) SWCNT/SiO<sub>2</sub>; b) “onion-like” carbon/SiO<sub>2</sub>; c) MWCNT/Al<sub>2</sub>O<sub>3</sub>; and d) Oxidized MWCNT/Al<sub>2</sub>O<sub>3</sub>.**

The higher viscosity of the medium when increasing the particle concentration may play a role in stabilizing smaller droplets [40]. Comparing the behaviour of the different nanohybrids, it can be concluded that the most effective nanohybrids in stabilizing interfacial area in emulsions are the oxidized MWCNT/Al<sub>2</sub>O<sub>3</sub>, since for a

given concentration they gave the highest values of emulsion fractions (up to 0.85) with the smallest droplet sizes (less than 2  $\mu\text{m}$ ). Accordingly, the effectiveness in stabilizing emulsions follows this sequence: oxidized MWCNT/ $\text{Al}_2\text{O}_3$  > MWCNT/ $\text{Al}_2\text{O}_3$  > “onion-like” carbon/ $\text{SiO}_2$  > SWCNT/ $\text{SiO}_2$ .



**Figure 1.16: Droplet size (left) and emulsion volume fraction (right) and vs. particle concentration for the water/decalin emulsions prepared with different nanohybrids: SWCNT/ $\text{SiO}_2$  [40], “onion-like” carbon/ $\text{SiO}_2$ , MWCNT/ $\text{Al}_2\text{O}_3$  and Oxidized MWCNT/ $\text{Al}_2\text{O}_3$ .**

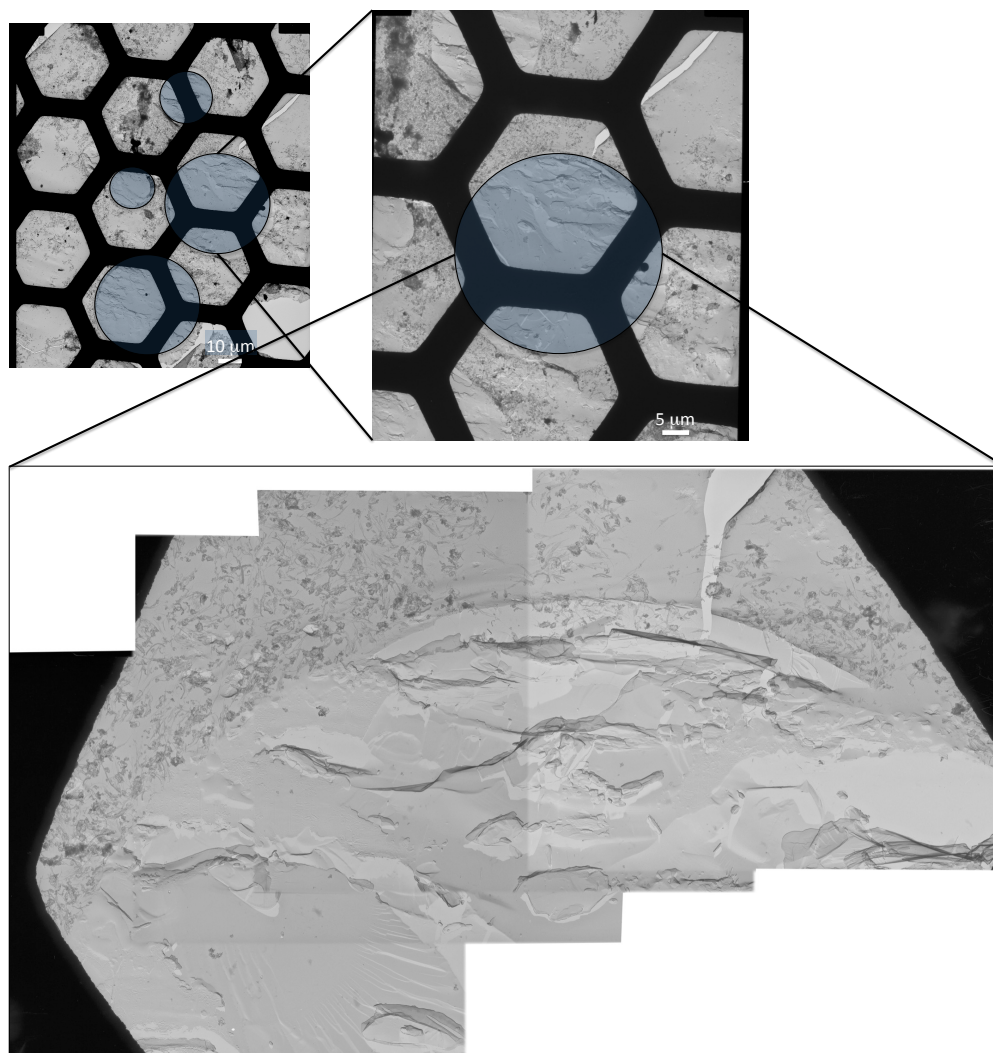
Depending on the hydrophobicity/hydrophilicity balance (HHB) in the composition of the nanohybrids, it is possible to stabilize either water-in-oil or oil-in-water emulsions (Figure 1.16). We have previously shown that when the particles were more hydrophilic, the wettability of the particles in water was enhanced, making the interface bend concave toward the oil and produce oil-in-water emulsions. In contrast, more hydrophobic particles tended to form water-in-oil emulsions [40]. Under the conditions studied here, the more hydrophobic SWCNT/ $\text{SiO}_2$  and MWCNT/ $\text{Al}_2\text{O}_3$  produced water-in-oil emulsions. In contrast, “onion-like” carbon/ $\text{SiO}_2$  and oxidized

MWCNT/Al<sub>2</sub>O<sub>3</sub> stabilized oil-in-water emulsions due to their higher hydrophilic character, due to their higher density of oxidized defects.

### *1.3.3. Freeze-fracture HRTEM of Nanohybrids-Stabilized Emulsions*

To investigate the structure of these solid-stabilized emulsions, we have used freeze fracture TEM. It is expected that the nanohybrids should orient themselves rather parallel to the interface, with the nonpolar nanotubes showing a preferential partition at the interface towards the oil side and the polar oxide nanoparticles silica toward the water side. One indication giving support to this structure comes from examining freeze fracture HRTEM images of the region around the emulsion droplets. These images are illustrated in Figure 1.17, which shows the image of the replica of a droplet at a magnification of 1000x, with a trace indicating the region of the interface at which the next images were captured, zoomed at increasing magnifications from 5000X to 12000X and to 48000X, respectively. The region that corresponded to the aqueous phase shows flat planes that are probably due to the cleavage of the frozen water droplets. These circular regions were rather clean and did not show features that can be ascribed to carbon nanotubes, but rather it can be observed clearly that the nanotubes and silica nanoparticles are indeed enriched near the interface. While they are not highly ordered, it does appear that some nanotubes protrude into the oil phase, and a significant amount of silica particles are aligned towards the water part of the interface. This provides further support that by depositing an active catalyst preferentially over either

the nanotubes or silica, selective reactions in either one phase or the other at the interface may potentially be achieved.

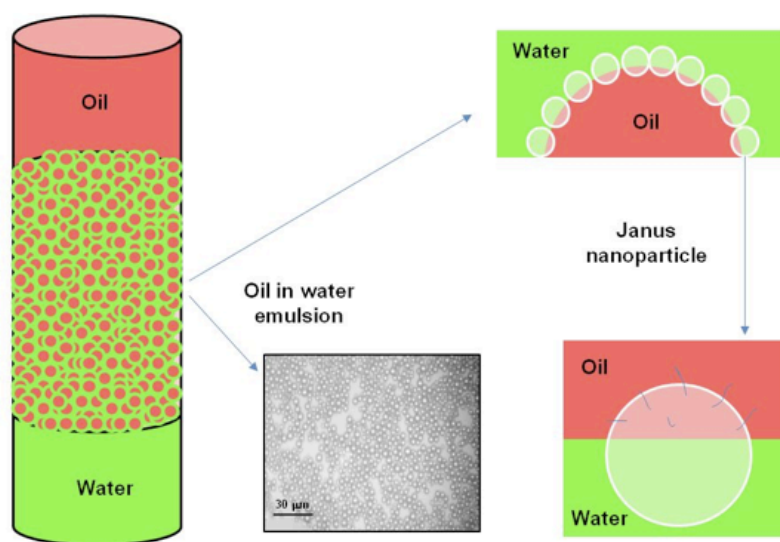


**Figure 1.17: Freeze-fracture HRTEM of the nanohybrid-stabilized emulsions.**

#### *1.3.4. Janus Nanoparticles as Emulsion Stabilizers*

Once the Janus particles were collected, a study of their capability to stabilize water/oil emulsions was carried out. To prepare the emulsions we used deionized water

and decalin (from Sigma-Aldrich) as oil. In order to detect more accurately the emulsion phase, a green water-soluble dye (fluorescent Na salt) and a red oil-soluble (Sudan III) were added to the system. As a result, we observed that the Janus silica-nanoparticles stabilized oil-in-water emulsions, since the emulsion droplets were red with a green continuous phase. This is due to the Janus particles synthesized are more hydrophilic than hydrophobic, which makes the oil-water interface bend in a way that produces oil-in-water emulsions. A microscopy image of the emulsion produced together with a schematic illustration of the three phases (oil/emulsion/water) present in the emulsion system is shown in Figure 1.18.



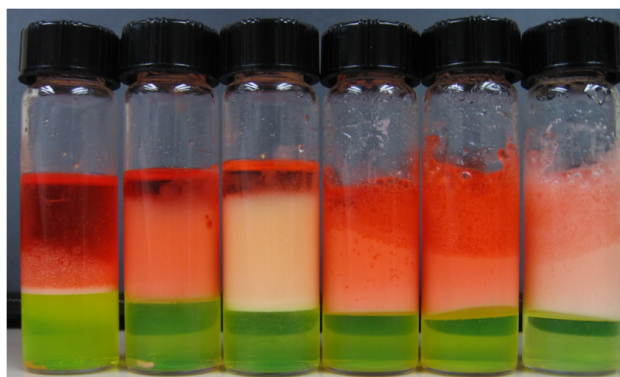
**Figure 1.18: Schematic description of the three phases (oil/emulsion/water) present in an oil-in-water emulsion stabilized by Janus silica-nanoparticles, together with a microscopy image of the emulsion phase.**

After proving the efficiency of the Janus silica nanoparticles to stabilize emulsions the following parameters were studied; concentration of Janus particles,

water/oil volume ratio, pre-sonication time (i.e. sonication time of the Janus particles in water, sonication time (which is the sonication time of the Janus particles in water and oil), temperature, pH, concentration of NaCl.

#### 1.3.4.1. Effect of Janus Nanoparticles Concentration

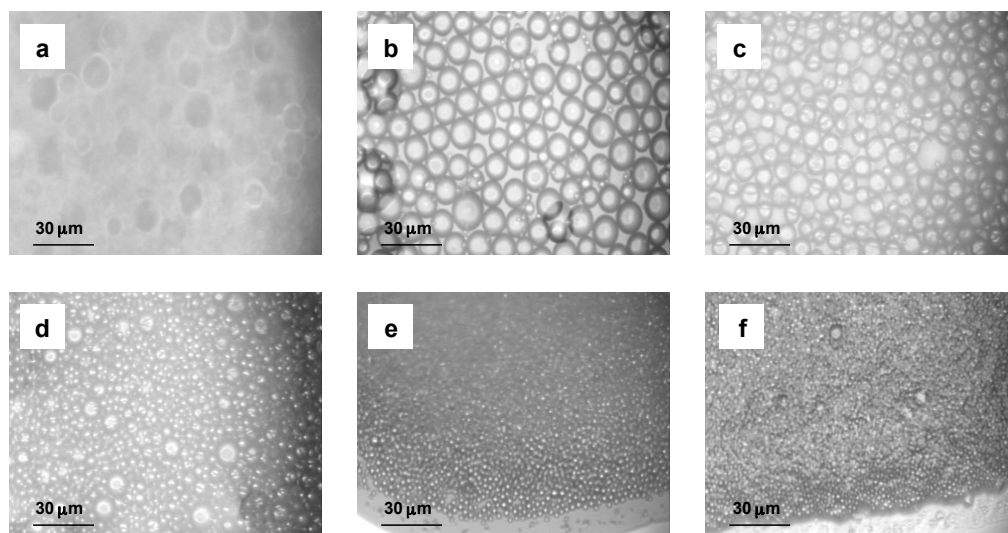
In order to analyze this effect, eight vials with 5 ml of water (with the green dye), 5 ml of decalin (with the red dye) and different concentrations of Janus particles were prepared. The concentrations studied were 0.05, 0.1, 0.15, 0.2, 0.3, 0.5, 1 and 2%. After mixing the three components, the mixture was sonicated in a Horn sonicator (Fisher Scientific 600W, 20 kHz) for 1 h. Some of the emulsions prepared are shown in Figure 1.19.



**Figure 1.19: Pictures of some of the emulsions prepared with different Janus particle concentration: from left to right, 0.05, 0.1, 0.15, 0.2, 0.3 and 0.5 % wt.**

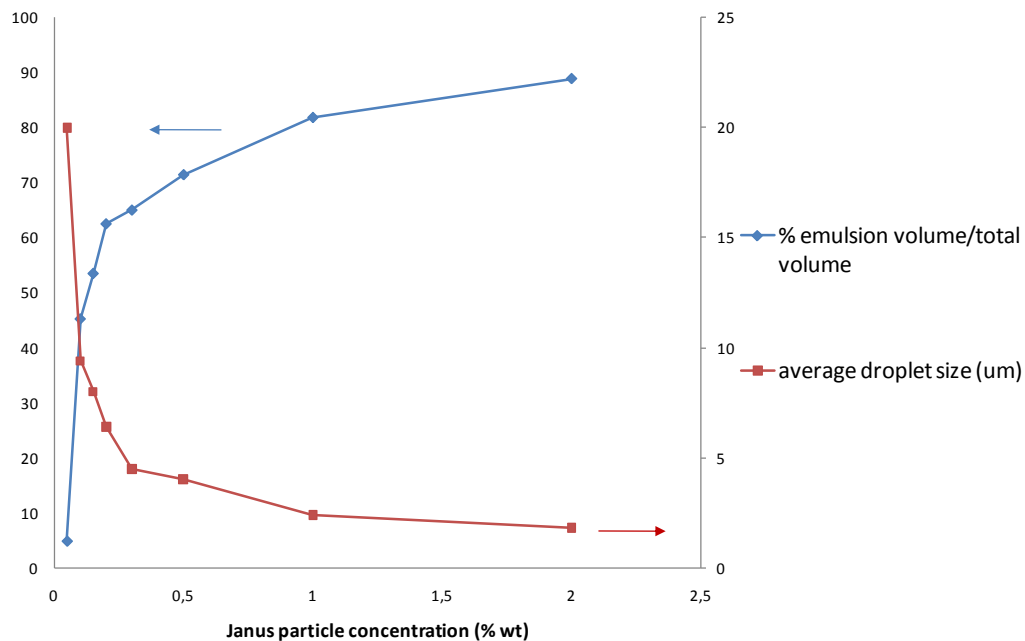
As it can be observed, there is an increase of the emulsion fraction obtained by increasing the amount of Janus particles added. Besides, microscopy images of these

emulsions were taken (Figure 1.20). From these pictures, an average droplet size of the emulsions was measured. The results of fraction emulsion and average droplet size are shown in Figure 1.21. The effect of the concentration of Janus particles on the emulsion properties is clear.



**Figure 1.20: Microscope images of emulsions prepared with different concentrations of Janus nanoparticles (wt. %): a) 0.05; b) 0.1; c) 0.15; d) 0.2; e) 1; f) 2.**

An increase in the particle concentration leads to an increase of the emulsion fraction and a decrease in the average droplet size. Both parameters seem to reach a plateau at higher concentrations. On the other hand, with the lowest concentration studied (0.05 % wt.), we observed that the emulsion fraction is very low and the droplet size is rather large, but for the next concentration (0.1 % wt.) the value of both parameters changed drastically. The fact that a minimum viscosity is necessary to stabilize small droplets of emulsion could be the reason why this happened.



**Figure 1.21: Results of % fraction of emulsion and average droplet size in the emulsions prepared with different concentrations of Janus particles.**

Regarding the other parameters, we can summarize with the following observations:

- 1) Water/oil volume ratio: we changed the water/oil volume ratio from 0.1 to 9. We observed a maximum in the surface utilization, since in the two extreme conditions (defect of oil or defect of water), the fractions of emulsion produced are lower than the rest ratios studied.
- 2) Pre-sonication time: varying this parameter from 15 to 180 min, it was observed that an increase in the pre-sonication time produces a slightly decrease in the droplet size.
- 3) Sonication time: varying this time from 15 to 180 min, no important differences were observed in the emulsion fraction or the droplet size.



- 4) Temperature: the emulsions were stable from 20 to 80 °C. No changes in the droplet size and emulsion fractions were observed.
- 5) pH: we can conclude that these emulsions are stable in the range of pH = 2-10.
- 6) Concentration of NaCl: we varied the concentration of NaCl in the aqueous phase from 0 to 1 M, and the results showed a slightly decrease in the surface utilization with increasing the salt concentration, but in general, they were stable and had small droplet sizes.

#### 1.3.4.2. Semi-Qualitative Study of the Surface Utilization in the Emulsions Stabilized by Janus Nanoparticles

With the volumetric fractions measured from the different fractions of the emulsion system, as well as the average droplet size, some calculations were done to determine the surface utilization of the emulsions. The values of the particle size of the Janus particles and their density were also necessary for these calculations. Since it is a semi-qualitative study to analyze the variation of the surface utilization in the different emulsions prepared, we assumed that the Janus particles were completely spherical particles with a diameter of 7 nm (the same as the primary particle size of the Aerosil 380).

In summary, the known parameters are the following: initial volumes of water and oil ( $V_{wi}$ ,  $V_{oi}$ ), density of the Janus particles (2.2 g/cc), particle size of the Janus particles

(7 nm), volumes of the different fractions after emulsion (oil:  $V_o$ , emulsion:  $V_e$ , water:  $V_w$ ), and the average droplet size of the emulsion (from the microscopy images).

With these parameters, it is possible to calculate the following parameters:

Number of droplets in the emulsion fraction (Eq. 1.1):

$$\text{Number of droplets} = \frac{V_e - (V_{wi} - V_w)}{V_{\text{one droplet}}} \quad (\text{Eq. 1.1})$$

Interfacial area (Eq. 1.2):

$$\text{Interfacial area} = A_{\text{external of one droplet}} \times \text{Number of droplets} \quad (\text{Eq. 1.2})$$

Number of Janus added (Eq. 1.3):

$$\text{Number of Janus added} = \frac{\text{mass}_{\text{total Janus particles added}}}{\text{mass}_{\text{one Janus particle}}} \quad (\text{Eq. 1.3})$$

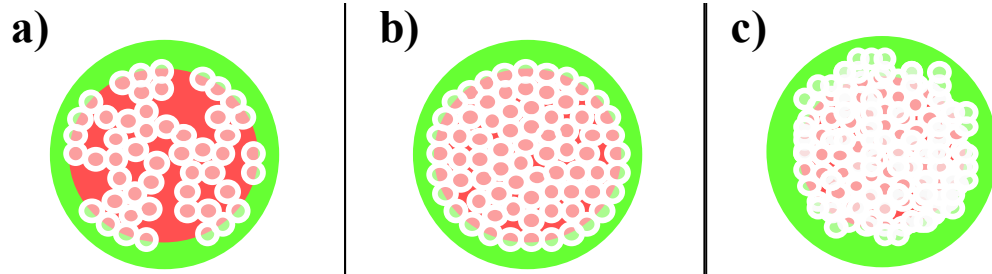
Surface utilization (Eq. 1.4):

$$\% \text{ Surface utilization} = 100 \times \frac{\text{Interfacial area}}{\text{Cross section area}_{\text{total Janus particles added}}} \quad (\text{Eq. 1.4})$$

Taking into account its definition, the value of surface utilization can be higher, equal or lower than 100%, which means three possible situations:

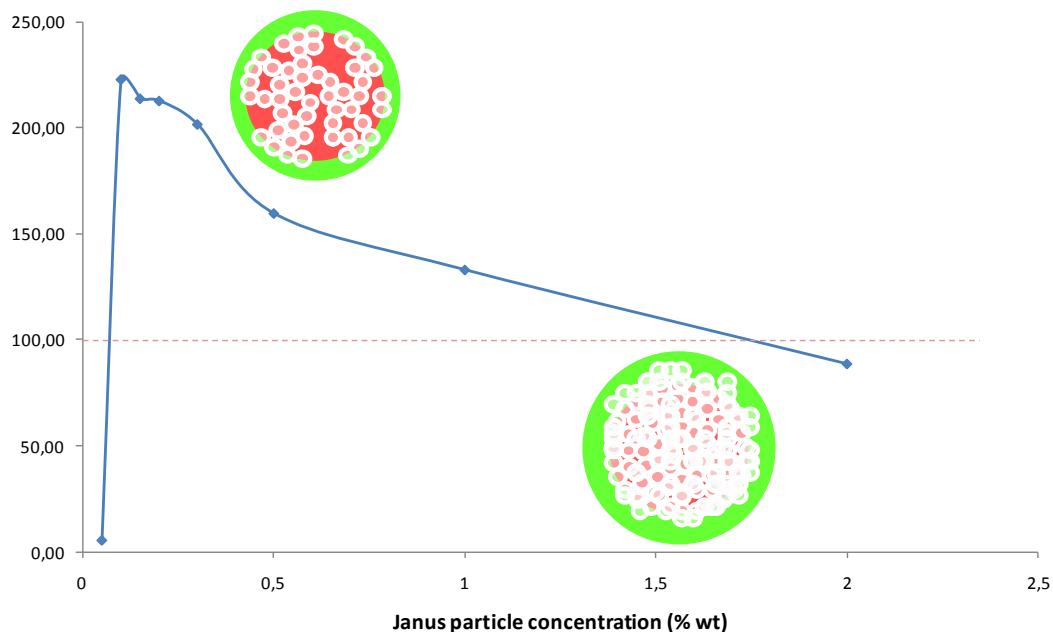
- 1) If surface utilization  $> 100 \%$ , the surface of the droplets is not completely covered by Janus particles (Figure 1.22a).
- 2) If surface utilization  $= 100 \%$ , the Janus particles exactly cover the surface of the droplets (Figure 1.22b).

- 3) If surface utilization  $< 100\%$ , there is an excess of Janus particles (Figure 1.22c).



**Figure 1.22: Schematic illustration of the different situations depending on the surface utilization values. a) Surface utilization  $> 100\%$ ; b) surface utilization =  $100\%$ ; c) surface utilization  $< 100\%$ .**

As an example, Figure 1.23 shows the results of surface utilization in the emulsions prepared with different concentrations of Janus silica nanoparticles. There is a decrease in the surface utilization value increasing the concentration of Janus particles, except for the lowest concentration (0.05 %). As we saw before, the decrease in the concentration of Janus particles reduces the number of droplets stabilized. On the other side, with higher concentrations, the surface utilization is lower due to the agglomeration of the Janus particles.

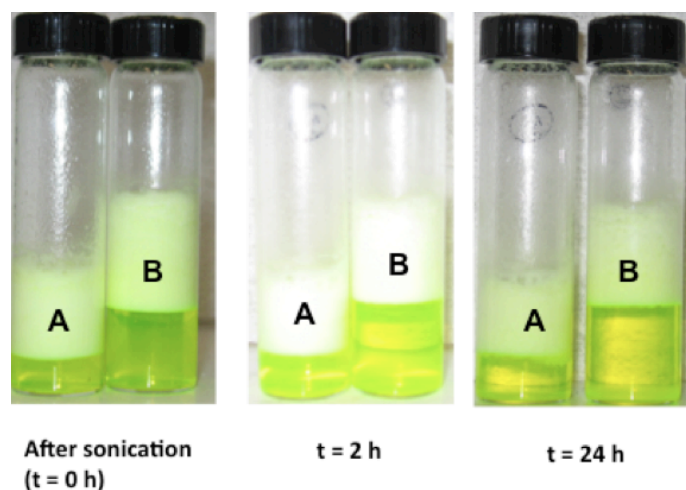


**Figure 1.23: Surface utilization values in the emulsions prepared with different concentrations of Janus particles.**

### *1.3.5. Nanoparticles-Stabilized Foams*

In a first approach, foams stabilized by hydrophobized silica particles were prepared. The hydrophobized silica (AEROSIL® R-972) is obtained after a treatment of hydrophilic silica with dichlorodimethylsilane.

Figure 1.24 shows the pictures of two different foams stabilized by the hydrophobic silica; foam A, which was prepared by 2 min of sonication of a mixture of 50 mg hydrophobic silica, 1 ml ethanol and 5 ml of deionized water; and foam B, which was prepared by 2 min of sonication of a mixture of 50 mg hydrophobic silica, 1 ml ethanol and 10 ml of deionized water.



**Figure 1.24: Pictures of the foams stabilized by hydrophobic silica nanoparticles, right after their formation and 2 and 24 h later.**

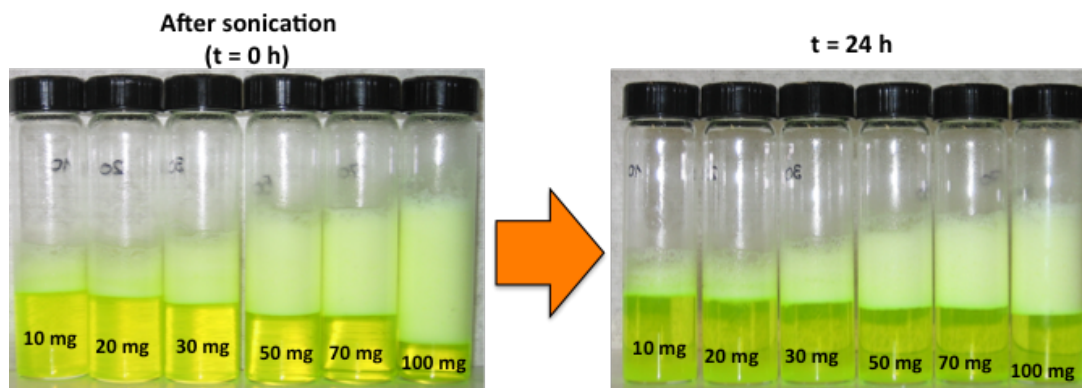
As it can be observed, in both cases foams were formed. The values of fraction of foam, defined as the percentage of volume of foam divided by the total volume, are summarized in Table 1.1. These values were measured right after the foam formation, and 2 and 24 h later. Once we tested the capability of these particles in stabilizing foams, the effect of different parameters was evaluated.

**Table 1.1: Values of fraction of foam formed (% vol) in the foams stabilized by hydrophobic silica particles.**

Foam	Foam Fraction		
	t = 0 h	t = 2 h	t = 24 h
A	70 %	70%	62 %
B	53 %	53 %	51 %

### 1.3.5.1. Effect of the Nanoparticles Concentration

In order to study the effect of particle concentration on the foam formation, foams with 1 ml ethanol, 10 ml of deionized water and different amounts of hydrophobic silica particles were prepared upon sonication for 2 min (Figure 1.25).

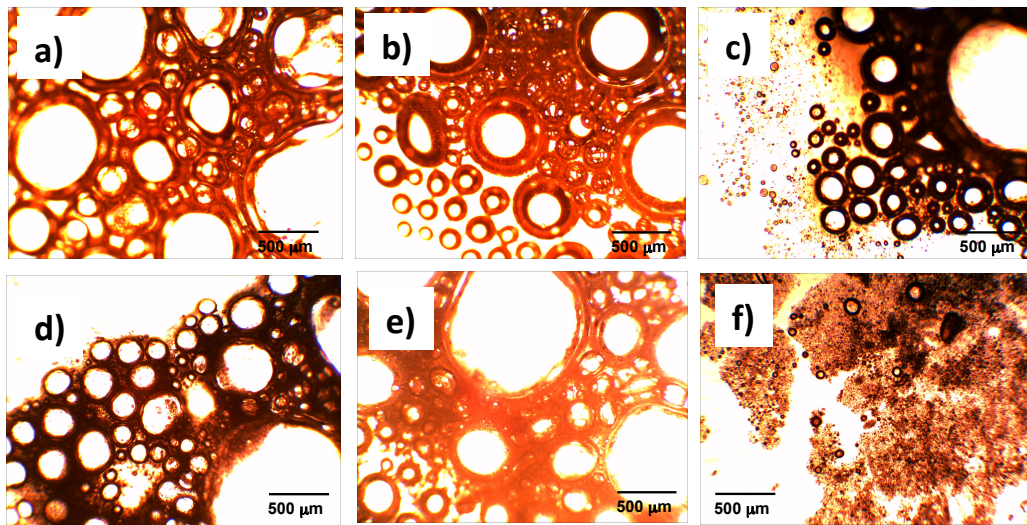


**Figure 1.25: Stability of foams after 24 hour at different concentrations of hydrophobic silica nanoparticles.**

As it can be observed in the results of fraction of foam formed (Table 1.2), an increase in the concentration of particles led to an increase in the fraction of foam stabilized. High fractions of foams were formed, up to 68 %, and they were very stable with time. In fact, after 6 months of their formation, they are still stable. Besides, from the optical microscope images of the emulsions (Figure 1.26), one can clearly distinguish the gas bubbles on the foam fraction, and also, how the bubbles are smaller with increasing the concentration of nanoparticles in the medium.

**Table 1.2: Stability of foams at different concentrations of hydrophobic silica nanoparticles.**

Mass of Hydrophobic Silica	Foam Fraction with Time		
	t = 0 h	t = 2 h	t = 24 h
10 mg	33 %	31 %	29 %
20 mg	37 %	35 %	32 %
30 mg	46 %	45 %	43 %
50 mg	53 %	53 %	51 %
70 mg	60 %	58 %	56 %
100 mg	68 %	62 %	60 %

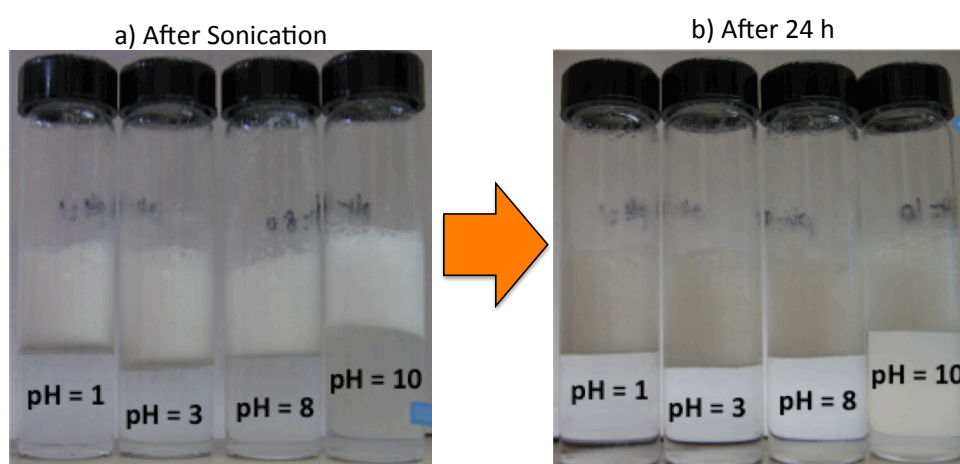


**Figure 1.26: Optical microscopy images of the nanoparticles-stabilized foams using different masses of hydrophobic silica particles; a) 10 mg, b) 20 mg, c) 30 mg, d) 50 mg, e) 70 mg, f) 100 mg. The particles were dispersed in 10 ml of DI water and 1 ml of ethanol using 2 minutes of horn sonication.**

#### 1.3.5.2. Effect of the pH on the Foam Stability

In order to study the effect of the pH on the foam properties, aqueous solutions of HCl and NaOH, reaching different pH, were prepared. Then, the foam was produced

by 2 min of sonication of 50 mg of hydrophobic silica particles, with 1 ml the ethanol and 10 ml of the solutions with different pH. The images of the resultant foams are shown in Figure 1.27, and the values of fraction of foam are summarized in Table 1.3. From these results it can be concluded that these foams can be stabilized under acid and basic conditions.



**Figure 1.27:** Pictures of the foams stabilized by hydrophobic silica nanoparticles, with aqueous solutions of different pH, right after their formation and 24 h later.

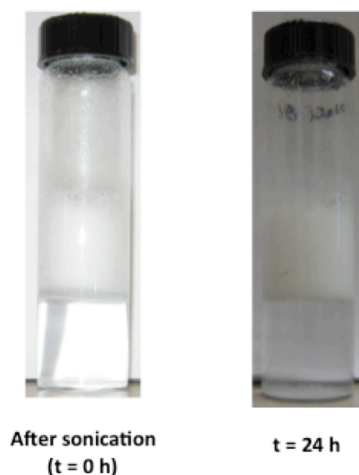
**Table 1.3:** Values of fraction of foam formed (% vol) in the foams stabilized by hydrophobic silica particles with aqueous solutions with different pH, right after the formation and 24 h later.

pH of the Solution	Foam Stability	
	t = 0 h	t = 24 h
pH = 1	53 %	47 %
pH = 3	57 %	49 %
pH = 8	49 %	48 %
pH = 10	42 %	38 %



### 1.3.5.3. Effect of the Salt Concentration on the Foam Stability

Finally, it was considered very important for this project to study the effect of the salt concentration on the formation of the foam. In this case, the foam was prepared by 2 min of sonication of a mixture of 50 mg hydrophobic silica particles, 1 ml of ethanol and 10 ml of a solution of 8 % wt. NaCl in deionized water. The results showed that these foams are also stable even at elevated ions concentrations (Figure 1.28). This striking result could be associated with the lack of ionizable functional groups at the nanoparticles surface, preventing the screening effect caused by the ions in solution.

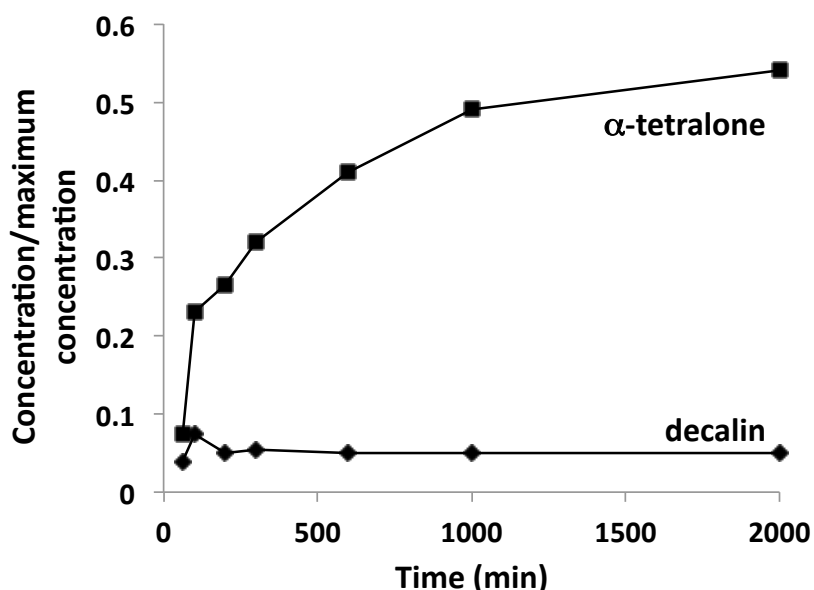


**Figure 1.28: Pictures of the foam stabilized by hydrophobic silica nanoparticles, with an aqueous of 8 % wt. NaCl, right after their formation and 24 h later.**

### 1.3.6. Mass Transport in Nanohybrids-Stabilized Emulsions

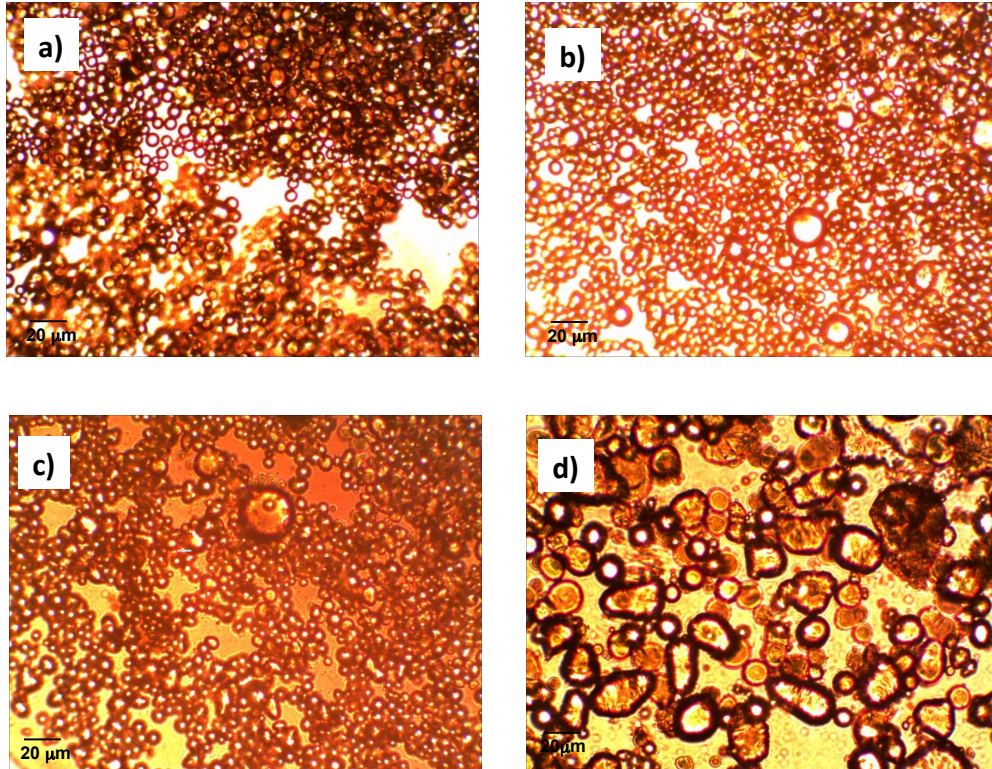
Figure 1.29 shows the amounts of decalin and  $\alpha$ -tetralone in the tetralin phase as a function of time. Under these conditions, diffusion governs the transportation of the

oil. It can be seen that the  $\alpha$ -tetralone amount increased linearly at initial stage but level off after elongated time, perhaps due to a smaller concentration gradient when transportation equilibrium was almost reached. In contrast, the decalin transportation appeared to be much slower throughout the process. This fact is a clear indicative of the strong dependence between the oil transportation on the oil type. This effect will be investigated in more detail below. Since it is a diffusion process, the transportation is mainly affected by the diffusivity of the oil through the water phase.



**Figure 1.29: Amounts of  $\alpha$ -tetralone and decalin transported from the emulsion phase (stabilized by 0.5 wt.% of oxidized MWCNT/ $\text{Al}_2\text{O}_3$ ) to the upper pure tetralin phase as a function of time under static conditions.**

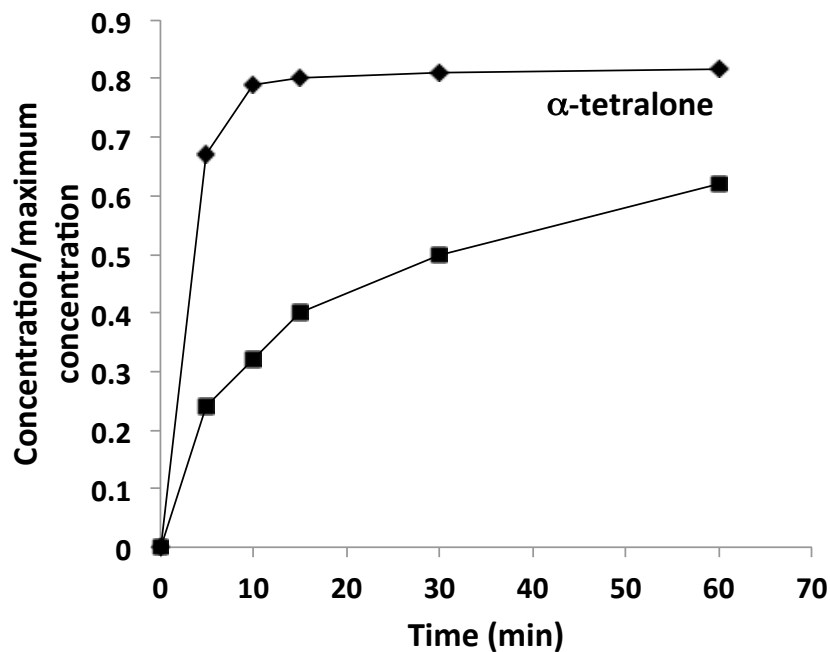
Besides, Figure 1.30 shows the microscope images of the emulsion right after its preparation (Figure 1.30a) and after 24 h under static conditions (Figure 1.30b). It can be observed that there is not an appreciable change in the droplet size of the emulsion.



**Figure 1.30: Microscope images of the emulsion stabilized by 2 wt.% of oxidized MWCNT/Al<sub>2</sub>O<sub>3</sub> a) right after preparation, and b) after 24 h of adding the free tetralin oil. Microscopy images of the emulsion stabilized by 6 wt.% of oxidized MWCNT/Al<sub>2</sub>O<sub>3</sub> c) right after preparation, and d) after being homogenized with the pure tetralin oil for 24 h by magnetically stirring at 200 rpm.**

### *1.3.7. Mass Transport in Nanohybrids-Stabilized Emulsions*

Next we turn our attention to the oil transportation phenomena under agitated conditions, which are closer to realistic reaction systems. The experiments were done in the same way as the above. The only difference is that, in this case, the whole solution was stirred continuously by a magnetic stirrer at 200 rpm to ensure the homogeneity of the mixture (no layer separation was found). Figure 1.31 shows the amounts of *a*-tetralone and decalin transported to the pure tetralin phase as a function of time.



**Figure 1.31: Amounts of  $\alpha$ -tetralone and decalin transported from the emulsion phase (stabilized by 0.5 wt.% of oxidized MWCNT/Al<sub>2</sub>O<sub>3</sub>) to the upper pure tetralin phase as a function of time under energy agitation.**

Clearly, the stirring greatly facilitates the oil transportation through the emulsion/oil interface. It can be observed that, under dynamic conditions, in 60 min the values of concentration/maximum concentration of the  $\alpha$ -tetralone and decalin in the free oil phase are 0.8 and 0.6, respectively, whereas under static conditions (Figure 1.31) after 2000 min, they are 0.5 and 0.05, respectively. This fact might be related to a higher chance of free oil-emulsion droplet oil contact because of the stirring, which might make the free oil phase split into many small oil droplets and mix with emulsion droplets, and also would favor the collision of droplets producing bigger ones. This result indicates that the mass transportation problem can be much lessened under realistic reaction conditions. Figures 1.30c and d show the microscopic images taken for

the emulsion phase at beginning and after been agitated with the pure tetralin phase for 24 h, respectively. Clearly, the emulsion droplet size becomes much bigger, indicating that the oil in the emulsion phase extensively exchanges with the pure oil phase. It is worth noticing that without this free oil phase, this emulsion is very stable and does not exhibit any significant droplet size change over time.

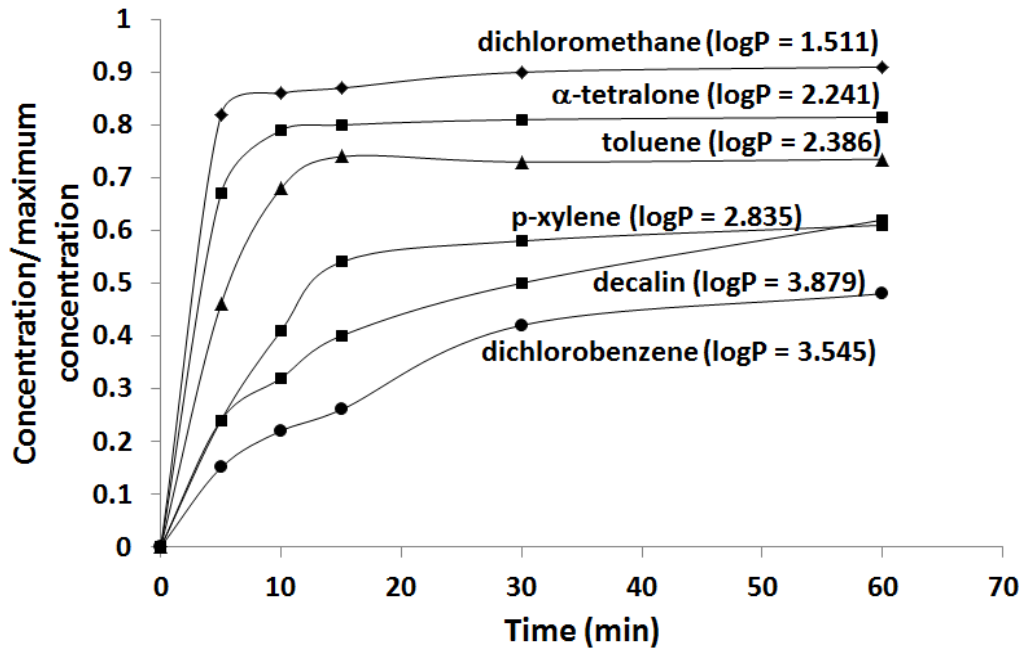
#### 1.3.7.1. Effect of the type of oil on the transportation

Figure 1.31 has shown that the oil type has a dramatic effect on its respective oil transportation rate through the emulsion phase. In order to understand this effect better, we have used seven different oils to prepare the initial oil-in-water emulsion. A mixture of equal volumes of tetralin,  $\alpha$ -tetralone, decalin, toluene, p-xylene, dichloromethane and 1,2-dichlorobenzene was used as organic phase to prepare the emulsion. All these oils have different log P values (Table 1.4) and, hence, different water solubility. The octanol-water partition coefficient logP is a parameter that can help to predict the solubility behaviour of a given molecule in water/oil systems. This value has been widely used in rational drug design and other QSAR property prediction studies as a measure of the hydrophobicity/hydrophilicity ratio of a given molecule. High values of logP are an indicative of a higher affinity of the molecule for the organic phase, and viceversa. The logP values can be calculated by using an Interactive logP calculator ([www.molinspiration.com/services/logp.html](http://www.molinspiration.com/services/logp.html)).

**Table 1.4: LogP values of the different types of oils used as the organic phase in the emulsion systems studied.**

<b>Organic Phase</b>	<b>Log P Value</b>
Tetralin	3.145
A-tetralone	2.241
Decalin	3.879
Toluene	2.386
P-Xylene	2.835
Dichloromethane	1.511
1,2-Dichlorobenzene	3.245

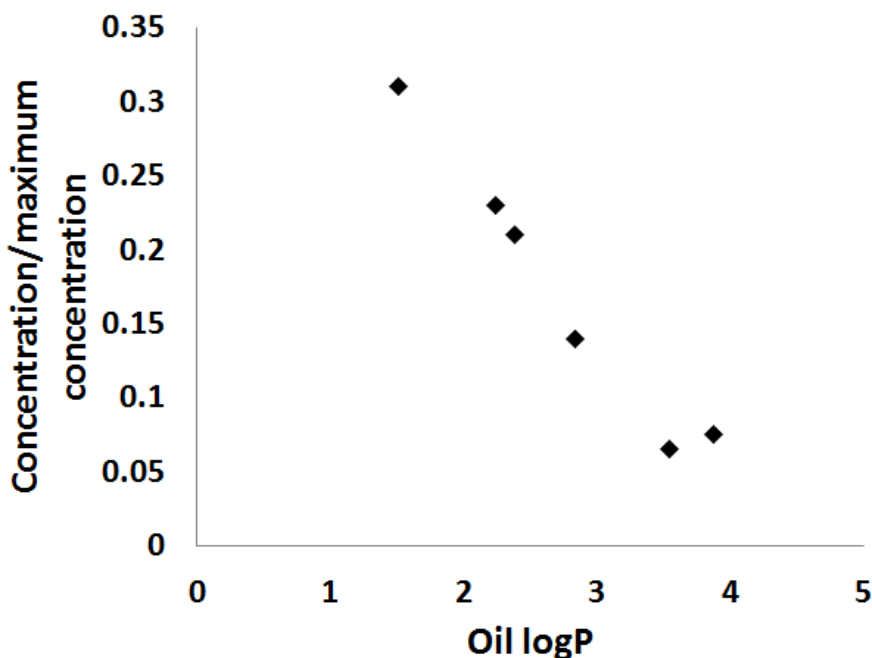
The transportation experiments were done in a similar way as the ones discussed above. The effect of the logP of the oils on the oil transportation rate was studied in agitated systems. The oil-in-water emulsion and the pure tetralin phase were continuously stirred to ensure homogeneity. Then the free oil phase was sampled after a certain period of time. Figure 1.32 shows the amount of different oils transported to the free oil phase. Overall, the agitation seems to enhance the oil transportation rate for all oil types. However, the oil solubility in water is also important for transport of the oils in an agitated system. For oil with high solubility, such as dichloromethane, the transport is much faster and its concentration in the free tetralin phase reach equilibrium earlier compared with the oils with lower solubility in water. This information is important for catalysis based on solid-stabilized emulsion systems. That means that in such agitated catalytic system, we can remove the reaction products and shift the reaction equilibrium to the right side by adding additional oils to the system and how this reaction equilibrium is shifted can be even governed by the compound solubility in water.



**Figure 1.32: Amounts of the different oils transported as a function of time (under energy agitation); the numbers in the parentheses are the logP values of the oils.**

The effect of the logP of the oils on the oil transportation rate was also investigated in static systems. Figure 1.32 shows the amounts of the six oils transported to the pure tetralin phase after 1200 minutes of adding the pure tetralin on the top of the emulsion layer (static conditions). As expected, the transportation under static conditions (Figure 1.29) is much slower than in agitated conditions (Figure 1.29). Similar to the agitated systems, the transportation rate of the six oils decreases as a function of logP value of the oils. This is clear evidence of the fact that the oil transportation speed is largely dependent on the solubility of the oil in water. Figure 1.33 also shows that the oil transportation rate becomes constant when the logP of the

oil is higher than 3, which might imply that other factors might become rate-limiting when the oil solubility in water becomes sufficiently low.

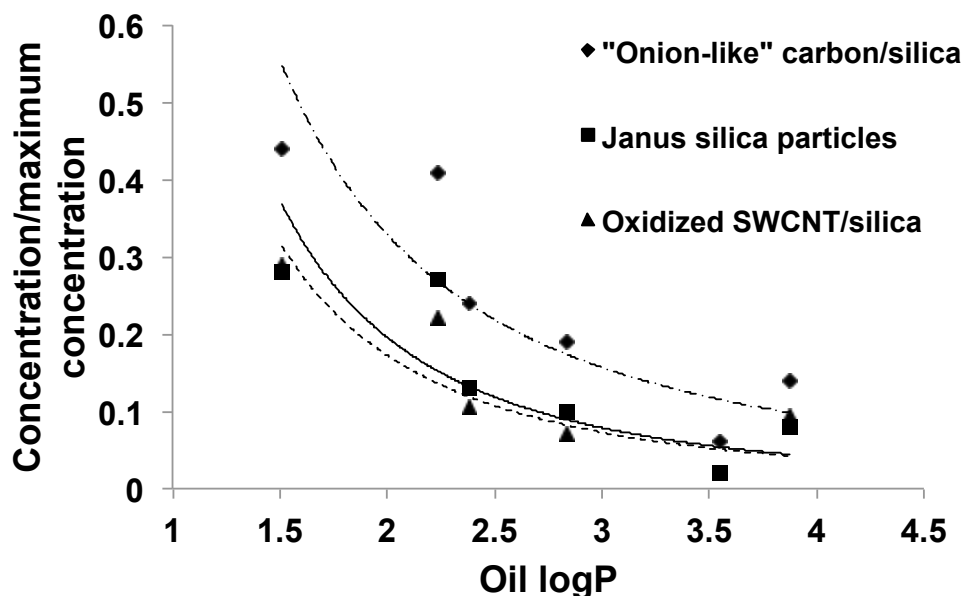


**Figure 1.33: Amounts of oil transported as a function of the log P of the oils (under static conditions).**

Other emulsifier particles were also tested to confirm if the above trend is general for o/w Pickering emulsion system. In previous studies, we have seen that Janus silica particles, “onion-like” carbon/silica [95], and oxidized SWCNT/silica are capable of stabilizing oil-in-water emulsions, and used for oil transport experiments here. Figure 1.34 shows the transport amounts of the six oils versus the logP of the oils for the three different emulsifier particle systems (the transportation has taken place after 1400 minutes). In general, the oil transportation using these particles to stabilize the initial emulsion exhibited the same trend as the one observed with the oxidized



MWCNT/Al<sub>2</sub>O<sub>3</sub>. Hence, the oil solubility in water appears to be a general factor in governing oil transportation rate in solid-stabilized emulsion systems.



**Figure 1.34: Amounts of oil transported as a function of the Log P of the oils for different particle systems (under static conditions).**

#### 1.4. Conclusions

A series of different amphiphilic nanohybrids based on carbon nanotubes (hydrophobic side) fused to different metal-oxide particles (hydrophilic side) have been investigated as stabilizers of water/oil emulsions. Also, Janus and completely hydrophobized nanoparticles have been developed for the stabilization of water-oil emulsions as well as water-air foams.

In addition, oil transport in an oil/emulsion/water system was systematically investigated by using gas chromatography (GC) and optical microscopy. The results

showed that the addition of energy in the form of agitation really enhance the transport rates. Under dynamic conditions, the transport is governed by convection and there is contact between the oil inside of the emulsion droplets and the free oil phase, favoring the transportation process. Furthermore, the emulsion droplets have been found to undergo substantial growth in size during the oil transport process under dynamic conditions. However, under static conditions, the transportation rate is much lower due to the absence of communication between both oil phases, and only depends on the diffusivity of the organic molecules in the water phase. Therefore, oils with a higher solubility in water transports faster to the free oil phase. These results have important implication for heterogeneous catalysis based on emulsion technology: by selectively removing or adding oils to an emulsion system the reaction equilibrium can be effectively shifted, depending on the species water solubility.

Finally, hydrophobic nanoparticles (silica AEROSIL R-972) have proven to stabilize foams with exceptional resistance towards high salinity, extreme basic and acid pH conditions. While, increasing the nanoparticles concentration enhanced the fraction of foam obtained the stability of the foams did not change dramatically

## References

- [1] M. Makosza and M. Fedorynski, *Cat. Rev. Sci. Eng.* 45 (2003) 321.
- [2] C. M. Starks, *J. Am. Chem. Soc.* 93 (1971) 195.
- [3] C. M. Starks and R. M. Owens, *J. Am. Chem. Soc.* 95 (1973) 3613.
- [4] E. V. Dehmlow and S. S. Dehmlow, in *Phase Transfer Catalysis*, 3<sup>rd</sup> Ed., Verlag Chemie, Weinheim, 1993.
- [5] C. M. Starks, C. L. Liotta and M. Halpern, in *Phase Transfer Catalysis: Fundamentals, Applications and Industrial Perspectives*, Chapman & Hall, New York, 1994.
- [6] Y. Sasson and R. Neumann, in *Handbook of Phase Transfer Catalysis*, Blackie Academic & Professional, London, 1997.
- [7] W. E. Keller, in *Phase-Transfer Reactions*, Fluka Compendium, Georg Thieme Verlag, Stuttgart-New York, Vol. I, 1986; Vol. II, 1987; Vol. III, 1992.
- [8] R. A. Jones, in *Quaternary Ammonium Salts: Their Use in Phase-Transfer Catalysis*, Academic Press, London, 2001.
- [9] Y. Goldberg, in *Phase Transfer Catalysis, Selected Problems and Applications*, Gordon & Breach Science, Switzerland, 1992.
- [10] E. Wiebus, B. Cornils. *Catalysis separation, recovery and recycling*. D. J. Cole-Hamilton, R. P. Tooze, Eds. Springer, Dordrecht, Netherlands, 2006, 105.
- [11] T.M. Schmitt. *Analysis of surfactants*. 2nd Ed. New York. Ed. Marcel Dekker, Inc. 2001.
- [12] D. J. Cole-Hamilton, *Science* 299 (2003) 1702.
- [13] S. Crossley, J. Faria, M. Shen, D. E. Resasco, *Science* 327 (2010) 68.

- [14] D. J. Cole-Hamilton, *Science* 41 (2010) 327.
- [15] S. Ungureanu, H. Deleuze, M.I. Popa, C. Sanchez and R. Backov, *Chem. Mater.* 20 (2008) 6494.
- [16] G.W. Huber, S. Iborra and A. Corma, *Chem. Rev.* 106 (2006) 4044.
- [17] T.P. Vispute, H. Zhang, A. Sanna, R. Xiao and G.W. Huber, *Science* 330 (2010) 1222.
- [18] G.W. Huber and J.A. Dumesic, *Catal. Today* 111 (2006) 119.
- [19] Y. Roman-Leshkov, C.J. Barrett, Z.Y. Liu and J.A. Dumesic, *Nature* 447 (2007) 982.
- [20] E.L. Kunkes, D.A. Simonetti, R.M. West, J.C. Serrano-Ruiz, C.A. Gartner and J.A. Dumesic, *Science* 322 (2008) 417.
- [21] O. Casanova, S. Iborra and A. Corma., *J. Catal.* 275 (2010) 236.
- [22] J. Gao, S.Wang, Z. Jiang, H. Lu, Y. Yang, F. Jing and C. Li, *J. Mol. Catal. A Chem.* 258 (2006) 261.
- [23] H. Lü, J. Gao, Z. Jiang, F. Jing, Y.Yang, G. Wang and C. Li, *J. Catal.* 239 (2006) 369.
- [24] V. Steen and E. Claeys, *Chem. Eng. Technol.* 31 (2008) 655.
- [25] A.V. Bridgwater, *Therm. Sci.* 8 (2004) 21.
- [26] B.P. Binks and P.D.I. Fletcher, *Langmuir* 17 (2001) 4708.
- [27] B.P. Binks and S.O. Lumsdon, *Phys. Chem. Chem. Phys.* 1 (1999) 3007.
- [28] T.N. Hunter, R.J. Pugh, G.V. Franks and G.J. Jameson, *Adv. Colloid Interface Sci.* 137 (2008) 57.

- [29] S. Arditty, C.P. Whitby, B.P. Binks, V. Schmitt and F. Leal-Calderon, *Eur. Phys. J. E* 11 (2003) 273.
- [30] R. Aveyard, J.H. Clint and T.S. Horozov, *Phys. Chem. Chem. Phys.* 5 (2003) 2398.
- [31] P. Kralchevsky, I. Ivanov, K.P. Ananthapadmanabhan and A. Lips, *Langmuir* 21 (2005) 50.
- [32] B.P. Binks, *Curr. Opin. Colloid Interface Sci.* 7 (2002) 21.
- [33] B.P. Binks and J.A. Rodrigues, *Angew. Chem. Int. Ed.* 44 (2005) 441.
- [34] R. Stadler, C. Auschra, J. Beckmann, U. Krappe, I. Voigt and L. Leibler, *Macromolecules* 28 (1995) 3080.
- [35] H. Takei and N. Shimizu, *Langmuir* 13 (1997) 1865.
- [36] S. Forster and M. Antonietti, *Adv. Mater.* 10 (1998) 195.
- [37] Y. Liu, V. Abetz and A.H.E. Muller, *Macromolecules* 36 (2003) 7894.
- [38] A.G. Vanakaras, *Langmuir* 22 (2006) 88.
- [39] O. Cayre, V. Paunov and O.D. Velev, *Chem. Commun.* 18 (2003) 2296.
- [40] M. Shen and D.E. Resasco, *Langmuir* 25 (2009) 10843.
- [41] J. Faria, M.P. Ruiz and D.E. Resasco, *Adv. Synth. Catal.* 352 (2010) 2359.
- [42] M.P. Ruiz, J. Faria, M. Shen, S. Drexler, T. Prasomsri and D.E. Resasco. *ChemSusChem* 4 (2011) 964.
- [43] S.U. Pickering, *J. Chem. Soc.* 91 (1907) 2001.
- [44] T.R. Briggs, *J. Ind. Eng. Chem.* 13 (1921) 1008.
- [45] S. Levine and E. Sanford, *Can. J. Chem. Eng.* 58 (1985) 622.
- [46] V.B. Menon and D.T. Wasan, *Colloids Surf.* 23 (1987) 353.

- [47] V.B. Menon and D.T. Wasan, *Sep. Sci. Technol.* 23 (1988) 2131.
- [48] D.E. Tambe and M.M. Shaftma, *Adv. Colloid Interface Sci.* 52 (1994) 1.
- [49] E.J. Johansen, I.M. Skjarvo, T. Lund, J. Sjoblom, H. Soderlund and G. Bostrom, *Colloids Surf.* 34 (1988) 353.
- [50] T.F. Tadros and B. Vincent, in *Encyclopedia of Emulsion Technology*, Vol. 1, Ed. P. Bercher, Marcel Decker, New York, 1983.
- [51] S. Levine, B. Bowen and S. Partridge, *Colloids Surf.* 38 (1989) 325.
- [52] N.D. Denkov, I.B. Ivanov and P.A. Kraichevsky, *J. Colloid Interface Sci.* 150 (1992) 589.
- [53] C.W. Bowman, *Proceedings of the 7<sup>th</sup> World Petroleum Congress*, Mexico City, 1967, 3, 583.
- [54] J.H. Schulman and J. Leja, *Trans. Faraday Soc.* 50 (1954) 598.
- [55] B.P. Binks and S.O. Lumsdon, *Langmuir* 17 (2001) 4540.
- [56] E.H. Lucassen-Reynders and M. Van den Tempel, *J. Phys. Chem.* 67 (1962) 731.
- [57] D.E. Tambe and M.M. Sharma, *J. Colloid Interface Sci.* 157 (1993) 244.
- [58] R. Aveyard, B.P. Binks and J.H. Clint, *Adv. Colloid Interface Sci.* 100-102, 2003, 503.
- [59] S. Arditty, C.P. Whitby, B.P. Binks, V. Schmitt and F. Leal-Calderon, *Eur. Phys. J.* 11 (2003) 273.
- [60] D.E. Tambe and M.M. Sharma, *J. Colloid Interface Sci.* 162 (1994) 1.
- [61] J.L. Sherrick, *J. Ind. Eng. Chem.* 13 (1921) 1010.
- [62] A.S. Lawrence and W.J. Kilner, *Inst. Petrol.* 34 (1948) 281.

- [63] H.N. Dunning, J.W. Moore and M.O. Denekas, *Ind. Eng. Chem.* 45 (1953) 1759.
- [64] M. Van der Waarden, *Kolloid-Z.* 156 (1957) 116.
- [65] C.M. Blair, *Chem. Ind.* 20 (1960) 538.
- [66] S.A. Berridge, M.A. and A. Loriston-Clarke, *J. Inst. Petrol.* 54 (1968) 333.
- [67] J.D. McLean and P.K. Kilpatrick, *J. Colloid Interface Sci.* 196 (1997) 23.
- [68] O.V. Gafonova and H.W. Yarranton, *J. Colloid Interface Sci.* 241 (2001) 469.
- [69] P.M. Spiecker, K.L. Gawrys, C.B. Trail and P.K. Kilpatrick, *Colloid Surf. A Physicochem. Eng. Aspects* 220 (2003) 9.
- [70] A.P. Sullivan and P.K. Kilpatrick, *Ind. Eng. Chem. Res.* 41 (2002) 3389.
- [71] T.A. Al-Sahhaf, M.A. Fahim and A.M. Elsharkawy, *J. Dispersion Sci. Technol.* 30 (2009) 597.
- [72] J.D. McLean and P.K. Kilpatrick, *J. Colloid Interface Sci.* 189 (1997) 242.
- [73] B.R. Midmore, *J. Colloid Interface Sci.* 213 (1999) 352.
- [74] N.P. Ashby and B.P. Binks, *Phys. Chem. Chem. Phys.* 2 (2000) 5640.
- [75] P. Finkle, H.D. Draper and J.H. Hildebrand, *J. Am. Chem. Soc.* 45 (1923) 2780.
- [76] J.H. Schulman and J. Leja, *Trans. Faraday Soc.*, 50 (1954) 598.
- [77] H. Barthel, *Colloids Surf.* 101 (1995) 217.
- [78] C. Casagrande and M. Veysie, *C. R. Acad. Sci. Paris II* 306 (1988) 1423.
- [79] C. Casagrande, P. Fabre, M. Veysie and E. Raphael, *Europhys. Lett.* 9 (1989) 251.
- [80] P. G. De Gennes Nobel Lecture, *Angew. Chem. Int. Ed. Engl.* 31 (1992) 842.
- [81] H. Fan, D. E. Resasco and A. Striolo, *Langmuir* 27 (2011) 5264.

- [82] M. Lattuada and T. A. Hatton, *Nano Today* 6 (2011) 286.
- [83] R. Taylor, *Adv. Colloid Interface Sci.* 75 (1998) 107.
- [84] A.J. Kabalnov, *J. Dispersion Sci. Technol.* 22 (2001) 1.
- [85] B.P. Binks, J.H. Clint, P.D.I. Fletcher, S. Rippon, S.D. Lubetkin and P.J. Mulqueen, *Langmuir* 15 (1999) 4495.
- [86] T.K.N. Hoang, V.B. La, L. Deriemaeker and R. Finsy. *Langmuir* 19 (2003) 6019.
- [87] L. Sacca, A. Drelich, F. Gomez, I. Pezron and D.J. Clause, *Dispersion Sci. Technol.* 29 (2008) 948.
- [88] B.P. Binks, P.D.I. Fletcher, B.L. Holt, P. Beaussoubre and K. Wong, *Phys. Chem. Chem. Phys.* 12 (2010) 2219.
- [89] J. Faria, M.P. Ruiz, D.E. Resasco, J. Harwell and B. Shiau 68930.159 – PCT Application No. PCTUS1257733 – Method and Foam Composition for recovering hydrocarbons from a subterranean reservoir.
- [90] T.N. Hunter, R.J. Pugh, G.V. Franks, G.J. Jameson, *Adv. Colloid Interface Sci.* 137 (2008) 57.
- [91] G. Kaptay, *Colloids Surf. A Physicochem. Eng. Asp.* 282-283, 2006, 387.
- [92] D.E. Tambe and M.M. Sharma, *J. Colloid Interface Sci.* 162 (1994) 1.
- [93] S. Levine, B.D. Bowen, S. Partridge. *J. Colloids Surf.* 38 (1989) 325.
- [94] P. Pieranski. *Phys. Rev. Lett.* 45 (1980) 569.
- [95] E.J. Stancik, M.J.O. Widenbrant, A.T. Laschitsch, J. Vermant, G.G. Fuller, *Langmuir* 18 (2002) 4372.



- [96] A. Perro, F. Meunier, V. Schmitt and S. Ravaine, *Colloids Surf. A* 332 (2009) 57.
- [97] A. Perro, S. Reculosa, S. Ravaine, E. B. Bourgeat- Lami and E. Duguet, *J. Mater. Chem.* 15 (2005) 3745.

## Chapter 2:

### Nanohybrid Catalysts for Bio-fuels Upgrading in Water-Oil Emulsions

#### 2.1. Introduction

The conversion of cellulosic biomass to transportation fuels and chemicals present important environmental, economic, and strategic advantages [1-3]. One of the main advantages is that the biomass-derived fuels can be CO<sub>2</sub>-neutral, since the CO<sub>2</sub> produced in their combustion can be reabsorbed by green plants and algae during photosynthesis [4-7]. However, it is a challenging and complex process that requires versatility to accept different kinds of biomass feedstocks and the ability to produce low-oxygen, high-energy content liquids, which should be fungible with conventional fuels [8], and also involves different catalytic technologies, such as the biomass acid hydrolysis, gasification and pyrolysis to produce sugars, syngas and bio-oil, respectively [9-13].

The arrival of biofuels in the energy and chemical industries, particularly those from second- and third-generation technologies, produced from non-food biomass resources, poses new challenges and research opportunities for fuel and chemicals development and catalytic upgrade [14]. Therefore, when designing an upgrading strategy, it is crucial to know how the product properties will be affected by the structure of the components that are being allowed into a given fuel or chemical stream. Thus, it is important to develop predicting tools to determine how the structure of a molecule added will affect each of the properties of interest. Since for many fuel and chemical properties the overall value of the property for the mixture depends non-

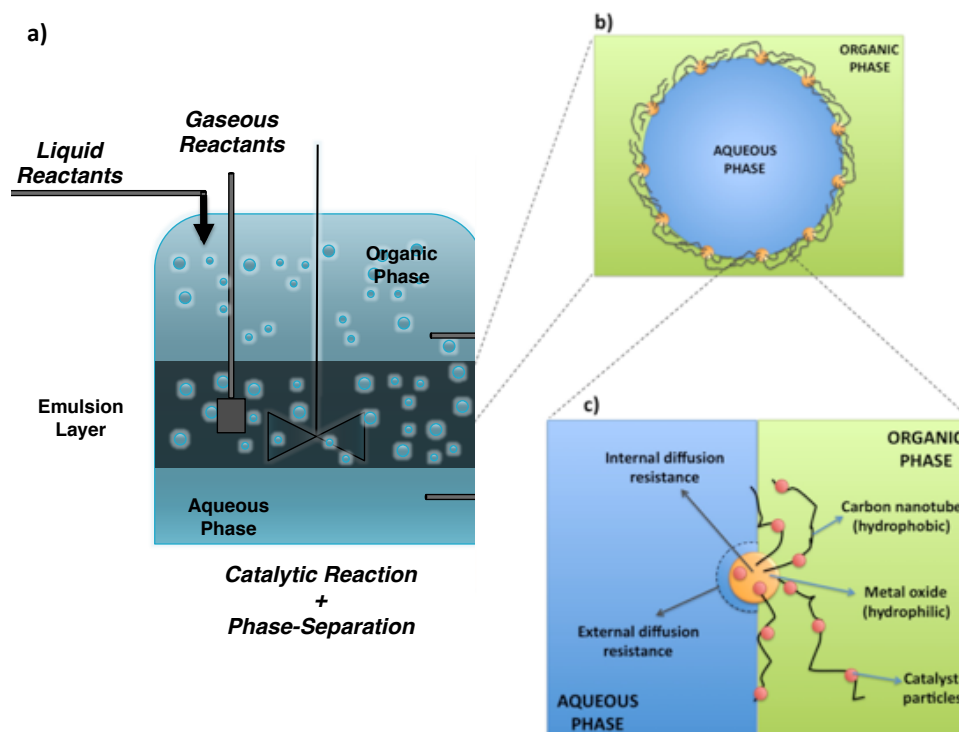
linearly on the individual contributions, the refiner also needs to be able to predict how new components behave in mixture.[15]

Revalorization of biomass, in contrast to crude oil, involves a more complex upgrading strategy, in which the functionalities of the molecules (-OH, CHO, COOH, etc.) must be exploited selectively build the molecular structure of the products, via coupling reaction, before the final removal of the excess oxygen via hydrotreating or decarbonylation/decarboxylation reactions. For example, condensation/hydrogenation reactions of biomass-derived molecules, such as furan compounds with ketones and aldehydes, have been studied using monophasic and biphasic systems [16-25]. Dumesic et al. [19] used a bifunctional catalyst (Pd/MgO-ZrO<sub>2</sub>) in a single aqueous phase reactor to perform aldol-condensation of furfural and 5-hydroxymethylfurfural (HMF) with acetone and, after the aldol-condensation reactions were completed, the products were dissolved in hexadecane and subjected to hydrogenation. In another study, Dumesic et al. [20] studied the condensation of furfural and HMF with acetone in aqueous phase using NaOH as catalyst, and then the condensation products were separated by adding an organic phase. The limited solubility of furfural in water and the degradation of HMF made necessary to use a relative high amount of base, and the addition of salt was needed to facilitate the products separation. Likewise, Huber [21] studied the performance of MgO-ZrO<sub>2</sub>, NaY and nitrogen substituted NaY (Nit-NaY) for the condensation of furfural compounds with acetone and propanal. They observed that, while MgO-ZrO<sub>2</sub> offered a higher selectivity to the double aldol-condensation products (C<sub>13</sub> and C<sub>15</sub>, respectively), NaY and Nit-NaY showed a better selectivity to the monomer products (C<sub>8</sub> and C<sub>9</sub>, respectively). The higher molecular weight products

obtained through these aldol-condensation/hydrogenation reactions could be used directly as fuel or additive to the current fuels. Besides, it is known that furfural and HMF are two important chemical building blocks for the production of transportation fuels as well as a variety of useful acids, aldehydes, alcohols, and amines [26-27].

The use of biphasic liquid systems in this type of reactions is a desirable strategy since water-soluble and organic-soluble compounds (catecols, syringols, guaiacols, phenolics, sugars, ketones, aldehydes, short carboxylic acids, and furfurals [28]) are present in the bio-oil. The water content in bio-oil is about 40% [29,30] and when it is contacted with hydrocarbons, or with partially deoxygenated fractions of the same bio-oil, a phase separation occurs, with a corresponding product distribution that depends on the partition coefficient of the compounds. Therefore, if properly handled, the presence of the two phases could be advantageously used in a reactive separation scheme in a continuous process.

In this context, our research group has pioneered the use of amphiphilic catalytic materials in the conversion of lignocellulosic biomass in biphasic liquid systems. Reactions take place at the water/oil interface in emulsions stabilized by catalytically active nanohybrids composed of carbon nanotubes fused to metal oxides. As shown in Figure 2.1 this strategy offers several advantages, such as: an enhancement in the rate of mass transfer between phases due to the generation of a higher interfacial area, the possibility of selectively convert molecules present in one of the phases, and the improvement in the separation of molecules, based on differences in relative solubilities [31-34].



**Figure 2.1: Schematic description of the triphasic system (Gas-Liquid-Solid) with a catalytically-reactive emulsion layer showing; a) continuous reactive-separation of the products and reactants based on solubility differences, b) emulsion droplet stabilized by nanohybrids composed of carbon nanotubes and metal oxide support, and c) schematic illustration of the amphiphilic catalyst particle adsorbed at the liquid/liquid interface.**

The amphiphilic character of these nanohybrids derives from the hydrophobicity of the carbon nanotubes [35,36] combined with the hydrophilicity of the metal oxides [37-39] used as supports to grow the nanotubes [32]. We have demonstrated that these amphiphilic catalytic nanoparticles are able to stabilize water/oil emulsions reproducibly and systematically. Further, fine tailoring of the nanohybrids surface chemistry and composition enabled us to modify the emulsion properties (volume, type of emulsion, droplet size), the metal dispersion and, therefore, the conversion of the reactants [33].

The present chapter reviews the promising results obtained with this novel technology for three major biomass conversion reactions; hydrodeoxygenation of lignin-derived molecules, aldol-condensation/hydrogenation of furan and ketones, and Fischer-Tropsch synthesis of bio-syngas. Additionally, Quantitative Structure Property Relationships (QSPR) have been developed to predict the relative response factors, relative retention times, octane and cetane numbers of some of the products from the condensation and hydrogenation reactions.

#### *2.1.1. Revalorization of Lignocellulosic Biomass*

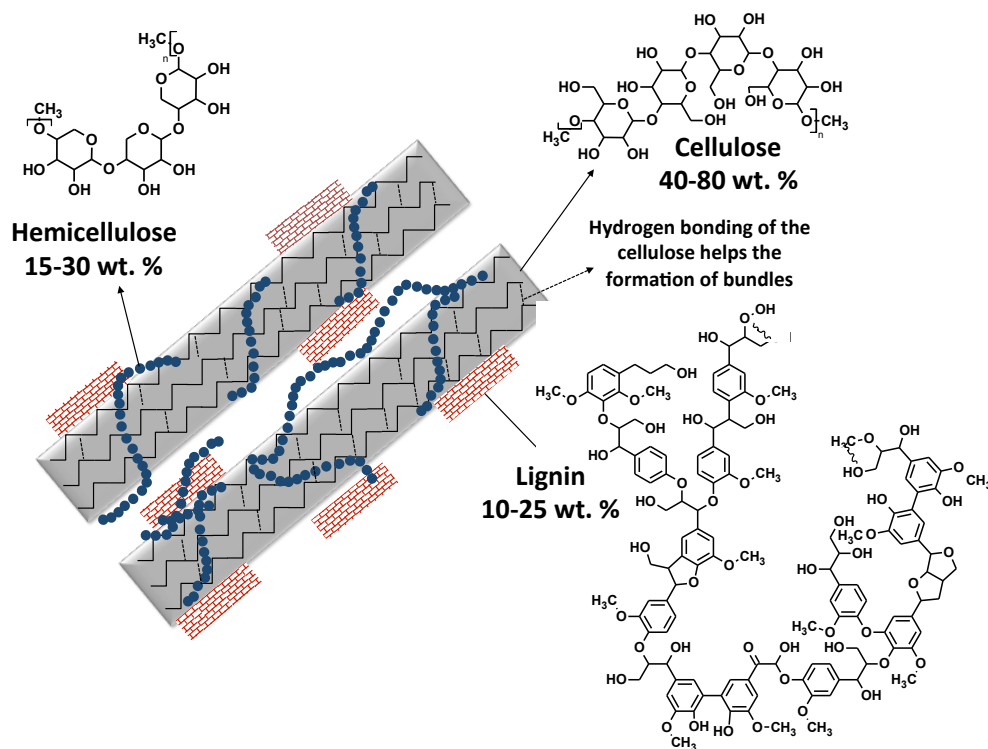
Photosynthesis uses solar radiation to convert energy-poor carbon dioxide and water into energy-rich carbohydrates  $(\text{CH}_2\text{O})_n$  and molecular oxygen ( $\text{O}_2$ ) [40]. These carbohydrates are stored in the plants in the form of polysaccharides that include starch, cellulose, and hemicellulose and account for up to 75 % of the plant mass. Although the energy efficiency of the photosynthesis process varies from 0.1 to 8.0 %, the areal growth rate of the plants is usually very high (6 to 90 metric tons/ha-year). There are many sources of biomass available that can be used the feedstock in the production of biofuels and chemical intermediates, including: waste materials (agricultural or urban), forest products (wood, logging residues, trees, shrubs), energy crops (starch crops such as corn, wheat, barley; sugar crops; grasses; woody crops; vegetable oils; hydrocarbon plants), or aquatic biomass (algae, water weed, water hyacinth) [8].

The availability of large quantities of biomass-derived materials is a key factor in the scaling process of biofuels production. In the U.S. only, it is estimated that  $1.3 \times 10^9$  metric tons of dry biomass/year could be sustainably produced for biofuels, without

any significant impact on its food, feed, and export demands [41]. This amount of biomass has an energy content of  $3.8 \times 10^9$  boe (barrels of oil energy equivalent), which represents 54% of the annual demand of crude oil in the U.S. [42,43].

### *2.1.2. Lignocellulosic Biomass Structure*

Polysaccharides in plants have very distinct functions and their molecular structures are the most appropriate for each purpose. For example, to give structural resistance to the plant, cellulose is a large and well-organized polymer and is located in the primary cell wall. In contrast, hemicellulose is a branched polysaccharide that is less rigid and able to wrap around the cellulose structure (Figure 2.2). Finally, starch is a polymer of d-glucose with  $\alpha$ -1,4-glycosidic bonds (repeating unit  $C_{12}H_{16}O_5$ ) [8,44]. Those linkages occur in chains of  $\alpha$ -1,4 linkages with branches formed as a result of  $\alpha$ -1,6 linkages, making its structure highly amorphous and readily attacked by enzymes in the digestive system of animals and humans. Starch is a main constituent of corn, rice, potato, etc. Although it has been widely used for fuels and chemicals production [42,45], starch should not be replaced as a source of food [46].



**Figure 2.2: Schematic representation of the composition of lignocellulosic biomass.**

Another major component of biomass is lignin (10-25 %), which has a noncarbohydrate polyphenolic structure that is encrusted in the walls of the cell and cement it together (Figure 2.2). This complex, cross-linked, highly aromatic structure (molecular weight  $\sim 10,000$  g/mol) is derived from three monomers called monolignols (coniferyl alcohol, sinapyl alcohol and p-coumaryl alcohol). Coniferyl alcohol is the predominant lignin monomer found in softwoods, while p-coumaryl alcohol is a minor component of grass and forage type lignins. Both coniferyl and sinapyl alcohols are the building blocks of hardwood lignin [47,48]. Other compounds present in biomass in smaller quantities include pigments, sterols, triglycerides, terpenoids, resins, waxes, alkaloids, and terpenes.



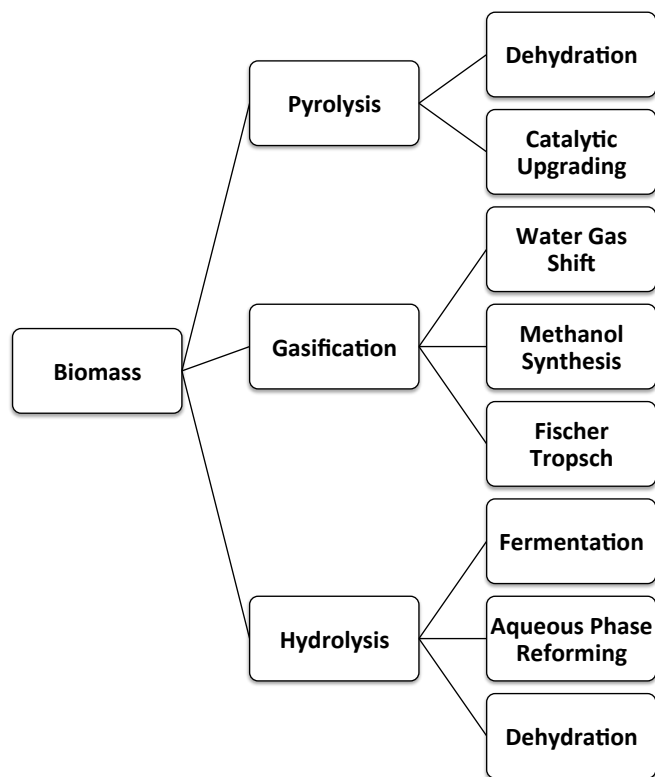
### *2.1.3. Primary Conversion of Lignocellulosic Biomass*

Although lignocellulose is one of the most abundant sources of biomass, its conversion into liquid fuels is a challenging task [49]. The more reactive sugar polymers in the plant are protected by the highly unreactive lignin fraction. For that reason, an effective pretreatment step is necessary to break down the refractory lignin seal, disrupt the crystalline structure of the cellulose, and increase the surface area of the biomass. A variety of methods are available to perform this pretreatment including immersion in hot water, dilute acid solutions, caustic lime/ammonia, and steam explosions [50,51].

Figure 2.3 summarizes the three major approaches suitable for primary processing of lignocellulosic biomass [52]. They are gasification to syngas [53,54], liquefaction (pyrolysis) to bio-oil [55], and hydrolysis for production of sugars [56]. Afterwards, further refining is necessary (secondary processing) to bring the mixture to the range of the desired fuel by reducing the oxygen concentration and maximizing the energy content of the liquid.

Several routes have been proposed for the secondary processing. They include (a) conversion of biomass-derived syngas into alkanes or methanol by Fischer-Tropsch or methanol synthesis [57,58], (b) catalytic aromatization, condensation and hydrodeoxygenation of bio-oil for hydrocarbons production [59-65], (c) enzymatic fermentation of sugars for methanol and butanol generation [66], (d) hydrogen synthesis by aqueous phase reforming of sugar-derived species [67], (e) conversion of monosaccharide molecules into aromatics and coke by zeolite upgrading [68-70], (f)

fuels production by biphasic processing of sugars and oxygen-containing molecules [71,72], and (g) esterification of triglycerides for biodiesel synthesis [73].



**Figure 2.3: Different strategies for primary conversion of lignocellulosic biomass.**

#### 2.1.3.1 Gasification of Lignocellulosic Biomass

The thermo-chemical conversion of biomass to gases has attracted significant attention in the research and industry community as it offers high conversion efficiency [74]. It is one of the strategies for exploitation of renewable fuels and power generation. Biomass gasification also assists the bioremediation plans as it converts the biomass wastes into clean fuel gases and biofuels. Biomass gasification is a rather complicated process in which mass and heat transport are coupled with the catalytic reactions promoted by the presence of impurities in the biomass (e.g. Na, Li, Ca, K). Such

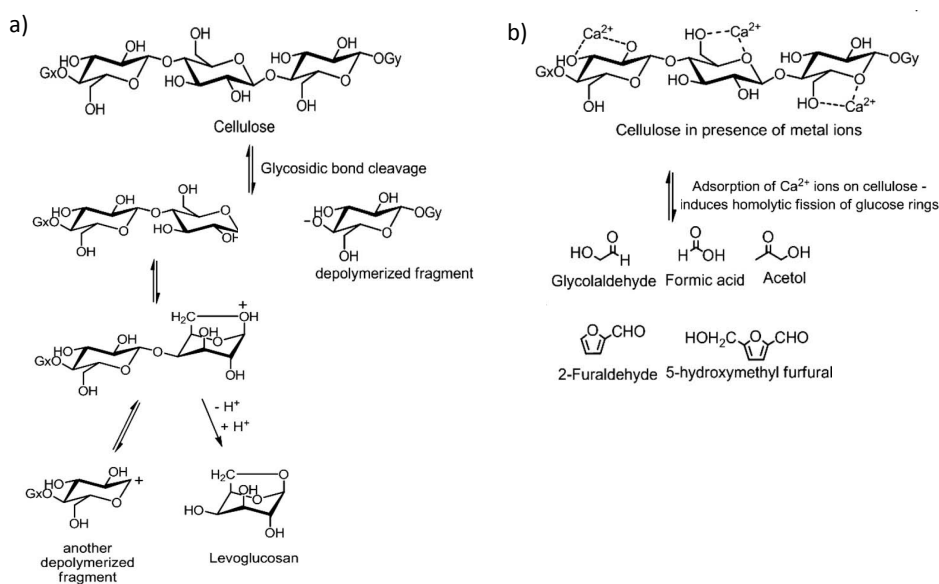
convoluted system requires the systematic study of the different phenomena involved, including effect of the biomass composition, process temperature, gasifying agent, steam to biomass ratio, particle size, bed materials. A more detail description of the influence of these parameters can be found in previous reviews [54,75,76].

Briefly, the process involves the conversion of biomass to a gaseous stream enriched in CO, H<sub>2</sub>, N<sub>2</sub> and CH<sub>4</sub> with medium to high Low Heating Value (LHV), which is suitable for further exploitation in internal combustion engines, turbines [77], and Fischer-Tropsch synthesis. For instance, commercialized production of various transportation fuels from coal and natural gas has been well demonstrated by Sasol and Mobil plants [78]. However, such process is not yet established for biomass due to the difficulties in synthesis gas production and clean-up and also low heating value of the product gas in comparison to natural gas.

#### 2.1.3.2. Pyrolysis of Lignocellulosic Biomass

Pyrolysis oil is produced during the fast heating of lignocellulosic biomass in the absence of oxygen. Depending on the feedstock and the pyrolysis conditions, mainly temperature, heating rate, and residence time, it is possible to produce yields of bio-oil ranging from 50 to 95 wt.% [79]. Bio-oil is a dark brown, highly viscous, and oxygenated liquid with up to 40 wt.% water content [80,81]. In addition to water, pyrolysis oil comprises catecols, syringols, guaiacols, phenolics, sugars, ketones, aldehydes, short carboxylic acids, and furfurals [82]. This mixture of highly reactive molecules makes the bio-oil an unstable system that requires further processing before its utilization for transportation fuels [55,83].

Pyrolysis of pure cellulose yields levoglucosan (up to 60 wt.%), via intramolecular condensation and sequential depolymerization of glycosidic units [84]. However, in the presence of alkali metals in concentrations as low as 0.005 mmoles/g, non-selective homolytic cleavage of carbon-carbon bonds occurs, favoring the formation of low molecular weight molecules including acids, furfurals, and linear aldehydes (Figure 2.4) [85-89].



**Figure 2.4: Reaction scheme for cellulose conversion a) in the absence and b) in the presence of metal ions (adapted from refs. 83,85,86).**

These undesired reactions are controlled by the ionic nature of the inorganic salts, the Lewis acidity/basicity and/or their ability to form complexes that stabilize particular reaction intermediates. For example, when  $CaCl_2$ ,  $Ca(NO_3)_2$  and  $CaHPO_4$  were added during the pyrolysis of cellulose, the yield of glycolaldehyde was reduced, while a remarkable increase was observed in the yield of formic acid and acetol. More interesting, the formation of furfural, hydroxymethyl furfural, and levoglucosone is

enhanced in the presence of  $\text{CaCl}_2$ , which indicates the participation of these salts in the dehydration reaction of the cellulose [84].

#### 2.1.3.3. Lignocellulose Hydrolysis and Dehydration

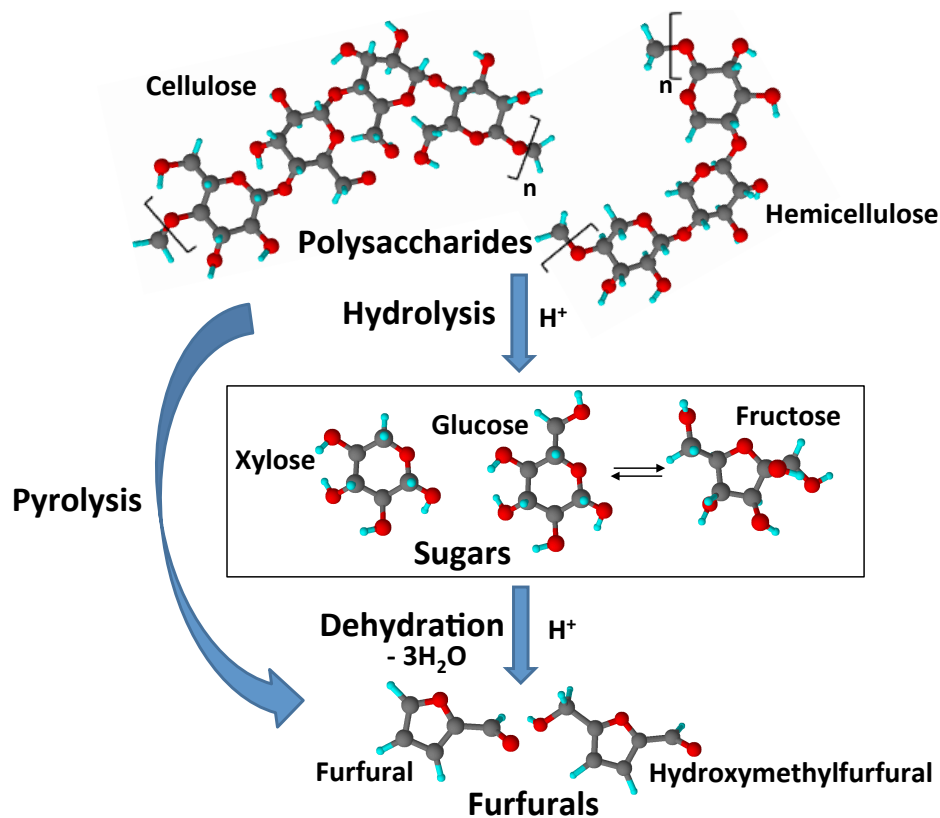
The deconstruction of lignocellulosic biomass via hydrolysis is readily catalyzed by strong acids, which speed up the protonation of the oxygen bridges connecting the sugar monomers. Mineral acids ( $\text{HCl}$ ,  $\text{H}_2\text{SO}_4$ , and  $\text{HNO}_3$ ) are effective catalysts for depolymerization of hemicellulose and cellulose, as they have the necessary strength to break down the crystalline structure of the cellulose fibers. Acid catalyzed hydrolysis has been conducted in industrial scale for a long time. In 1922, The Quaker Oat Company developed the first commercial process for production of furfural from oat hulls in Cedar Rapids, Iowa, using liquid acid catalysts [90]. The first production of furfural was achieved by passing superheated steam through biomass. However, at high enough temperatures, sulfuric acid is not necessary since the acetic acid released during the depolymerization of hemicellulose is able to catalyze the dehydration reaction and produce furfural.

The acid catalyzed hydrolysis of polysaccharides comprises the following steps [91]; (1) protonation of an oxygen link leading to a trivalent oxygen, (2) heterolytic cleavage of a C-O bond to form a carbocation and a hydroxyl group, (3) reaction of a water molecule with the carbocation, and (4) release of a proton from the resulting  $\text{H}_2\text{O}^+$  with consequent regeneration of the catalyst and yield of a hydroxyl group. The sequence is repeated until the polysaccharide is fully converted into the corresponding sugars. However, during this process the lignin fraction cannot be dissolved and

remains unreacted. Therefore, further refining is necessary. The catalytic effect of the acid is highly dependent on the proton transfer efficiency of the catalyst, rather than the proton concentration in the system. In fact, it has been observed that even negligible hydrogen ion concentrations may have a catalytic effect [92]. In this context, the hydrogen ion concentration is highly dependent on the temperature. It has been observed that the dielectric constant of water, responsible for the dissociation of the acids, decreases with temperature, which strongly diminishes the dissociation of the acid [93].

#### 2.1.3.4. Dehydration of Sugars

The formation of furfural and hydroxymethylfurfural can be accomplished by triple dehydration of xylose (pentose) and glucose (hexose), respectively, in the presence of an acid catalyst (Figure 2.5). Pentoses and hexoses are mostly present in the ring form, since the open-chain aldehydes only amount to less than 1 wt.% [94]. Isomerization of glucose to fructose is desirable because the latter is more effective for production of HMF. For example, Sn-containing zeolites have been found to be very active and selective towards fructose (31 wt.%), with small production of mannose (9 wt.%) at mild temperatures (110-140 °C) [95].

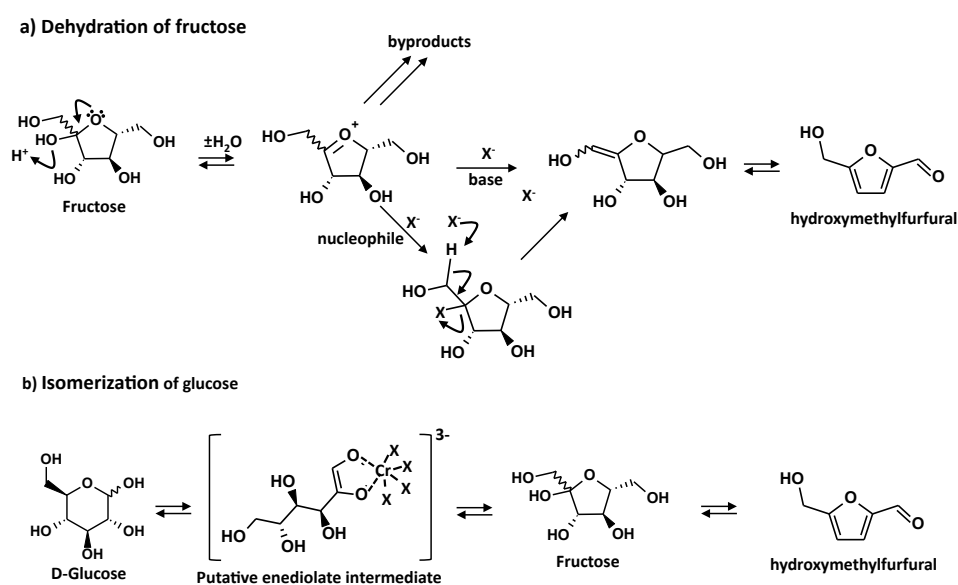


**Figure 2.5: Production of furfurals (2-furfuraldehyde and hydroxymethylfurfural) from lignocellulosic biomass.**

The transformation of the  $C_5$ ,  $C_6$  sugars is performed through the sequence of two 1,2-eliminations, followed by 1,4-elimination of water molecules. In the final step, ring formation occurs facilitated by the tendency of  $sp^2$  carbon atoms to form planar structures [96]. After the 1,4-elimination, the hydrogen ion is eliminated and furfurals are obtained.

Ionic liquids have also been tested for the production of furfurals [97-99]. In this approach, the ionic liquid stabilizes the furfural (FAL) or hydroxymethylfurfural (HMF) product from the reaction mixture and increases the reaction selectivity. However, the detailed role of the ionic liquid in the catalytic cycle is still under study [100].

Possible mechanisms have been proposed for the dehydration of fructose in the presence of halides, as well as for the isomerization of glucose to fructose catalyzed by hexacoordinated chromium (II) complexes (Figure 2.6) [99]. It appears that the halide ( $X^-$ ) attacks the oxocarbenium ion to form a 2-deoxy-2-halo-intermediate that is more stable and, therefore, less prone to oligomerization and reversion reactions (Figure 2.6a).



**Figure 2.6: Putative mechanisms of dehydration of fructose and isomerization of glucose in the presence of halides and hexacoordinate chromium (II) complex, respectively [97,99].**

An alternative explanation has been given by Zhao et al. [97] (Figure 2.6b), who proposed that, when ionic liquids like 1-methyl-3-methylimidazolium chloride [EMIM]Cl are mixed with chromium chloride ( $CrCl_2$ ), the Lewis acid formed ( $CrCl_3^-$ ) plays a critical role in the proton transfer, which facilitates the mutarotation of glucose.



### 2.1.4. Catalytic Strategies for Conversion of Furfurals to Fuel and Chemical Intermediates

Several pathways for conversion of furfurals are considered in Figures 2.7 and 2.8. Among these routes, aldol-condensation has been proposed to increase the molecule length through the formation of carbon-carbon bonds [101,102], and etherification has been presented as an alternative to produce specialty chemicals for pharmaceutical industry [103].

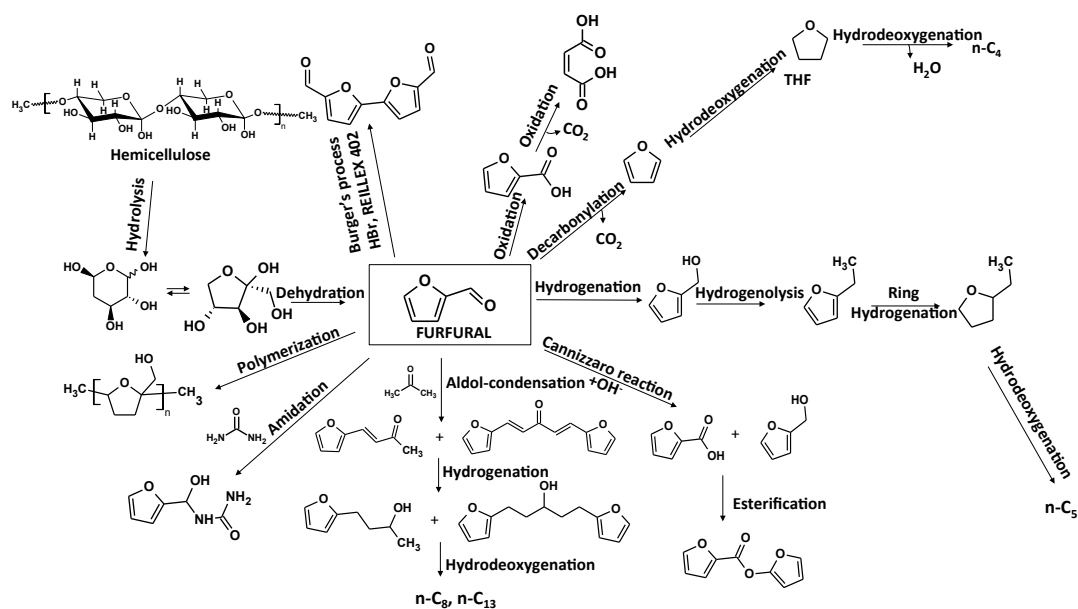
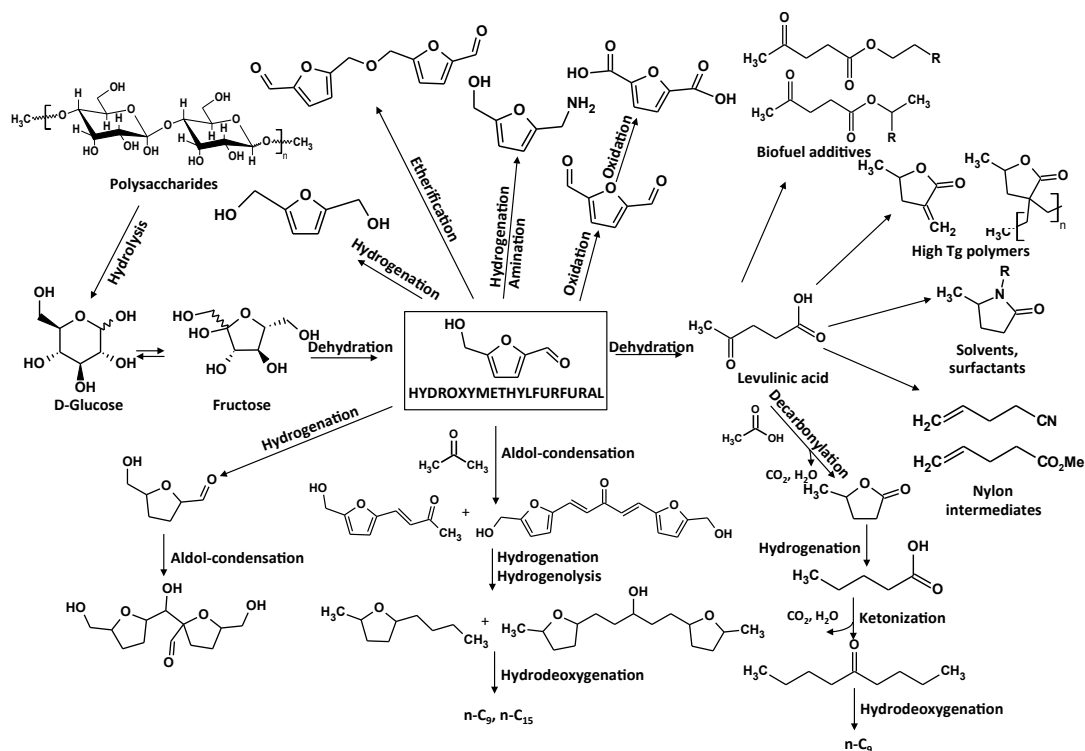


Figure 2.7: Catalytic pathways for the conversion of furfural.



**Figure 2.8: Catalytic pathways for the conversion of hydroxymethylfurfural.**

#### 2.1.4.1. Aldol-condensation of Furans and Ketones

Biomass-derived sugars can be upgraded to conventional fuels through the combination of aldol-condensation reactions and hydrogenation/dehydration reactions. Dumesic et al. [52,71,104-107] have done seminal work in this area, applying molecular engineering concepts to formulate refining strategies for the production of renewable fuels.

The aldol-condensation reaction is initiated by the abstraction of the  $\alpha$ -hydrogen from aldehydes and ketones, in the presence of a basic catalyst. The resulting enolate reacts with the carbonyl carbon of another molecule to form the aldol-product that, after dehydration, forms an  $\alpha,\beta$ -unsaturated carbonyl molecule.

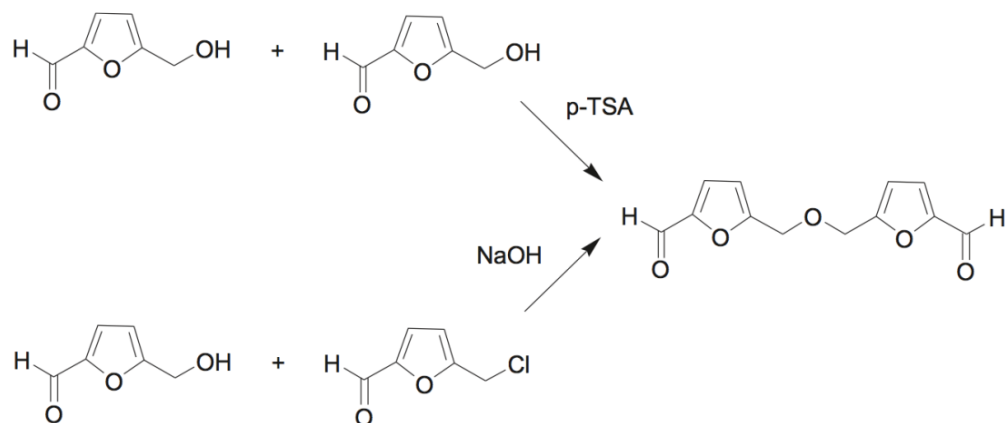
Although furfural molecules do not have  $\alpha$ -hydrogens, it is possible to perform cross-condensation reactions with other aldehydes and ketones, like acetone and propanal. In this approach, diesel and jet fuel can be produced by the coupling of C<sub>5</sub>-C<sub>6</sub> furfural molecules with C<sub>3</sub> aldehydes and ketones (Figure 2.7 and 2.8, respectively) [108]. The cross-condensed products, ranging from C<sub>8</sub> to C<sub>15</sub>, can be hydrogenated at low temperatures (100-150 °C) to decrease their solubility in the aqueous phase and their oxygen content. High temperatures and bifunctional catalysts (acid and metal) are required to perform dehydration and hydrogenation reactions in order to remove the residual oxygen and produce C<sub>8</sub> to C<sub>15</sub> alkanes. Another route proposed by these authors [108] was based on the partial hydrogenation of the aromatic ring in the furfural molecules, in which an  $\alpha$ -hydrogen is generated and 5-hydroxymethyl-tetrahydrofurfural (HMTHFA) and tetrahydro-2-furfural (THF2A) are formed as products. These molecules can then react by self aldol-condensation to generate C<sub>10</sub> to C<sub>12</sub> products.

The aldol-condensation reactions are carried out in polar solvents, such as water or water-methanol, and usually catalyzed by homogeneous bases like NaOH or Ca(OH)<sub>2</sub> [109]. However, in homogeneous catalysis, for every 10 parts of product formed, 1 part of spent catalyst is generated, which increases up to 13 % the selling price of the product due to required purification, recovery, and waste treatments [109]. In contrast, heterogeneous catalysts are readily separated by filtration methods and, depending on the reactor configuration, they can be used for vapor-phase [110,111], liquid-phase [112,113] or biphasic liquid [72,102] systems.

#### 2.1.4.2. Etherification of Biomass-Derived Furfural

The production of chemical intermediates derived from fossil resources is of great importance for the pharmaceutical and polymer industries, as more than 90 % of the major organic chemicals manufactured in the US in 1995 were produced from conventional hydrocarbon sources [114]. Nevertheless, the diminishing of the crude oil reserves and the ever-increasing environmental regulations has boosted the interest in the conversion of biomass into chemicals [116]. A perfect example of this is the etherification of hydroxymethylfurfural to produce 5,5-oxy(bis-meth-ylene)-2-furaldehyde (OBMF), which can be used in the synthesis of imine-based polymers with high glass transition temperatures (300 °C), as well as in the preparation of hepatitis antiviral precursors [103]. In that case, the catalyst used were zeolites and mesoporous aluminosilicates with Brønsted and Lewis acid sites, which offer high temperature resistance and size-shape selectivity [116].

Two different etherification processes can be found in the literature (Figure 2.9) [103]: 1) etherification of HMF catalyzed by acids in organic solvents [117-119], and 2) the Williamson reaction of HMF and 5-chloro-methyl-2-furfural in an excess of base [120].



**Figure 2.9: Synthetic pathways for the production of 5,5'-oxy(bis-methylene)-2-furaldehyde (OBMF). Reproduced from ref. 103.**

#### 2.1.4.3. Hydrodeoxygenation of Biomass-Derived Furans

Hydrogenation of furfural with hydrogen gas on metal catalysts produces mainly furfuryl alcohol. This alcohol finds uses as a solvent, but is primarily used as an ingredient in the manufacture of chemical products such as foundry resins, adhesives, and wetting agents [94]. The catalysts most typically used in furfural hydrogenation are metals because they are able to dissociate hydrogen, thus making hydrogenation possible. The choice of catalyst support is based on its ability to disperse and stabilize metal particles enhancing the active surface area. Compared to other aldehydes, in addition to the carbonyl group, furfural contains an aromatic furanyl ring that could be also hydrogenated. While carbonyl hydrogenation is usually preferred due to the high stability of the aromatic ring, metal catalysts that have strong interactions with the unsaturated C=C bonds can still saturate the ring. Therefore, the selectivity toward aromatic alcohols is strongly dependent on the metal catalyst used. Furthermore, the geometric and electronic properties of different metals can affect both hydrogenation activity and selectivity by influencing the type of adsorption intermediates. In this

section we will primarily discuss the differences observed in furfural hydrogenation on group IB and VIII metals.

Among the group IB metals, Cu has been the most intensively investigated as a catalyst for furfural hydrogenation [121-127]. Silver has been used in a few studies while there is no report on Au catalysts [128]. The group IB metals are significantly less active than other metals. However, they exhibit a remarkable selectivity towards hydrogenation of the carbonyl group leaving the C=C double bonds in the furanyl ring unreacted. In this sense, Cu has been found to be the most selective among all tested metal catalysts. Selectivities above 98 % to furfuryl alcohol have been achieved over monometallic Cu/SiO<sub>2</sub> catalysts [127]. Also, monometallic Ag catalysts have been found able to hydrogenate the C=O group of furfural with relatively good selectivity, but not as high as that of Cu. For example, 80 % selectivity was obtained over a Ag/SiO<sub>2</sub> catalyst prepared by the sol-gel method [128].

The group VIII metals (Ni, Pd, and Pt) have also been used for furfural hydrogenation in both vapor and liquid phases on different supports; they all exhibit significant activity and selectivity [128], particularly at low temperatures (i.e., below 200 °C). For example, Ni catalysts have been used at low temperatures (100 °C) in liquid phase, exhibiting > 95 % selectivity to furfuryl alcohol [129-130]. Likewise, supported Pt catalysts doped with transition metal oxides have exhibited high selectivity, e.g., Pt/TiO<sub>2</sub>/SiO<sub>2</sub> (selectivity = 94 %) and Pt/ZrO<sub>2</sub>/TiO<sub>2</sub> (selectivity = 95%) [131]. However, at higher temperatures (> 200 °C) the selectivity to alcohols on group VIII metals drops significantly upon the appearance of other reactions. For example, over a Ni/SiO<sub>2</sub> catalyst at 230 °C and excess of hydrogen (H<sub>2</sub>/feed ratio = 25), only 25

% selectivity to furfuryl alcohol was observed [132]. On Pd catalysts, it is even lower, e.g., a Pd/SiO<sub>2</sub> catalyst at 230 °C yielded 14 % selectivity [133] and a Pd-Y catalysts at 350 °C rendered only 1 % selectivity to furfuryl alcohol [121]. The lower selectivities observed at high temperatures on group VIII metals can be ascribed to the emergence of decarbonylation and ring opening reactions. In addition, hydrogenation of the furanyl ring yielding the saturated alcohol is also observed over group VIII metal catalysts due to a stronger interaction of the furanyl ring with the metal surface than that obtained with group IB metals [134]. As a result, Cu and Ag should be the preferred catalysts if high selectivity to furfuryl alcohol is desirable, particularly at high temperatures. However, the intrinsic activity for furfural hydrogenation is lower on group IB metals than on group VIII metals, which is typically explained by the difference in extent of d-orbital filling. That is, the d-orbitals are filled in the group IB, reducing the bond strength.

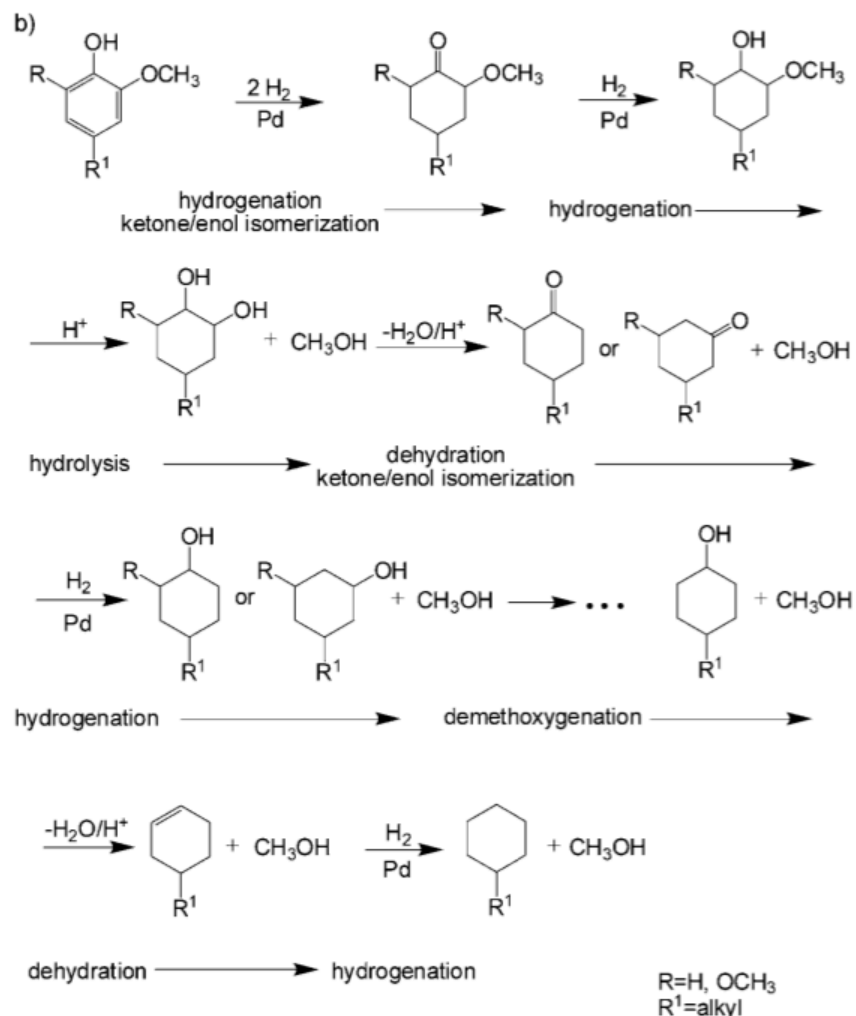
#### 2.1.4.4. Hydrodeoxygenation of Lignin-Derived Phenolics

The depolymerization of the lignin fraction in the biomass involves the cleavage of the aryl-alkyl and aryl-aryl ether bonds. The first one, is rather weak therefore bond-scission can be achieved in subcritical water without adding a catalyst [25], Meanwhile, the aryl-aryl ether bonds are rather stable [26], and likewise carbon-carbon bonds between aromatic lignin units need more severe conditions to be broken. Hence, thermochemical conversion processes like pyrolysis, gasification or severe hydrolysis are required to breakdown the lignin polymer into the small units. Once depolymerization is accomplished a mixture of multifunctional aromatic molecules are

generated. In order to upgrade these phenolic fractions a severe hydrotreating is required to remove the excess oxygen using either gas phase or liquid phase processing. However, gas phase processing is limited by the poor thermal stability of the oxygenated molecules (acids, ketones, aldehydes, sugars) that accompanied the phenolic fraction upon biomass depolymerization. For this reason liquid phase processing has drawn significant attention as it is possible to convert these heavy phenolic molecules with minimum catalyst deactivation by coke and oligomerization reactions caused by small oxygenates.

For instance, Lercher and co-workers [135-138], have shown that hydrodeoxygenation of phenolic molecules is possible using a catalyst with acid/metal functions in liquid-phase. As shown in Figure 2.10 the reaction pathway for the hydrodeoxygenation of alkyl-containing methoxy phenols using Pd/C catalysts in an aqueous solution acidified with  $H_3PO_4$ . First the alkyl-containing methoxy phenol is hydrogenated to the 2-methoxy-cycloalcohol, which is a clear indication that metal-catalyzed hydrogenation of the aromatic ring is the fastest step and not the hydrolysis of the methoxy group. Then, the acid-catalyzed ether hydrolysis of methoxycyclohexanol takes place, producing cyclodiol and methanol that undergoes dehydration to cycloketone. The latter is readily hydrogenated cyclohexanol over the metal catalyst and dehydrated to the cycloalkane that is saturated to generate the desired cycloalkane.





**Figure 2.10: Proposed reaction pathway for aqueous-phase hydrodeoxygenation of phenolic aromatics to alkanes and methanol over a metal catalyst and with an acid [138].**

### 2.1.5. Quantitative Structure and Properties Relationships (QSPR) for Fuel and Chemical Properties Optimization in Biomass Processing

The molecular engineering approach has been applied for upgrading of fossil fuels and there are many examples in the literature. For instance, gasoline and diesel are archetypal commodities that have been optimized through many years of commercial practice and dedicated research. The notion of molecular management and molecular engineering of fuels has been put into action in refining operations of petroleum fuels.

These terms entail having the right molecule in the right place, at the right time, and at the right price [139], and at even higher level of molecular manipulation, they imply a purposeful design of molecules with precise structures and well-defined properties. To achieve this high level of chemical specificity, the continuous development of better catalytic materials is crucial [140].

However, the application of this rational approach in the upgrading of biomass to chemicals and fuels is just starting [141]. For example, to optimize a fuel property of interest it is necessary to develop first an experimental database of known properties for components chemically similar to those to be incorporated in the fuels. Then, one needs to use correlations such as Quantitative Structure Property Relationships (QSPR) to expand the database to all the possible components of the fuel. QSPR generates correlations with specific properties of the corresponding compounds utilizing molecular descriptors, (i.e., numerical values calculated from the molecular structure). Molecular descriptors involve geometric, steric, and electronic aspects of the molecule and can range from very simple physical parameters such as the number of carbon atoms or branches in a molecule, to more complex parameters such as dipole moment or surface area. Application of QSPR to fuel properties has resulted in models that can estimate Cetane Number [142,143], Octane Number (RON and MON) [144], and sooting tendencies [145] of any fuel component, only on the basis of the molecular structure. With these structure-property relationships the researcher can evaluate whether a given potential catalyst and conversion process modify the structure of a given reactant in a favorable way regarding the desired fuel properties [146]. Likewise, in the production of chemicals for the polymer and solvent industries the manipulation

of the molecular structure with atomic precision enables the optimization of the process towards the right composition.

## **2.2. Experimental Section**

### *2.2.1. Catalyst Preparation and Characterization*

Different nanohybrids were synthesized for the different reactions performed. For aldol-condensation reactions, nanohybrids composed of carbon nanotubes grown on basic metal oxides were used, whereas for hydrogenation reactions, palladium was anchored on the nanohybrids. Additionally, in order to increase the yield of the long-chain products, aldol-condensation reactions catalyzed by NaOH were also performed. Finally, for hydrodeoxygenation reactions, palladium, platinum or nickel were deposited on the nanohybrids.

#### 2.2.1.1. Aldol-condensation Reaction Catalysts

For the aldol-condensation reactions, a basic catalyst was needed. Thus, several nanohybrids composed of carbon nanotubes grown on different basic metal oxides were prepared and their activities for the aldol-condensation of furfural and acetone were compared. The basic metal oxides chosen were MgO, mixture of MgO and Al<sub>2</sub>O<sub>3</sub>, Ce<sub>x</sub>Zr<sub>1-x</sub>O<sub>2</sub>, ZnO and TiO<sub>2</sub>.

##### 2.2.1.1.1. SWCNT/MgO and MWCNT/MgO

In these nanohybrids, the carbon nanotubes were grown on the same MgO-based catalyst. Depending on the gas and the conditions used later to grow the carbon

nanotubes, we could obtain single-wall (SWCNT) or multi-wall (MWCNT) carbon nanotubes. The initial catalyst was prepared by a combustion method in which a solution of the precursors,  $\text{Mg}(\text{NO}_3)_2 \cdot 6\text{H}_2\text{O}$ ,  $\text{Fe}(\text{NO}_3)_3 \cdot 9\text{H}_2\text{O}$  and  $(\text{NH}_4)_6\text{Mo}_7\text{O}_{24} \cdot 4\text{H}_2\text{O}$  (provided by Sigma Aldrich), was mixed with citric acid (combustible agent, Sigma Aldrich), and then calcined at 500 °C for 2 h. The total metal loading (Fe and Mo) was 4 wt. % with a molar ratio Fe:Mo of 10:1. In order to grow SWCNT, this catalyst was first reduced under 200 sccm of  $\text{H}_2$  at 500 °C for 30 min, then heated in 200 sccm of He up to 850 °C, and finally exposed to a flow of 200 sccm of 3 % of  $\text{CH}_4$  in He at this temperature for 1 h. The total carbon yield obtained from this reaction was around 16 wt. %. For MWCNT, the catalyst was first reduced under 300 sccm of  $\text{H}_2$  at 500 °C for 30 min, then heated in 300 sccm of He up to 700 °C, and finally exposed to a flow of 400 sccm of 25 % of  $\text{C}_2\text{H}_4$  in He at this temperature for 20 min. The total carbon yield obtained from this reaction was ~ 36 wt. %.

#### 2.2.1.1.2. MWCNT/MgO\_Al<sub>2</sub>O<sub>3</sub>

The MgO/Al<sub>2</sub>O<sub>3</sub>-based catalyst was also synthesized by the combustion method explained above. A solution of the precursors,  $\text{Mg}(\text{NO}_3)_2 \cdot 6\text{H}_2\text{O}$ ,  $\text{Fe}(\text{NO}_3)_3 \cdot 9\text{H}_2\text{O}$ ,  $(\text{NH}_4)_6\text{Mo}_7\text{O}_{24} \cdot 4\text{H}_2\text{O}$  and  $\text{Al}(\text{NO}_3)_3 \cdot 9\text{H}_2\text{O}$  (Sigma Aldrich), was mixed with citric acid (combustible agent) and then calcined at 500 °C for 2 h. The total metal loading (Fe and Mo) was 4 wt. % with a molar ratio Fe:Mo:Mg:Al of 1:0.1:16:7. The MWCNT were grown on this catalyst following the same procedure to grow MWCNT on the MgO catalyst.

#### 2.2.1.1.3. MWCNT/Ce<sub>x</sub>Zr<sub>1-x</sub>O<sub>2</sub>, MWCNT/V<sub>2</sub>O<sub>5</sub>, MWCNT/ZnO and MWCNT/TiO<sub>2</sub>

The method of preparation of all these four nanohybrids was the same. The only difference is the initial support (Ce<sub>x</sub>Zr<sub>1-x</sub>O<sub>2</sub>, V<sub>2</sub>O<sub>5</sub>, ZnO or TiO<sub>2</sub>). V<sub>2</sub>O<sub>5</sub>, ZnO and TiO<sub>2</sub> were provided by Sigma Aldrich. Ce<sub>x</sub>Zr<sub>1-x</sub>O<sub>2</sub> mixed oxide was prepared by a precipitation method with aqueous solutions of cerium (IV) ammonium nitrate and zirconium nitrate as described in the literature [147-149]. First of all, each support was impregnated by incipient wetness impregnation with an aqueous solution of Co(NO<sub>3</sub>)<sub>2</sub>.6H<sub>2</sub>O and Fe(NO<sub>3</sub>)<sub>3</sub>.9H<sub>2</sub>O (Sigma Aldrich), reaching a final metal loading of 2 wt. %, with a Fe:Co molar ratio of 2:1. The powder was then dried overnight at 100 °C and calcined in air 2 h at 450 °C. After cooling down, 0.3 g of the catalyst was placed in a reactor where it was first reduced under 300 sccm of H<sub>2</sub> at 500 °C for 30 min, then heated up to 700 °C in 300 sccm of He, and finally exposed at that temperature to a 400 sccm flow of 25 % of C<sub>2</sub>H<sub>4</sub> in He for 30 min at 700 °C.

#### 2.2.2. Hydrogenation Reaction Catalysts

In order to perform the hydrogenation of the aldol-condensation products, three different nanohybrid-supported catalysts were tested, a mixture of SWCNT/MgO and Pd/SWCNT, Pd/MWCNT\_Al<sub>2</sub>O<sub>3</sub> and Pt/MWCNT\_Al<sub>2</sub>O<sub>3</sub>.

##### 2.2.2.1. Mixture of SWCNT/MgO and Pd/SWCNT

In order to perform the hydrogenation of the aldol-condensation products, a catalyst was prepared by a physical mixture (mass ratio 2:1) of metal-free SWCNT/MgO and pure SWCNT (MgO-free) doped with 10 wt. % Pd. To deposit Pd,

purified SWCNT provided by SouthWest NanoTechnologies Inc. were sonicated for 15 min with 20 ml of a solution of  $\text{Pd}(\text{NO}_3)_2 \cdot 6\text{H}_2\text{O}$  (Sigma-Aldrich) in water. The suspension was then dried in a vacuum oven at 60 °C for 2 days. Finally, the resultant powder was calcined in He at 300 °C for 2 h. In the final mixture, since Pd was only anchored on the purified SWCNT, which are hydrophobic, the metal placed at the water/oil interface in the emulsion system, towards to the oil phase. Therefore, with this catalyst, one could expect only hydrogenation of the products present in the organic phase.

#### 2.2.2.2. Pd/MWCNT\_ $\text{Al}_2\text{O}_3$ and Pt/MWCNT\_ $\text{Al}_2\text{O}_3$

Nanohybrids consisting of MWCNT fused to  $\text{Al}_2\text{O}_3$  were provided by SouthWest NanoTechnologies Inc. These nanohybrids were used as support of palladium or platinum particles for the hydrogenation reactions. Both metals were anchored by incipient wetness impregnation of their corresponding precursors ( $\text{Pd}(\text{NO}_3)_2 \cdot 6\text{H}_2\text{O}$  or  $\text{H}_2\text{PtCl}_6 \cdot 6\text{H}_2\text{O}$ , respectively). The final metal loading was 5 wt. % of Pd or Pt, respectively. After the impregnation, the catalysts were dried overnight at 100 °C and then calcined at 300 °C for 2 h in He.

### 2.2.3. *Hydrodeoxygenation Reaction Catalysts*

#### 2.2.3.1. Catalyst for the Hydrodeoxygenation of the Aldol-Condensation Products

Hydrodeoxygenation reactions of the aldol-condensation products were carried out using a catalyst consisted of silica alumina grade 135 (Sigma Aldrich) functionalized with 5 wt. % Ni and 1 wt. % Pt, prepared by incipient wetness

impregnation of the support with the respective metal precursors ( $\text{NiCl}_2 \cdot \text{H}_2\text{O}$  and  $\text{H}_2\text{PtCl}_6 \cdot 6\text{H}_2\text{O}$ , Sigma Aldrich). The catalyst was then dried overnight at 100 °C and calcined at 400 °C for 2 h. The catalyst was reduced ex-situ in  $\text{H}_2$  at 450 °C for 2 h before being used in the hydrodeoxygenation reactions.

#### 2.2.3.2 Catalyst for the Conversion of Synthetic Bio-oils

Some synthetic bio-oils (SBO) were also tested as feed for the aldol-condensation and hydrogenation/hydrodeoxygenation reactions. For the aldol-condensation reactions, MWCNT/MgO and MWCNT/ZnO nanohybrids were employed as catalysts. On the other hand, for the hydrogenation/hydrodeoxygenation reactions, two different catalysts were used. The first catalyst consisted on a physical mixture (wt. ratio 1:1) of MWCNT/ZnO nanohybrids with 10 wt. % Pd deposited on purified SWCNT (described above, in the hydrogenation catalysts section). The second catalyst consisted of MWCNT/ZnO mixed with 5 wt. % Ni on purified SWCNT (wt. ratio 1:1), prepared by following the same procedure as in the Pd catalyst, but using  $\text{Ni}(\text{NO}_3)_2 \cdot 6\text{H}_2\text{O}$  as the metal precursor. The Ni catalyst was also reduced ex-situ in  $\text{H}_2$  at 500 °C for 2 h before the hydrodeoxygenation reactions.

#### 2.2.4 Reactions in Particles-Stabilized Emulsion

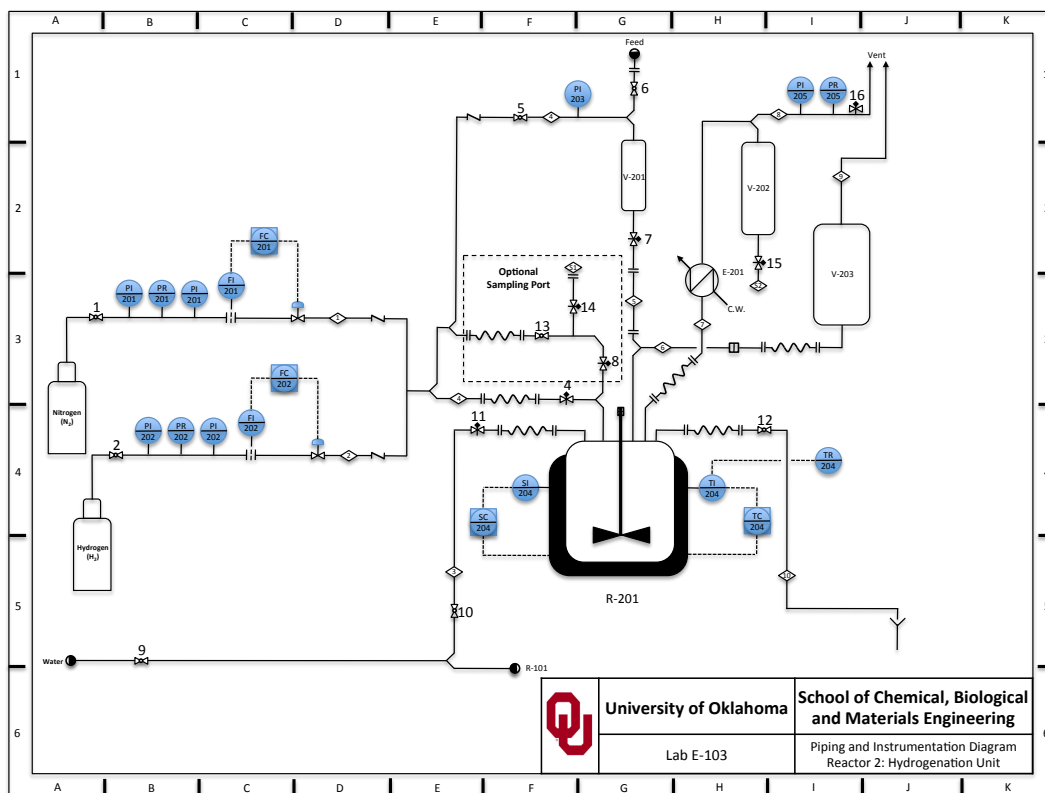
The catalytic experiments of aldol-condensation, hydrogenation and hydrodeoxygenation were carried out in two Parr 4843 reactors of 50 ml and 300 ml. The typical experimental set up is presented in Figures 2.11 and 2.12. The temperature inside the reactor was measured by a J-Type thermocouple (OMEGA) and controlled by

a temperature controller CAL 9500P from CAL Controls Ltd. For each reaction, the catalyst was dispersed in a mixture of equal volumes of deionized water and decalin, by sonicating for 15 min with a horn sonicator at 25 % of amplitude. The mixture was poured inside the stainless steel reactor and the system was connected and then purged with nitrogen gas for 1 h at 200 sccm. The magnetic stirrer was operated at 200 rpm while the pressure was raised up to desired reaction pressure. During that process the pressure was regulated using a backpressure regulator. The reactants were transferred into the feeding cylinder, which was pressurized with nitrogen at a pressure 50 psi above than the one in the reactor. The reactor was then heated up to the reaction temperature.



**Figure 2.11: Semi-continuous batch reactor.**





**Figure 2.12: Piping and instrumentation diagram of the semi-continuous batch reactor.**

#### 2.2.4.1 Aldol-Condensation Reactions

For the aldol-condensation reactions, once the reaction conditions were reached in the system, the nitrogen flow was stopped, the gas outlet was closed to operate the reactor in the batch mode, and the reactant mixture was injected. The aldol-condensation reactions were performed at 80 °C when nanohybrid were used as catalysts, and 40 °C when NaOH was used as catalyst. In the aldol-condensation reactions catalyzed by NaOH, NaOH was dissolved in deionized water and mixed with decalin in a volume ratio 1:1 and then MWCNT/Al<sub>2</sub>O<sub>3</sub> were added in order to stabilize the emulsion. The final concentration of NaOH in the reaction system was 0.0567 mol/l. The emulsion was also formed by sonicating with the Horn sonicator for 15 min.

#### 2.2.4.2. Hydrogenation and Hydrodeoxygenation Reactions

For the hydrogenation and hydrodeoxygenation reactions, an additional step was incorporated, where, before the reaction, the catalyst is pre-reduced in H<sub>2</sub> at 300 psi and 100 °C for 1-3 h. These reactions were run in a semi-batch mode, by flowing H<sub>2</sub> through the system at the desired pressure and conditions.

For the hydrogenation reactions, the reaction conditions were 300 psi of H<sub>2</sub> and a temperature of 100 °C. For the hydrodeoxygenation reactions of the aldol-condensation products, the pressure and temperature conditions were 700 psi of H<sub>2</sub> and 240 °C, respectively. The hydrodeoxygenation of synthetic bio-oils was performed as follows. The reduction conditions were 400 psi and 100 °C for the palladium catalyst, and 1500 psi and 300 °C for the nickel one. After the reduction of the catalyst, the conditions were adjusted to 400 psi and 100 °C, and the reactant mixture was injected in order to perform the hydrodeoxygenation with a hydrogen flow of 110 sccm for 3 h.

#### 2.2.4.3. Products Analysis and Quantification

After reaction, the reactor was taken apart and the content was filtered in two steps. In the first one, a common paper filter was used. This coarse filter (8 mm pore) was able to trap a large fraction of nanohybrids as they quickly agglomerated when they contacted the filter. In the second step, a PTFE (0.2 micron pores) filter was used to separate the small fraction of nanohybrids that passed the first filter. The two phases obtained were separated and samples of 500 ml of each one were analyzed by gas chromatography, GC-FID and GC-MS. The concentration of water in decalin was negligible and the presence of decalin in water was around 0.05 %. The GC-FID used

was a 6890A series from Agilent Technologies with a capillary column of polyethylene glycol (HP-INNOWAX) of 60.0 m x 0.32 mm x 0.25 mm nominal from Hewlett Packard. The GC-MS was a Shimadzu QP2010S equipped with an HP-INNOWAX polyethylene glycol capillary column, 30.0 m long x 0.25 mm nominal, from Hewlett Packard. In all the GC-FID analyses methanol and 1,2-dichloromethane were used as internal standards to close the mass balances. The reactants and products were calibrated in the GC- FID using commercial standards. All the aqueous fractions were extracted into a methanol solvent before injecting them in the GC, to avoid damaging the column.

In addition, Quantitative Structure Properties Relationships (QSPR) software was used to predict the relative retention times (RRT) and relative response factors (RRF) of a flame ionization detection (FID) system for the products that were not commercially available, in order to close the carbon mass balance. It is known that application of QSPR to fuel properties has resulted in models that can estimate Cetane Number [150,151], Octane Number (RON and MON) [144], and sooting tendencies [145] of any fuel component, only on the basis of the molecular structure. QSPR has also been extensively used to predict chromatographic factors using multiple linear regressions and artificial neural networks [152]. Thermal conductivity detector response factor was predicted for a set of organic compounds that includes hydrocarbons, benzene derivatives, esters, alcohols, aldehydes, ketones and heterocyclic molecules using an artificial neuronal network. When experimental and calculated data were compared, negligible differences were found. In this work, quantum-chemical descriptors and physical properties were calculated based on the molecular structures of

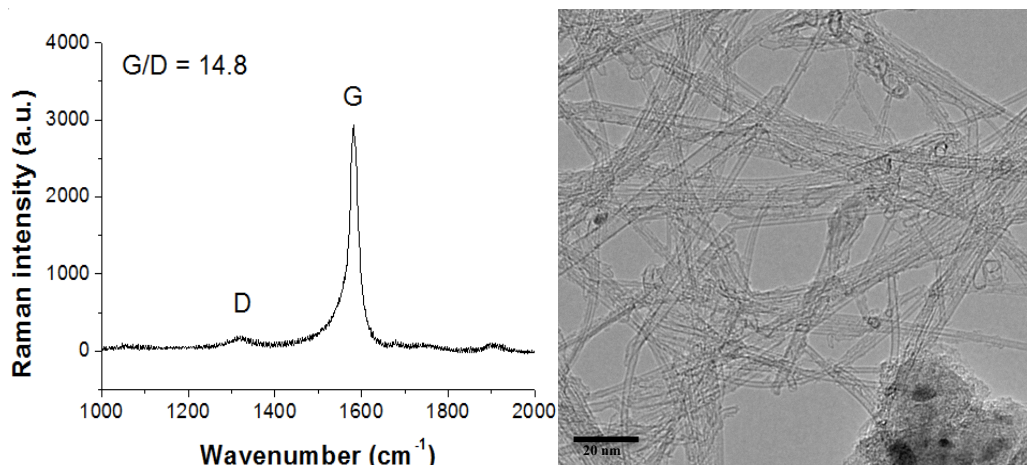
the compounds by using QSAR MDL. The boiling point of the compounds was taken from the literature and added to the model descriptors. Finally, multiple linear regressions were done in order to develop Quantitative Structure Property Relationships to predict retention time and relative response factors to the compounds of interest.

## **2.3. Results and Discussion**

### *2.3.1. Nanohybrid Catalyst Characterization by HRTEM and Raman Spectroscopy*

#### 2.3.1.1. SWCNT/MgO and MWCNT/MgO

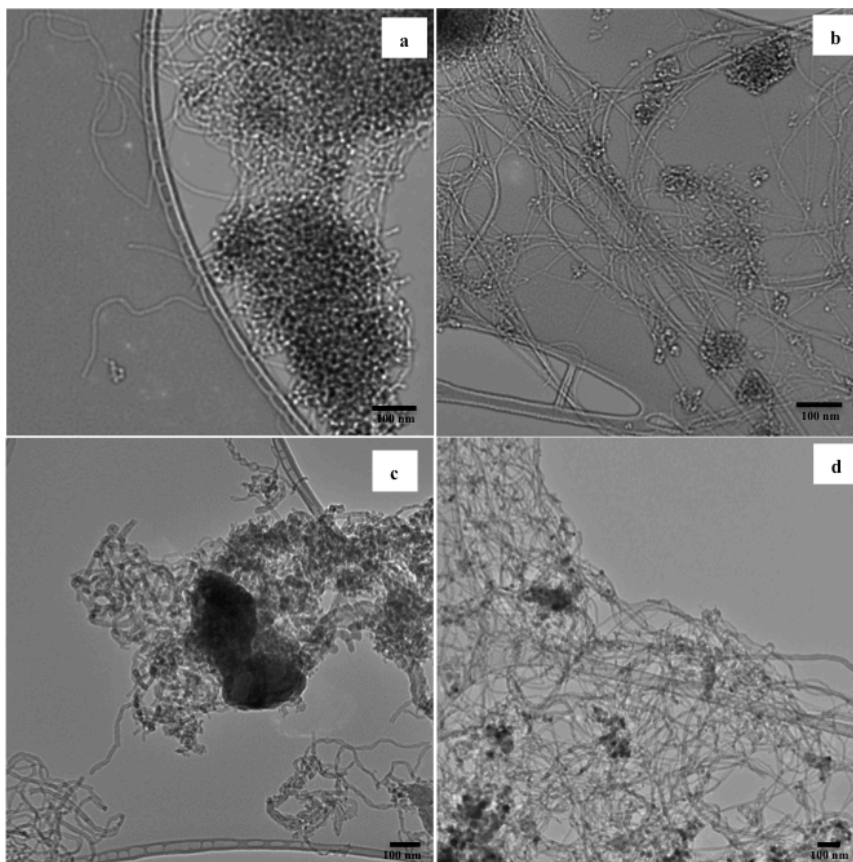
Figure 2.13 shows the Raman spectrum and the high-resolution transmission electron microscopy (HRTEM) image of the nanohybrids composed of SWCNT and MgO. Raman spectroscopy has been widely employed in evaluating the purity and quality of CNT products [153-155]. The relative density of defects in different CNT samples has been typically evaluated in terms of two characteristic bands, the G band, which appears at  $\sim 1590\text{ cm}^{-1}$ , is ascribed to  $\text{sp}^2$  ordered carbon, and the D band, which appears around  $1350\text{ cm}^{-1}$ , is commonly ascribed to  $\text{sp}^3$  carbon associated with defects [156-158]. The Raman spectrum corresponding to SWCNT/MgO (Figure 2.13 left) shows a G band with very high intensity, while the D band has a very low intensity. This is an indicative of the high quality of these CNT (high G/D intensity ratio, 14.8). Besides, Figure 2.14a shows the HRTEM image of the MWCNT/MgO. It can be observed that the yield to CNT in those nanohybrids is higher than in SWCNT/MgO (Figure 2.13 right).



**Figure 2.13: Raman spectrum (left) and HRTEM image (right) of the nanohybrids composed of SWCNT and MgO.**

2.3.1.2. MWCNT/MgO, MWCNT/MgO<sub>2</sub>, MWCNT/Ce<sub>x</sub>Zr<sub>1-x</sub>O<sub>2</sub>, MWCNT/V<sub>2</sub>O<sub>5</sub>, MWCNT/ZnO and MWCNT/TiO<sub>2</sub>

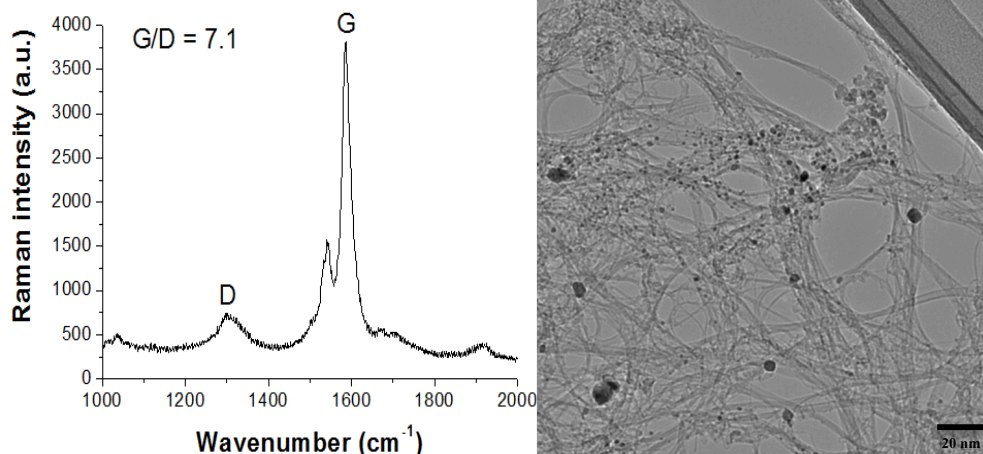
Figure 2.14 shows HRTEM images of some of these nanohybrids. It can be noted that the sample of MWCNT/ZnO (Figure 2.14c) is the most defective one. As we have shown before, the carbon nanostructure of the nanohybrids greatly affects the emulsion properties as well as the dispersion of metal particles, obtaining a better dispersion of the metal with more defective nanohybrids [33].



**Figure 2.14: HRTEM images of some of the nanohybrids used in this study: a) MWCNT/MgO, b) MWCNT/ MgO\_ Al<sub>2</sub>O<sub>3</sub>, c) MWCNT/ ZnO, and d) MWCNT/ TiO<sub>2</sub>.**

### 2.3.1.3. Mixture of SWCNT/MgO and Pd/SWCNT

Figure 2.15 shows the Raman spectrum of the purified SWCNT and a HRTEM image of the catalyst of 10 wt. % Pd on those purified SWCNT. It can be observed that the G band presents a high intensity, but the G/D ratio is lower (7.1) than in the case of the as-produced material (14.8, Figure 2.13 left). This decrease in the G/D ratio is due to the attack with acids of the SWCNT during the purification process, in which the initial catalyst particles are removed. Therefore, some defects were created in the surface of the SWCNT, which increased the intensity of the D band.



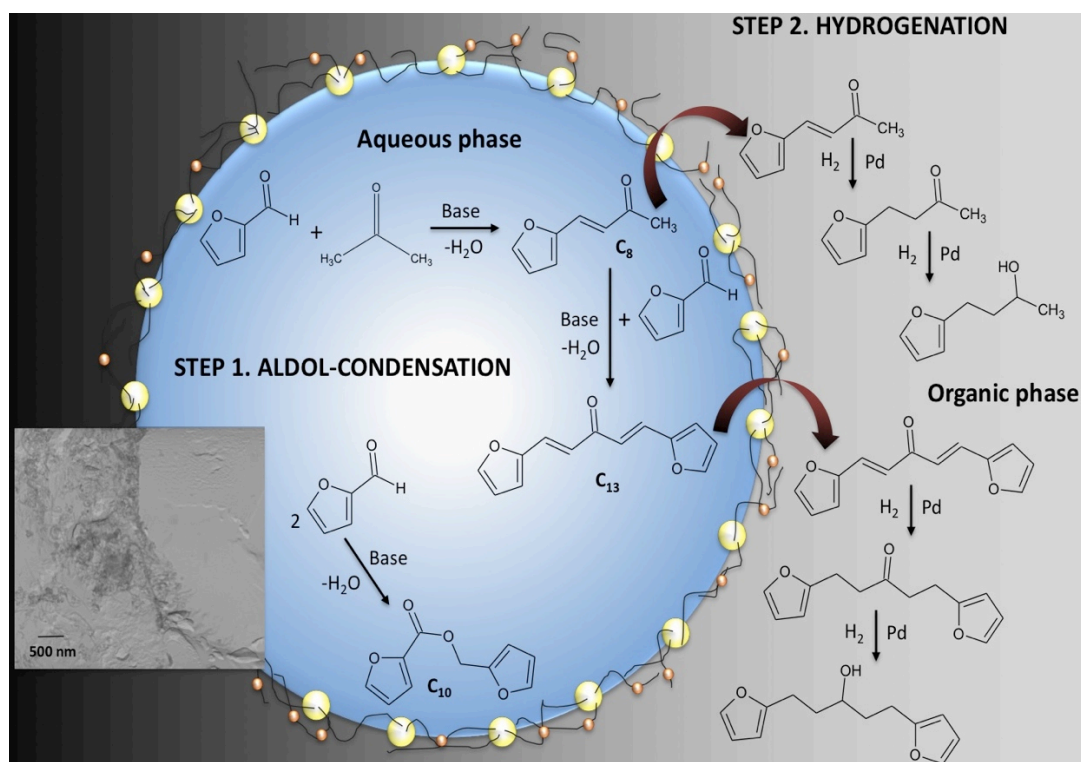
**Figure 2.15: Left) Raman spectrum of the purified SWCNT, and right) HRTEM image of the catalyst of 10 wt. % Pd on purified SWCNT.**

### 2.3.2. Biofuel Upgrading Reactions at the Water-Oil Interface of Nanoparticles-Stabilized Emulsions

#### 2.3.2.1 Aldol-Condensation of Furan and Ketones in Emulsion

In general, studies of upgrading strategies have been focused on the aldol-condensation of the biomass derived aldehydes and ketones, and subsequent hydrogenation of the products is typically performed in a separate reactor, which often limits the possibility of fully utilizing intermediates and products. An example of effective process integration would be the condensation of furfurals with short ketones, such as acetone, which can be readily obtained by ketonization of acetic acid, one of the major components in the aqueous fraction of pyrolysis oil. In turn, furfural is produced by dehydration of sugars, from either hydrolysis of cellulose or pyrolysis of lignocellulosic biomass. Hence, one can envision a reaction system that combines acetone (from pyrolysis) and furfurals (from hydrolysis and/or pyrolysis). Small ketones can act as effective linkers of furfural to produce larger hydrocarbon molecules ( $C_8$ – $C_{13}$ ), which fall in the gasoline/diesel range.

Figure 2.16 illustrates the reaction paths and phase migrations involved in the biphasic emulsion upgrading process used in this study. In the first-step, aldol-condensation of furfural and acetone produces compounds in the range C<sub>8</sub>–C<sub>13</sub> in an emulsion stabilized by nano hybrid catalysts that incorporate a basic oxide catalyst. Once the long-chain products are formed, their solubility in water greatly decreases and they migrate to the organic phase. In the second step, metallized nano hybrids catalyze subsequent hydrogenation reactions, which depending on the degree of severity, partially improve the stability of the product or completely

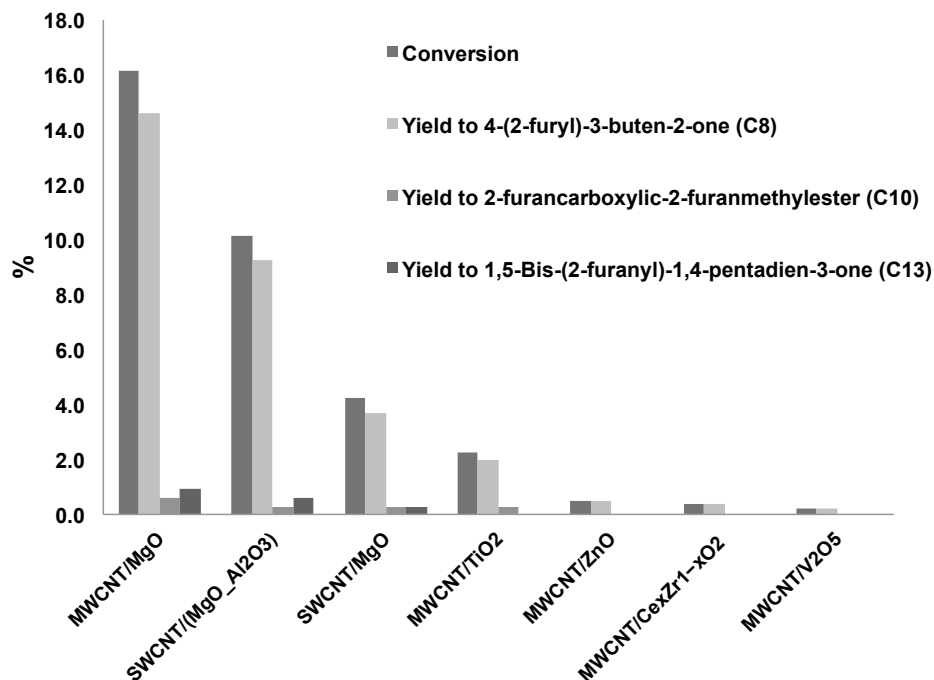


**Figure 2.16: Schematic illustration of the aldol-condensation and hydrogenation reactions taking place at the water/oil interface in nano hybrid-stabilized emulsions.**



#### 2.3.2.1.1. Catalyst Screening for the Aldol-Condensation of Furans and Ketones in Emulsion

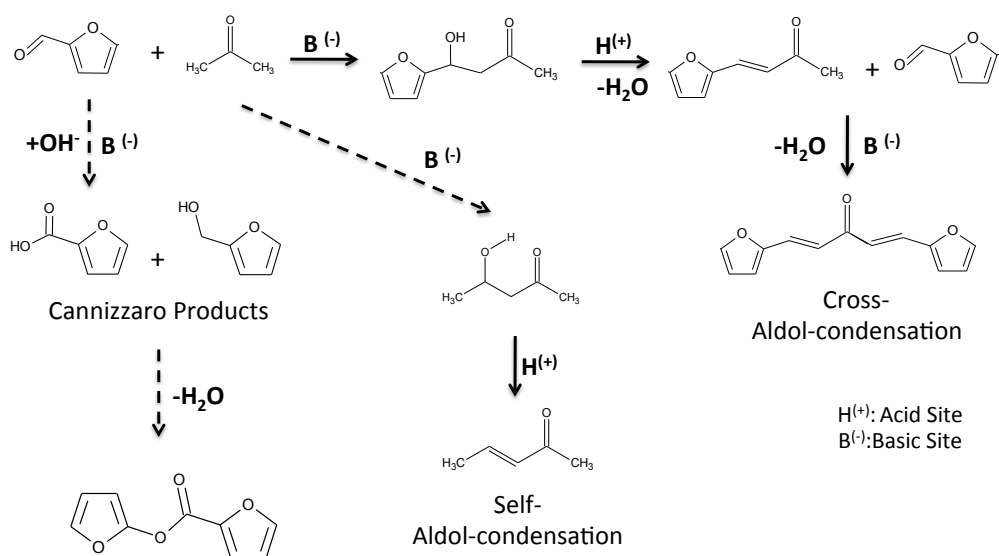
For the aldol-condensation reaction of furfural and acetone, a catalyst screening of different nanohybrids was done. Since a basic catalyst is needed for this type of reactions, six different basic metal oxides (MgO, MgO/Al<sub>2</sub>O<sub>3</sub>, TiO<sub>2</sub>, ZnO, Ce<sub>x</sub>Zr<sub>1-x</sub>O<sub>2</sub> and V<sub>2</sub>O<sub>5</sub>). Therefore, they were first used as a support for the growth of SWCNT or MWCNT to produce the corresponding CNT/oxide nanohybrids. Figure 2.17 shows the results of conversion and product yield in the aldol-condensation of furfural and acetone over the different catalysts prepared after 3 h of reaction at 100 °C and 400 psi of N<sub>2</sub>. As it can be observed in Figure 2.17, the most active nanohybrids for the aldol-condensation reaction were the ones supported on MgO (MWCNT/MgO, MWCNT/MgO\_Al<sub>2</sub>O<sub>3</sub> and SWCNT/MgO), reaching conversion values of up to 16 %. Nanohybrids of MWCNT/TiO<sub>2</sub> presented some activity, but the ones supported on ZnO, Ce<sub>x</sub>Zr<sub>1-x</sub>O<sub>2</sub> and V<sub>2</sub>O<sub>5</sub> led to conversion values lower than 1 %.



**Figure 2.17: Conversion and product yields (%) in the aldol-condensation of furfural and acetone over different nano hybrids for 3 h at 100 °C and 400 psi of N<sub>2</sub>. Feed: total molar concentration (furfural + acetone) of 1.8 M; furfural/acetone ratio of 1.5.**

The main product observed in all the cases was 4-(2-furyl)-3-buten-2-one (C<sub>8</sub>), while small amounts of 2-furancarboxylic 2-furanmethyl ester (C<sub>10</sub>) and 1,5-bis-(2-furanyl)-1,4-pentadien-3-one (C<sub>13</sub>) were detected. The reaction pathways that explain the formation of these products are summarized in Figure 2.18. The C<sub>8</sub> product is obtained from the coupling of acetone and furfural via aldol-condensation. This molecule undergoes an additional condensation with a second furfural molecule upon deprotonation of the alpha hydrogen, obtaining then the double condensation product, 1,5-bis-(2-furanyl)-1,4-pentadien-3-one (C<sub>13</sub>). Furthermore, since MgO is active to form the intermediate species for the Cannizzaro reaction [159-161], furfural was also converted to furoic acid and furfuryl alcohol, which later reacted to form the esterification product (Figure 2.18), 2-furancarboxylic 2-furanmethyl ester (C<sub>10</sub>). From

Cannizzaro reaction it is expected that equal moles of furoic acid and furfuryl alcohol will be formed [162], which agrees with the fact that both products were present the same selectivity. As expected products derived from acetone coupling were not observed since the correspondent reaction rate is smaller than the ketone-aldehyde coupling [163]. Based on these preliminary results, for a deeper study of the aldol-condensation reaction, we decided to focus on the nano hybrids supported on MgO, both SWCNT and MWCNT.

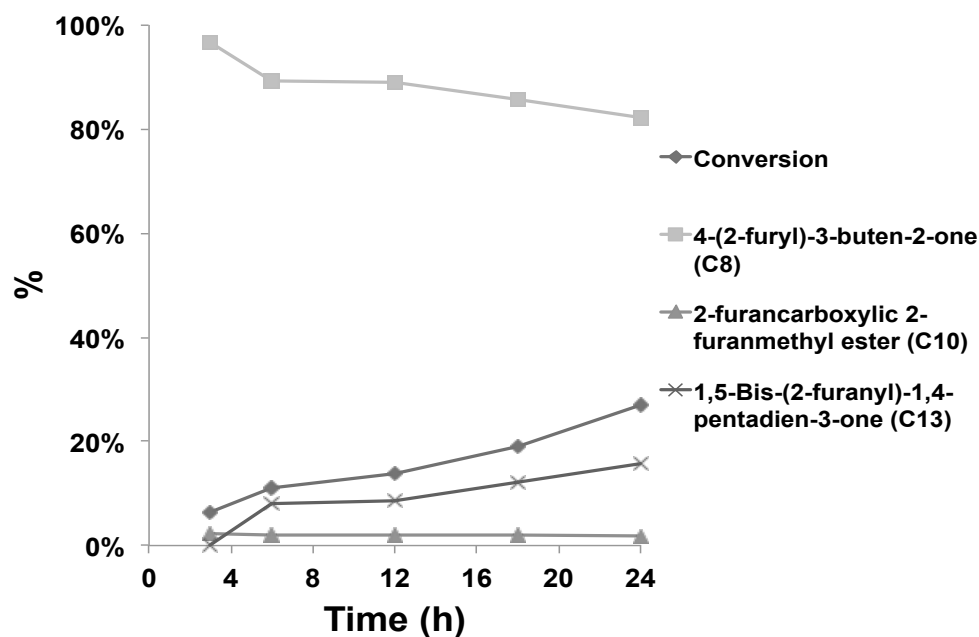


**Figure 2.18: Mechanism of the condensation reactions of furfural and acetone over CNT/MgO nano hybrids.**

#### 2.3.2.1.2. Products Evolution during Aldol-Condensation of Furans and Ketones in Emulsion

Condensation reactions were also studied over time using nano hybrids supported on MgO in an emulsion system stabilized by MWCNT/MgO nano hybrids. Figure 2.19 shows the results of conversion and product yields for the reaction

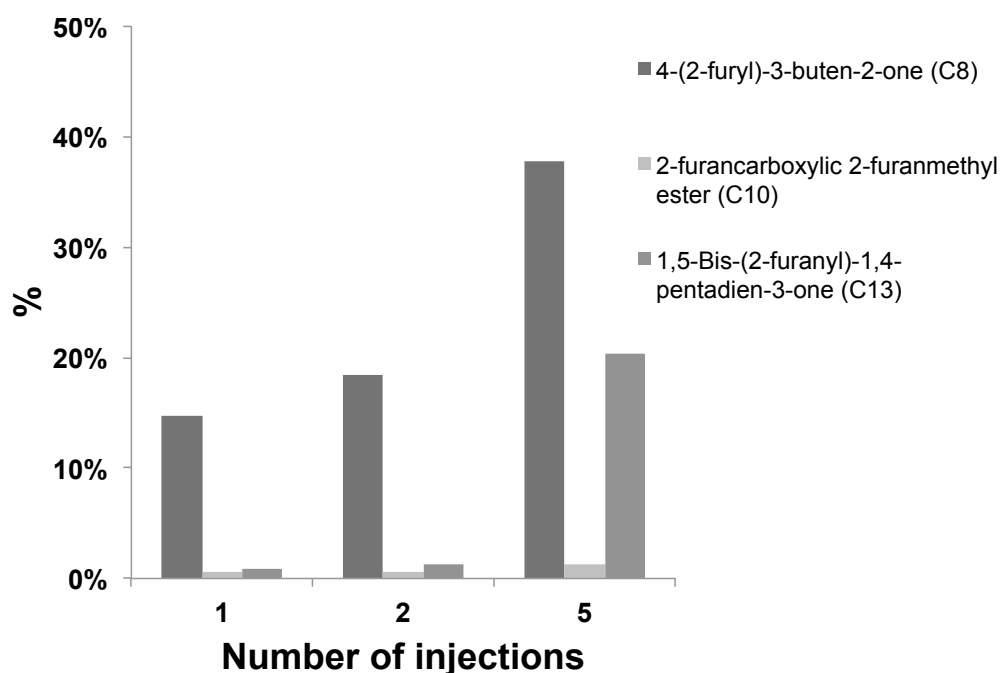
catalyzed by MWCNT/MgO nanohybrids and performed at 100 °C and 400 psi N<sub>2</sub>. It can be observed an increase in the conversion of the reactants with time, going from ~ 6 % after 3 h of reaction, up to ~ 25 % after 24 h. The main product in all the cases was C<sub>8</sub>, which formation decreased with time due to its conversion to produce the C<sub>13</sub> product.



**Figure 2.19: Conversion and product yields (%) in the aldol-condensation of furfural and acetone over MWCNT/MgO nanohybrids at 100 °C and 400 psi of N<sub>2</sub>. Feed: total molar concentration (furfural + acetone) of 1.8 M; furfural/acetone molar ratio of 1:5.**

In order to increase the production of the C<sub>13</sub> product, it was considering interesting to study the effect of injecting new feeds after 3 h reaction periods, to see if the addition of more furfural favored the conversion of the C<sub>8</sub> product to the C<sub>13</sub> one. Figure 2.20 shows the values of product yields after 1, 2 and 5 feed injections. It is

worth noting that the formation of C<sub>13</sub> was slightly favored when increasing from 1 to 2 injections, but it was highly favored after 5 feed injections.



**Figure 2.20: Product yields (%) in the aldol-condensation of furfural and acetone over MWCNT/MgO nanohybrids at 100 °C and 400 psi of N<sub>2</sub> after different number of injections and corresponding 3 h reaction/injection. Feed: total molar concentration (furfural + acetone) of 1.8 M; furfural/acetone molar ratio of 1:5.**

#### 2.3.2.2. Cascade Aldol-Condensation and Hydrogenation Reactions in Emulsions

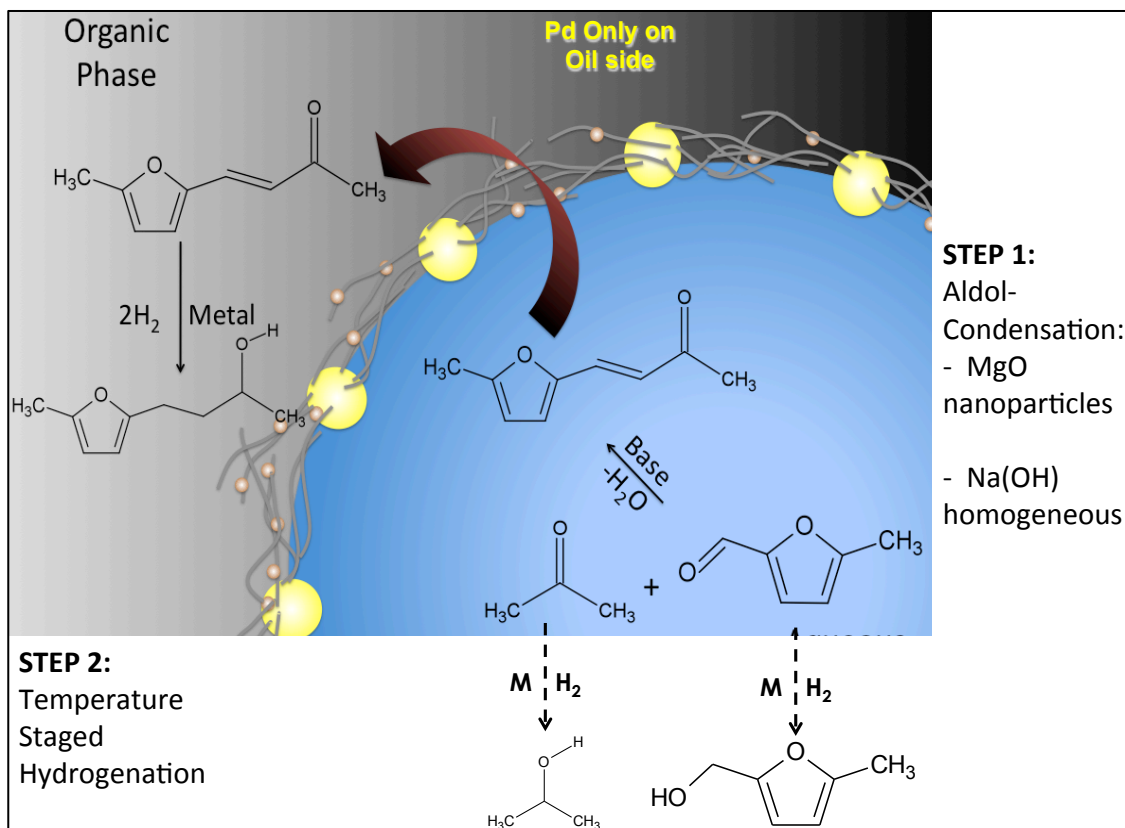
In this section is explored a tandem reaction sequence in which Pd-catalyzed hydrogenation was paired with a preceding aldol-condensation of 5-methylfurfural and acetone. This reaction was catalyzed by MgO, which was incorporated in the nanohybrids instead of silica. In many aqueous-phase processes the use of metal-oxides with basic character is hindered as they readily undergo hydration to hydroxides, which then dissolves favoring unselective homogeneous catalysis and reducing the catalyst recyclability. By adding the hydrophobic carbon nanotubes to the basic metal-oxides we

have been able to minimize the leaching of the catalyst in aqueous environments, while providing the amphiphilicity required to stabilize emulsions.

When using MgO during the nanotube synthesis, the SWNT product contains about 20 % multiwalled carbon nanotubes (MWNTs) as an impurity; however, the use of MgO imparts basicity to the nano-hybrids, which is crucial for the Aldol condensation. Therefore, because the MgO-based nanohybrids are still effective in stabilizing emulsions, we have been able to conduct reactions at the liquid/liquid interface by using a bifunctional catalyst that contains both metal and basic sites. Moreover, as mentioned above, this nanohybrid contains nanotubes that are more defective and is able to stabilize Pd particles not only on the hydrophilic side but also on the hydrophobic side. Therefore, hydrogenation can occur on both sides of the emulsion.

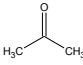
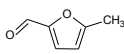
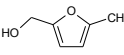
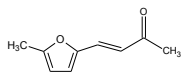
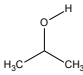
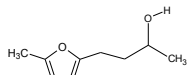
As represented in Figure 2.21, the expected products from the combination of these reactions are 4-(5-methylfuran-2-yl)buten-2-one, 4-(5-methylfuran-2-yl)buten-2-ol, 5-methylfuran-2-yl methanol, and 2-propanol. To better determine how these products evolve, we conducted this reaction in tandem. That is, we first ran the reaction under N<sub>2</sub> at 80°C for 3 hours and analyzed the products, which is indicated as condensation in Table 2.1. In this case, no hydrogenation took place. Self-condensation of acetone was not observed. Ketone-ketone condensation reactions are thermodynamically less favorable and much slower than ketone-aldehyde condensation, as pointed out by West et al. [113]. As a result, the major product was 4-(5-methylfuran-2-yl)buten-2-one, which in line with its high log P value (~1.5) migrated almost completely to the organic phase. In the second experiment, which is indicated as

hydrogenation in Table 2.1, an additional 1-hour reaction step at 100°C under H<sub>2</sub> flow was added to the initial 3 hours at 80°C under N<sub>2</sub>. The 4-(5-methylfuran-2-yl)buten-2-one is totally hydrogenated in the second step, indicating that hydrogenation has occurred in the organic phase as well as in the aqueous phase.



**Figure 2.21: Possible reaction paths and products arising from the condensation and direct hydrogenation of 5-methylfurfural and acetone over 5 wt % Pd/CNT/MgO.**

**Table 2.1: Product distribution of the Aldol-condensation–hydrogenation reaction of 5-methylfurfural and acetone over 5 wt% Pd/(CNT/MgO). Reaction conditions were 3 hours at 80°C in 250 pounds per square inch (psi) of N<sub>2</sub> and then 1 hour at 100°C in 250 psi of H<sub>2</sub>. (Aq) aqueous phase; (Org) organic phase.**

Name	Structure	Before Reaction (%)		Condensation (%)		Hydrogenation (%)	
		Aq.	Org.	Aq.	Org.	Aq.	Org.
Acetone		92.5	60.8	91.7	56.0	85.7	56.7
5-Methylfurfural		7.5	39.2	6.3	31.6	4.2	24.6
(5-methylfuran-2-yl) methanol		0.0	0.0	0.0	0.0	3.6	2.3
4-(5-methylfuran-2-yl)butan-2-ol		0.0	0.0	0.0	0.0	<b>2.5</b>	<b>16.4</b>
2-propanol		0.0	0.0	0.0	0.0	4.0	0.0
4-(2-furyl)-3-buten-2-one		0.0	0.0	<b>2.0</b>	<b>12.4</b>	0.0	0.0

The shorter oxygenates, in this case propanol, remain in the aqueous phase, thus enhancing the probability of realizing further condensation reactions that would be advantageous in the production of fuel components. The advantage of operating in a biphasic system, with the catalyst at the liquid/liquid interface, is the possibility of conducting the sequential reactions in a single reactor instead of two. The carbon chains migrate to the organic phase after growing long enough to become hydrophobic, facilitating their isolation as desirable products, whereas the shorter chains remained in the aqueous phase to undergo further growth. The use of a biphasic system provides the possibility of doing the next reaction (for example, hydrogenation- hydrogenolysis exclusively in the oil phase) but in the same reactor. In previous studies conducted in a monophasic aqueous system, once the water solubility of the condensed product



becomes low enough, it leaves this phase, stopping the conversion. In many cases, these intermediate products still contain oxygen, and the only way to completely deoxygenate them is by using a second reactor operating in the organic phase or a high- temperature vapor phase hydrotreatment.

#### 2.3.2.3. Conversion of Synthetic Bio-oils in Emulsion

In order to further explore the effectiveness of this system in a more realistic situation, three different synthetic bio-oils (SBO) were prepared and used as feed for aldol-condensation and hydrogenation/hydrodeoxygenation reactions. The composition of the different synthetic bio-oils is summarized in Table 2.2. The composition of SBO #1 and 2 was the very similar, mainly composed of short oxygenates, but with or without acetic acid, respectively. SBO #3 was mainly composed of phenolics compounds.

**Table 2.2: Composition (mol/l) of the different synthetic bio-oils prepared.**

Component	SBO #1 (mol/l)	SBO #2 (mol/l)	SBO #3 (mol/l)
Acetone	1.00	1.00	--
Propanal	1.00	1.00	--
2-Furfural	2.00	2.00	--
Methanol	1.00	1.00	--
Acetic acid	1.30	--	--
Acetol	0.50	0.50	--
m-Anisaldehyde	--	--	0.50
m-Cresol	--	--	0.50
Anisol	--	--	0.50
Benzaldehyde	--	--	0.50
2-methoxy-4-methyl phenol	--	--	0.30
Cathecol	--	--	0.10
Guaiacol	--	--	0.50
4-Hydroxy-3-methoxy benzyl alcohol	--	--	0.05
Vanillin	--	--	0.05
Phenol	--	--	0.10
4-Hydroxy benzaldehyde	--	--	0.05

#### 2.3.2.3.1. Aldol-condensation and Hydrogenation Reactions of Synthetic Bio-oil in Emulsions

For these reactions, the performance of MWCNT/MgO and MWCNT/ZnO nanohybrids were compared. Additionally, the effect of adding acetic acid in the feed was also evaluated, using SBO #1 with acid and SBO #2 without acid (Table 2.2). The results of conversion, product yield and total carbon balance are presented in Table 2.3. As it can be noted, the conversion in the aldol-condensation reaction for SBO # 1 (acid) was low with both catalysts, taking values of less than 3 % (Reactions #1 and #2). However, in the same reactions carried out with SBO #2 (no acid), while the conversion with the catalyst supported on ZnO was still low (1.9 %, Reaction #4), the conversion with MWCNT/MgO (Reaction #5) reached a value of 13.7 %. Such decrease in the

performance of the MgO catalyst when acetic acid was present could be due to the chemical adsorption of the acetic acid on the basic sides of the MgO surface, which deactivated the catalyst rapidly. On the other hand, ZnO was not so sensitive to the presence of acid.

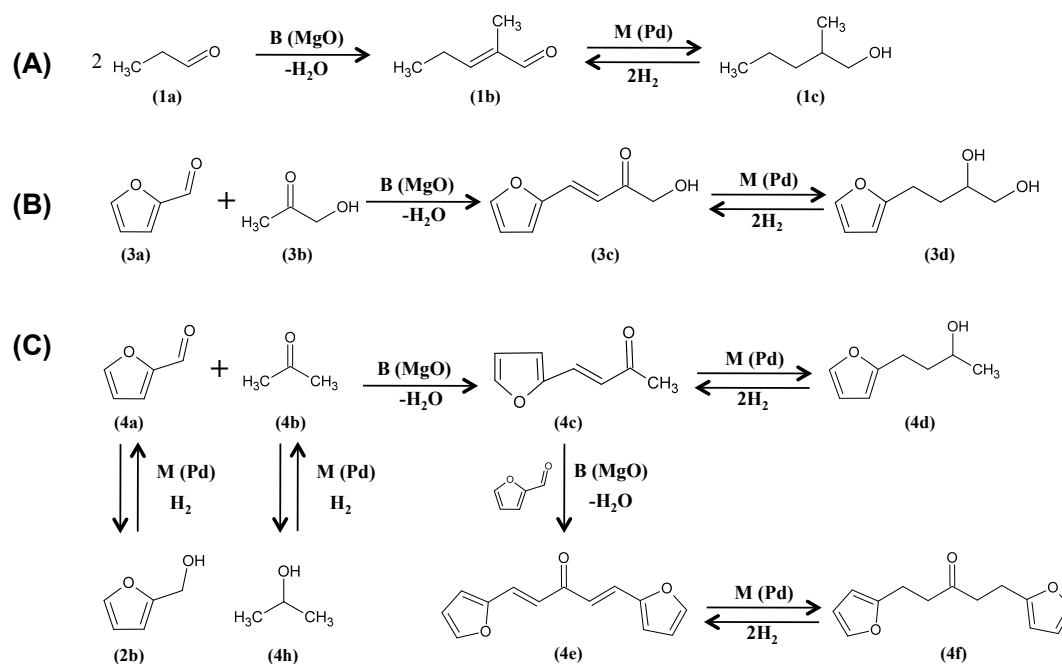
**Table 2.3: Total yield, product yield and total carbon balance obtained in the aldol-condensation and hydrogenation reactions of synthetic bio-oils SBO #1 and #2 at 100 °C and 400 psi in a biphasic system of decalin/water with an aqueous/organic ratio = 1.0.**

Feed SBO #	Catalyst	Reaction Time (h)		Total Yield (%)	Yield (%)										Carbon Balance (%)		
		N <sub>2</sub>	H <sub>2</sub>		3g	2b	1b	1c	4c	4d	3c	3d	2d	4e		4f	
1	MWCNT/ZnO	3	--	2.6					0.2	1.8		0.2		0.1	0.4		95.3
1	MWCNT/MgO	3	--	0.8				0.2	0.3					0.1	0.2		98.7
1	MWCNT/ZnO +10 Pd/SWCNT	3	3	4.5	0.1	0.2	0.6	0.2	0.5	1.0	0.1	0.2	0.1	0.4	1.2		93.2
2	MWCNT/ZnO	3	--	1.9				0.2	1.1		0.3			0.1	0.1		92.8
2	MWCNT/MgO	3	--	13.7				0.6	2.5	8.3		1.6		0.7			98.5
2	MWCNT/ZnO + 5% Ni/SWCNT	3	3	2.0		0.1		0.1	0.9	0.2	0.2		0.1		0.3		91.4

Note: The molecules presented in the table are: isopropanol (3g), furfuryl alcohol (2b), 2-methyl-pentaldehyde (1b), 2-methyl-pentanol (1c), 4-(2-furyl)-3-buten-2-one (4c), 4-(furan-2-yl)butan-2-ol (4d), 4-(furan-2-yl)-1-hydroxybut-3-en-2-one (3c), 4-(furan-2-yl)butan-1,2-diol (3d), 2-furancarboxylic 2-furanmethyl ester (2d), 1,5-bis-(2-furanyl)-1,4-pentadien-3-one (4e) and 1,5-di(furan-2-yl)pentan-3-one (4f).

Besides, when a hydrogenation reaction was run after the aldol-condensation one (Reactions #3 and #6 of Table 2.3), it was observed an increase in the conversion when the ZnO nanohybrids were functionalized with Pd (from 2.6 to 4.5 %). However,

when Ni was used instead of Pd, the conversion did not change. This result could be related to the higher activity of the noble metal in comparison to the nickel catalyst. As expected, the major products in these reactions came from the self-condensation of propanal and the cross-coupling of furfurals and acetones (2-methyl-pentanol (1c), 4-(2-furyl)-3-buten-2-one (4c) and 4-(furan-2-yl)-1-hydroxybut-3-en-2-one (3c)). The reactions observed are shown in Figure 2.22. Also, a secondary esterification reaction took place between the products of the Canizzaro reaction (Figure 2.17), producing 2-furancarboxylic 2-furanmethyl ester (C<sub>10</sub>).

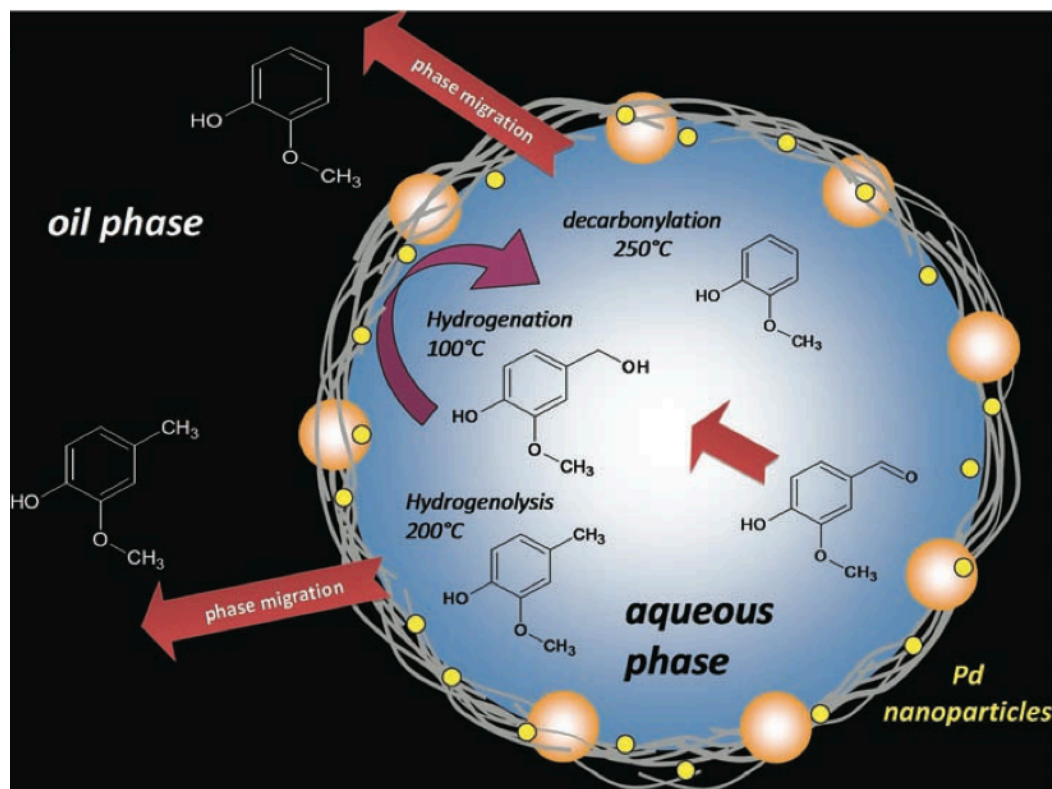


**Figure 2.22: Aldol-condensation and hydrogenation reactions of SBO #1 and #2 at 100 °C and 400 psi in a biphasic system of decalin/water with an aqueous/organic ratio = 1.0.**

### 2.3.2.4. Hydrodeoxygenation of Phenolics Molecules in Emulsion

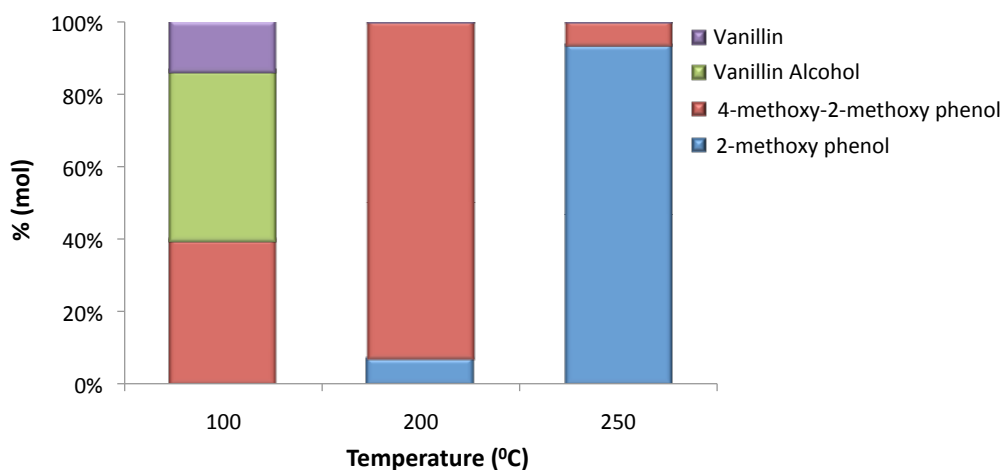
#### 2.3.2.4.1. Hydrodeoxygenation of Vanillin in Emulsion

To explore the catalytic application of Pd-containing nanohybrids to phenolic hydrodeoxygenation in a water-in-decalin emulsion, we chose vanillin (4-hydroxy-3-methoxybenzaldehyde) as a test substrate because it is a common component of pyrolysis oil derived from the lignin fraction. This compound was appealing for study because of its three different types of oxygenated functional groups (aldehyde, ether, and hydroxyl) and its partial solubility in both the organic and aqueous phases. It was then possible to monitor the migration that the different products underwent from the aqueous to the organic phase, as summarized in Figures 2.23 and 2.24.



**Figure 2.23: Schematic illustration of the reactions taking place at the water/oil interface in the solid-stabilized emulsions.**

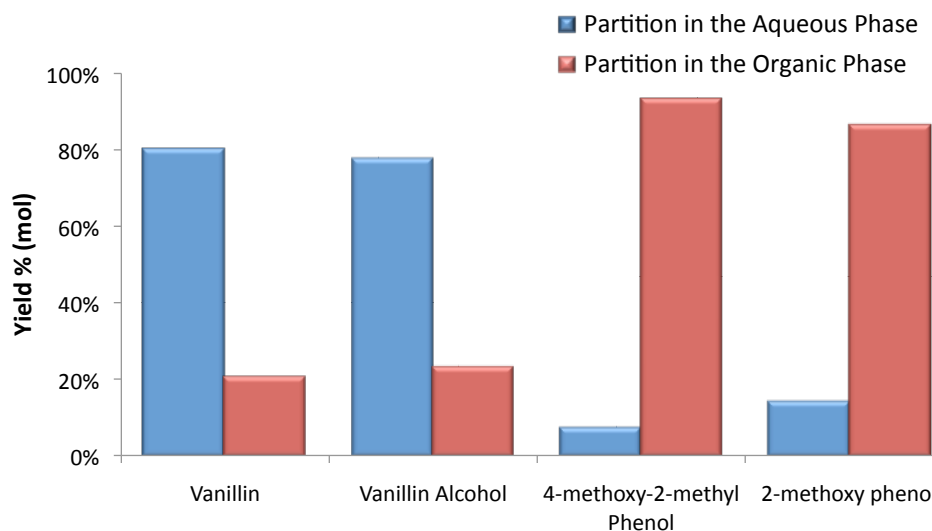
As shown in Figure 2.24, the chemoselectivity changes significantly with increasing temperature. At 100°C, initially only hydrogenation of the aldehyde to the vanillin alcohol is observed, whereas at longer reaction times the alcohol is further converted into 2-methoxy-4-methylphenol (p-cresol) via hydrogenolysis. At 200°C, hydrogenolysis becomes the dominant path even at short reaction times. At 250°C, the dominant reaction is the decarbonylation of the aldehyde group, leading primarily to o-methoxyphenol (guaiacol).



**Figure 2.24: Total weight fraction of the various products as a function of temperature after 30-min reaction in a batch reactor, from gas chromatographic analysis of each phase (combined).**

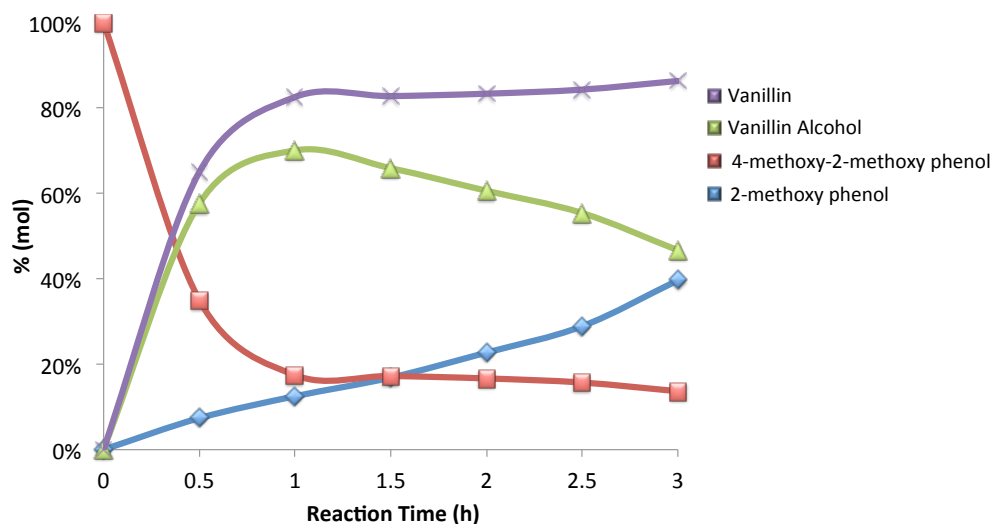
As illustrated schematically in Figure 2.23, we observed a range of different products and phase-migration processes that were due to the varying extents of hydrogenation, hydrogenolysis, and decarbonylation reactions catalyzed by Pd as the reaction conditions were modified. Whereas vanillin and vanillin alcohol were highly soluble in the aqueous phase (Figure 2.25), the products resulting from both hydrogenolysis and decarbonylation were much more soluble in the decalin phase. As a

result, the water-insoluble compounds, which are more valuable as fuel components, can be readily incorporated in the product stream.



**Figure 2.25: Partition of the various products in between the individual aqueous and organic phases after hydrogenation reaction of vanillin over 5 wt. % Pd/SWCNT/SiO<sub>2</sub>.**

The variation of product distribution with reaction time in the batch reactor at 100°C is shown in Figure 2.26. The vanillin alcohol is the primary product, but at longer times it is consumed by hydrogenolysis to form p-cresol, which migrates to the organic phase upon formation, preventing further conversion. In contrast, the alcohol remains in the aqueous phase and continues reacting. This result illustrates the concept of simultaneous reaction and separation of intermediate products.

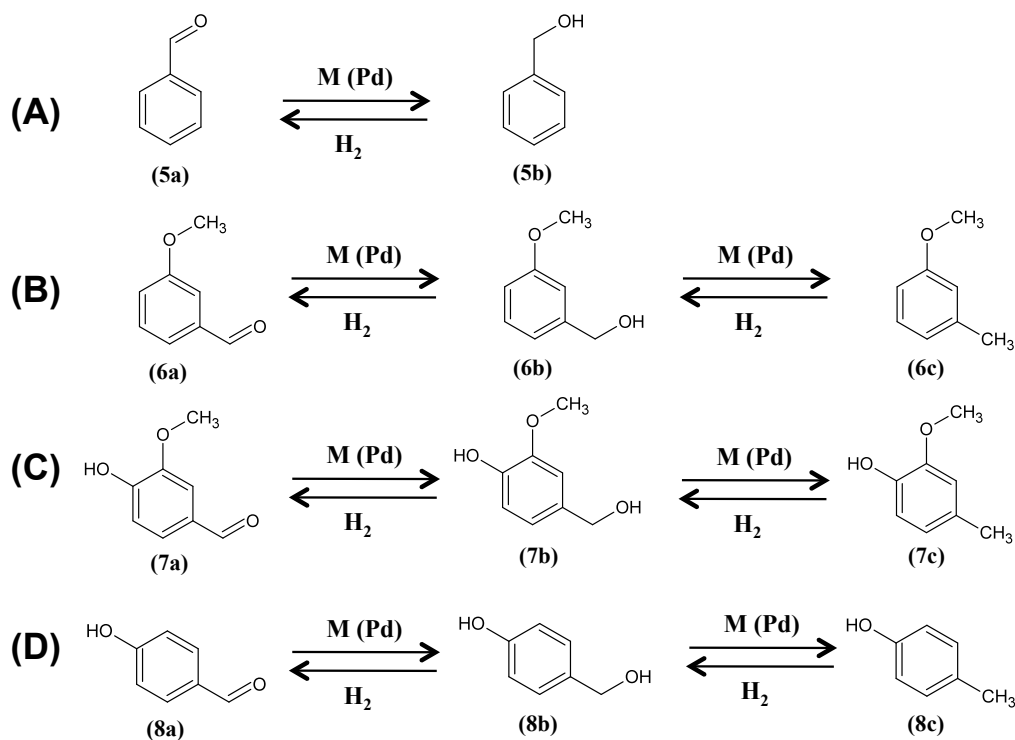


**Figure 2.26: Evolution of products and reactant concentration with the reaction time in the experiments performed with vanillin over 5 wt. % of Palladium supported on SWNT grown on silica oxide at 100 °C.**

#### 2.3.2.4.2. Hydrodeoxygenation of Synthetic Bio-oil Mixtures in Emulsion

A reaction of hydrodeoxygenation using SBO #3 (Table 2.2) as feed, which is a mixture of eleven different phenolic compounds, including alcohols, ethers, aldehydes, was carried out at 100 °C and 400 psi of H<sub>2</sub> for 3 h over 5 wt. % Pd/MWCNT<sub>2</sub>Al<sub>2</sub>O<sub>3</sub>. The reaction mechanism is shown in Figure 2.27, and the results of conversion, product yield, selectivity and carbon balance are summarized in Table 2.4. The conversion observed in this reaction was 49.2 %, being benzyl alcohol and 4-hydroxybenzyl alcohol the main products (44.7 and 49.5 % of selectivity, respectively). As expected, under these mild reaction conditions, the aldehydes present in the feed were the only molecules that reacted to produce the corresponding hydrogenation products (alcohols) and hydrogenolysis products (deoxygenated phenolic molecules).





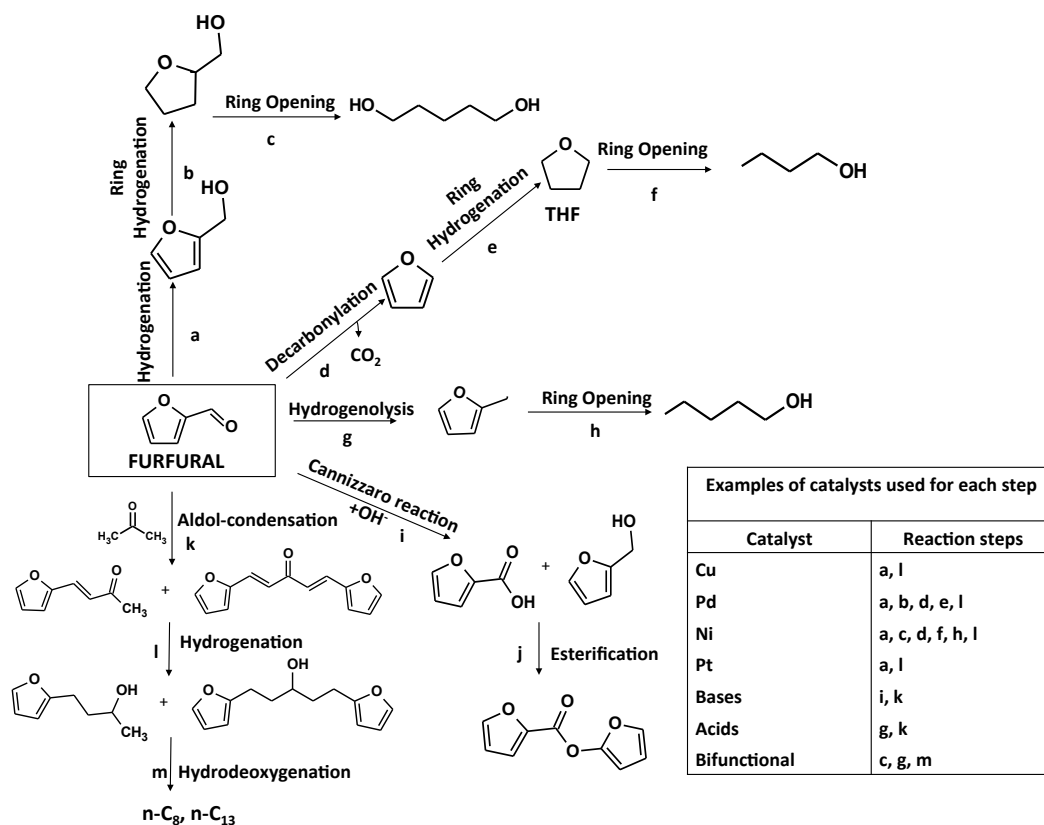
**Figure 2.27: Hydrodeoxygenation reaction of SBO #3 at 100 °C and 400 psi of H<sub>2</sub> over 5 wt. % Pd/MWNT-Al<sub>2</sub>O<sub>3</sub> in a biphasic system of decalin/water with an aqueous/organic ratio = 1.0.**

**Table 2.4: Conversion, product yields, selectivity and total carbon balance after 3 h of reaction over 5 wt. % Pd/MWNT-Al<sub>2</sub>O<sub>3</sub> at 100 °C and 400 psi of H<sub>2</sub> in a biphasic system of decalin/water with an aqueous/organic ratio = 1.0.**

Component	Conversion (%)	Yield (%)	Selectivity (%)	Carbon Balance (%)
1-methoxy-3-methylbenzene (6c)	49.2	0.2	0.3	98.1
benzyl alcohol (5b)		22.0	44.7	
2-Methoxy-4-methyl phenol (7c)		2.5	5.0	
p-cresol (8c)		0.0	0.1	
3-methoxybenzyl alcohol (6b)		24.4	49.5	
4-hydroxybenzyl alcohol (8b)		0.2	0.4	

### *2.3.3. Molecular Engineering of Fuel Components Derived from Biomass*

A quick examination of the different furfural conversion strategies reviewed above indicates that by choosing the right catalyst and reaction conditions the researcher can pick and choose from a broad range of potential fuel components. As summarized in Figure 2.28, starting with furfural, one can start with hydrogenation on a metal (Cu, Pd, Ni, Pt). The product furfuryl alcohol would not be the most desirable fuel component since it is fully miscible in water (see Table 2.5). If the furanyl ring is further hydrogenated and then the ring opened (e.g. on Pd and Ni, respectively), 1,5-pentanediol can be obtained. As shown in Table 2.5, this diol has a very good octane number, but its high solubility in water may also hinder its applications as a fuel component, similar to furfuryl alcohol. A similar situation may occur with butanol, which can be relatively easily obtained with a combination of decarbonylation/hydrogenation and ring opening (on Ni). While this potential fuel component has a relatively good octane number and vapor pressure, its water solubility is also high. However, it must be noted that, in this sense, butanol appears much better than ethanol, a fuel component widely used today despite its high water solubility. Two interesting alcohols that can be obtained from furfural and methyl furfural via hydrogenolysis followed by ring opening are pentanol and hexanol, respectively. While their octane numbers are not as high as those of the shorter alcohols, their vapor pressures and water solubilities are very attractive for gasoline components. This is an example of the fuel component analysis that can be done with the molecular engineering approach, in which the researcher may have the possibility of choosing reaction path that optimize several fuel properties simultaneously.



**Figure 2.28: Catalytic strategies for the conversion of furfural to fuel components and chemicals. The possible reaction steps are indicated with lowercase letters and the corresponding catalysts listed in the inset.**

Avoiding ring opening produces furan and methyl furan, aromatic compounds that have remarkably high octane numbers and low solubility in water. The only serious limitation of these compounds that may hinder their use as fuel components is their high vapor pressure, which is much higher than those of their corresponding ring-opening derivatives.

**Table 2.5: Summary of the possible reactions taking place in the conversion of furfural (FAL) and hydroxymethylfurfural (HMF), with the respective products and their properties.**

Feedstock	Reactions	Products	ON (CN)	Water Solubility (g/l) at 25 °C
FAL	Hydrogenation	Furfuryl alcohol	134	miscible
FAL	Decarbonylation	Furan	109	no
FAL	Ring opening	Butanol	96	77.0
FAL	Hydrogenolysis	Methyl furan	131	7.0
HMF	Ring opening	hexanol	56	8.2
HMF	Hydrogenolysis	Dimethylfuran	119	2.3
HMF	Aldol Condensation	C8	(74)	--
HMF	Aldol Condensation	1,5-di-2-furylpenta-1,4-dien-3-one	(81)	immiscible
HMF	Aldol Condensation + Hydrogenation	n-tridecane	(89)	immiscible

Finally, the path that combines aldol-condensation with hydrogenation and hydrodeoxygenation appears greatly attractive for the production of diesel fuel components. As shown in Figure 2.28, while the C<sub>8</sub> compound that results from the condensation of one molecule of acetone with one molecule of furfural is in the gasoline range, the C<sub>13</sub> compound that results from two furfurals and one acetone is in the diesel range and has a high cetane number, even after hydrodeoxygenation, resulting in an appealing alternative for green diesel fuel.

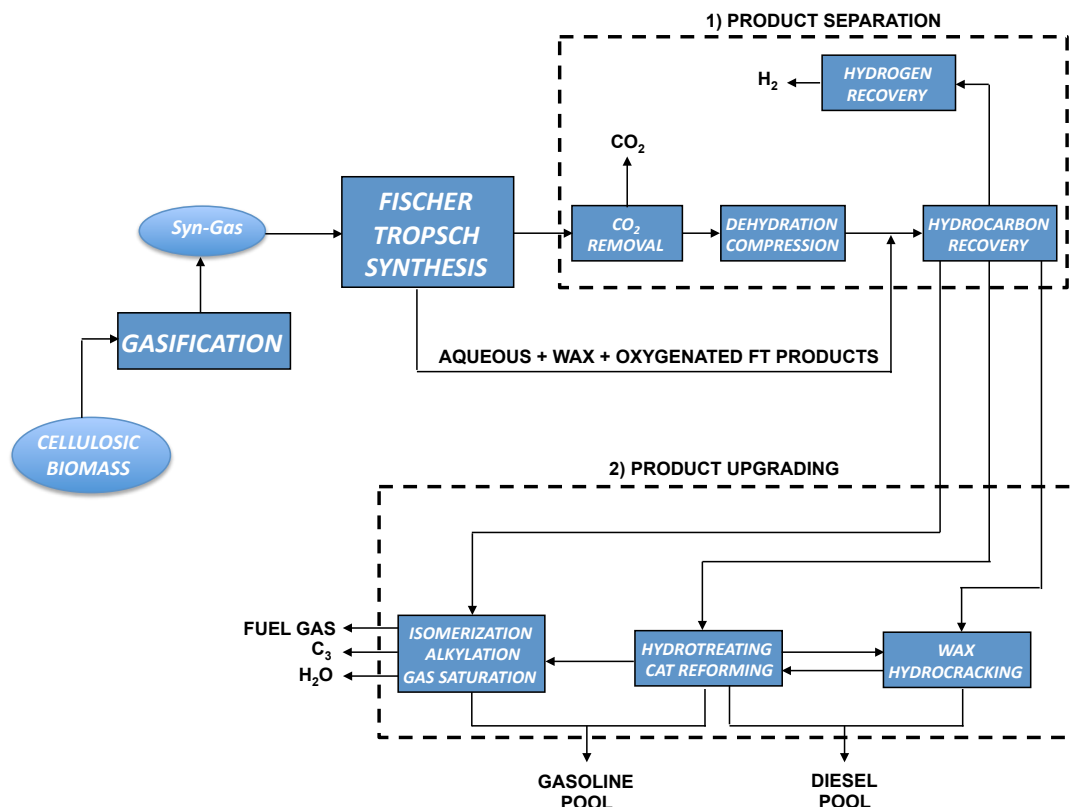
In this section we have reviewed the possible reaction paths that could be followed for upgrading furfurals (e.g. 2-furfuraldehyde and 5-hydroxymethyl furfural), intermediates from biomass to fuel components and chemicals. It is concluded that by varying the catalyst composition (metal, additives, support), as well as reaction conditions (pressure, temperature, liquid/vapor phase, etc.), one can obtain a rich variety of products with different fuel properties.

#### *2.3.4. Fischer-Tropsch Reaction in Emulsion coupled with Aldol-condensation*

The biomass-to-liquids (BTL) processes have the potential to provide a renewable source of useful fuels and chemicals. The production of liquid transportation fuels from conventional hydrocarbon resources (e.g. natural gas and coal) using the Fischer-Tropsch (FT) process has been demonstrated on large scale. Similarly, biomass also could serve as a Fischer-Tropsch feedstock, alone or in conjunction with fossil fuels to produce cleaner fuels with zero or nearly zero CO<sub>2</sub> generation [164]. Although the purification and conditioning of the syngas produced by biomass gasification increase operational cost, this technology has received great attention due its fungibility with conventional fuels, highly competitive vehicle performance, and reduced regulated exhaust emissions (near-zero sulfur content).

A serious drawback in such systems, however, is the significant amount of oxygenated molecules (mainly alcohols, aldehydes and acids) produced, which reduces the carbon efficiency of the process and generates incrustations/plugs downstream, more specifically in the hydrocracking reactors. Typically, most of these oxygenated molecules are extracted in an aqueous stream that is treated in a

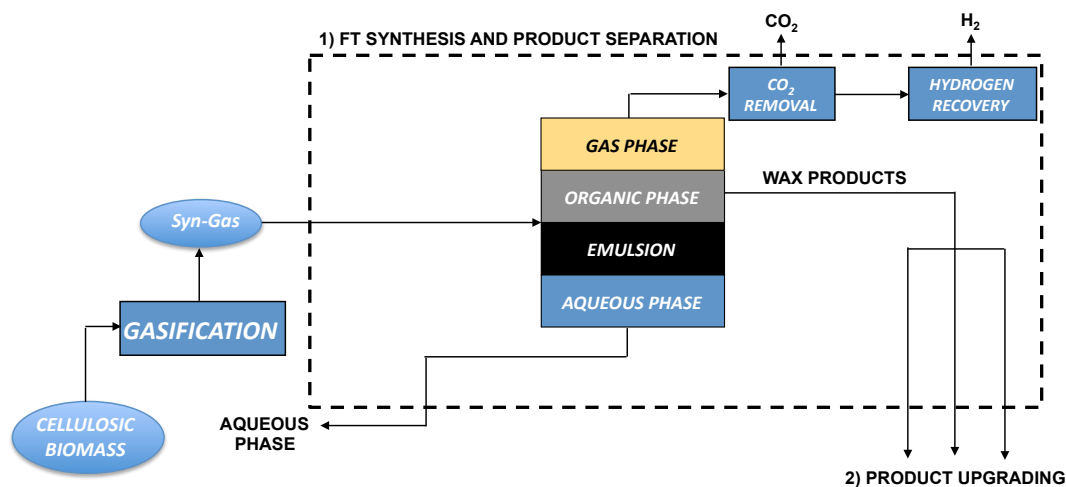
dehydration/compression unit, in which the oxygen is removed as water and the olefins produced are compressed (Figure 2.29).



**Figure 2.29: Process diagram for the conversion of biomass to liquid hydrocarbons based on Fischer-Tropsch synthesis.**

An interesting proposition could be the utilization of solid-stabilize emulsions as a catalyst reaction media in which the amphiphilic catalyst nanoparticles were specially functionalized with acid moieties in the hydrophilic side and metal catalyst on the hydrophobic side (Figure 2.30). These bifunctional catalysts would be able to perform simultaneously the Fischer-Tropsch synthesis of the hydrocarbons and the dehydration of the alcohols produced during the undesired oxo-mechanism. The olefins resulting from the dehydration of the alcohols could undergo partitioning into either the organic

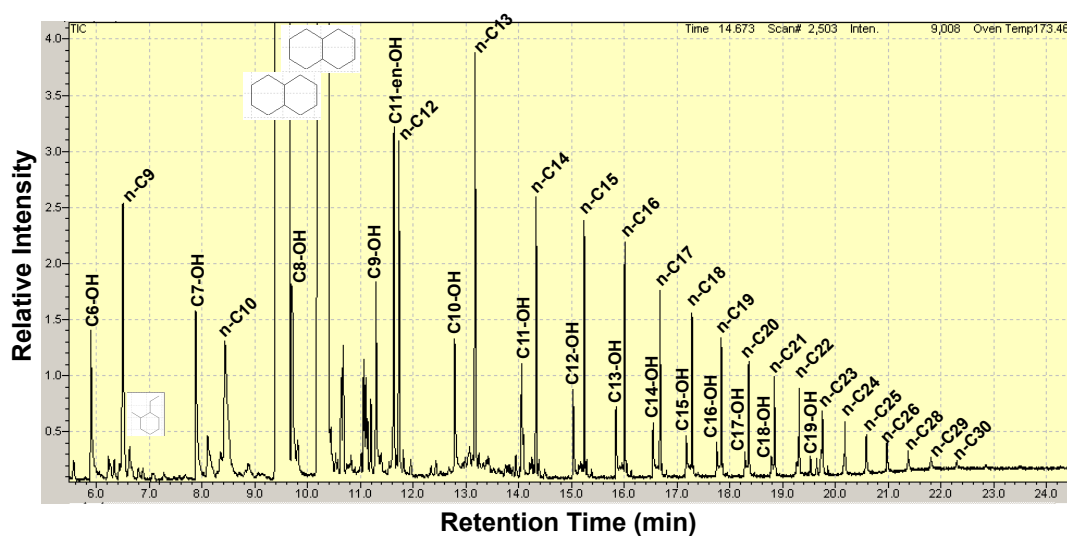
or gaseous phases depending on its relative solubilities and volatilities. Such process could result in substantial simplifications at the isolation and purification stages, obviating the need of hydrocarbon recovery procedures.



**Figure 2.30: Process diagram for the conversion of biomass to liquid hydrocarbons based on a modified Fischer-Tropsch synthesis using the nano-hybrid-stabilized emulsion.**

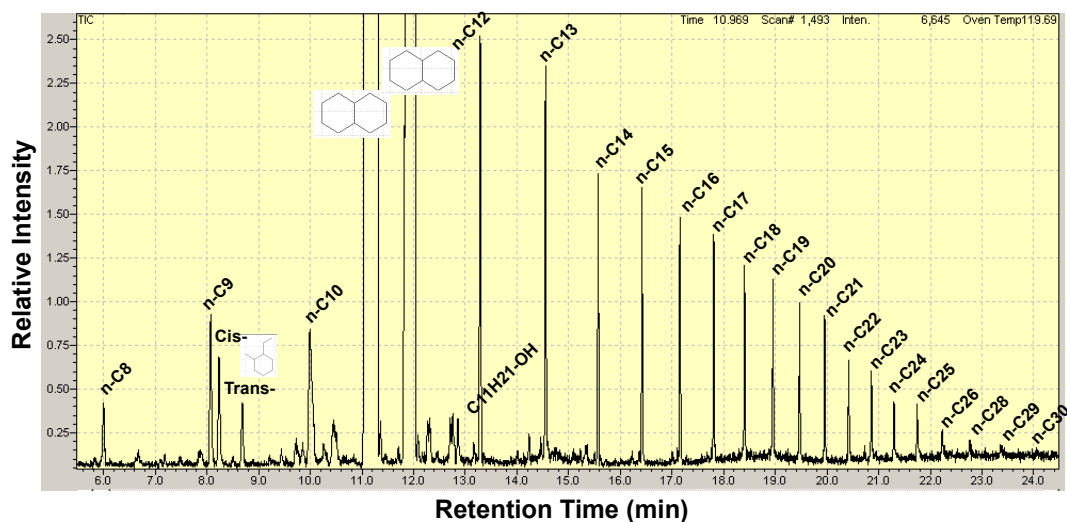
In this regard, a preliminary catalytic test has been carried out using MWCNT/Al<sub>2</sub>O<sub>3</sub> functionalized with Ruthenium (5 wt. %) catalyst in decalin as a solvent, compared with a water/decalin emulsion system. As it can be observed in Figures 2.31 and 2.32 there was a remarkable improvement in the selectivity of the FT reaction towards the alkanes when the catalyst was at the liquid-liquid interface of the decalin-water emulsion. This striking result indicates that the utilization of the nano-hybrid-stabilized emulsions could improve the selectivity of the reaction, and furthermore it could simplify the process scheme by obviating the separation units used in the current technologies.

Nevertheless, the physico-chemical phenomena behind these experimental observations are still unclear and further study is currently undergoing. Therefore, further study of this catalytic system using kinetic reaction and mass transport data in single phase (decalin or dodecane solvents) and in emulsion for the FT reaction over ruthenium catalyst is required. In addition, the coupling of FT-synthesis and dehydration reactions will be explored as proof-of-concept system for the simplification of the FT-processes commercially available.



**Figure 2.31: Gas chromatography and mass spectrum (GC-MS) of the decalin phase after 24 h of reaction of CO:H<sub>2</sub> (1:2) 600 psi at 200 °C over 5 % wt. Ru/MWCNT/Al<sub>2</sub>O<sub>3</sub> (250 mg). The catalyst was reduced in a flow reactor in gas phase for 1 h at 500 °C in H<sub>2</sub>.**





**Figure 2.32: Gas chromatography and mass spectrum (GC-MS) of the decalin fraction of the emulsion after 24 h of reaction of CO:H<sub>2</sub> (1:2) 600 psi at 200 °C over 5 % wt. Ru/MWCNT/Al<sub>2</sub>O<sub>3</sub> (250 mg) reduced in a gas phase reactor for 1 h at 500 °C in H<sub>2</sub>.**

## 2.4. Conclusions

It has been shown in the present study that it is possible to perform the simultaneous condensation/hydrogenation of biomass-derived oxygenates in emulsions stabilized by nanohybrids catalysts. The advantages of using this emulsion system stabilized by nanohybrids include an enhancement in the rate of mass transfer between phases due to the generation of a higher interfacial area, the possibility of maximizing the selective conversion of molecules present in each of the phases (phase-selectivity), and the direct partitioning and separation of molecules (phase-migration), simply based on differences in relative solubilities. We have seen that the aldol-condensation reaction of furfural and acetone is more effective in an emulsion system than in single aqueous phase, and it is favored when the furfural is in excess in relation to the acetone. Besides, the presence of the two phases in the emulsion system (aqueous and organic) facilitates the separation of the products. We have performed a catalyst screening for the aldol-

condensation reactions, demonstrating that by tailoring the catalyst surface, we can improve the conversion of the reactants. Among the different basic oxides employed to grow carbon nanotubes on their surface, the nanohybrids supported on MgO have resulted to be the most effective for the aldol-condensation reactions. Using both SWCNT/MgO and MWCNT/MgO as catalysts, we have studied how the reaction time and the furfural/acetone ratio in the feed can change the product distribution. In all the cases, the main product obtained is 4-(2-furanyl)-3-buten-2-one (C<sub>8</sub>), which later reacts to produce the double condensation product 1,5-bis-(2-furanyl)-1,4-pentadien-3-one (C<sub>13</sub>). Besides, as a secondary reaction, it has been seen that the Canizzaro reaction of disproportionation of furfural in the presence of hydroxyl groups also takes place. The products of this reaction undergo through an esterification step, giving place to the formation of 2-furancarboxylic 2-furanmethyl ester (C<sub>10</sub>).

Additionally, as a preliminary study of a more realistic situation, some synthetic bio-oils have been prepared and used as feed for the same type of reactions (aldol-condensation, hydrogenation and hydrodeoxygenation). Under the mild conditions employed for these reactions, we have been able to favorably convert the aldehydes present in the feed.

For the conversion of bio-syngas via Fischer-Tropsch we have shown some intriguing results. For instance when the reaction was performed in emulsion the selectivity shifted to long alcohols while in the case of single organic phase the long paraffins are favored. Meanwhile, when the reaction was performed in aqueous phase the activity decreased dramatically, and almost no products were observed. This change the selectivity towards oxygenated molecules in emulsion perhaps might be related to

the termination step during Fischer-Tropsch, in which the chemisorbed olefin undergoes hydroxylation to the aldehyde and hydrogenation to the alcohol.

## References

- [1] L.D. Schmidt and P.J. Dauenhauer, *Nature* 447 (2007) 914.
- [2] J.R. Rostrup-Nielsen, *Science* 308 (2005) 1421.
- [3] C. Somerville, H. Youngs, C. Taylor, S.C. Davis and S.P. Long, *Science* 309 (2010) 790.
- [4] C.E. Wyman and N.D. Hinman, *Appl. Biochem. Biotechnol.* 24/25 (1990) 735.
- [5] C.E. Wyman, *Appl. Biochem. Biotechnol.* 45/46 (1994) 897.
- [6] K.S. Tyson, *Fuel Cycle Evaluations of Biomass-Ethanol and Reformulated Gasoline*; Report No. NREL/TP-263-2950, DE94000227, National Renewable Energy Laboratory: Golden, CO, 1993.
- [7] L.R. Lynd, J.H. Cushman, R.J. Nichols and C.E. Wyman, *Science* 251 (1991) 1318.
- [8] U.S. Department of Energy, *Feedstock Composition Gallery*, Washington, DC, 2005; [http://www.eere.energy.gov/biomass/feedstock\\_glossary.html](http://www.eere.energy.gov/biomass/feedstock_glossary.html).
- [9] G.W. Huber and J.A. Dumesic, *Catal. Today* 111 (2006) 119.
- [10] A.V. Bridgwater, *Fuel* 14 (1995) 631.
- [11] D. Sutton, B. Kelleher and J.R.H Ross, *Fuel Process. Technol.* 73 (2001) 155.
- [12] D. Mohan, C.U. Pittman and P.H. Steele, *Energy Fuels* 20 (2006) 848.
- [13] A. Demirbas, *Prog. Energy Combust. Sci.* 33 (2007) 1.
- [14] J.P. Lange, *Biofuels Bioprod. Bioref.* 1 (2007) 39.
- [15] N.V. Pasadakis, V. Gaganis and C. Foteinopoulos, *Fuel Proc. Technol.* 87 (2006) 505.

- [16] K.I. Matsumoto, Toshiyuki and J. Mizuie, Tetrahydrofurfuryl alcohols. Jpn. Kokai Tokkyo Koho, Arakawa Chemical Industries, Ltd., Japan, 1986.
- [17] N. Fakhfakh, P. Cognet and M. Cabassud, J. Soc. Chim. Tunisie 8 (2006) 203.
- [18] N. Fakhfakh, P. Cognet, M. Cabassud, Y. Luchesse and M. Dias de los Rios, Chem. Eng. Process. 4 (2008) 349.
- [19] C.J. Barrett, J.N. Chheda, G.W. Huber and J.A. Dumesic, Appl. Catal. B 66 (2006) 111.
- [20] R.M. West, Z.Y. Liu, M. Peter, C.A. Gärtner and J.A. Dumesic, J. Mol. Catal. A 296 (2008) 18.
- [21] W. Shen, G.A. Tompsett, K.D. Hammond, R. Xing, F. Dogan, C.P. Grey, W.C. Conner Jr., S.M. Auerbach and G.W. Huber, Appl. Catal. A 392 (2011) 57.
- [22] I. Sádaba, M. Ojeda, R. Mariscal, J.L.G. Fierro and M. López Granados, Appl. Catal. B 101 (2011) 638.
- [23] I. Sádaba, M. Ojeda, R. Mariscal, R. Richards and M. López Granados, Catal. Today 167 (2011) 77.
- [24] B. Choudary, M. Kantam, P. Sreekanth, T. Bandopadhyay, F. Figueras and A. Tuel, J. Mol. Catal. A Chem. 142 (1999) 361.
- [25] H. Liu, L. Peng, T. Zhang and Y. Li, New J. Chem. 27 (2003) 1159.
- [26] F.W. Lichtenthaler, Acc. Chem. Res. 35 (2002) 728.
- [27] J. Lewkowski, ARKIVOC (2001) 17.
- [28] J. Piskorz, D.S. Scott and D. Radlien, D. Composition of Oils Obtained by Fast Pyrolysis of Different Woods. In Pyrolysis Oils from Biomass: Producing

Analyzing and Upgrading; American Chemical Society: Washington, DC, 1988, 167-178.

- [29] S. Czernik and A.V. Bridgwater, *Energy Fuels* 18 (2004) 590.
- [30] G.V.C. Peacocke, P.A. Russel, J.D. Jenkins and A.V. Bridgwater, *Biomass Bioenergy* 7 (1994) 169.
- [31] S. Crossley, J. Faria, M. Shen and D.E. Resasco, *Science* 327 (2010) 68.
- [32] M. Shen and D.E. Resasco, *Langmuir* 25 (2009) 10843.
- [33] M.P. Ruiz, J. Faria, M. Shen, S. Drexler, T. Prasomsri and D.E. Resasco, *ChemSusChem* 4 (2011) 964.
- [34] J. Faria, M.P. Ruiz and D.E. Resasco, *Adv. Synth. Catal.* 352 (2010) 2359.
- [35] X.M. Li, D. Reinhoudt and M. Crego-Calama, *Chem. Soc. Rev.* 36 (2007) 1350.
- [36] L. Zhang and D.E. Resasco, *Langmuir* 25 (2009) 4792.
- [37] B.P. Binks and J.A. Rodrigues, *Angew. Chem. Int. Ed.* 44 (2005) 441.
- [38] D.E. Tambe and M.M. Sharma, *Adv. Colloid Interface Sci.* 52 (1994) 1.
- [39] J.R. Bragg, US Pat. 5,855,243 (1999).
- [40] D.O. Hall and K.K. Rao, *Photosynthesis (Studies in Biology)*. Cambridge University Press 1999, 6th Ed.
- [41] R.D. Perlack, L.L. Wright, A. Turhollow, R.L. Graham, B. Stokes and D.C. Erbach, *Biomass as Feedstock for a Bioenergy and Bioproducts Industry: The Technical Feasibility of a Billion-Ton Annual Supply*, Report No. DOE/GO-102995-2135; Oak Ridge National Laboratory: Oak Ridge, TN, 2005; <http://www.osti.gov/bridge>.

- [42] D.L. Klass, Biomass for Renewable Energy, Fuels and Chemicals; Academic Press: San Diego, 1998.
- [43] Energy Information Administration Annual Energy Outlook 2005; Report. No. DOE/EIA-0383; U.S. Department of Energy: Washington, DC, 2006; <http://www.eia.doe.gov>.
- [44] M.L. Sinnott, Carbohydrate Chemistry and Biochemistry Structure and Mechanism, The Royal Society of Chemistry 2007.
- [45] C.E. Wyman, S.R. Decker, M.E. Himmel, J.W. Brady, C.E. Skopec and L. Viikari. In Polysaccharides; S. Dumitriu, Ed.; Marcel Dekker: New York, 2005, 2nd Ed.
- [46] Public Law 110-140. Energy Independence and Security Act, Dec. 2007.
- [47] M. Ek, G. Gellerstedt and G. Henriksson. Wood Chemistry and Biotechnology. Ed. De Gruyter, 2009, 121-145.
- [48] N.G. Lewis and S. Sarkanen, Lignin and Lignan Biosynthesis, Vol. 697, 1998 American Chemical Society.
- [49] Y. Sun and J. Cheng, Bioresour. Technol. 83 (2002) 1.
- [50] N. Mosier, C. Wyman, B. Dale, R. Elander, Y.Y. Lee, M. Holtzapple and M. Ladisch, Bioresour. Technol. 96 (2005) 673.
- [51] A.M. Azzam, J. Environ. Sci. Health. B. 24 (1989) 421.
- [52] G.W. Huber, J.A. Dumesic, Catal. Today 111 (2006) 119.
- [53] A.V. Bridgwater, Fuel 14 (1995) 631.
- [54] D. Sutton and B. Kelleher, J.R.H. Ross, Fuel Process. Technol. 73 (2001) 155.
- [55] D. Mohan, C.U. Pittman and P.H. Steele, Energy Fuels 20 (2006) 848.

- [56] A. Demirbas, Prog. Energy Combust. Sci. 33 (2007) 1.
- [57] E. Van Steen and M. Claeys, Chem. Eng. Technol. 31 (2008) 655.
- [58] A.V. Bridgwater, Therm. Sci. 8 (2004) 21.
- [59] D.C. Elliott and G.F. Schiefelbein, Amer. Chem. Soc. Div. Fuel Chem. Preprints 34 (1989) 1160.
- [60] T.P. Vispute, H. Zhang, A. Sanna, R. Xiao and G.W. Huber, Science 330 (2010) 1222.
- [61] A. Gangadharam, M. Shen, T. Sooknoi, D.E. Resasco and R.G. Mallinson, Appl. Catal. A 385 (2010) 80.
- [62] X. Zhu, L.L. Lobban, R.G. Mallinson and D.E. Resasco, J. Catal. 271 (2010) 88.
- [63] T. Pham, L.L. Lobban, D.E. Resasco and R.G. Mallinson, J. Catal. 266 (2009) 9.
- [64] M.A. Peralta, T. Sooknoi, T. Danuthai and D.E. Resasco, J. Molec. Catal. A 312 (2009) 78.
- [65] A. Ausavasukhi, T. Sooknoi and D.E. Resasco, J. Catal. 268 (2009) 68.
- [66] M.R. Ladish, K.W. Lin, M. Voloch and G.T. Tsao, Enzyme Microb. Technol. 5 (1983) 82.
- [67] J.P. Diebold, A Review of the Chemical and Physical Mechanisms of the Storage Stability of Fast Pyrolysis Bio-Oils. 2000. Thermalchemie, Inc. Lakewood, Colorado National Renewable Energy Laboratory <http://www.doe.gov/bridge>
- [68] J.D. Adjaye, S.P.R. Katikaneni, N.N. Bakhshi, Fuel Process. Technol. 48 (1996) 115.
- [69] R.K. Sharma and N.N. Bakhshi, Energy Fuels 7 (1993) 306.



- [70] S.P.R. Katikaneni, J.D. Adjaye and N.N. Bakhshi, *Energy Fuels* 9 (1995) 1065.
- [71] Y. Roman-Leshkov, C.J. Barrett, Z.Y. Liu, J.A. Dumesic, *Nature* 447 (2007) 982.
- [72] S. Crossley, J. Faria, M. Shen and D.E. Resasco, *Science* 327 (2010) 68.
- [73] H. Fukuda, A. Kondo and H.J. Noda. *Biosci. Bioeng.* 92 (2001) 405.
- [74] L. Devi, K. Ptasinski and F. Janssen, *Biomass Bioenergy* 24 (2003) 125.
- [75] V. Kirubakaran, V. Sivaramakrishnan, R. Nalini, T. Sekar, M. Premalatha and P. Subramanian, *Renew. Sustain. Energ. Rev.* 13 (2009) 179.
- [76] Z.A.B.Z. Alauddin, P. Lahijani, M. Mohammadi and A.R. Mohamed, *Renew. Sustain. Energ. Rev.* 14 (2010) 2852.
- [77] V. Koulou, G. Koufodimos, Z. Samaras and A. Zabaniotou, *Int J Hydrogen Energy* 33 (2008) 6515.
- [78] W. Zhang, Automotive fuels from biomass via gasification. *Fuel Process. Tech.* 91 (2010) 866.
- [79] The Conversion of Wood and other Biomass to Bio-oil; ENSYN Group, Inc.: Greely, CA, June 2001.
- [80] S. Czernik and A.V. Bridgwater, *Energy Fuels* 18 (2004) 590.
- [81] G.V.C. Peacocke, P.A. Russel, J.D. Jenkins and A.V. Bridgwater, *Biomass Bioenergy* 7 (1994) 169.
- [82] J. Piskorz, D.S. Scott and D. Radlien, Composition of Oils Obtained by Fast Pyrolysis of Different Woods. In *Pyrolysis Oils from Biomass: Producing Analyzing and Upgrading*; American Chemical Society: Washington, DC, 1988; pp 167-178.

- [83] A.V. Bridgwater and G.V.C. Peacocke, *Energy Rev.* 204 (2000) 117.
- [84] M.J. Antal and G. Varhegyi, *Ind. Eng. Chem. Res.* 34 (1995) 703.
- [85] Hallen, R.T.; Sealock, L.T.; Cuello, R.; Bridgwater, A.V. In *Research in Thermochemical Biomass Conversion*; Kuester, J. L., Ed.; Elsevier: London, UK, 1988.
- [86] P.R. Patwardhan, J.A. Satrio, R.C. Brown and B.H. Shanks, *Biores. Technol.* 101 (2010) 4646.
- [87] P.R. Patwardhan, J.A. Satrio, R.C. Brown and B.H. Shanks, *J. Anal. Appl. Pyrol.* 86 (2009) 323.
- [88] G.R. Ponder, G.N. Richards and T.T. Stevenson, *J. Anal. Appl. Pyrol.* 22 (1992) 217.
- [89] C. Yang, X. Lu, W. Lin, X. Yang and J. Yao, *J. Chem. Res. Chinese U.* 22 (2006) 524.
- [90] H.J. Brownlee and C.S. Miner, *Ind. Eng. Chem.* 40 (1948) 201.
- [91] J. March, *Advanced Organic Chemistry*, John Wiley & Sons, New York, 1992.
- [92] T.M. Lowry, *J. Chem. Soc.* (1927) 2554.
- [93] E.U.Z. Franck, *Phys. Chem. Neue Folge* 8 (1956) 107.
- [94] K.J. Zeitsch, *The Chemistry and technology of furfural and its many by-products*. Elsevier Science B.V. Amsterdam, 2000.
- [95] M. Moliner, Y. Roman-Leshkov and M.E. Davis, *PNAS* 107 (2010) 6164.
- [96] C.D. Hurd and L.L. Isenhour, *J. Amer. Chem. Soc.* 54 (1932) 317.
- [97] H. Zhao, J.E. Holladay, H. Brown and Z.C. Zhang, *Science* 316 (2007) 1597.

- [98] S. Lima, P. Neves, M.M. Antunes, M. Pillinger, N. Ignatyev and A.A. Valente, *Appl. Catal. A* 363 (2009) 93.
- [99] J.B. Binder and R.T. Raines, *J. Am. Chem. Soc.* 131 (2009) 1979.
- [100] L. Lai and Y. Zhang, *ChemSusChem* 3 (2010) 1257.
- [101] J.N. Chheda and J.A. Dumesic, *Catal. Today* 123 (2007) 59.
- [102] C.J. Barrett, J.N. Chheda, G.W. Huber and J.A. Dumesic, *Appl. Catal. B* 66 (2006) 111.
- [103] O. Casanova, S. Iborra, A. Corma, *J. Catal.* 275 (2010) 236.
- [104] E.L. Kunkes, D.A. Simonetti, R.M. West, J.C. Serrano-Ruiz, C.A. Gartner and J.A. Dumesic, *Science*. 332 (2008) 417.
- [105] D.A. Simonetti and J.A. Dumesic, *ChemSusChem* 1 (2008) 725.
- [106] R.M. West, Z.Y. Liu, M. Peter and J.A. Dumesic, *ChemSusChem* 1 (2008) 417.
- [107] J.N. Chheda, Y. Roman-Leshkov and J.A. Dumesic, *Green Chem.* 9 (2007) 342.
- [108] J.N. Chheda, G.W. Huber and J.A. Dumesic, *Angew. Chem. Int. Ed.* 46 (2007) 7164.
- [109] G.J. Kelly and S.D. Jackson, *Aldol Condensation of Aldehydes and Ketones over Solid Base Catalysts. Catalysis in Application*, Jackson, S.D.; Hargreaves, J.S.J.; Lennon, D. Royal Society of Chemistry (Great Britain).
- [110] J.C. Serrano-Ruiz, D.J. Braden, R.M. West and J.A. Dumesic, *App. Catal. B* 100 (2010) 184.
- [111] E.L. Kunkes, E.I. Gürbüz and J.A. Dumesic, *J. Catal.* 266 (2009) 236.
- [112] G.W. Huber, J.N. Chheda, C.J. Barrett and J.A. Dumesic, *Science* 308 (2005) 1446.

- [113] R.M. West, E.L. Kunkes, D.A. Simonetti and J.A. Dumesic, *Catal. Today* 147 (2009) 115.
- [114] D.L. Klass, *Organic Commodity Chemicals from Biomass*, ref. 2, 495-546.
- [115] *Carbohydrates as Organic Raw Materials I*, Ed. Lichtenthaler, F.W. VCH, Weinheim, 1991, 367.
- [116] J.S. Beck, J.C. Vartuli, W.J. Roth, M.E. Leonowicz, C.T. Kresge, K.D. Schmitt, C.T.W. Chu, D.H. Olson, E.W. Sheppard, S.B. McCullen, J.B. Higgins and J.L. Schlenkert, *J. Am. Chem. Soc.* 114 (1992) 10834.
- [117] Merck Company, Inc., GB 887360, 1962.
- [118] D.J. Cram, DE 2539324, 1976.
- [119] D. Chundury and H.H. Szmant, *Ind. Eng. Chem. Prod. Res. Dev.* 20 (1981) 158.
- [120] R. Wen, F. Yu, X. Dong, Y. Miao, P. Zhou, Z. Lin, J. Zheng, H. Wang, L. Huang and D. Qing, CN 1456556, 2003.
- [121] G. Seo and H. Chon, *J. Catal.* 67 (1981) 424.
- [122] R. Rao, A. Dandekar, R.T.K. Baker and M.A. Vannice, *J. Catal.* 171 (1997) 406.
- [123] H.Y. Zheng, Y.L. Zhu, B.T. Teng, Z.Q. Bai, C.H. Zhang, H.W. Xiang and Y.W. Li, *J. Mol. Catal. A* 246 (2006) 18.
- [124] B.M. Nagaraja, A.H. Padmasri, B. David Raju and K.S. Rama Rao, *J. Mol. Catal. A* 265 (2007) 90.
- [125] B.M. Reddy, G.K. Reddy, K.N. Rao, A. Khan, I. Ganesh, *J. Mol. Catal. A* 265 (2007) 276.
- [126] W. Huang, H. Li, B. Zhu, Y. Feng, S. Wang and S. Zhang, *Ultrason. Sonochem.* 14 (2007) 67.

- [127] S. Sitthisa, T. Sooknoi, Y. Ma, P.B. Balbuena and D.E. Resasco, *J. Catal.* 277 (2011) 1.
- [128] P. Claus, *Top. Catal.* 5 (1998) 51.
- [129] H. Li, H. Luo, L. Zhuang, W. Dai and M. Qiao, *J. Mol. Catal. A.* 203 (2003,) 267.
- [130] B. Liaw, S. Chiang, S. Chen and Y. Chen, *Appl. Catal. A* 346 (2008) 179.
- [131] J. Kijeński, P. Winiarek, T. Paryjczak, A. Lewicki and A. Mikolajska, *Appl. Catal. A* 233 (2002) 171.
- [132] S. Sitthisa and D.E. Resasco, *Catal. Lett.* 141 (2011) 784.
- [133] S. Sitthisa, T. Pham, T. Prasomsri, T. Sooknoi, R.G. Mallinson and D.E. Resasco, *J. Catal.* 280 (2011) 17.
- [134] M.K. Bradley, J. Robinson and D.P. Woodruff, *Surf. Sci.* 604 (2010) 920.
- [135] V.M. Roberts, V. Stein, T. Reiner, A. Lemonidou, X. Li and J.A. Lercher, *Chem. Eur. J.* 17 (2011) 5939.
- [136] C. Zhao and J.A. Lercher, *ChemCatChem* 4 (2012) 64.
- [137] C. Zhao and J.A. Lercher, *Angew. Chem.* 124 (2012) 6037.
- [138] C. Zhao, Y. Kou, A.A. Lemonidou, X. Li and J.A. Lercher, *Angew. Chem. Int. Ed.* 48 (2009) 3987.
- [139] M.M.S. Aye and M. Zhang, *Chem. Eng. Sci.* 60 (2005) 6702.
- [140] J.R. Katzer, *Interface Challenges and Opportunities in Energy and Transportation. Energy and Transportation: Challenges for the Chemical Sciences in the 21<sup>st</sup> Century*, The National Academy Press 2003.
- [141] D.E. Resasco and S. Crossley, *AIChE J.* 55 (2009) 1082.

- [142] R.C. Santana, P.T. Do, W.E. Alvarez, J.D. Taylor, E.L. Sughrue and D.E. Resasco, *Fuel* 85 (2006) 643.
- [143] J. Taylor, R. McCormick and W. Clark, Relationship between Molecular Structure and Compression Ignition Fuels, both Conventional and HCCI. August 2004 NREL Report on the MP-540-36726, Non-Petroleum-Based Fuels.
- [144] P. Do, S. Crossley, M. Santikunaporn and D.E. Resasco, Catalytic Strategies for Improving Specific Fuel Properties. *Catalysis: Specialist Periodical Reports*. The Royal Society of Chemistry, London 20 (2007) 33.
- [145] S. Crossley, W.E. Alvarez and D.E. Resasco, *Energy Fuels*. 22 (2008) 2455.
- [146] P.T. Do, W.E. Alvarez and D.E. Resasco, *J. Catal.* 238 (2006) 477.
- [147] A. Gangadharan, M. Shen, T.Sooknoi<sup>1</sup>, D.E. Resasco and R.G. Mallinson, *Appl. Catal. A-Gen.* 385 (2010) 80.
- [148] C.E. Hori, H. Permana, K.Y. Simon Ng, A. Brenner, K. More, K.M. Rahmoeller and D. Belton, *Appl. Catal. B* 16 (1998) 105.
- [149] F.B. Noronha, E.C. Fendley, R.R. Soares, W.E. Alvarez and D.E. Resasco, *Chem. Eng. J.* 82 (2001) 21.
- [150] R.C. Santana, P.T. Do, W.E. Alvarez, J.D. Taylor, E.L. Sughrue and D.E. Resasco, *Fuel* 85 (2006) 643.
- [151] J. Taylor, R. McCormick and W. Clark, Relationship between Molecular Structure and Compression Ignition Fuels, both Conventional and HCCI. August 2004 NREL Report on the MP-540-36726, Non-Petroleum-Based Fuels.
- [152] M. Jalali-Heravi and M.H. Fatemi, *J. Chromatogr. A* 897 (2000) 227.

- [153] A.C. Dillon, M. Yudasaka and M.S. Dresselhaus, *J. Nanosci. Nanotechnol.* 4 (2004) 691.
- [154] A.W. Musumeci, E.R. Waclawik and R.L. Frost, *Spectrochim. Acta A* 71 (2008) 140.
- [155] Y. Kobayashi, D. Takagi, Y. Ueno and Y. Homma, *Phys E* 24 (2004) 26.
- [156] S.M. Bachilo, L. Balzano, J.E. Herrera, F. Pompeo, D.E. Resasco and R.B. Weisman, *J. Am. Chem. Soc.* 125 (2003) 11186.
- [157] J.R. Simpson, J.A. Fagan, M.L. Becker, E.K. Hobbie, A.R. and H. Walker, *Carbon* 47 (2009) 3238.
- [158] P. Delhaes, M. Couzi, M. Trinquocoste, J. Dentzer, H. Hamidou and C. Vix-Guterl, *Carbon* 44 (2006) 3005.
- [159] X.D. Peng and M.A. Barteau, *Langmuir* 5 (1989) 1051.
- [160] X.D. Peng and M.A. Barteau, *Catal. Lett.* 12 (1992) 245.
- [161] C. Keresszegi, D. Ferri, T. Mallat, and A. Baiker, *J. Phys. Chem. B* 109 (2005) 958.
- [162] W.C. Wilson, in: *Organic Synthesis*, Vol. 1, Wiley, New York, 1932, 269.
- [163] G. Solomons and C. Fryhle, *Organic Chemistry*, 7<sup>th</sup> Ed., (1999), 1264.
- [164] U.S. Department of Energy - Energy efficiency and renewable energy. Alternative fuels and advanced vehicles data center (13-10-2010): [http://www.afdc.energy.gov/afdc/fuels/emerging\\_biomass\\_liquids\\_what\\_is.html?print](http://www.afdc.energy.gov/afdc/fuels/emerging_biomass_liquids_what_is.html?print)

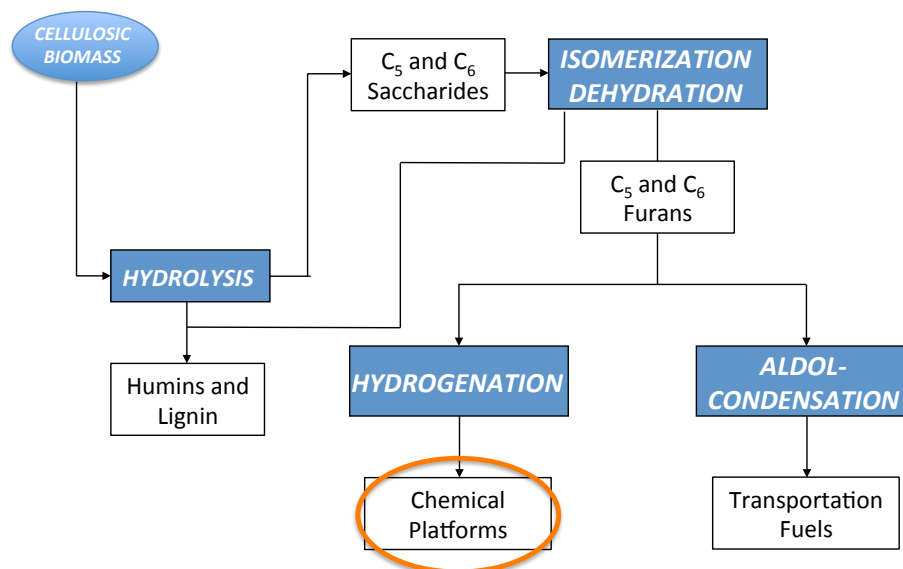
## Chapter 3:

# Catalytic Conversion of Sugars to Fuels and Chemicals in Solid-stabilized Emulsions

### 3.1. Introduction

Conversion of biomass-derived carbohydrates requires the selective removal of excess oxygen atoms, skeletal isomerization, and/or C-C bond formation reactions to produce branched molecules valuable as chemical intermediates and green-fuels (Figure 3.1). For instance, conventional petrochemical upgrading processes, usually performed in gas phase, are hindered since carbohydrates have an oxygenated structure that results in products with low vapor pressure, poor thermal stability, and high water solubility [1,2]. In contrast, liquid phase processing in polar solvents is a more advantageous strategy, as these highly reactive mixtures can be readily solubilized in high concentrations with minimum thermal decomposition [3]. However, in the presence of protic polar solvents (e.g. water) two major challenges must be carefully considered in the catalyst and process design; 1) the stability of the catalyst in hot condensed water, and 2) the cross-condensation of reactants and products, which greatly increases since water facilitates proton transfer reactions.





**Figure 3.1: Flow diagram for the conversion of bio-derived saccharides into chemical intermediates and fuels.**

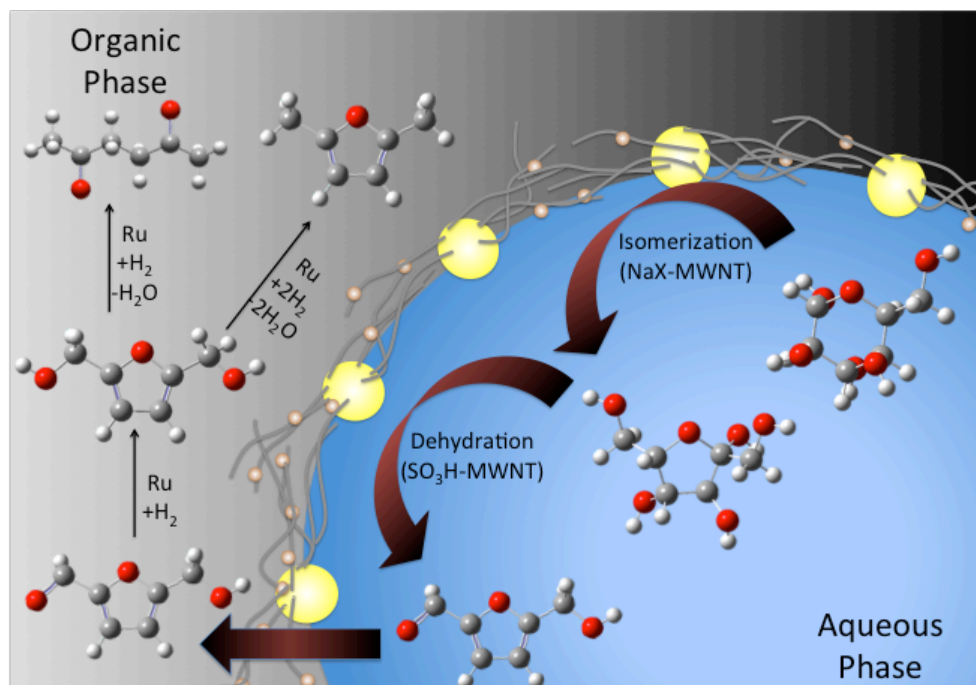
For example, acid catalysts like zeolites that are very effective in the activation of C-O bonds for dehydration, alkylation, isomerization and oligomerization reactions, are very unstable in hot aqueous environments, as hydrolysis of the Si-O-Si collapses the catalyst framework and consequently reduces the catalytic activity [4]. Some authors have proposed the use of high Si/Al zeolites as well as the use of HF as synthesis media to reduce the terminal defects (Si-OH) and therefore the hydrophilicity of the catalyst [5,6]. However, in this approach the high Si/Al ratio limits the use of these zeolites to Lewis-acid catalyzed reactions. In a recent report we have shown that hydrophobization of HY zeolites with octadecyltrichlorosilane can greatly increase the catalyst stability even after several reaction cycles, during alkylation reactions in hot liquid water, without significant changes in the density of Brønsted and Lewis acid sites [7]. Conversely, their counterparts (untreated HY zeolites) rapidly lose their crystalline structure and catalytic activity when heated in this aqueous environment at temperatures

above 423 K. Furthermore, upon functionalization their affinity for liquid-liquid interfaces greatly increases, as a result it was possible to form very stable water/oil emulsions with small droplet size.

Our research group have previously demonstrated that nanohybrid particles comprising on metalized single walled and multi walled carbon nanotubes (SWCNT, MWCNT) fused to metal oxides ( $\text{SiO}_2$ ,  $\text{Al}_2\text{O}_3$  and  $\text{MgO}$ ) can simultaneously stabilize emulsions and catalyze biofuel upgrading reactions at the water-oil interface [8-12]. Moreover, by tuning the nanohybrids composition and surface functionalities we can systematically control the type of emulsion obtained (water-in-oil or oil-in-water), and particle size distribution of the metal clusters with high reproducibility. This concept is particularly advantageous for reaction-separation processes in biphasic liquid systems, since it is possible to continuously extract products from the aqueous phase into low boiling point organic solvents after rapid formation, suppressing undesired reactions [13,14]. In addition, they enhance the liquid/solid/liquid interfacial area, and open the possibility of selectively converting molecules in only one of the liquid phases (i.e., phase-selectivity), simply based on the differences in solubility [15].

The aim of the present chapter is to extend the utility of these amphiphilic catalysts to the isomerization, dehydration, and hydrogenation of sugars and furan molecules in a sequential reaction-separation system based on nanoparticles-stabilized water/oil emulsions, as depicted in Figure 3.2. For the isomerization reaction of glucose to fructose NaX faujasite zeolites were hydrophobized by anchoring carbon nanotubes on the surface. Then sulfonated multi walled carbon nanotubes (MWCNT- $\text{SO}_3\text{H}$ ) were used as Brønsted acid catalyst for the dehydration reaction of fructose to

hydroxymethylfurfural (HMF). Finally, surface-decorated multi walled carbon nanotubes (MWCNT) with palladium or ruthenium clusters were used for the hydrodeoxygenation of the resulting furan. Moreover, we demonstrate that the functionalization of the NaX faujasites zeolites greatly improves the catalyst stability in hot liquid water, and when used in water/oil emulsions high yields of HMF (70%) can be readily achieved. More broadly, we anticipate that this technology could allow us to avoid frequent replacement of the catalyst and expensive purification methods to produce the final liquid fuel by using low boiling point organic solvents that are both excellent fuel components and extractive phase.



**Figure 3.2: Schematic illustration of the reactions taking place at the liquid-liquid interface in the nanohybrid-stabilized emulsions. In the aqueous phase the glucose rapidly isomerizes to fructose on the Lewis acid catalyst (NaX-MWNT) followed by dehydration on the on the Brønsted acid site (MWNT-SO<sub>3</sub>H). Upon formation the hydroxymethylfurfural migrates to the organic phase and reacts on the metal catalyst, either 5% Ru/MWNT/Al<sub>2</sub>O<sub>3</sub> or 5% Pd/MWNT/Al<sub>2</sub>O<sub>3</sub> to form 2,5-hexadione or g-hydroxyvaleric acid, respectively.**

## 3.2. Experimental Section

### 3.2.1. Catalyst Preparation and Characterization

Different nanostructured catalysts were synthesized for the different reactions performed. For isomerization reactions, nanohybrids composed of carbon nanotubes grown on faujasite NaX zeolites (MWCNT-NaX) were used, whereas for dehydration reactions, sulfonated multi-walled carbon nanotubes (MWCNT-SO<sub>3</sub>H) were employed as catalysts. In addition, we studied the hydrogenation of the dehydration product from glucose (hydroxymethylfurfuraldehyde) on nanohybrids based on multi walled carbon nanotubes fused to aluminum oxide (MWCNT-Al<sub>2</sub>O<sub>3</sub>) functionalized with palladium and ruthenium catalysts.

#### 3.2.1.1. Isomerization Nanohybrid Catalyst (MWCNT- and SWCNT- NaX)

NaX was purchased from Sigma-Aldrich with average particle size of 2 mm. For the Cs-containing zeolite (CsNaX) we did ion exchange of molecular sieve 13X with 0.1 M CsNO<sub>3</sub>/ CsOH (4/1 v/v) at 353 K for 24 h. The solid material was filtered and left to dry at 353 K overnight. The sample was then calcined at 723 K for 2 h in a flow of dry air. It has been demonstrated that crystallinity in CsNaX samples is largely retained after this treatment [16]. The MWCNT and SWCNT were synthesized following a procedure previously reported by our group [17,18]. For the synthesis of MWCNT the support was impregnated by incipient wetness impregnation (IWI) method with an aqueous solution of Co(NO<sub>3</sub>)<sub>2</sub>.6H<sub>2</sub>O and Fe(NO<sub>3</sub>)<sub>3</sub>.9H<sub>2</sub>O (Sigma Aldrich), reaching a final metal loading of 2 wt. %, with a Fe:Co molar ratio of 2:1. In the case of the SWCNT the aqueous solution comprised of Co(NO<sub>3</sub>)<sub>2</sub>.6H<sub>2</sub>O and (NH<sub>4</sub>)<sub>6</sub>Mo<sub>7</sub>O<sub>24</sub>.4H<sub>2</sub>O

(Sigma Aldrich) with a final metal loading of 5 wt. % and a Co:Mo molar ratio of 1:3. The two samples were then dried overnight at 373 K and calcined in air 2 h at 723 K. After cooling down, 300 mg of the catalyst was placed in a reactor where it was first reduced under 300 sccm of H<sub>2</sub> at 773 K for 30 min, then heated up to 973 K in 300 sccm of He, and finally exposed to a flow of gas phase reactant. In the case of the SWCNT the CoMo/NaX catalyst was exposed to CO (4000 sccm 60% of He), while in the case of FeCo supported on NaX C<sub>2</sub>H<sub>4</sub> (500 sccm with 60 % of He) was the carbon source for synthesis of MWCNT.

#### 3.2.1.2. Preparation of Sulfonated Multi-Walled Carbon Nanotubes (MWCNT-SO<sub>3</sub>H)

Purified multi-walled carbon nanotubes (MWCNT-p) were provided by SouthWest NanoTechnologies Inc. The sulfonic functionalization of the MWCNT-p was performed following the procedure proposed by B. Srinivas [19]. Initially, 1 g of MWCNT-p were treated with 50 ml of nitric acid (HNO<sub>3</sub>, 16 M) with stirring for 3 h at 393 K. The resulting product was cooled to room temperature and then filtered using nylon filters of 0.22 mm of pore size. The collected solids were repeatedly washed with deionized water until neutral pH was achieved. The oxidized (acid treated) multi-walled carbon nanotubes (MWCNT-COOH) were dried at 343 K overnight in a vacuum oven. Then, 1 g of MWCNT-COOH were added to a mixture of 20 ml of sulfuric acid (H<sub>2</sub>SO<sub>4</sub>, 18 M) and 300 ml of acetic anhydride ((CH<sub>3</sub>-CO)<sub>2</sub>O), under continuous stirring at 353 K. After 2 h, the reaction mixture was cooled down to room temperature and the slurry was filtered and thoroughly washed with deionized water to remove any residual acids, and then overnight in a vacuum oven at 343 K.

### 3.2.1.3. Synthesis of the Hydrogenation Catalysts (Pd-MWCNT-Al<sub>2</sub>O<sub>3</sub> and Ru-MWCNT-Al<sub>2</sub>O<sub>3</sub>)

Multi-walled carbon nanotubes fused to aluminum oxide (MWCNT-Al<sub>2</sub>O<sub>3</sub>) were provided by SouthWest NanoTechnologies Inc. These nanohybrids were used as support of palladium or ruthenium particles for the hydrogenation reactions. Both metals were anchored by incipient wetness impregnation of their corresponding precursors (Pd(NO<sub>3</sub>)<sub>2</sub>.6H<sub>2</sub>O or RuCl<sub>3</sub>.6H<sub>2</sub>O, respectively). The final metal loading was 5 wt. % of Pd or Ru. After the impregnation, the catalysts were dried overnight at 373 K and then calcined at 673 K for 2 h in He.

### 3.2.2. Characterization Techniques

Several techniques were employed to characterize the properties and structure of both the MWNT-NaX and the MWNT-SO<sub>3</sub>H, including; thermogravimetric/differential thermal analysis coupled with mass spectroscopy (TG-DTA-MS), diffuse reflectance infrared Fourier transformation spectroscopy (DRIFT), X-ray photoelectron spectroscopy (XPS), X-ray diffraction (XRD), N<sub>2</sub> physisorption, and high-resolution transmission electron microscopy (HRTEM).

#### 3.2.2.1. Thermogravimetric/Differential Thermal Analysis Coupled with Mass Spectroscopy (TG-DTA-MS)

Thermogravimetric analysis of the sulfonic functionalized MWCNT was conducted in a Netzsch STA 449 F3 Jupiter TG-DSC equipment, under flow of air (50

ml/min) at 373 K for 30 min, followed by a heating ramp of 10 K/min up to 1073 K, and a cooling ramp of 20 K/min up to 673 K. This equipment was coupled with an Aëolos mass spectrometer in SIM mode to analyze the gas phase composition throughout the TGA experiment.

#### 3.2.2.2. Diffuse Reflectance Infrared Fourier Transformation Spectroscopy (DRIFT)

Diffuse reflectance infrared Fourier transformation (DRIFT) spectra were recorded in a high temperature DRIFT cell (HVC, Harrick) with CaF<sub>2</sub> windows. The sample powder (100 mg) was loaded in the sample cup of the cell and at room conditions the background spectrum was recorded. The DRIFT spectra were recorded at a resolution of 4 cm<sup>-1</sup> and accumulating 256 scans.

#### 3.2.2.3. X-ray Photoelectron Spectroscopy (XPS)

X-ray photoelectron spectroscopy data were recorded on a Physical Electronics PHI 5800 ESCA system with standard non-monochromatic Al X-rays (1486.6 eV) operated at 250W and 15 kV in a chamber pumped down to a pressure of approximately 1.0x10<sup>-8</sup> Torr. A 93.9 eV and 58.7 eV pass energy were typically used for survey and specific element analysis, respectively. The electron takeoff angle was 45° with respect to the sample surface. The binding energies were corrected with reference to carbon at 284.8 eV. Samples were attached to aluminum stage via carbon tape. Atomic composition analyses of carbon, oxygen, and sulfur were carried out on each sample.

#### 3.2.2.4. X-ray Diffraction (XRD)

X-ray powder diffraction patterns (XRD) for the untreated NaX faujasite zeolite and the MWCNT-NaX nanohybrid catalysts were collected on a D8 Series II X-ray diffractometer (BRUKER AXS), using Cu K $\alpha$  radiation generated at 40 kV and 35 mA. The scans covered the 2 $\theta$  range from 10° to 35°.

#### 3.2.2.5. N<sub>2</sub> Physisorption

The pore volume distribution and BET surface area of the MWCNT-p, MWCNT-NaX and NaX were determined by N<sub>2</sub> physisorption using a Micromeritics ASAP 2010 with micropore option.

#### 3.2.2.6. High-Resolution Transmission Electron Microscopy (HRTEM)

The samples for HRTEM were prepared by dispersing NaX faujasite zeolites and MWNT-NaX nanohybrids in anhydrous ethanol using a Horn sonicator (Fisher Scientific 600W, 20 kHz) at 25 % of amplitude for 5 min to produce a suspension. Then, drops of the suspension were loaded on holey carbon film on 300 mesh copper grids. HRTEM images were obtained on a JEOL 2010-F field emission intermediate voltage (200,000 volt) scanning transmission research electron microscope, with a magnification of up to x 8,000,000.

#### 3.2.3. *Preparation of Nanohybrid-Stabilized Emulsions*

In order to prepare water/oil emulsions stabilized by the different nanohybrids mentioned, 30 mg of the nanohybrids were dispersed in 30 ml of a biphasic mixture of



the aqueous and organic solvents with a volume ratio of 1. The biphasic system was sonicated with a Horn sonicator at 25 % of amplitude for 30 min. It is worth to mention that, for the dehydration of glucose/fructose and the hydrogenation of hydromethylfurfural, the aqueous and organic phases employed were deionized water and decalin (decahydronaphthalene from Sigma-Aldrich). On the other hand, for the isomerization-dehydration reactions the aqueous and organic phases were 35 wt. % NaCl aqueous solution and tetrahydrofuran (THF 99.9 wt. % from Sigma-Aldrich), respectively.

#### *3.2.4. Reaction Systems*

The batch catalytic experiments of isomerization, dehydration and hydrogenation were carried out in a Parr 4843 reactor of 50 ml. The temperature inside the reactor was measured by a J-Type thermocouple (OMEGA) and controlled by a temperature controller CAL 9500P from CAL Controls Ltd.

##### *3.2.4.1. Isomerization-Dehydration of Glucose/Fructose*

The dehydration and isomerization reactions were performed in a semi-batch Parr 4843 reactor of 50 ml. In a typical single-phase experiment, 200 mg of nanohybrid catalyst were poured in the reactor vessel and 20 ml of deionized water were added. The catalyst was dispersed using a Horn sonicator at 25 % of amplitude for 30 min. Then, the reactor vessel was assembled in the reaction system.

Initially, the reactor was pressurized up to 400 psi of nitrogen, followed by the increase of the temperature to 383 K. Then, the reaction time was started upon injection

of 10 ml of glucose aqueous solution. The resulting concentration of glucose inside the reactor was 10 wt. %. To finish the reaction, the heater and stirring were turned off. The biphasic experiments required the formation of the nanohybrid-stabilized emulsions prior the assembling of the reactor as it was described in the previous section. Similarly to the reactions in single phase, the reactions were performed at 400 psi of pressure and 423 K.

Once the reaction was stopped, the reactor was depressurized and taken apart. The content was filtered using a nylon filter (0.2 mm pore size). The resulting samples were analyzed by means of high performance liquid chromatography (HPLC) using a Waters Millipore system (Waters Corp.) equipped with 486 Waters UV (320 nm) and 410 Waters refractive index detectors. Glucose, fructose, and hydroxymethylfurfural concentrations were obtained with a Biorad Aminex HPX87C (300 x 7.8) column (Phenomenex), using ultrapure water (pH = 7) as the mobile phase at a flow rate of 0.60 ml/min and a column temperature of 353 K. All the reactants and products were calibrated HPLC using commercial standards. Conversion of glucose and selectivities were defined as follows:

$$Conversion_{Glucose} = 100x \frac{n_{Glucose,reacted}}{n_{Glucose,initial}} \quad (\text{Eq. 3.1})$$

$$Yield_{Product} = 100x \frac{n_{Product}}{n_{Glucose,initial}} \quad (\text{Eq. 3.2})$$

#### 3.2.4.2. Hydrogenation of Hydroxymethylfurfural

The hydrogenation reactions were carried out in a semi-batch Parr 4843 reactor of 50 ml. A detailed description of the reaction system can be found in a previous work

of our group [8,9]. The catalysts used to perform this reaction were 5 wt. % Pd-MWCNT- $\text{Al}_2\text{O}_3$  or Ru-MWCNT- $\text{Al}_2\text{O}_3$ . In each experiment, 15 ml of deionized water and 15 ml of decalin were poured into the reactor vessel with 30 mg of the catalyst. The mixture was sonicated for 15 min using a Horn sonicator in order to produce the emulsion. Then, the reactor vessel was assembled in the reaction system.

First of all, a reduction step of the catalyst was done. Thus, after purging with  $\text{N}_2$ , 110 sccm of pure  $\text{H}_2$  was flown for 3 h at 373 K and 200 psi. Then, the temperature and pressure were adjusted to 423 K and 400 psi of  $\text{H}_2$ , respectively, before the reactant (a solution of hydroxymethylfurfural with a concentration of 0.03 M) was injected. After 2 h, the reaction was stopped by turning off the heater and switching  $\text{H}_2$  to  $\text{N}_2$ .

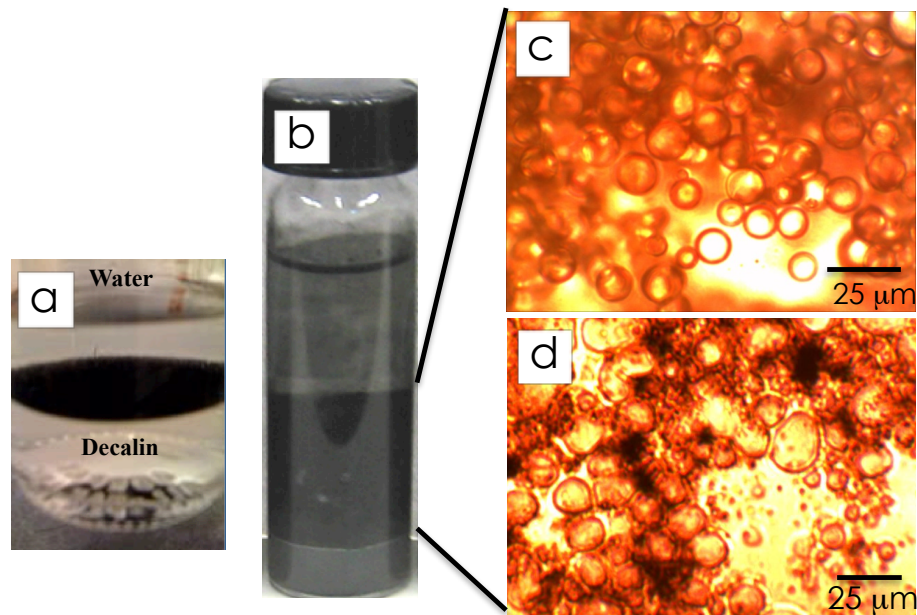
Once the reaction was finished, the reactor was taken apart and the content was filtered in two steps. In the first one, a coarse filter paper (8 mm pore size) collected a large fraction of nanohybrids as they agglomerate upon contacting the filter. For the second step, a nylon filter (0.2 mm pore size) separated the small fraction of nanohybrids that passed the first filter. The two phases obtained were separated and samples of 500 ml of each one were analyzed by gas chromatography, GC-FID and GC-MS. The GC-FID used was a 6890A series from Agilent Technologies with a capillary column of polyethylene glycol (HP-INNOWAX) of 60.0 m x 0.32 mm x 0.25 mm nominal from Hewlett Packard. The GC-MS was a Shimadzu QP2010S equipped with an HP-INNOWAX polyethylene glycol capillary column, 30.0 m long x 0.25 mm nominal, from Hewlett Packard. In all the GC-FID analyses, methanol and 1,2-dichloroethane were used as internal standards for the aqueous and organic phases, respectively. The reactants and products were calibrated in the GC-FID using

commercial standards. All the aqueous fractions were extracted into a methanol solvent before injecting them in the GC, to avoid damaging the chromatographic column.

### **3.3. Results and Discussion**

#### *3.3.1. Particle-Stabilized Emulsions*

The ability of the different nanohybrid catalysts to form stable water-oil emulsions, with large interfacial surface areas, is a key parameter for the reactions at the liquid-liquid interface as demonstrated in our previous reports [10,12,20]. Figure 3.3a shows the absorption of the amphiphilic catalyst towards the liquid-liquid interface of the decalin-water biphasic system. Upon the addition of energy by sonication, highly stable and reproducible particle-stabilized emulsions were obtained (Figure 3.3b). In this process, the emulsion formed is a kinetically stable system characterized by; 1) the formation of a rigid film of particles, at the liquid-liquid interface, that suppresses the coalescence of the droplets by steric obstruction [21-24], and 2) the modification of the rheological properties (viscosity) of the liquid at droplet-droplet interface, that retards the liquid drainage between coalescing droplets [25,26]. Illustrative microscopy images of the emulsions prepared using the sulfonated multi walled carbon nanotubes (MWCNT-SO<sub>3</sub>H) and multi walled carbon nanotubes fused to NaX faujasite zeolites (MWCNT-NaX) are shown in Figures 3.3c and d.



**Figure 3.3: a) Preferential adsorption the nanohybrids at the water-oil interface, b) the same mixture as in a) after horn sonication of the water:decalin with 1 mg/ml of MWNT-SO<sub>3</sub>H for 15 minutes at 25% amplitude, c) optical microscope image of the water/decalin (1:1) emulsion stabilized by MWNT-SO<sub>3</sub>H (1 mg/ml), and d) optical microscope image of the water + sodium chloride (35 wt. %)/tetrahydrofuran (1:1) emulsion stabilized by MWNT-NaX (6.7 mg/ml).**

Table 3.1 summarizes the emulsion fraction, type of emulsion and droplet size obtained for the two catalysts studied. It can be noted that both systems, MWCNT-SO<sub>3</sub>H and MWCNT-NaX, yielded emulsions with similar average droplet size ( $11.8 \pm 4.4$  and  $8.7 \pm 1.3$  nm, respectively), while the fraction of emulsion for the sulfonated nanohybrid was slightly larger (71 vol. %) when compared to the MWCNT-NaX nanohybrid (50 vol. %). As expected, the type of emulsion was oil-in-water for the MWCNT-SO<sub>3</sub>H. In previous studies we have shown that transition from water-in-oil to oil-in-water emulsions can be achieved upon functionalization of the carbon nanotubes with polar moieties (e.g. -COOH, -COH, -CHO), likewise, during the sulfonation of the nanohybrids a significant increase of the surface density of defects was achieved, favoring the formation of oil-in-water emulsions [9-11].

**Table 3.1: Type of emulsion, average droplet size and emulsion fraction for the nanohybrid-stabilized emulsions. The MWNT-SO<sub>3</sub>H measurements correspond to a water:decalin (1:1) emulsion with a 1mg/ml of particle concentration. For the MWNT-NaX the emulsion consisted on an aqueous solution of sodium chloride (35 wt.%) and tetrahydrofuran (1:1) with 6.7 mg/ml of particles concentration.**

Nanohybrids	Type of emulsion	Average droplet size (μm)	Emulsion fraction (% vol)
MWCNT-NaX	O/W	11.8 ± 4.4	50.5
MWCNT-SO <sub>3</sub> H	O/W	8.7 ± 1.3	71.2

In contrast, the MWCNT-NaX stabilized the inversed type of emulsion. It has been observed that for contact angles at the oil-water-solid interface (as measured across the aqueous phase) slightly lower than 90 degrees, the type of emulsion obtained is oil-in-water, and when the contact angles are slightly greater than 90 degrees, the type of emulsion is inversed to water-in-oil [27-31]. Hence, it is not surprising that the highly hydrophobic surface of the MWCNT-NaX generates water-in-oil emulsions.

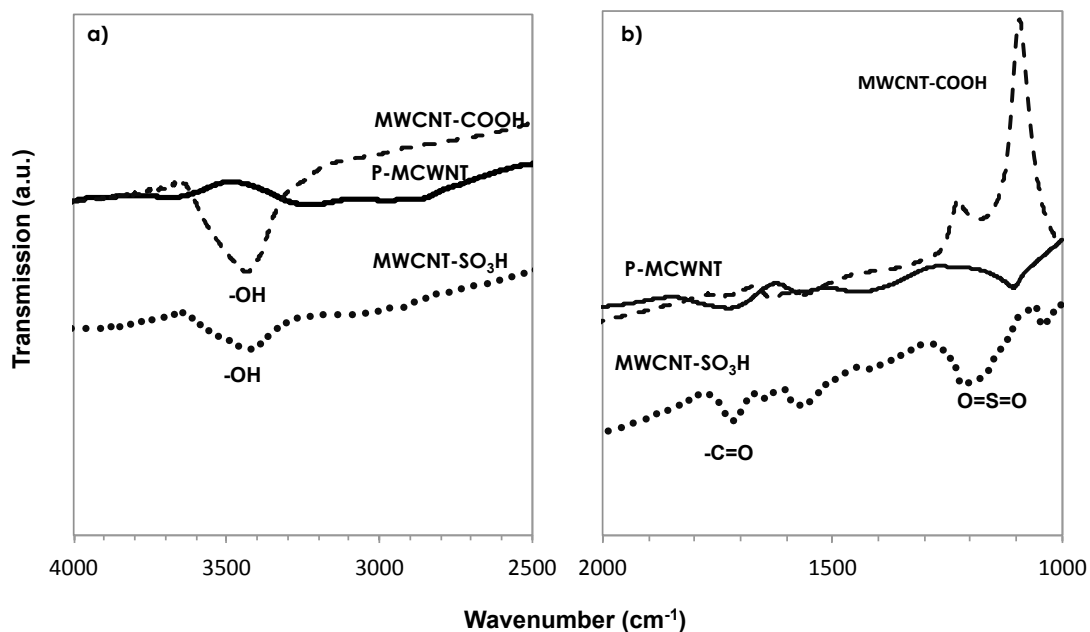
### 3.3.2. Nanohybrid Catalyst Characterization

A complete picture of the structure and composition of the MWCNT-SO<sub>3</sub>H and MWCNT-NaX nanohybrids was assessed by combining different characterization techniques (DRIFTS, TG-DTA-MS, XRD, XPS, SEM, HRTEM and N<sub>2</sub> physisorption).

#### 3.3.2.1. DRIFTS Characterization of the Functionalized MWCNT Catalysts

In Figures 3.4a and b show the DRIFTS spectrum of the purified multi-walled carbon nanotubes (MWCNT-p), oxidized multi-walled carbon nanotubes (MWCNT-COOH), and sulfonated multi walled carbon nanotubes (MWCNT-SO<sub>3</sub>H). Consistently

with previously reported data [32], no detectable transmission bands were observed for the pristine MWCNT-p (Fig. 3.4a) in the wavenumber range between 2500 and 4000  $\text{cm}^{-1}$ , while the spectra of the MWCNT-COOH and MWCNT-SO<sub>3</sub>H showed a mode centered at about 3450  $\text{cm}^{-1}$  assigned to stretching mode of the -OH groups from the defects created during the functionalization [33]. Another evidence of the effect of the functionalization on the generation of oxidized defects is presented in Figure 3.4b. Here, the MWCNT-SO<sub>3</sub>H displayed a stretching mode centered at 1732  $\text{cm}^{-1}$  characteristic of conjugated -CO on the carbon framework. In particular, the successful functionalization of MWCNT-p with -SO<sub>3</sub>H was confirmed by the presence of absorption bands centered around 1223 and 1050  $\text{cm}^{-1}$  (Figure 3.4b), which are attributed to the -SO<sub>3</sub>H and -SH functionalities, respectively [34].



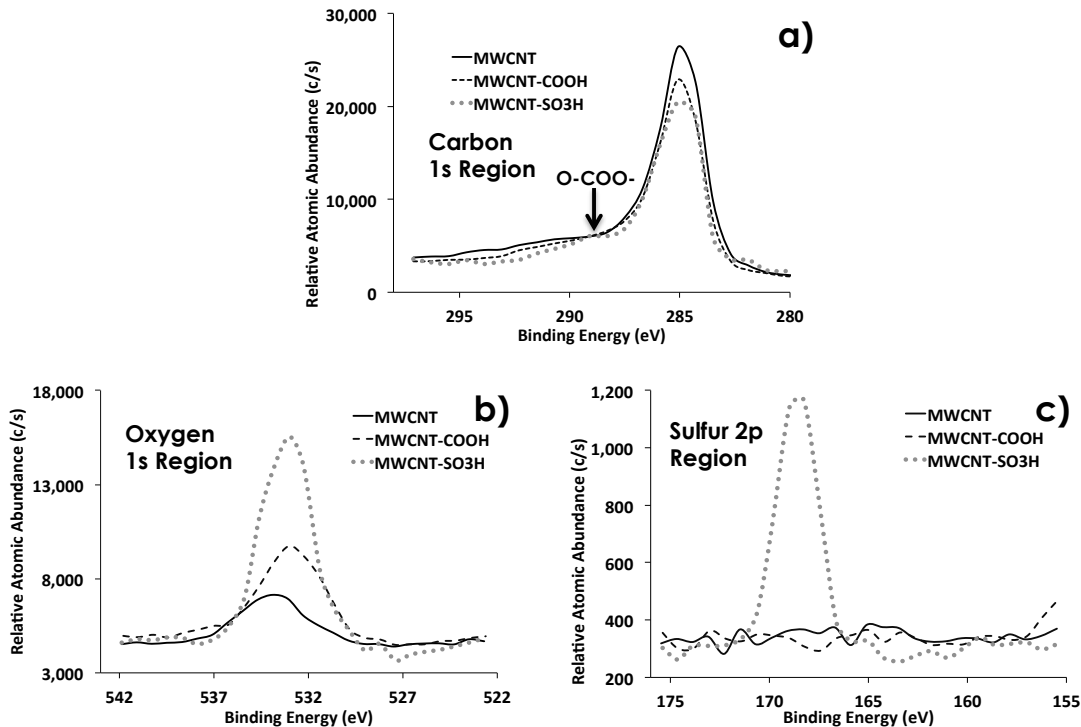
**Figure 3.4: DRIFT spectra of the purified MWNT (p-MWNT), oxidized MWNT (MWNT-COOH), and sulfonic functionalized MWNT (MWNT-SO<sub>3</sub>H).**

### 3.3.2.2. XPS Characterization of the Functionalized MWCNT Catalysts

X-ray photoelectron spectroscopy was used to obtain information on the functional groups on the carbon nanotubes surface. The XPS analysis was performed on MWCNT-p, and the following derivatives, MWCNT-COOH and MWCNT-SO<sub>3</sub>H and the results are shown in (Figures 3.5(a-c)).

The XPS obtained in the carbon 1s region is presented in Figure 3.5a. The major peak appear at around 285.1 eV with a non-symmetrical edge at higher binding energies that has been generally assigned to the sp<sup>2</sup> and sp<sup>3</sup> hybridization of the carbon atoms [35]. Also, it is possible to notice that the peak at 291 eV for the MWCNT-p corresponding to the carbon p-p\* shake up satellite peak of the sp<sup>2</sup>-hybridized carbon, which is less prominent for the MWCNT-COOH and MWCNT-SO<sub>3</sub>H. Interestingly, a raised bump at around 289.1 eV appears on the MWCNT-COOH and more prominent on the MWCNT-SO<sub>3</sub>H, similar to that reported in the literature [36]. This is likely due to carboxylates functional groups (-COO<sup>-</sup>) formed during the sulfonation process [37,38].





**Figure 3.5: XPS Spectra in the regions of a) carbon 1s, b) oxygen 1s, and c) sulfur 2p for the MWCNT (p-MWCNT), oxidized MWCNT (MWCNT-COOH), and sulfonated MWCNT (MWCNT-SO<sub>3</sub>H).**

Figure 3.5b shows the spectrum obtained in the oxygen 1s region. The typical band of O-C at around 533.1 eV was observed in both MWCNT-SO<sub>3</sub>H and MWCNT-COOH. The intensity of this band in the MWCNT-SO<sub>3</sub>H was higher, compared to the MWCNT-COOH, most likely due to a more severe oxidation of the carbon framework upon functionalization with the sulfuric acid and acetic anhydride. The pristine MWCNT-p showed a smaller band at around 534.7 eV associated to the H-O-H on the surface [39].

As expected, the spectrum of the sulfur 2p region (Fig. 3.5c) indicates that no sulfur moiety is present in the MWCNT-p and MWCNT-COOH. Only the peak at around 168.3 eV was observed in the MWCNT-SO<sub>3</sub>H, which corresponds to a higher

oxidation state of sulfur [40], indicating the presence of surface oxidized sulfur species covalently bonded to the surface.

**Table 3.2: Surface atomic composition from XPS data and density of acid sites of the purified MWCNT (p-MWCNT), oxidized MWCNT (MWCNT-COOH), and sulfonated MWCNT (MWNT-SO<sub>3</sub>H).**

Catalysts	Surface Atomic Content (%)			Acid Sites Density (mmol/g of Carbon)
	Carbon	Oxygen	Sulfur	
P-MWNT	94.8	5.2	--	0.1
MWNT-COOH	89.7	10.3	--	55.9
MWNT-SO <sub>3</sub> H	82.1	13.8	4.1	80.7

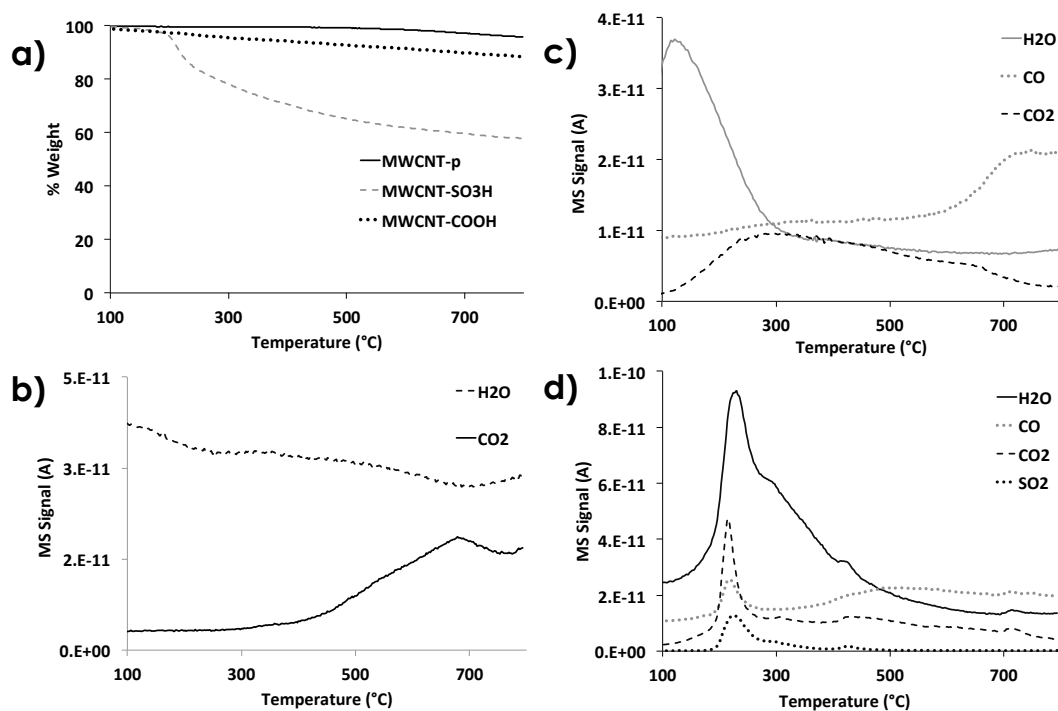
Likewise, the results obtained from the atomic surface composition, summarized in Table 3.2, show that MWCNT-SO<sub>3</sub>H have about 4% of atomic sulfur on the surface, while the MWCNT-COOH and MWCNT-p have no detectable sulfur. In addition, it is worth mentioning that oxygen content increased from 5.2% in MWCNT-p to 10.3 and 13.8 % in MWCNT-COOH and MWCNT-SO<sub>3</sub>H, respectively, which is consistent with the degree of surface modification endured during the acid treatment.

### 3.3.2.3. TGA Characterization of the Functionalized MWCNT Catalysts

In order to assess the thermal stability of the catalyst, TGA coupled with a mass spectrometer, to monitor the evolution of the gas phase products, was performed for the MWCNT-p, MWCNT-COOH and MWCNT-SO<sub>3</sub>H. The thermal analyses were measured under argon flow (50 ml/min) at a heating rate of 10 K/min from 273 K up to 1073 K. As shown in Figure 3.6a the MWCNT-p, MWCNT-COOH displayed a

gradual trend of decomposition from 373 to 1073 K with a mass loss around 4.36 wt. % and 12.20 wt. %, respectively. As it can be seen from Figures 3.6 b and c, this mass loss is associated to both desorption of water at low temperatures ( $< 473$  K), and decomposition of the surface oxidized groups (i.e.  $-\text{CO}$ ,  $\text{COOH}$ ,  $-\text{OH}$ ,  $-\text{CHO}$ , and  $\text{C-O-C}$ ) at high temperatures ( $> 523$  K). In the case of MWCNT- $\text{SO}_3\text{H}$  the weight loss was steady up to 493 K (Figure 3.6a), after this a sharp weight loss occurs, yielding a total mass loss around 34.64 wt. %.

The evolution of the decomposition products from this TGA is presented in Figure 3.6d. Here, we can identify that a significant amount of water in the gas phase is detected even at low temperatures. Further water evolution is observed when temperature increases, reaching its maximum at around 503 K. Likewise,  $\text{SO}_2$ ,  $\text{CO}_2$  and  $\text{CO}$  MS signals quickly evolved at around 491 K. This initial increase in the water and  $\text{SO}_2$  MS signal is due to the decomposition of the  $-\text{SO}_3\text{H}$  functional groups into  $\text{SO}_2$  and  $\text{H}_2\text{O}$  [41], while  $\text{CO}$  and  $\text{CO}_2$  peaks are related to the decomposition of the carbonyl moieties on the surface of carbon nanotubes [42]. Any additional water evolution could be attributed to the increase in the surface hydrophilicity of the CNT upon sulfonation.



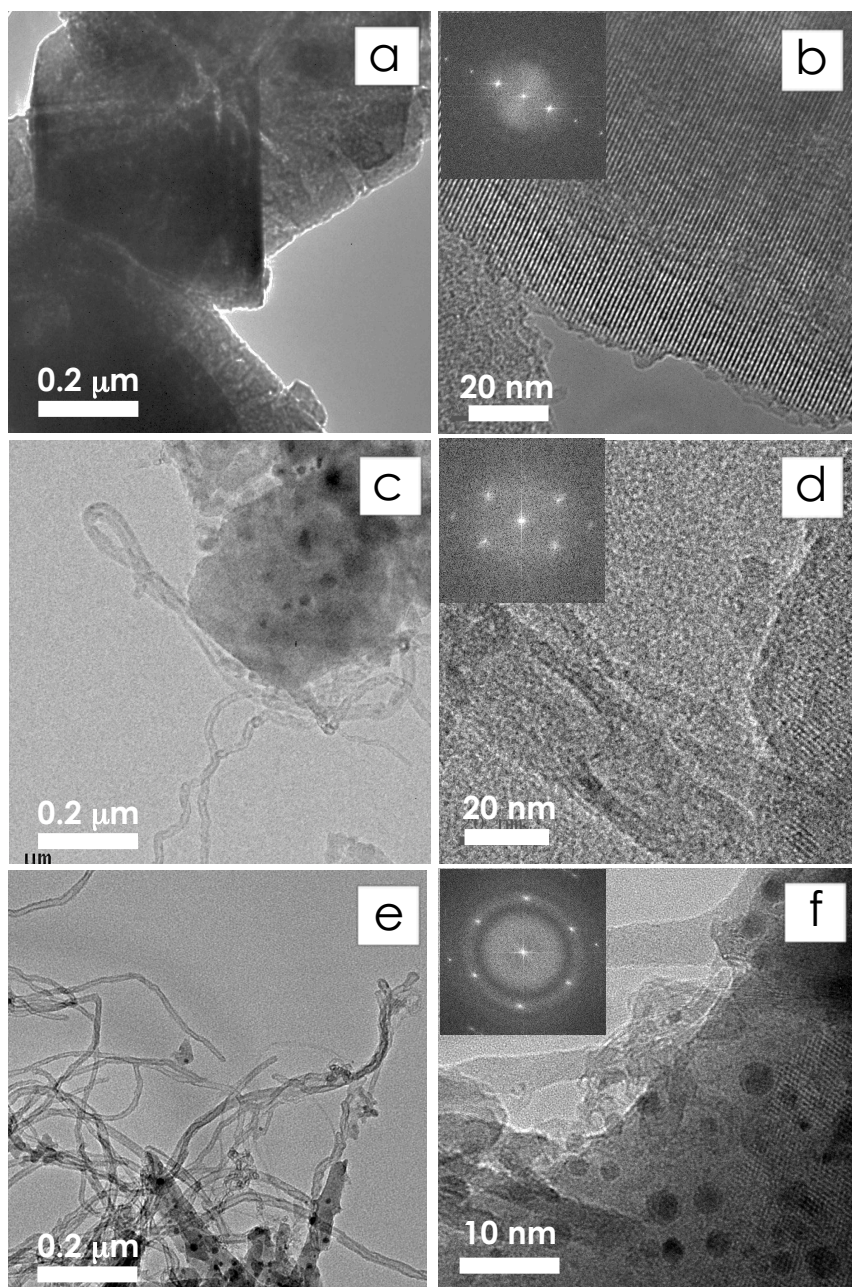
**Figure 3.6: TGA and gas phase composition of the nanohybrids: a) TGA of the purified MWNT (p-MWNT), oxidized MWNT (MWNT-COOH), and sulfonic functionalized MWNT (MWNT-SO<sub>3</sub>H), and MS of the gas phase products for the b) purified MWNT (p-MWNT), c) oxidized MWNT (MWNT-COOH), and d) sulfonic functionalized MWNT (MWNT-SO<sub>3</sub>H).**

These results clearly show that the Bronsted acid sites on the MWCNT-SO<sub>3</sub>H hybrid catalysts are stable at temperatures up to 493 K. Furthermore, this carbon-based solid acid contains a high density of Bronsted acid groups, as determined by acid base titration method published elsewhere [43]. In Table 3.2, it can be seen the acid concentrations per gram of carbon for the MWCNT-SO<sub>3</sub>H was around 81 mmol/g, while the MWCNT-COOH and p-MWCNT had an acid density of 55.9 and 0.1 mmol/g, respectively.

#### 3.3.2.4. HRTEM the MWCNT-NaX and NaX Catalysts

Further characterization of the structure of the MWCNT-NaX and SWCNT-NaX nanohybrids was done by high-resolution transmission electron microscopy (HRTEM). In Figure 3.7 are presented the images, at two different magnifications, for the NaX zeolite before the synthesis of the carbon nanotubes (Figures 3.7 a and b), as well as, the amphiphilic catalysts MWCNT-NaX and SWCNT-NaX (Figures 3.7c-d and d-f, respectively).

A germane observation is that the nanohybrids materials retained the crystallinity of the parent zeolite, even after the treatment at high temperature required for the synthesis of the carbon nanotubes. Additionally, the 5 wt. % Pd/MWCNT, and 5 wt. % Ru/MWCNT were characterized the by HRTEM (Figures 3.7 a and b), which yield average particle sizes around 2.3 and 1.3 nm, respectively (Figure 3.7c).

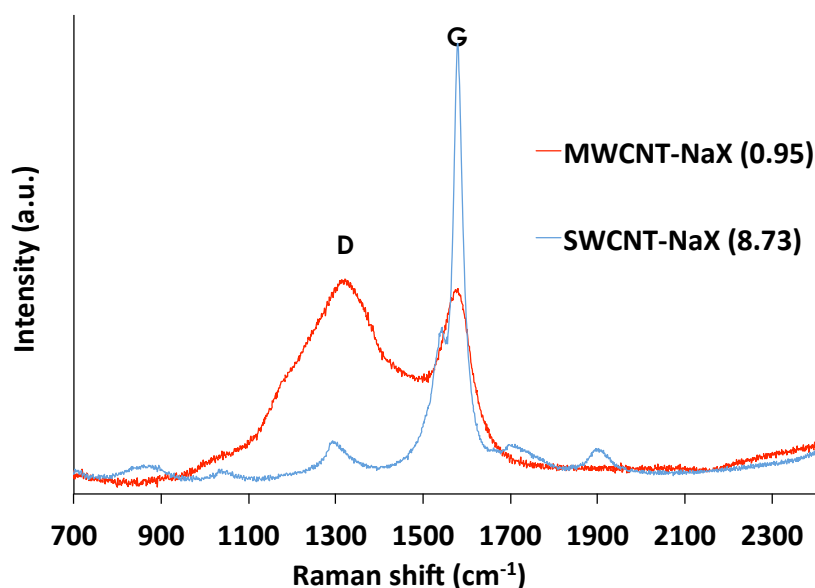


**Figure 3.7: HRTEM images at different magnifications and the diffraction pattern of the materials before and after the synthesis of carbon nanotubes; a-b) commercial NaX faujasite zeolite, c-d) MWNT-NaX, and e-f) SWNT-NaX.**

### 3.3.2.5 Raman Characterization of the MWCNT-NaX and NaX Catalysts

Further characterization by Raman spectroscopy was conducted for the various nanohybrids. The technique has been extensively used to assess the quality and purity

of carbon nanotubes [44-46]. Typically, the relative density of defects on carbon nanotubes can be expressed as the ratio of two characteristic bands, the G band, which appears at  $\sim 1590\text{ cm}^{-1}$  is ascribed to  $\text{sp}^2$  ordered carbon, and the D band, which appears around  $1350\text{ cm}^{-1}$ , is commonly ascribed to  $\text{sp}^3$  carbon associated with defects [47-49]. Figure 3.8 shows the normalized Raman spectra and the G/D ratios for the MWCNT-NaX and SWCNT-NaX. As expected the G/D ratio for the SWCNT-NaX (8.73) was significantly larger than the one obtained for the MWCNT-NaX (0.95), since the SWCNT are highly pristine they mainly have  $\text{sp}^2$  hybridized carbon while MWCNT have a more defective structure with a larger fraction of  $\text{sp}^3$  hybridized carbon.

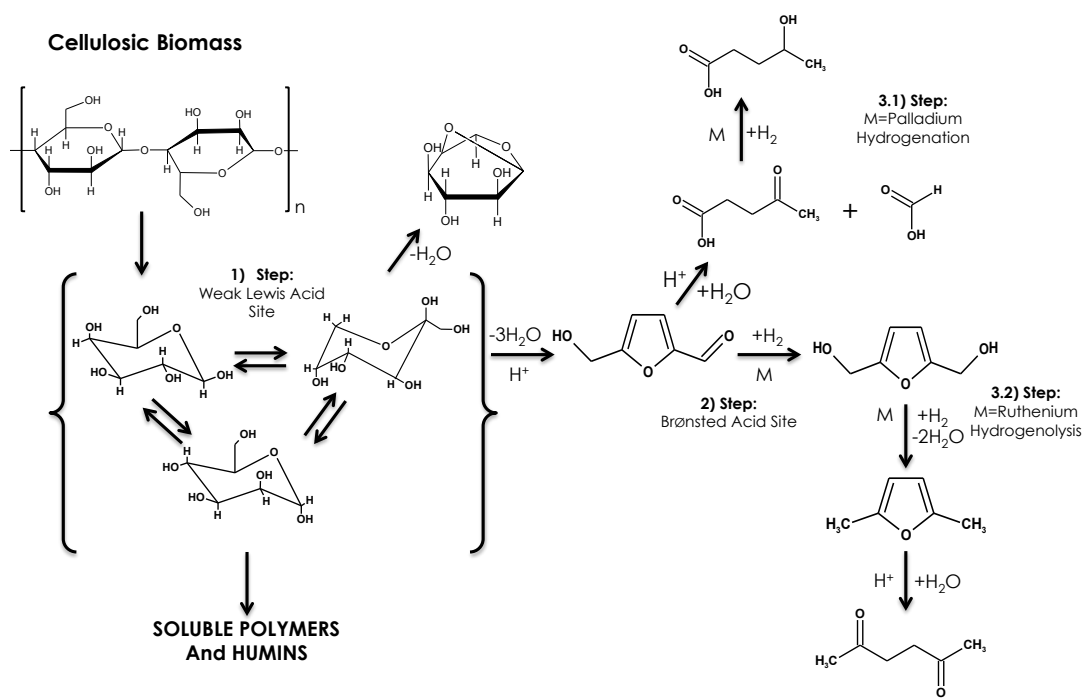


**Figure 3.8: Normalized Raman spectrum of the SWCNT-NaX and MWCNT-NaX nanohybrids.**

### 3.3.3. Glucose Isomerization Over Nanohybrid CNT-NaX Catalysts

Figure 3.9 shows our integrated approach to convert glucose to chemical intermediates and fuels at the liquid-liquid interface of water-oil emulsions. The

sequence entails the; 1) isomerization of hexoses (glucose) to keto-hexoses (fructose), 2) the selective fructose dehydration towards hydroxymethylfurfural (HMF), and 3) the phase transfer of the latter from the aqueous to the organic phase and hydrogenation towards either g-hydroxyvaleric acid or 2,5-hexadione, depending on the catalyst (i.e. ruthenium or platinum).

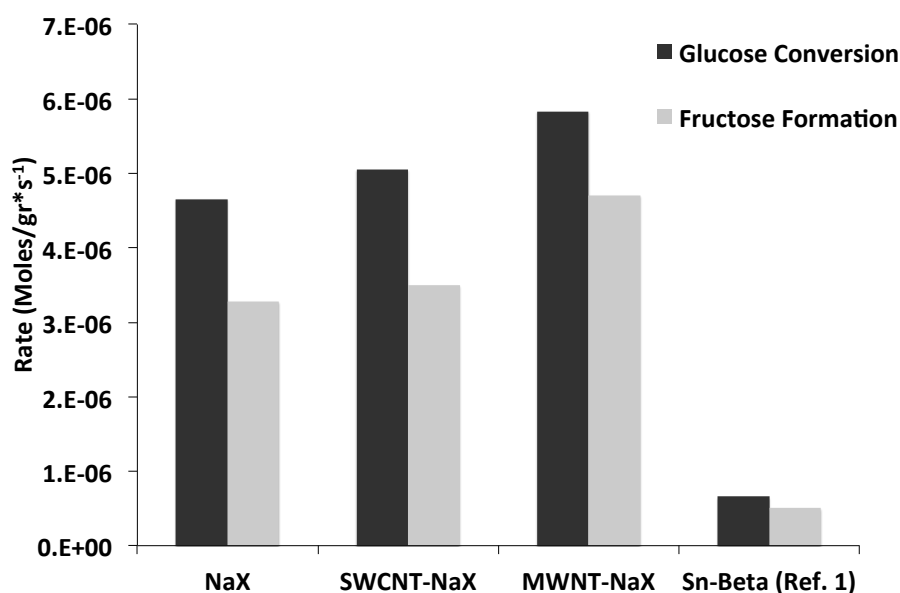


**Figure 3.9: Reaction scheme for the integrated isomerization-dehydration and hydroprocessing of the cellulosic biomass. The process includes; 1) isomerization of the glucose on a weak Lewis acid site, 2) dehydration of the fructose on a Brønsted acid site; 3.1) hydrolysis of the hydroxymethylfurfural on an acid site followed by hydrogenation of the levulinic acid on a metal site to produce g-hydroxyvaleric acid, and 3.2) hydrogenolysis/hydration of the hydroxymethylfurfural to produce 2,5-hexadione.**

Initially, a series of X faujasites zeolites functionalized with either SWCNT or MWCNT were screened for their catalytic activity in the isomerization of glucose. Specifically, we compared ion exchanged CsNaX and NaX faujasites with the

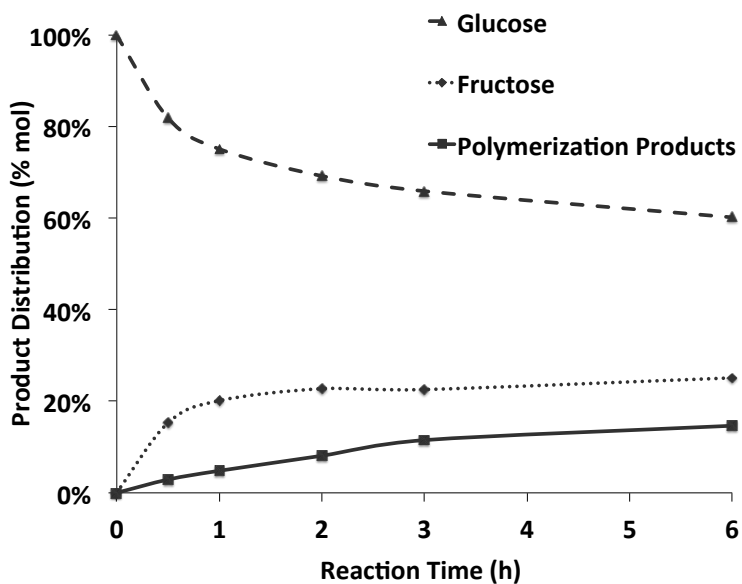


amphiphilic nanohybrids SWCNT-NaX and MWCNT-NaX. The MWCNT-NaX and SWCNT-NaX showed the highest rate of glucose conversion, reaching values above  $5.0 \times 10^{-6} \text{ mol/gr}\cdot\text{s}^{-1}$  at  $110 \text{ }^\circ\text{C}$  and 400 psi of  $\text{N}_2$  (Figure 3.10). Even though the  $\text{Na}^+$  ions in the NaX faujasite have a weak Lewis character, capable of catalyze Meerwein-Ponndorf-Verley reductions (MPV) [50], similar to that of Sn-Beta zeolites [51], the rates of glucose isomerization per gram of nanohybrid are one order of magnitude larger than those reported by M. Moliner et al. for the Sn-Beta zeolite at similar initial concentrations (10 wt. % glucose) and reaction conditions (383 K and 90 min). In that case the low density of active sites (Sn atoms in the framework) per unit of mass forced the use of large ratios of catalyst to feed, which may complicate process scale-up.



**Figure 3.10: Rate of glucose conversion and fructose formation for the commercial NaX zeolite, nanohybrid MWNT-NaX, and nanohybrid SWNT-NaX. Obtained from the glucose isomerization in aqueous phase at  $110 \text{ }^\circ\text{C}$ , 600 rpm of agitation and 400 psi of  $\text{N}_2$  over 200 mg of catalyst. Feed: 10 wt.% of glucose in a total reaction volume of 30 ml.**

Further reaction experiments with the most active nanohybrid catalyst (MWCNT-NaX) were performed over time in aqueous phase at 383 K and 400 psi of N<sub>2</sub> (Figure 3.11). Initially, the fructose selectivity reached values around 84 % for 20 % of glucose conversion, however after two hours of reaction, the fructose plateaued while the conversion of glucose increased to 40 %. It is well known that isomerization of glucose to fructose is governed by the thermodynamic equilibrium at the reaction temperature [52]. In fact, industrial enzymatic isomerization reactions carried out at 60 °C generate an equilibrium mixture of 42 wt. % fructose, 50 wt. % glucose and 8 wt. % of other saccharides [53]. Therefore, the observed additional disappearance of the glucose can be ascribed to the thermal-catalyzed degradation of the saccharides towards soluble polymers and humins, as others have reported it previously [54-57].



**Figure 3.11: Product distribution form the isomerization reaction of glucose with time in aqueous phase at 110 °C, 600 rpm of agitation and 400 psi of N<sub>2</sub> over NaX-MWNT nanohybrid catalyst (200 mg). Feed: Feed: 10 wt.% of glucose in a total reaction volume of 30 ml.**

One could overcome these thermodynamic and kinetic limitations by continuously extracting the fructose as dehydrated hydroxymethylfurfuraldehyde (HMF) into an organic phase. In such approach low yields products can be isolated at high concentrations in the extraction solvent. Furthermore, refining in the organic phase can be accomplished by selective conversion of the HMF into chemical platforms for the production of fuels or polymers, simplifying the upgrading process.

In order to test this concept we decided to test the dehydration of the keto- and aldose- hexose over Brønsted acid sites anchored on the surface of the functionalized MWCNT. Sulfonic (-SO<sub>3</sub>H) moieties resulted appealing for this study due to their strong Brønsted acidity and thermal stability as reported by Hara and coworkers [58]. They found that carbon based materials bearing acid sulfonic groups have an enhanced catalytic activity and stability for the production of biodiesel and cellulose hydrolysis when compared to conventional solid acid catalysts. Table 3.3 shows the evolution of the yield/conversion with time for the dehydration reaction of glucose (10 wt. %) at 150 °C and 400 psi of N<sub>2</sub> in a water-decalin emulsion (1:1 volume ratio) that was stabilized by 1 mg/ml of MWCNT-SO<sub>3</sub>H. At this elevated temperature, the yield of the HMF slightly increased with time, while the glucose concentration decreased due to the onset of the re-polymerization reactions. The formic and levulinic acids formed as results of the hydrolysis of HMF were observed even at short reaction times, but as the time evolved they reached a maximum yield at around 10 %. In sharp contrast, fructose dehydration at the same reactions conditions showed a much more selective conversion towards HMF (Table 3.3).

**Table 3.3: Conversion and product distribution obtained in the dehydration reaction of glucose and fructose at 150 °C, 300 rpm of agitation and 600 psi of N<sub>2</sub> over 50 mg of nanohybrid catalyst (MWNT-SO<sub>3</sub>H), in water:decalin (1:1) emulsion emulsion. Reactant concentration: 10 % vol. in 40 ml of total volume.**

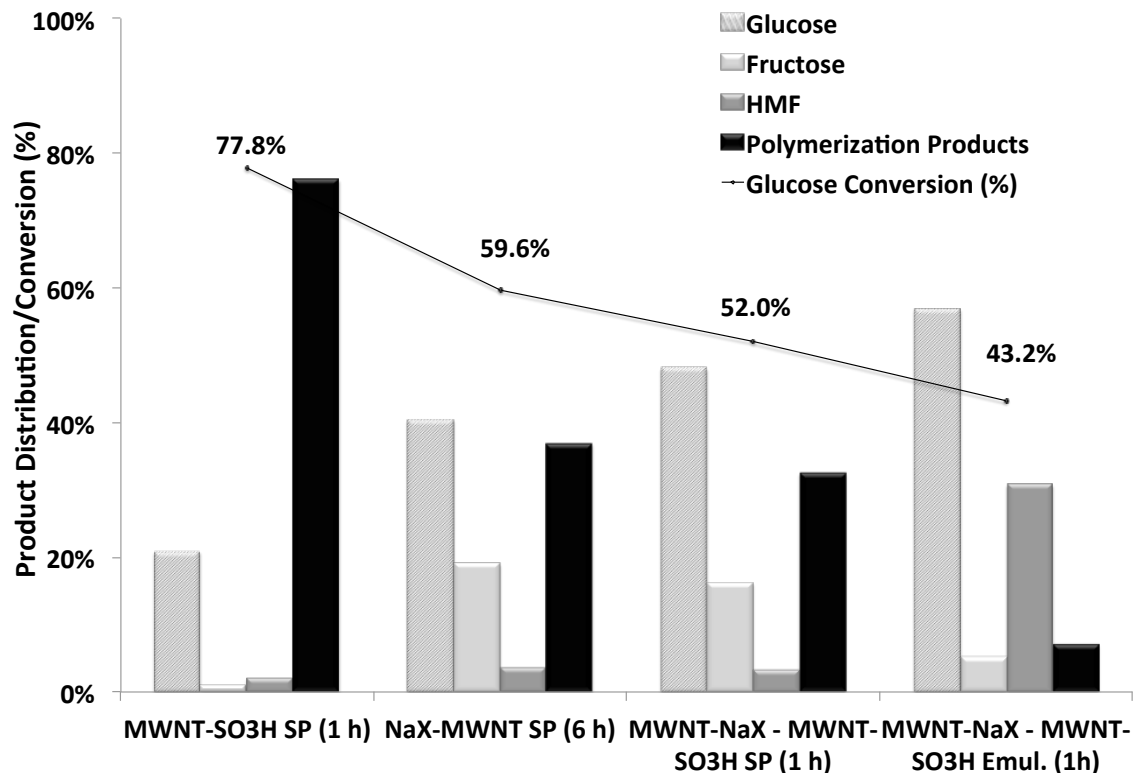
Reactant	Reaction Time (min)	% Conversion	Product Distribution (mol%)		
			5-Hydroxymethyl furfural	Formic Acid	Levulinic Acid
Glucose	30	34.4	1.4	5.0	5.5
	60	76.3	3.5	6.3	6.9
Fructose	30	40.1	5.7	4.5	5.2
	60	65.5	31.5	8.2	8.6

It can be noted that, for 60 min of reaction (65 % of conversion), the yield of HMF from fructose was around 32 %, much higher than the 3.5 % yield observed for the glucose at 75 % of conversion. These differences in HMF selectivity can be endorsed to the relative stability of the glucose and fructose ring structures. In the former, the stability of the C6 member ring is very high, in consequence the concentration of the open chain form in solution is smaller, while in the second the opposite occurs. This is especially relevant, as the rate of enolization of the open-chain saccharides is believed to be rate-limiting step [59]. Additionally, fructose forms di-fructose-di-anhydrides in an equilibrium reaction that are sterically hindered in such a way that cross-polymerization are less favorable than the oligosaccharides formed from glucose [60-63]. These molecules contain reducing groups that can react with reaction intermediates and HMF [64].

In an effort to improve the poor selectivity obtained in the dehydration of the sugars in the water-decalin nanohybrid-stabilized emulsions, we decided to couple the

isomerization and dehydration catalysts at the liquid-liquid interface of the water-oil emulsion. Also, tetrahydrofuran (THF) and saturated sodium chloride aqueous solutions (35 wt. %) were used to enhance the extractive capacity of organic solvent [13,14,65]. The products distribution obtained after one hour of reaction using 10 wt.% glucose, 423 K, and 400 psi of N<sub>2</sub> are presented in Figure 3.12.

Here, a remarkable increase in the selectivity to HMF (around 71 %) is observed when the two nanohybrid catalysts, MWCNT-SO<sub>3</sub>H + MWCNT-NaX, are combined with the water + NaCl + THF emulsions. For comparison, we carried out the same reaction in aqueous phase only, but the resulting selectivity for the HMF decreased to a value close 6 %, while glucose disappearance remained at around 52 %. The remarkable enhancement in the selectivity to HMF, even in these harsh conditions, observed in the nanohybrid-stabilized emulsions are mainly due to two factors; a) the aldose-ketose isomerization to fructose, which can selectively dehydrate to HMF, and b) the partition of the HMF into the organic phase, preventing its cross-condensation with the saccharides even at high levels of conversion.



**Figure 3.12: Conversion of glucose and product distribution from the reaction of isomerization-dehydration in single phase and in water (35 wt.% NaCl):tetrahydrofuran emulsion of glucose.**

#### 3.3.4. Catalyst Regenerability and Reusability

In order to test the reusability of the MWCNT-NaX and the parent NaX faujasite zeolite, we performed three consecutive isomerization cycles at 383 K for 1 h reaction/cycle. The reactions were carried out using 10 wt.% of glucose in a total reaction volume of 30 ml at 110 °C, 600 rpm of agitation and 400 psi of N<sub>2</sub> over 200 mg of catalyst. After each reaction the catalyst was filtered using a 0.2 mm nylon filter, followed by water and acetone washing. Then, the catalyst was dried in vacuum at 373 K for 12 h and reused for the isomerization of freshly prepared glucose solution. As it can be seen from the data listed on Table 3.4 the initial rate of glucose conversion for the conventional NaX faujasite greatly decreased after the first cycle, i.e. around 85%

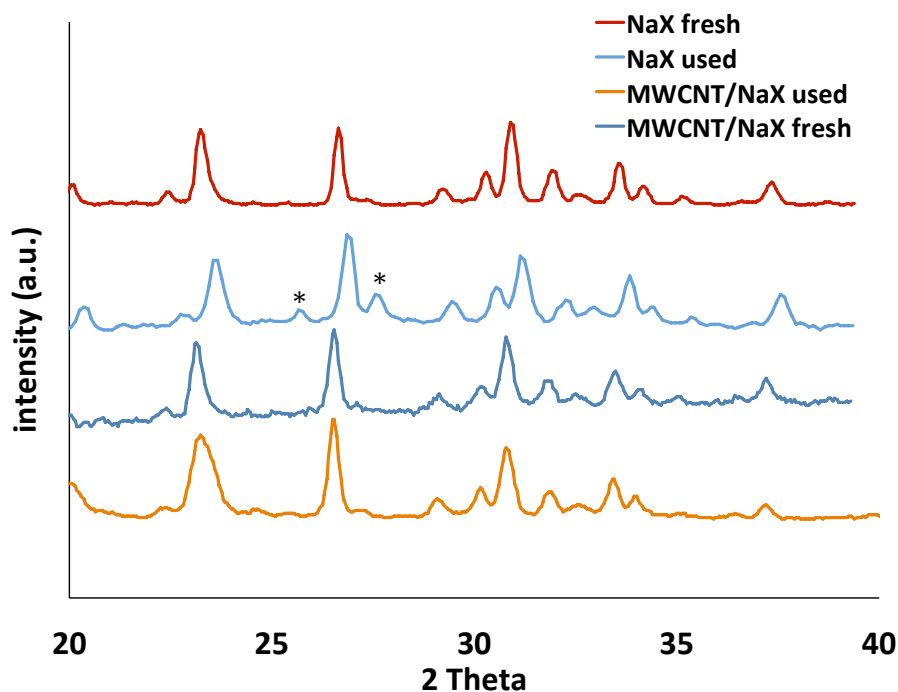
loss in activity, while the MWCNT-NaX retained almost 70% of their initial activity, even after three reaction cycles. Also, the fructose selectivity was affected when the NaX zeolite was recycled, with selectivities around 38 % in the third reaction. In contrast, the selectivity of the nanohybrid MWCNT-NaX was maintained around 70% for the three cycles.

**Table 3.4: Rate of glucose conversion and fructose selectivity for the commercial NaX zeolite and nanohybrid MWNT-NaX after recycling the catalysts three times.**

Catalyst	NaX		MWNT-NaX		
	Number of Cycle	Rate of Glucose Conv. (mol/g x s <sup>-1</sup> )	Fructose Selectivity (%)	Rate of Glucose Conv. (mol/g x s <sup>-1</sup> )	Fructose Selectivity (%)
1		4.7E-06	70.4	5.8E-06	80.7
2		6.9E-07	71.7	4.2E-06	78.8
3		5.9E-07	38.3	3.8E-06	69.5

Further characterization by XRD the NaX and MWCNT-NaX before and after the first reaction cycle (Figure 3.13) was performed to assess the changes in the catalyst crystallinity. Here, it is important to mention that no significant changes in the XRD patterns were observed between the nanohybrid MWCNT-NaX and NaX zeolite before reaction. This is consistent with the HRTEM images previously presented (Figure 3.7) and the lattice constants (Table 3.5) obtained for the NaX and MWCNT-NaX before reaction, with values around 25.01 and 25.05 Å, respectively, corroborating that crystalline structure is not affected by the synthesis of the carbon nanotubes. Upon reaction in hot liquid water, however, a significant shift and advent of new diffraction peaks (2θ of 25.55° and 27.55) were observed for the regular NaX faujatise zeolite,

while in the case of the nanohybrid MWCNT-NaX catalyst the diffractogram remained unaltered.



**Figure 3.13: X-ray diffraction of the NaX zeolites and MWCN-NaX nanohybrids before and after 1 h of isomerization reaction of glucose at 383 K, 600 rpm of agitation and 400 psi of N<sub>2</sub> over 200 mg of catalyst. Feed: 10 wt.% of glucose. Reaction volume: 30 ml.**

This shift on the position of XRD peaks is a clear indication of unit cell shrinkage, as shown in Table 3.5, the lattice constant and unit cell volume decreased to values around 24.82 Å and 15.29 nm<sup>3</sup>, respectively. Such reduction of the unit cell has been associated previously with leaching of the sodium ions from the zeolite framework [66]. In fact, similar observations have been reported during isomerization of aldoses with cation-exchanged zeolites in aqueous environments [67]. The high mobility and chemical potential of the ions inside the zeolite favored the diffusion towards the



aqueous phase. In a minor extent, carbon deposition, as deactivation mechanism, has been reported [68]. Hence, it is not surprising that the MWCNT acted as a hydrophobic barrier for the water diffusion into the zeolite framework, improving their hydrothermal stability and preventing the migration of the sodium ions out of the zeolite.

**Table 3.5: Lattice constants and unit cell volumes for the different catalysts before and after 1 h of isomerization reaction of glucose at 383 K, 600 rpm of agitation and 400 psi of N<sub>2</sub> over 200 mg of catalyst. Feed: 10 wt.% of glucose. Reaction volume: 30 ml.**

Sample	Lattice constant (Å)	$\pm \sigma$ (Å)	Unit Cell Volume (nm <sup>3</sup> )	$\pm \sigma$ (Å)
NaX Fresh	25.01	0.0119	15.65	0.23
NaX Used	24.82	0.0117	15.29	0.22
MWCNT-NaX Fresh	25.05	0.0119	15.72	0.23
MWCNT-NaX Used	25.03	0.0118	15.68	0.23

### 3.3.5. Hydrodeoxygenation of 5-Hydroxymethylfurfural on Ru or Pd/MWCNT/Al<sub>2</sub>O<sub>3</sub> Nanohybrids

Finally, we conducted proof-of-concept reactions of HMF hydrogenation at the liquid-liquid interface of water-decalin emulsions. The aim was to selectively convert the HMF, in the organic phase, into chemical platforms for the production of renewable fuels and polymeric resins. Table 3.6 summarizes the product distribution obtained after two hours of reaction of HMF over 5 wt. % Ru or Pd supported on MWCNT-Al<sub>2</sub>O<sub>3</sub> nanohybrids at 423 K and 600 psi of N<sub>2</sub>.

**Table 3.6: Conversion of 5-hydroxymethylfurfural and product distribution obtained in the hydrogenation reaction of hydroxymethylfurfural after 2 h of reaction at 150 °C, 300 rpm of agitation and 600 psi of N<sub>2</sub> over 50mg of nanohybrid catalyst (5% Ru/MWNT/Al<sub>2</sub>O<sub>3</sub> and 5% Pd/MWNT/Al<sub>2</sub>O<sub>3</sub>), in water:decalin (1:1) emulsion emulsion.**

Catalysts	% Conversion	TOF (s <sup>-1</sup> )	Product Distribution (mol%)		
			2,5-Bis (hydroxymethyl) furan	2,5-Hexanedione	γ-hydroxyvaleric acid
5% Ru/MWNT/Al <sub>2</sub> O <sub>3</sub>	70.7	0.25	15.0	47.8	7.8
5% Pd/MWNT/Al <sub>2</sub> O <sub>3</sub>	87.0	0.34	2.9	0	84.1

Interestingly, significant differences were observed between the Ru and Pd MWCNT-Al<sub>2</sub>O<sub>3</sub> catalysts at similar levels of conversion, 70% and 80%, respectively. In the former, the 2,5-hexanedione was the major product (47.8 mol. %), followed by 2,5-bis(hydroxymethyl)furan (15 mol. %) and g-hydroxyvaleric acid (7.8 mol. %). In sharp contrast, the latter showed only two species; the hydrolysis-hydrogenation product (84.1 mol. % of g-hydroxyvaleric acid), and the hydrogenated HMF (2.9 mol. % of 2,5-bis(hydroxymethyl)furan). From these results it seems that the rate of C-O hydrogenolysis is much faster for the ruthenium catalysts, which increases the yield of 2,5-dimethylfuran (DMF), followed by alkene hydrolysis and ring opening to form 2,5-hexanedione. In the case of the palladium catalyst, the hydrogenation activity is lower allowing the acid hydrolysis to convert the HMF into levulinic acid and formic acid that then can be hydrogenated to g-hydroxyvaleric acid and light gases.

### 3.4. Conclusions

In summary, we have demonstrated that Lewis acid, Brønsted acid, and supported-metal catalysts bearing hydrophobic-functionalities exhibited exceptional hydrothermal stability and improved resistance to leaching of the active sites, which are crucial requirements in large-scale refining of biomass-derived carbohydrates. While, conventional NaX faujasite zeolites, in which the sodium ions act as weak Lewis acid sites for the keto-aldose isomerization of glucose, are rapidly deactivated after one of reaction at 383 K due to leaching of the sodium ions, as demonstrated by the XRD experiments, the MWCNT-NaX zeolite kept its catalytic activity and crystalline structure in this harsh environment.

Furthermore, the combination of the Lewis acid catalyst (i.e. MWCNT-NaX) and Brønsted acid (i.e. MWCNT-SO<sub>3</sub>H) in water (NaCl 35 wt. %) - THF emulsions, in which upon isomerization of the glucose to fructose the dehydration reaction is carried and the resulting HMF rapidly transfer to the organic phase, greatly enhances the selectivity of the reaction with selectivities of HMF above 71 % at conversions around 57 %.

We also explored the concept of continuous extraction and selective hydrogenation of the HMF in the organic solvent over metal clusters anchored on hydrophobic MWCNT fused to aluminum oxide (Metal-MWCNT-Al<sub>2</sub>O<sub>3</sub>) in water-oil emulsions. Indeed, it was possible to improve the selectivity of the hydrogenation reaction by both preventing the competitive hydrogenation of the sugars from the aqueous phase, and producing more stable hydrodeoxygenated molecules 2,5-

hexadinone and g-hydroxyvaleric acid; excellent candidates for the chemical and fuel industries.

Indeed, this technology offers many advantages, including: a) simplified refining scheme by avoiding surfactants, b) enhanced mass transfer of molecules between the two phases due to the higher interfacial surface area, c) improved selectivity as products are separated from the reaction mixture by differences in the water-oil solubility (avoiding heat-intense distillation processes and preventing cross-polymerization reactions), d) and phase-selective catalysis based on the preferential exposure of the catalyst to one of the phases. Thereby, we envision that hydrophobic catalysts stables liquid hot water coupled with fast reactive-separation will be crucial in the development of sustainable technologies for the catalytic upgrading of biomass-derived carbohydrates.

## References

- [1] J.P. Lange, *Biofuels Bioprod. Biorefin.* 1 (2007) 39.
- [2] G.W. Huber, S. Iborra and A. Corma, *Chem. Rev.* 106 (2006) 4044.
- [3] D.E. Resasco and S. Crossley, *AIChE J.* 55 (2009) 1082.
- [4] R.M. Ravenelle, F. Schüàler, A. D'Amico, N. Danilina, J.A. van Bokhoven, J.A. Lercher, C.W. Jones and C. Sievers, *J. Phys. Chem. C* 114 (2010) 19582.
- [5] A. Corma, L.T. Nemeth, M. Renz and S. Valencia, *Nature* 412 (2011) 423.
- [6] M. Moliner, Y. Roman-Leshkov and M.E. Davis, *Proc. Natl. Acad. Sci. USA* 107 (2010) 6164.
- [7] P.A. Zapata, J. Faria, M.P. Ruiz, R.E. Jentoft and D.E. Resasco, *J. Am. Chem. Soc.* (2012) DOI: [dx.doi.org/10.1021/ja3015082](https://doi.org/10.1021/ja3015082).
- [8] S. Crossley, J. Faria, M. Shen and D.E. Resasco, *Science* 1 (2010) 68.
- [9] J. Faria, M.P. Ruiz and D.E. Resasco, *Adv. Synth. Catal.* 352 (2010) 2359.
- [10] M. Shen and D.E. Resasco, *Langmuir* 25 (2010) 10843.
- [11] T. Prasomsri, D. Shi and D.E. Resasco, *Chem. Phys. Lett.* 497 (2010) 103.
- [12] M.P. Ruiz, J. Faria, M. Shen, S. Drexler, T. Prasomsri and D.E. Resasco, *ChemSusChem* 4 (2011) 964.
- [13] Y. Roman-Leshkov, J.N. Chheda and J.A. Dumesic, *Science* 312 (2006) 1933.
- [14] Y. Roman-Leshkov, C.J. Barrett, Z.Y. Liu and J.A. Dumesic, *Nature* 447 (2007) 982.
- [15] D.J. Cole-Hamilton, *Science* 327 (2010) 41.
- [16] M. Lasperas, H. Cambon, D. Brunel, I. Rodriguez and P. Geneste, *Microporous Mater* 7 (1996) 61.

- [17] W.E. Alvarez, B. Kitiyanan, A. Borgna and D.E. Resasco, *Carbon* 39 (2001) 547.
- [18] D.E. Resasco, B. Kitiyanan, J.H. Harwell and W. Alvarez (2001) Method of producing carbon nanotubes. U.S. Patent No. 6,333,016.
- [19] S. Bollepalli (2007) Sulfonated carbonaceous materials. US Patent 7,241,334.
- [20] P.A. Zapata, J. Faria, M.P. Ruiz and D.E. Resasco, *Top. Catal.* 55 (2012) 38.
- [21] T.R. Briggs, *Ind. Eng. Chem.* 13 (1921)1008.
- [22] S. Levine and E. Sanford, *Can. J. Chem. Eng.* 63 (1985) 258.
- [23] V.B. Menon, D.T. Wasan, *Colloids. Surf.* 23 (1987) 353.
- [24] V.B. Menon and D.T. Wasan, *Sep. Sci. Technol.* 23 (1988) 2131.
- [25] D.E. Tambe and M.M. Shaftma, *Adv. Colloid Interface Sci.* 52 (1994) 1.
- [26] E.J. Johansen, M.I. Skjarvo, T. Lund, J. Sjoblom, H. Soderlund and G. Bostrom, *Colloid Surf* 34 (1988/1989) 353.
- [27] P. Finkle, H.D. Draper and J.H. Hilderbrand, *J. Am. Chem. Soc.* 45 (1923) 2780.
- [28] J.H. Schulman and J. Leja, *Trans. Faraday Sot* 50 (1954) 598.
- [29] B.P. Binks, *Curr. Opin. Colloid Interface Sci.* 7 (2002) 21.
- [30] B.P. Binks and S.O. Lumsdon, *Langmuir* 17 (2011) 4540.
- [31] B.P. Binks, J. Philip and J.A. Rodrigues, *Langmuir* 21 (2005) 3296.
- [32] A. Koshio, M. Yudasaka, M. Zhang and S. Iijima, *Nano. Lett.* 1 (2001) 361.
- [33] F. Pompeo and D.E. Resasco, *Nano. Lett.* 2 (2002) 369.
- [34] L. Adams, A. Oki, T. Grady, H. McWhinney and Z. Luo, *Physica E* 41 (2009) 723.

- [35] T.I.T. Okpalugo, P. Papakonstantinou, H. Murphy, J. McLaughlin and N.M.D. Brown, *Carbon* 43 (2005) 153.
- [36] M. Holzinger, A. Hirsch, F. Hennrick, M.M. Kappes, A. Dziakowa, L. Ley et al., *Am. Inst. Phys. Conf. Proc.* 633 (2002) 96.
- [37] S.E. Baker, W. Cai, T.L. Kasser, K.P. Weidkamp and R.J. Hamers, *Nano. Lett.* 2 (2002) 1413.
- [38] H. Hiura, T.W. Ebbesen and K. Tanigaki, *Adv. Mater.* 7 (1995) 275.
- [39] M.T. Martinez, M.A. Callejas, A.M. Benito, M. Cochet et al., *Carbon* 41 (2003) 2247.
- [40] E. Cano-Serrano, G. Blanco-Brieva, J.M. Campos-Martin and J.L.G. Fierro, *Langmuir* 19 (2003) 7621.
- [41] M. Hara, T. Yoshida, A. Takagaki, T. Takata, J.N. Kondo, S. Hayashi and K. Domen, *Angew. Chem. Int. Ed.* 43 (2004) 2955.
- [42] F. Peng, L. Zhang, H. Wang, P. Lv, Y. Hao, *Carbon* 43 (2005) 2397.
- [43] H. Hu, P. Bhowmik, B. Zhao, M.A. Hamon, M.E. Itkis and R.C. Haddon, *Chem. Phys. Lett.* 345 (2001) 25.
- [44] A.C. Dillon, M. Yudasaka and M.S. Dresselhaus, *J. Nanosci. Nanotechnol.* 4 (2001) 691.
- [45] A.W. Musumeci, E.R. Waclawik and R.L. Frost, *Spectrochim. Acta A* 71 (2008) 140.
- [46] Y. Kobayashi, D. Takagi, Y. Ueno and Y. Homma, *Phys. E* 24 (2004) 26.
- [47] S.M. Bachilo, L. Balzano, J.E. Herrera, F. Pompeo, D.E. Resasco and R.B. Weisman, *J Am Chem Soc* 125 (2003) 11186.

- [48] J.R. Simpson, J.A. Fagan, M.L. Becker, E.K. Hobbie and A.R. Hight Walker, *Carbon* 47 (2009) 3238.
- [49] P. Delhaes, M. Couzi, M. Trinquécoste, J. Dentzer, H. Hamidou and C. Vix-Guterl, *Carbon* 44 (2006) 3005.
- [50] J. Shabtai, R. Lazar and E. Biron, *J. Molec. Catal.* 27 (1984) 35.
- [51] A. Corma, M.E. Domine and S. Valencia, *J. Catal.* 215 (2003) 294.
- [52] Y. Tewari, *Appl. Biochem. Biotech.* 23 (1990) 187.
- [53] S. Bhosale, M. Rao and V. Deshpande, *Microbiol. Rev.* 60 (1996) 280.
- [54] X. Qian, M.R. Nimlos, M. Davis, D.K. Johnson and M.E. Himmel, *Carbohydr. Res.* 340 (2005) 2319.
- [55] E.R. Garrett and B.H.J. Dvorchik, *J. Pharm. Sci.* 58 (1969) 813.
- [56] N. Abatzoglou, J. Bouchard, E. Chornet and R.P. Overend, *Can. J. Chem. Eng.* 64 (1986) 781.
- [57] R. Weingarten, G.A. Tompsett, Jr. C. Conner and G.W. Huber, *J. Catal.* 279 (2011) 174.
- [58] M. Hara, *Energy Environ. Sci.* 3 (2010) 601.
- [59] B.F.M. Kuster, *Starch* 8 (1990) 314.
- [60] R.W. Binkley, W.W. Binkley and A.A. Grey, *Carbohydr. Res.* 28 (1973) 365.
- [61] R.W. Binkley, W.W. Binkley and B. Wickberg, *Carbohydr. Res.* 36 (1974) 196.
- [62] K. Hamada, H. Yoshihara, G. Suzukamo and O. Hiroaki, *Bull. Chem. Soc. Jpn* 57 (1984) 307.
- [63] J. Defaye, A. Gadelle and C. Pedersen, *Carbohydr. Res.* 136 (1985) 53.
- [64] H.E. Van Dam, A.P.G. Kieboom and H. Van Bakkum, *Starch* 38 (1986) 95.



- [65] E. Nikolla, Y. Roman-Leshkov, M. Moliner and M.E. Davis, *ACS Catal.* 1 (2011) 408.
- [66] W. Lutz, C.H. Rüschler and D. Heidemann, *Microporous Mesoporous Mater.* 55 (2002) 193.
- [67] Y. Roman-Leshkov and M.E. Davis, *ACS Catal* 1 (2011) 1566.
- [68] C. Morea, R. Durand, A. Roux and D. Tichit, *Appl. Catal. A General* 193 (2000) 257.

## **Chapter 4:**

### **Phase Selective Conversion at the Liquid-Liquid Interface of Nanoparticle-stabilized Emulsions**

#### **4.1. Introduction**

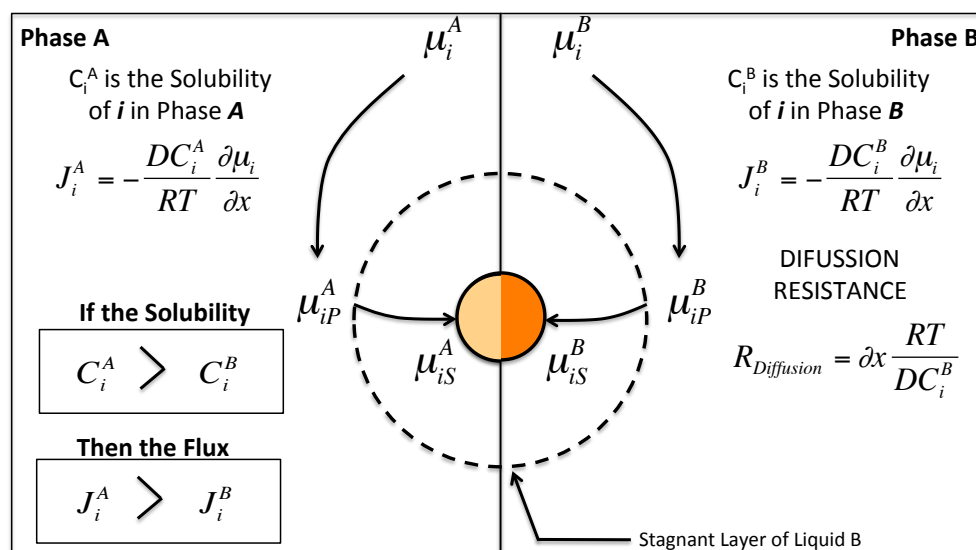
It is clear that the entire area of solvent effects in heterogeneous catalysis requires further attention, particularly in complex systems of great current interest, such as biofuel refining, in which strongly adsorbing oxygenates and aqueous phase solutions are used in combination with an organic phase. It is well known that the driving force that determines chemical reaction and diffusion rates is given by thermodynamic properties, such as chemical affinity, chemical potential or activity. Only in ideal reaction mixtures it is possible to express the reaction and mass transport rates as a function of the concentration of the species present in the system [1]. Specifically, in the case of catalytic reactions in gas-liquid-solid systems, reacting molecules are solvated and, in general, in a non-ideal environment. Boudart et al. [2] pointed out that when the liquid and gas phases reach the thermodynamic equilibrium, the chemical potential of those phases becomes equal. Therefore, when the phases are equilibrated, the reaction rate should be independent of the location of the reactants and catalysts.

The chemical potential controlled-kinetics principle, however, does not apply when: a) the phases are not in thermodynamic equilibrium, due to mass transfer limitations, b) the solvent competes with the reactant molecules for adsorption on the active sites [1-5], or c) the liquid does not solvate kinetically relevant adsorbed intermediates and activated complexes to the same extent.

In Figure 4.1 it is presented the diffusion of molecules from the bulk liquid phases towards the catalyst located at the liquid-liquid interface. As explained above when the phases are in equilibrium the reaction rate is the same in both phases, unless a mass transport is present in the system. Mass transport limitations are considered undesirable, however, in many industrial applications the size and shape of reacting molecules is used to control the access to the active site. Here we propose a new tunable property of the catalyst to control the catalyst selectivity based on the solubility or polarity of the molecules. One can imagine a system in which the catalyst is selectively deposited on one of the two phases of the liquid-liquid interface, allowing selective conversion of the molecules with the highest solubility.

Some authors have correlated the observed reaction rates and product distributions with solvent polarity or dielectric constant [6-9]. For example, it has been observed that the rate of cyclohexene (non-polar) hydrogenation was higher than the reaction rate observed for acetone (polar) hydrogenation when a polar solvent was used. Such difference in kinetic rates was ascribed to the strong interactions between the polar solvent and acetone in the bulk fluid phase, resulting in reduced affinity for acetone adsorption [10,11]. By contrast, Vannice et al. [3,4] compared the catalytic hydrogenation reaction of citral molecules over Pt supported on silica, on eight nonreactive solvents (n-amyl acetate, ethyl acetate, n-hexane, cyclohexane, tetrahydrofuran, p-dioxane, ethanol, and cyclohexanol) that have significantly different dielectric constants, polarities, and hydrogen solubilities. Using Langmuir-Hinshelwood kinetics models, they concluded that the rate of citral hydrogenation was strongly influenced by the competition of the solvent with the reacting species for adsorption

sites on the catalyst surface, rather than dielectric constant, dipole moment, hydrogen solubility, or viscosity. This result demonstrates the important role of the competitive adsorption of the solvent in gas-liquid-solid catalytic reactions.

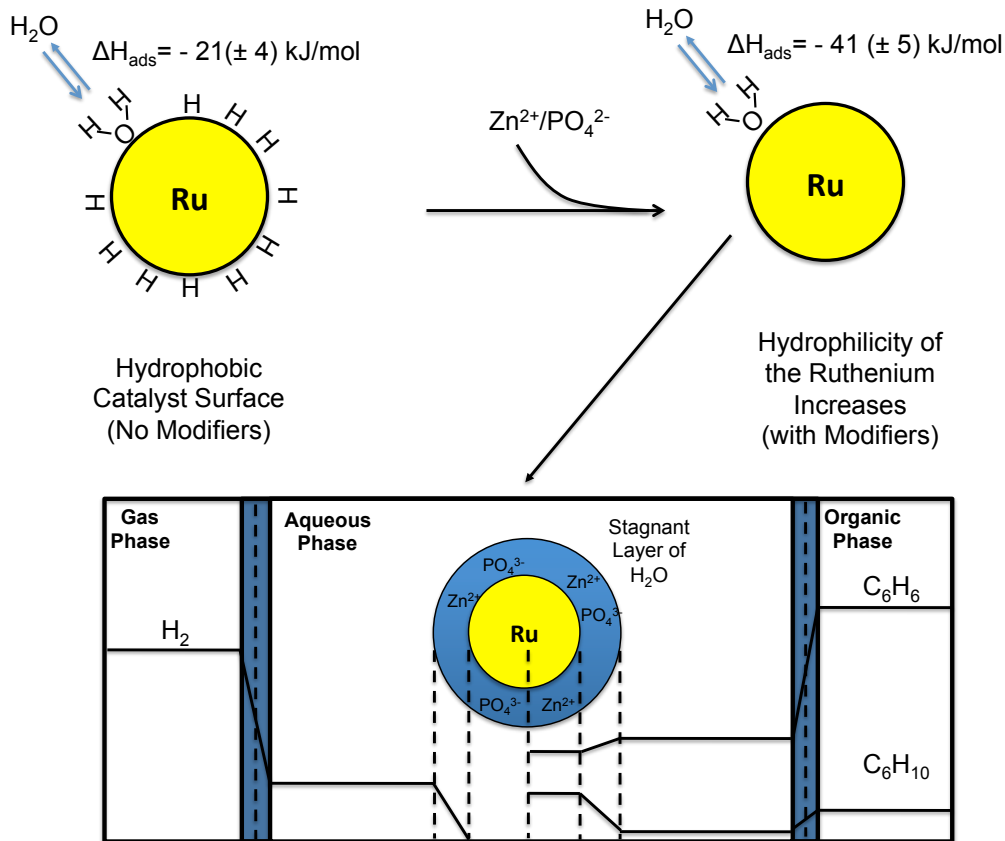


**Figure 4.1: The Fick's first law of molecular diffusion in a biphasic liquid catalytic system.**

Furthermore, Struijk et al. [5] reported that during the catalytic hydrogenation of benzene over a Ru catalyst in a water/benzene biphasic system, a significant increase in cyclohexene yield was observed when ionic salts ( $ZnSO_4$ ,  $Zn_3(PO_4)_2$ ) were dissolved in the aqueous phase (Figure 4.2). This result was attributed to the increase in surface hydrophilicity of the catalyst upon the addition of salt. This increase favored the physisorption of water molecules on the catalyst, which diminished the diffusion rate of cyclohexene towards the catalyst surface since its solubility on the stagnant water layer was also low. This explanation was based on mass transport analysis at the liquid-solid interface and experimental water microcalorimetry measurements on clean- and H-

saturated Ru surfaces. The diffusion study showed that the rate of hydrogen and cyclohexene transfer through the water layer was controlling the reaction rate, rather than the kinetics. The heat of adsorption of water on the H-covered Ru exhibited a decrease of  $\sim 20$  kJ/mol, which was attributed to an increase in the hydrophobicity of the Ru surface upon the adsorption of H.

Another important concept to analyze the effect of solvents in reaction rates was first presented by Boudart et al. [2], who showed that using transition state theory it is possible to capture the solvation effect of the solvent on the species involved in the rate-limiting step. They also proposed that when the rate-limiting step is the adsorption of the reactant, a fortuitous cancelation of activity coefficients occurs. As a result of this coincidence, the reaction rate became a function of the solubility of the reactant in the solvent. However, this direct proportionality between reaction rates and concentration in the liquid phase was an exception rather than a rule. In the general case, the rates of reaction are a function of the chemical potential of the reacting species, and consequently the solubility of the reactant in the given solvent does not affect the reaction rate. For example, Gonzo and Boudart [12] found that the turnover frequency of cyclohexene hydrogenation on Pd in the liquid phase was the same regardless of the nature of the solvent, when the solvent was not an aromatic. The situation becomes more complicated when catalyst deactivation and competitive adsorption of the solvent are not negligible, particularly with solvents with relatively high heats of adsorption. Also, complications to the analysis arise when the product readsorbs from the liquid phase and changes the fugacity of the species on the surface.



**Figure 4.2: Schematic illustration of the surface modification (top) observed upon addition of polarity modifiers (ZnSO<sub>4</sub>, Zn<sub>3</sub>(PO<sub>4</sub>)<sub>2</sub>) to ruthenium catalyst nanoparticles during the hydrogenation of benzene in liquid phase (bottom) [5].**

These, and many other examples found in the literature for heterogeneous catalytic reactions in condensed liquid phase, combined with our own experimental results (e.g., the concept of phase-selectivity), convince us that a deeper understanding of these systems is crucially important. In order to be able to fully utilize the potential benefits of phase-selectivity and reactive separation in bi-phasic systems catalyzed by particles at the liquid/liquid interface, a more detailed knowledge of the physical and chemical phenomena occurring in these thermodynamically non-ideal systems is required. Furthermore, such fundamental and comprehensive study will be a starting point for the future generation of detailed thermodynamics, kinetics and mass-heat

transport schemes, which can be directly implemented in reactor-level modeling and optimization software for specific industrial processes.

Our research group have recently shown that carbon nanotubes fused to oxide nanoparticles are able to stabilize emulsions, and when properly functionalized, catalyze reactions at the oil-water interface (i.e., liquid/solid/liquid interfacial catalysis). To catalyze hydrodeoxygenation and etherification reactions, a noble metal was anchored to the surface of the nanohybrid, and to catalyze condensation reactions a solid basic function was incorporated [13,14]. Although the use of interfacial catalysts has been reported in previous studies, they either used liquid surfactants to stabilize emulsions [15,16] or did not generate emulsions [17,18]. The advantage of the novel methodology is that the amphiphilic nanohybrids stabilize a high interfacial area, which results in higher conversions, and it does not require the use of a liquid surfactant that could not be separated from the reaction mixture. In contrast to homogeneous catalysts previously used, the recoverable solid stabilizes a water-in-oil emulsion and catalyzes reactions. This combination of heterogeneous and phase transfer catalysis presents several advantages: a) increased interfacial area, b) enhanced mass transfer of molecules between the two phases, c) simplified reaction / separation process by using a recoverable solid catalyst instead of surfactant, and d) effective separation of products from the reaction mixture by differences in the water-oil solubility (avoiding heating that leads to product decomposition) [14].

In this chapter, it is explored the application of another class of amphiphilic material, the so-called Janus nanoparticles, as interfacial catalyst emulsifiers. The tuneable surface properties of Janus nanoparticles have attracted attention for

applications as diverse as sensing, electronics, photonics, and drug delivery [19-24]. Moreover, they can stabilize emulsions more efficiently than homogenous solid particles. The compartmentalized surface of Janus nanoparticles displays two opposite sides with different wettability, which are known to stabilize emulsions effectively [25-32]. Here, we have combined the concepts of two-phase catalysis and the surface compartmentalization to maximize “*phase-selectivity*” of target reactions, i.e. achieve conversion only on one side of the emulsion. As a proof-of-concept, we have conducted the phase-selective hydrogenation of an aldehyde dissolved in the organic phase, while avoiding reaction of another aldehyde dissolved in the aqueous phase, a process with potential application in biofuel refining [33].

Also, it is presented the concept of phase-selective catalysis in the aqueous phase of a biphasic system [14]. In that case, we used Pd clusters deposited on the hydrophilic side of nanohybrids composed of carbon nanotubes and silica oxide. We indicated that it is challenging to selectively deposit a metal on the hydrophobic side because pristine nanotubes do not anchor metal particles as effectively as the oxide supports. Therefore, one of the goals of the present work is to achieve phase-selectivity in the organic phase, without conversion in the aqueous phase.

One can envision many cases in which oil-phase-selectivity will be desirable. For example, in biofuel refining it is desirable to combine the dehydration of sugars catalyzed by acid-base catalysts with the metal-catalyzed hydrogenation of the dehydrated product. If the hydrogenation catalyst used in a biphasic system has no preferential orientation at the interface, the dehydration of the sugar will compete with hydrogenation, resulting in a decreased yield. By contrast, in this work a phase-

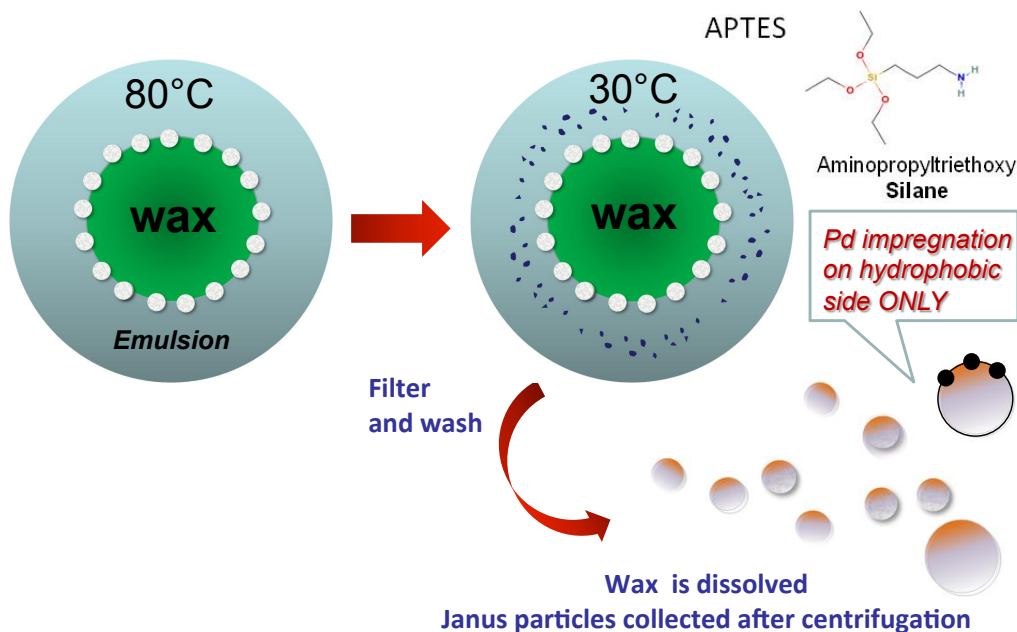


selective hydrogenation catalyst has been placed in the hydrophobic side and consequently, only the molecules stable in the organic phase can undergo hydrogenation. For comparison, we have tested two types of Janus particles. In one of them, the catalytic species are selectively anchored on the hydrophobic side while in the other they are deposited on both sides of the particle.

## **4.2. Experimental Section**

### *4.2.1. Synthesis of Janus Catalyst Nanoparticles*

The synthesis of the Janus silica-nanoparticles was based on the procedure described by Perro et al. [34] This procedure basically consists of preparing emulsions of paraffin wax and water, stabilized by silica particles. The silica used in our work was Aerosil 380 (provided by Evonik Industries AG), hydrophilic fumed silica with a surface area of 380 m<sup>2</sup>/g and a primary particle size of 7 nm. First, 1 g of silica was dispersed in a 150 ml solution of ethanol and water (6.7 % w/w), in which a surfactant (CTAB, hexacetyl trimethyl ammonium bromide, provided by Sigma Aldrich) with a molar concentration of  $9 \cdot 10^{-4}$  M (that is its critical micellar concentration [35]) was added to partially hydrophobize the silica particles. Then, in order to produce the emulsion of water and wax, the suspension of water and silica was heated up to 80 °C to assure that the wax (10 g) was completely melted when added to the suspension. The suspension was then sonicated with a horn sonicator (Fisher Scientific 600W, 20 kHz) for 30 min to produce the water/wax emulsion (Figure 4.3).



**Figure 4.3: Illustration of the synthetic approach for the preparation of the Janus catalysts using the masking technique.**

The emulsion was cooled down at room temperature. At this temperature, the wax particles solidify and kept the silica nanoparticles trapped on the surface of the wax. The side of the silica particles that was not covered by wax was functionalized with a solution of APTES (aminopropyltriethoxysilane, from Sigma Aldrich). These functional groups make this side of the silica particles hydrophobic. Specifically, the functionalization was conducted as follows; 150 ml of an aqueous solution of ethanol (6.7 wt. %), ammonium hydroxide (7 vol. %) and APTES was added to the suspension of silica particles and wax at room temperature. The amount of APTES added was calculated to obtain 15 functional groups per nm of the silica particles. The final mixture was stirred without any heating for 12 hours, and after that, it was filtered to separate the wax/silica particles. Finally, the wax was dissolved with dichloromethane and the Janus silica-nanoparticles were collected after centrifugation.

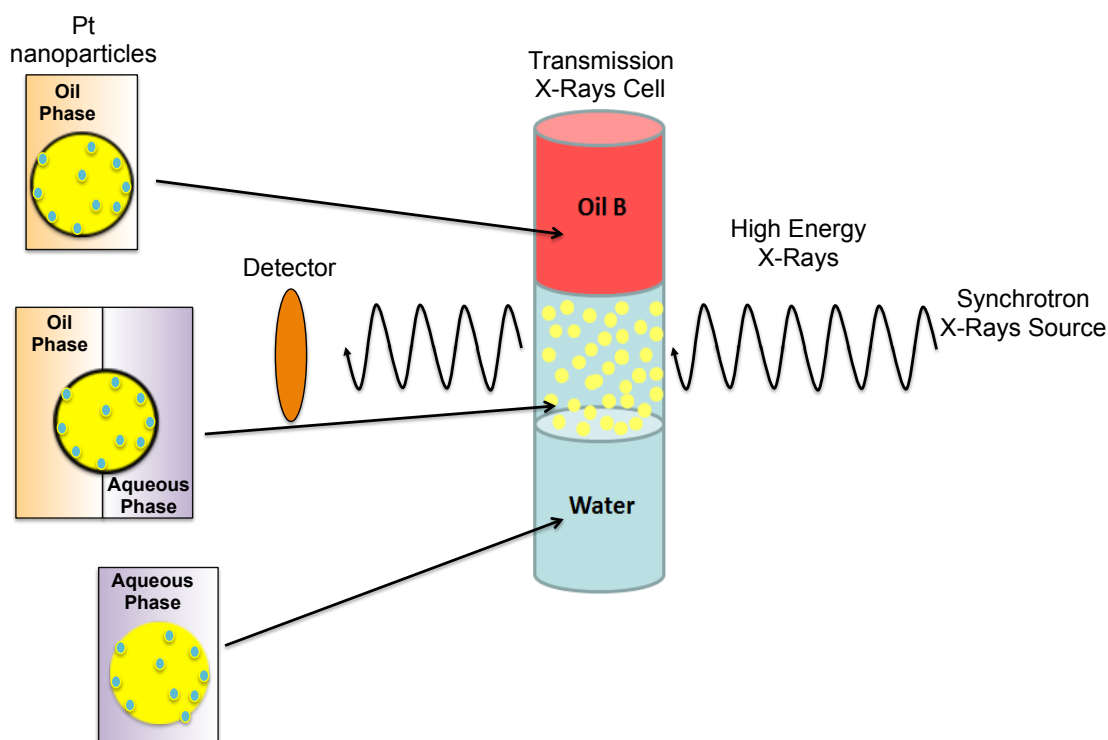
#### *4.2.2. Nanoparticles Characterization Techniques*

The Janus nanoparticles and nanohybrids were characterized by high-resolution transmission electron microscopy (HRTEM), Raman spectroscopy, and X-ray photoelectron spectroscopy (XPS). The HRTEM images were obtained on a JEOL JEM-2100 transmission electron microscope system. The Raman spectra were acquired on a Jovin Yvon-Horiba Lab Ram equipped with a charge-coupled detector and a He-Ne laser (632 nm) as excitation source. The XPS spectra were recorded on a Physical Electronics PHI 5800 ESCA system, equipped with an Al KR X-ray anode operated at 350 W and 15 kV. The base pressure of the main chamber was kept at about  $1.0 \times 10^{-8}$  torr.

#### *4.2.3. X-Ray Absorption Near de Edge (XANE) and Extended X-Ray Absorption Fine Structure (EXAFS) Characterization of hydrophobized Pt/NaX*

We conducted direct measurement of the surroundings of catalyst particles within the emulsion system. To date we have evidence from reaction selectivity that the Janus particles are oriented in a relatively rigid fashion at the emulsions liquid-liquid interface. However, there is no direct measurement of the degree to which the surface of the catalyst is covered with one of the emulsion liquids, or quantification of the coverage. X-ray absorption spectroscopy (XAS) offers a unique possibility to measure the amount of metal surface that is covered by aqueous vs. hydrophobic liquid within the emulsion. These studies will also allow us to connect to theory-based studies of the movement of amphiphilic particles in biphasic liquids. For this purpose we conducted experiments in the high-energy synchrotron in Argonne National Laboratories with the

collaboration of Dr. J. Miller. The emulsions stabilized with catalytic nanoparticles were characterized using a transmission liquid cell (Figure 4.4).

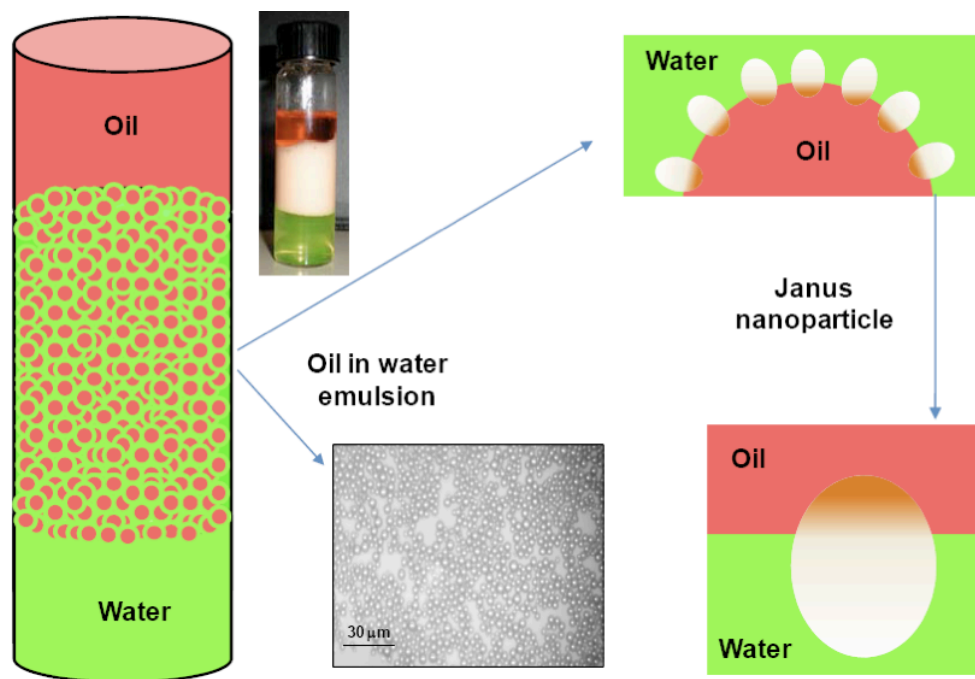


**Figure 4.4: X-Ray transmission cell for EXAFS and XANES characterization of nanoparticles-stabilized emulsions.**

#### *4.2.4 Preparation of Nanoparticles-Stabilized Emulsions*

In order to prepare the water/oil emulsions for characterization of the properties (type of emulsion, droplet size, etc) with the different nanohybrids, DI water and decalin were used as the aqueous and organic phases, respectively. The nanohybrids were first dispersed in the water phase by sonication with a Horn sonicator (Fisher Scientific 600W, 20 kHz) at 25 % of amplitude for 30 min. Then, decalin was added (water/decalin volume ratio =1) and the final mixture sonicated for 1 h. The amount of nanohybrids was varied as described above. A green water-soluble dye (fluorescent Na

salt) and a red oil-soluble (Sudan III) were added to the respective phases to identify the corresponding emulsion fractions (Figure 4.5).



**Figure 4.5: Schematic illustration of the three phases (oil/emulsion/water) present in the oil-in-water emulsions, together with a picture of a vial with the emulsion system and a microscopy image of the emulsion phase.**

#### *4.2.5. Catalytic Conversion of Aqueous- and Organic- Soluble Aldehydes in Nanoparticles-Stabilized Emulsions*

##### *4.2.5.1. Hydrogenation of Glutaraldehyde and Benzaldehyde and Octanal*

The hydrogenation reactions were carried out in a semi-batch Parr 4843 reactor of 50 ml. A detailed description of the reaction system can be found in a previous work of our group. In each experiment, 15 ml of DI water and 15 ml of decalin were placed into the reactor vessel with 30 mg of the catalyst. The mixture was sonicated for 15 min

using a Horn sonicator in order to produce the emulsion in-situ. Then, the reactor vessel was assembled in the reaction system.

After purging with N<sub>2</sub>, a 110 sccm flow of pure H<sub>2</sub> was passed through the reactor for 3 h at 100°C and 200 psi. Then, the temperature and pressure were adjusted to 100°C and 200 psi, respectively, before the reactant was injected. During the entire reaction period the flow of gases was kept constant at 110 sccm, while the liquid mixture was kept in the reactor with the use of a condenser that returns the vapors back to the vessel and minimize liquid loss. After 24 h, the reaction was stopped by turning off the heater and switching H<sub>2</sub> to N<sub>2</sub>. Once the reactor reached room temperature, it was taken apart and the content filtered, which caused the full recovery of the catalysts and the breaking of the emulsion in two clear liquid phases (aqueous and organic). The composition of each phase was analyzed independently by GC-FID and GC-MS. The initial concentration of reactants was 0.3 M glutaraldehyde in the water phase and 0.3 M benzaldehyde or Octanal in the oil phase (decalin).

In the case of organic-phase selective conversion two different catalytic systems were used. The first one using nanohybrids, in which the performance of a catalyst composed of 5 % wt. Pd on SWCNT/SiO<sub>2</sub> was compared with another a physical mixture (wt. ratio 1:1) of metal-free SWCNT/SiO<sub>2</sub> and pure SWCNT doped with 10 % wt. Pd. In the former, the Pd was deposited on the entire surface of the nanohybrids (on both SWCNT and silica) while in the latter the Pd particles were only deposited on the SWCNT. In order to deposit Pd, both SWCNT/SiO<sub>2</sub> and purified SWCNT were impregnated with the same procedure as described above for the catalysts used in the hydrogenation of phenanthrene. The drying and calcination conditions were also the

same. In the second, the hydrogenation activity of Janus silica nanoparticles with selectively deposited clusters of palladium in the hydrophobic face was compared with Janus catalysts with the metal deposited on the entire surface.

### **4.3. Results and Discussion**

#### *4.3.1. Characterization of Janus-Stabilized Emulsions and Pd/Janus Catalyst*

The synthesized Janus nanoparticles exhibited remarkable ability to stabilize oil-in-water emulsions using decalin as the organic phase. They produced similar or higher fractions of emulsion (up to 90 %) and smaller droplet sizes (1-7 mm) than those previously obtained with nanotubes/silica nanohybrids [13,14]. The stabilization of droplets of oil in water indicates that the interface is concave towards the oil, which is related to the higher extent of hydrophilic character of the particles [25,26,31].

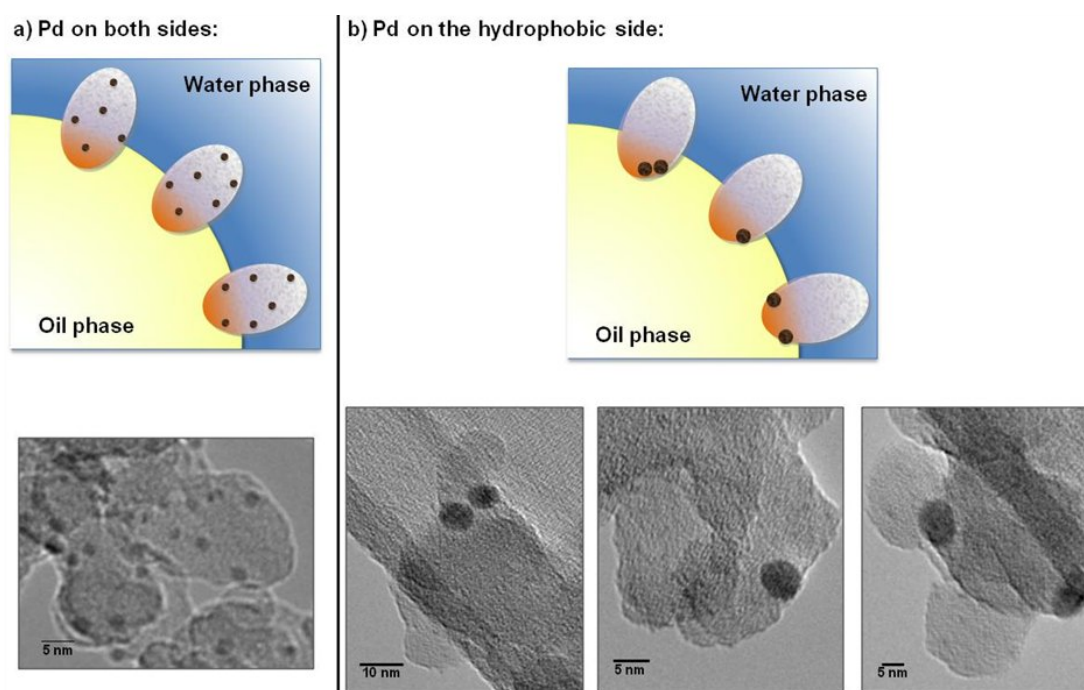
##### 4.3.1.1. HRTEM Characterization

###### 4.3.1.1.1. Janus Catalytic Nanoparticles (5 wt. % Pd/Janus Silica)

Once the Janus particles were synthesized, two different catalysts were prepared anchoring Pd on them. In the first one, Pd was deposited on the entire surface of the Janus particles, while in the second one, Pd was only deposited on the hydrophobic side.

High-resolution TEM images were obtained to characterize the products of the two different preparations. As shown in Figure 4.6, the differences are obvious. The first preparation (Figure 4.6.a) had Pd clusters distributed rather uniformly on the entire surface with an average particle size of 2.5 nm. The second preparation (Figure 4.6.b)

had a lower density of Pd particles, deposited on one side of each silica particle. In this case, the size of the Pd particles was larger, around 6 nm. The lower density and larger size of Pd clusters in the second preparation can be explained by: a) a smaller fraction of support surface available for Pd deposition, and b) a decreased anchoring ability of the silica support as a result of the functionalization, making sintering of the metal clusters more favourable during calcination.



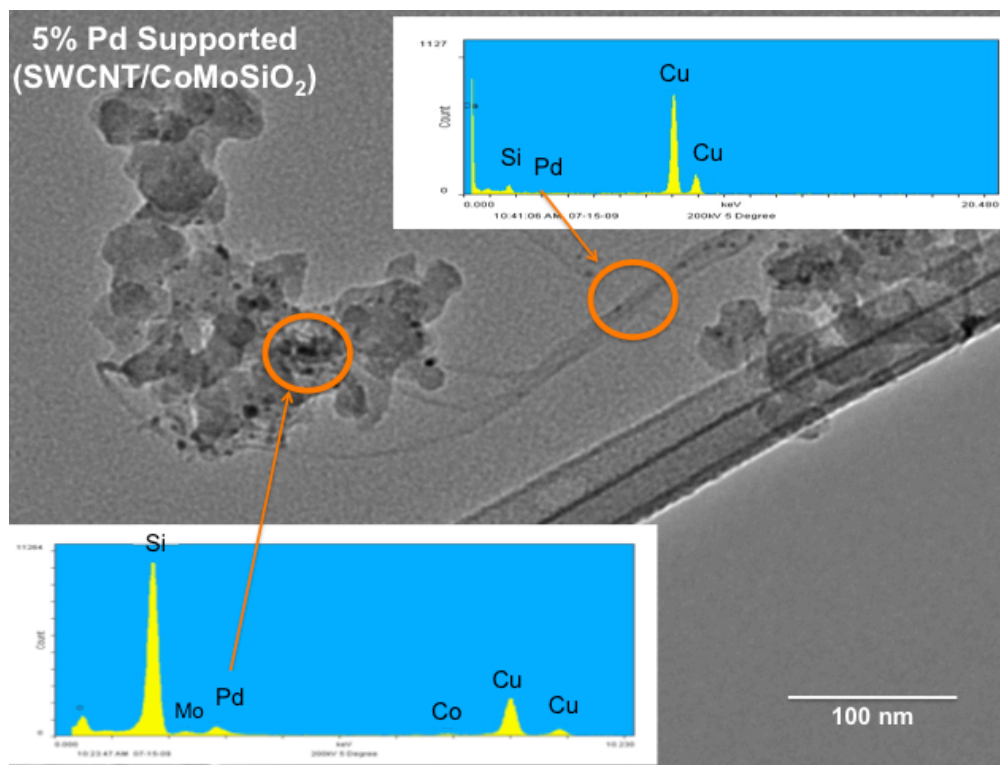
**Figure 4.6: HRTEM images of the Pd/Janus nanoparticles. a) Pd deposited on the two sides of the Janus nanoparticles; b) Pd selectively deposited on the hydrophobic side.**

#### 4.3.1.1.2. Nanohybrid Catalysts (5 wt. % SWCNT/SiO<sub>2</sub>)

HRTEM and Energy-Dispersive X-ray (EDS) spectroscopy were used to characterize the 5 wt. % Pd/SWCNT/SiO<sub>2</sub> nanohybrid catalysts. As shown in Figure 4.7 the cluster size of the palladium catalyst was around  $5 \pm 1$  nm, however, the particles



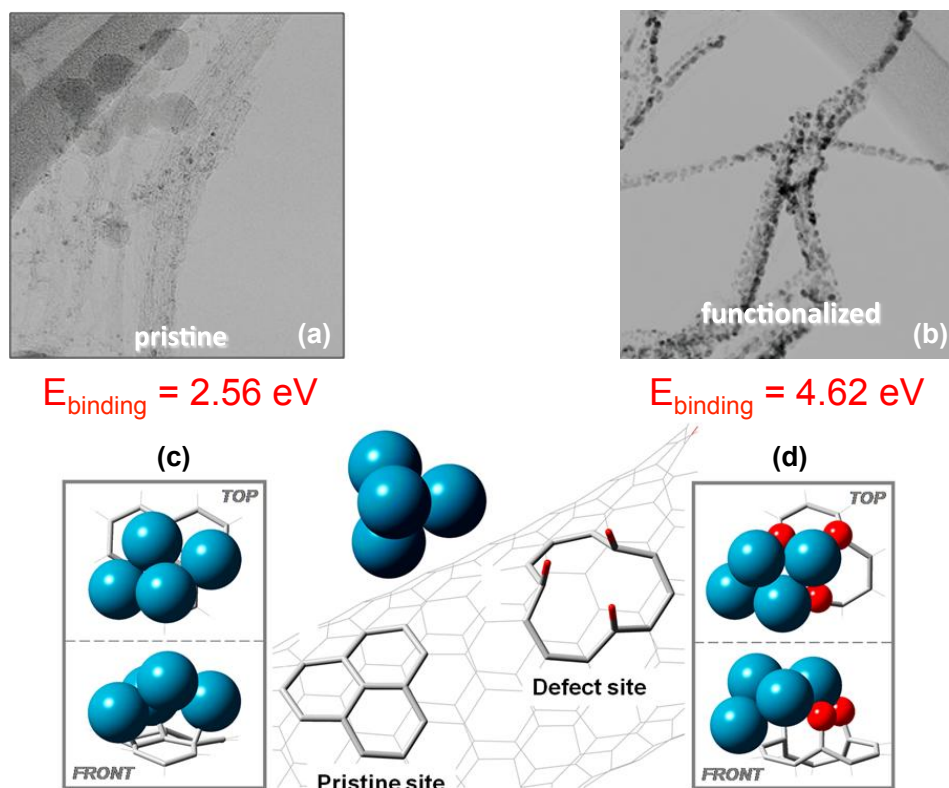
were distributed non-uniformly. In fact, the majority of the palladium nanoparticles were located on the metal oxide support rather than on the single walled carbon nanotubes. This is confirmed by the EDS spectra of the nano hybrids on the SWCNT and SiO<sub>2</sub>.



**Figure 4.7: HRTEM images of 5 wt. % Pd/SWCNT/SiO<sub>2</sub> and Energy Dispersive X-ray spectroscopy (EDS) of the palladium clusters deposited on the pristine SWCNT and silica.**

The results are in agreement with previously reported calculations by our research group of palladium clusters adsorbed on pristine and oxidized SWCNT Density Functional Theory (DFT) and HRTEM. In Figure 4.8 the results for pristine and oxidized SWCNT are presented, in which the binding energy of the palladium cluster increased from 2.56 to 4.65 eV upon oxidation of the SWCNT. The strong

interaction of the oxygen containing defects in the SWCNT and the palladium clusters is the responsible for high particle dispersion observed in the HRTEM [36].



**Figure 4.8: HRTEM and DFT calculations of Pd cluster on pristine SWCNT (a and c) and plasma treated SWCNT (b-d) [36].**

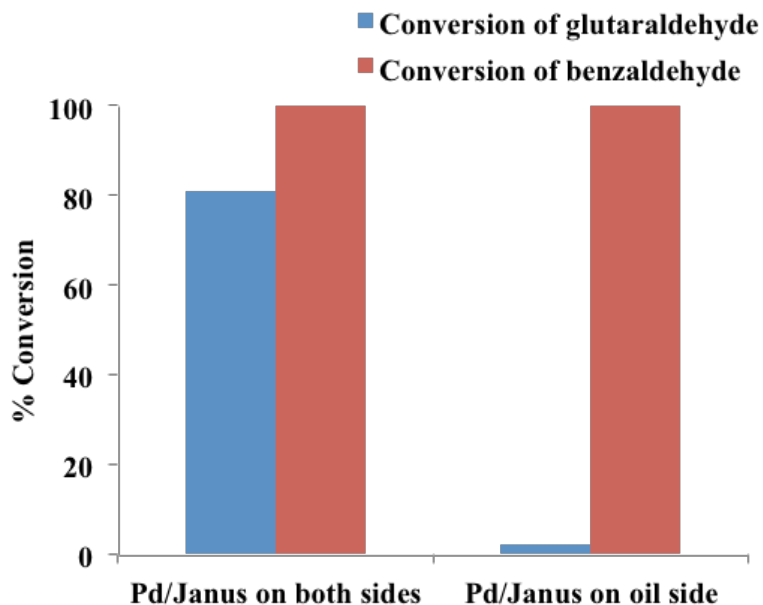
#### 4.3.2. Organic-Phase Selective Catalysis on Pd/Janus Catalysts

To investigate the concept of phase-selectivity in emulsion systems two aldehydes with different solubilities were chosen, benzaldehyde (oil-soluble) and glutaraldehyde (water-soluble). The contrasting solubilities allowed us to follow the evolution of the hydrogenation activity for each molecule, simultaneously and independently, in the organic and aqueous phases.

The reactants, benzaldehyde and glutaraldehyde, were dissolved in decalin and deionized (DI) water, respectively, before the emulsion was prepared. The concentration was 0.03 M for each aldehyde in each phase. The total volume of the biphasic liquid was 35 ml, keeping an equimolar water/decalin ratio.

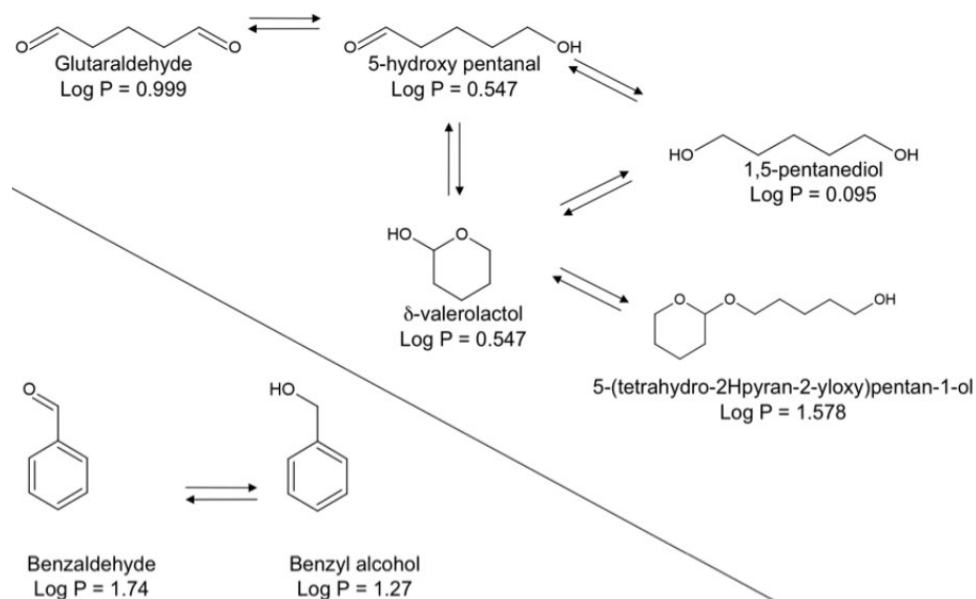
Two separate studies were conducted in the emulsion system. In the first run, the Janus catalyst with Pd loaded on both sides of the particles was used to convert the mixture; in the second run, the catalyst with Pd selectively loaded on the hydrophobic side was used. In each run, 30 mg of catalyst was loaded and the reaction time was 3 h.

As shown in Figure 4.9, the differences in behavior were dramatic. The total turnover number (TON) of the hydrogenation of benzaldehyde is 2800 for the catalyst with Pd on both sides and 1488 for the catalyst with Pd on the hydrophobic side. The resulting turnover frequencies (TOF) are 0.99 and 0.49 s<sup>-1</sup>, respectively, calculated based on HRTEM of the catalysts cluster size. When the catalyst contained Pd on both sides of the Janus particles, high conversion levels were obtained for both reactants, about 80 % for glutaraldehyde in the water phase and 100 % for benzaldehyde in the oil phase. However, when the catalyst had Pd selectively deposited on the hydrophobic side, the conversion of benzaldehyde was kept at 100 %, while the conversion of glutaraldehyde decreased to 2 %, demonstrating high phase-selectivity.



**Figure 4.9: Aldehyde conversion in a semi-batch reactor at 100 °C. Left: Pd deposited on the two sides of the Janus nanoparticles; Right: Pd selectively deposited on the hydrophobic side.**

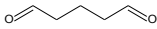
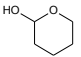

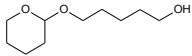
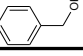
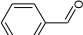
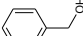
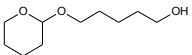
The possible hydrogenation products from each aldehyde are summarized in Figure 4.10, along with the simplified reaction network. Benzaldehyde hydrogenation only produces benzyl alcohol. As shown in Table 4.1, while benzaldehyde only appeared in the organic phase, its product, benzyl alcohol partitioned between the two phases, in a ratio that did not vary with the catalyst used.



**Figure 4.10: Reaction network and corresponding products for the hydrogenation of glutaraldehyde (top) and benzaldehyde (bottom) catalyzed by Pd.**

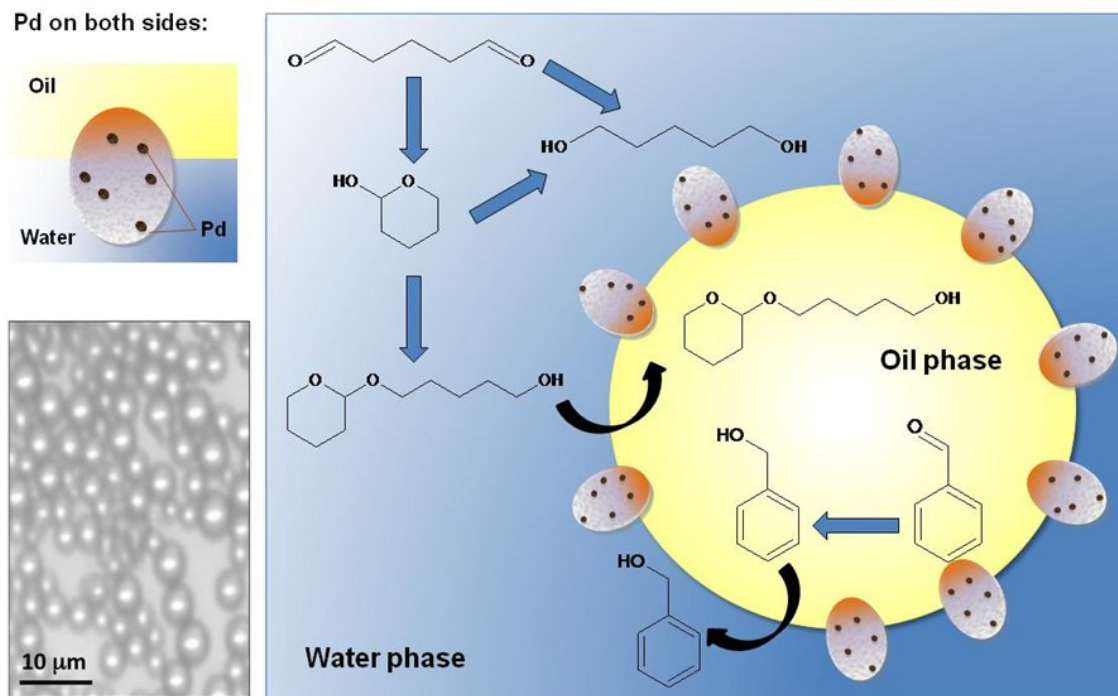
On the other hand, as summarized in Table 4.1, a number of products were obtained from glutaraldehyde. By inspecting the distribution of products between the two phases, an interesting analysis of the reaction/phase migration processes can be made. While glutaraldehyde only appears in the aqueous phase, some of its products distribute between the two phases.

**Table 4.1: Phase composition (before and after reaction). Hydrogenation of aldehydes catalyzed by Pd/Janus nanoparticles at the oil/water interface of the emulsion.**

Phase	Compound	Composition (moles)		
		Before Reaction	After reaction	
			Pd on Janus (Only oil side)	Pd on Janus (Both sides)
Water		1.05E-03	1.03E-03	1.99E-04
		0.00	2.15E-05	3.39E-04
		0.00	0.00	5.07E-04
		0.00	0.00	1.89E-06
		0.00	5.47E-04	5.87E-04
		1.05E-03	1.60E-03	1.63E-03
Oil		1.05E-03	0.00	0.00
		0.00	5.03E-04	4.63E-04
		0.00	0.00	6.10E-07
		1.05E-03	5.03E-04	4.64E-04

The expected primary product from the hydrogenation of the first carbonyl group, 5-hydroxypentanal, was not observed. By contrast, the cyclic hemiacetal,  $\delta$ -valerolactol, was observed as a major product, together with the fully hydrogenated 1,5-pentanediol when Pd was only on the hydrophilic side. An interesting product that is observed in lower yields is the ether 5-(tetrahydro-2H-pyran-2-yloxy)pentan-1-ol. As shown by Van Der Burg et al. [37], alcohols and aldehydes can form ethers on metal surfaces. In this specific case, it appears that  $\delta$ -valerolactol and 5-hydroxypentanal form the ether in the aqueous phase; and, after forming, this long ether partitions between the organic and aqueous phases with higher concentration in the oil.

The network of reactions and transport is schematically illustrated in Figure 4.11, together with a microscopy image of the type of emulsions stabilized by these Janus catalysts.



**Figure 4.11: Microscopy image of the oil-in-water emulsion produced with the Janus particles together with an schematic illustration of the hydrogenation reactions taking place at the water/oil interface catalyzed by Pd clusters supported on both sides of the Janus nanoparticles. At the beginning of the reaction, glutaraldehyde is present in the aqueous phase and benzaldehyde in the oil phase.**

To investigate the effect of varying droplet size and interfacial area on the resulting conversion we have conducted two reaction runs varying the number of Janus particles while keeping constant the amount of catalyst. It has been previously shown [1,13,14,19] that increasing the particle concentration causes a decrease in droplet size and a consequent enhancement in interfacial area. Therefore, in the first run, we used 30 mg of the catalyst of 5 % Pd deposited on the hydrophobic side of the Janus particles, and in the second one we mixed 30 mg of this catalyst with 30 mg of pristine Janus particles.

The benzaldehyde conversion obtained in each run, together with the observed droplet size and interfacial area are shown in Table 4.2. We observe that, while the

interfacial area per mass of nanoparticles slightly decreases in the second run, the total interfacial area increases by almost a factor of two. By contrast, the resulting benzaldehyde conversion does not increase, but rather decreases almost by the same factor as the drop in specific interfacial area. This loss in activity could be due to the aggregation of particles near the interface, which makes the access of the catalytic particles to the interface less effective.

**Table 4.2: Conversion of benzaldehyde, droplet size and interfacial area in the systems prepared with different particle concentrations.**

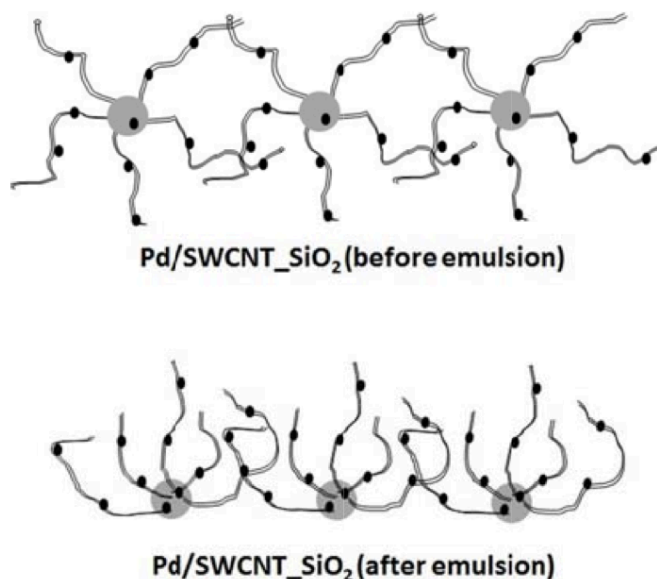
Catalyst	Droplet Size ( $\mu\text{m}$ )	Interfacial area ( $\text{m}^2$ )	Specific Interfacial area ( $\text{m}^2\text{g}^{-1}$ part.)	Benzaldehyde Conversion
5 wt. % Pd/ Janus oil side	9.4	2.2	73	88 %
5 wt. % Pd/ Janus oil side + Janus (ratio 1:1)	6.4	4.1	68	77 %

#### 4.3.3. Organic-Phase Selective Catalysis on Pd/SWCNT/SiO<sub>2</sub> Nanohybrids

Further characterization of the interface using XPS has been performed. A catalyst composed by Pd anchored on SWCNT/SiO<sub>2</sub> was analyzed, before and after being used to stabilize an emulsion. In the first case, the catalyst was analyzed directly after its preparation, while in the second case it was first used to stabilize a water-in-oil (decalin) emulsion, and then vacuum-dried and the remaining catalyst particles were analyzed. Figure 4.12 illustrates the expected morphology of the catalyst aggregates in both cases. When the catalyst was used to stabilize the emulsion, we expected that the carbon nanotubes on the nanohybrids particles preferentially orient towards the oil



phase (Figure 4.12), with more metal particles facing the surface than in the absence of the interface.



**Figure 4.12: Illustration of Pd/SWCNT/SiO<sub>2</sub> before and after emulsion.**

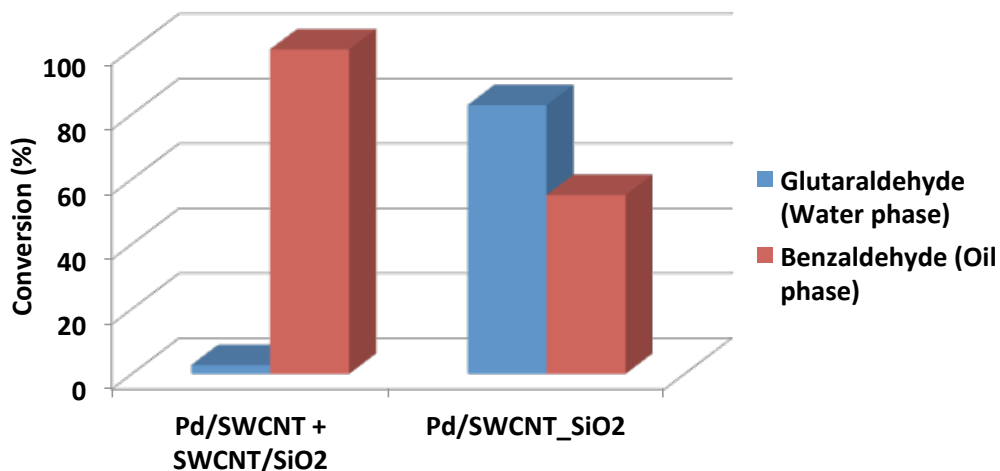
The previous observations are in accordance with the results obtained by XPS (Table 4.3), showing a higher intensity ratio of C/Si and Pd/Si when the catalyst has been used to stabilize the emulsion (20.8 and 15.4x10<sup>-2</sup>, respectively), in comparison with the initial catalyst (6.9 and 5.2x10<sup>-2</sup>, respectively).

**Table 4.3: C/Si and Pd/Si Intensity ratios obtained from the XPS analysis of the dried Pd/SWCNT/SiO<sub>2</sub> and Pd/SWCNT/SiO<sub>2</sub> in emulsion.**

Catalysts	Atomic Ratios	
	C/Si	Pd/Si (x10 <sup>-2</sup> )
Pd/SWCNT/SiO <sub>2</sub> (dried)	6.9	5.2
Pd/SWCNT/SiO <sub>2</sub> (in Emulsion)	20.8	15.4

The simultaneous hydrogenation of glutaraldehyde (water-soluble) and benzaldehyde (oil-soluble) has been studied in an emulsion system. Two different catalysts have been used as stabilizers/catalysts in these reactions to test the concept of phase-selectivity. One of the catalysts was a 5 % wt. Pd on SWCNT/SiO<sub>2</sub> and the other was a physical mixture of metal-free nanohybrids (SWCNT/SiO<sub>2</sub>) and silica-free 10 % wt. Pd/SWCNT (wt. ratio 1:1). In this mixture, the hydrophobic Pd/SWCNT remains in the oil side, but the strong tube-tube interaction keeps them at the water/oil interface, connected to the amphiphilic nanohybrids. Therefore, this system results in efficiently dispersed Pd catalyst, but located only on the organic phase. On the contrary, in the Pd-SWCNT/SiO<sub>2</sub> the metal is deposited over the entire support, i.e. on the hydrophobic as well as hydrophilic sides. Therefore, this catalyst should be able to catalyze reactions in the two phases of the emulsion. However, we cannot expect that the amount of Pd on the SWNT will be as high as on the silica, since during the incipient wetness impregnation, the metal precursors tends to deposit more on the oxide support than on the pristine (non-functionalized) SWCNT.

The conversions of glutaraldehyde and benzaldehyde obtained with the two different catalysts after 3 h of reaction at 100°C and 200 psi of H<sub>2</sub>, are shown in Figure 4.13. First, it is noted that the conversion of the organic-soluble benzaldehyde is 100 % when Pd is only in the oil phase and 55 % when Pd is present in the two phases. As mentioned above, a larger fraction of Pd deposits on the oxide than on the SWCNT, which explains the lower conversion obtained when Pd is distributed between the two parts of the nanohybrid.



**Figure 4.13: Conversion of glutaraldehyde and benzaldehyde obtained in the hydrogenation reactions over two different catalysts; the former composed of a mixture of SWCNT/SiO<sub>2</sub> nanohybrids and Pd deposited on purified SWCNT (Pd present only in the oil phase), and the latter composed of Pd deposited on SWCNT/SiO<sub>2</sub> nanohybrids (Pd present in both phases).**

The behavior observed with the water-soluble glutaraldehyde under the same conditions was, as expected, opposite to that of benzaldehyde. That is, the conversion was 83 % when the catalyst with Pd deposited on the two sides of the nanohybrids was employed, but less than 3 % when the catalyst with Pd only deposited on the hydrophobic side was present. The phase-selective catalysis in the organic phase is clearly demonstrated in these experiments.

The final composition of both phases after these reactions is summarized in Table 4.4. The reaction network and corresponding products for the hydrogenation of glutaraldehyde catalyzed by Pd can be found in our previous report. As can be observed in Table 4.4, the hydrogenation of benzaldehyde only produced benzyl alcohol. It is worth noting that, while benzaldehyde only appeared in the organic phase, benzyl alcohol partitioned between the two phases (logP values are 1.740 and 1.270, respectively).

**Table 4.4: Product composition (%) obtained in the hydrogenation reactions over two different catalysts; the former composed of a mixture of SWCNT/SiO<sub>2</sub> nanohybrids and Pd deposited on purified SWCNT (Pd present only in the oil phase), and the latter composed of Pd deposited on SWCNT/SiO<sub>2</sub> nanohybrids (Pd present in both phases).**

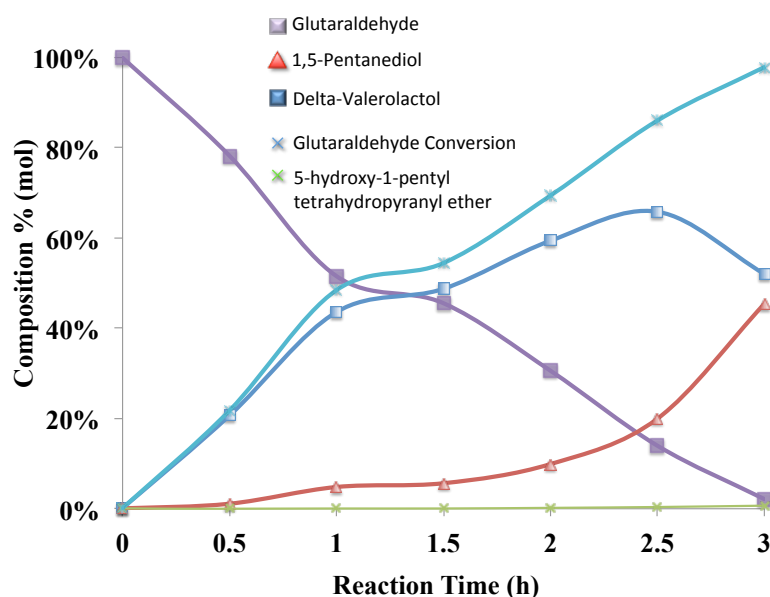
Phase	Molecules	Pd/SWCNT + SWCNT/SiO <sub>2</sub>	Pd/SWCNT/SiO <sub>2</sub>
Water Phase	glutaraldehyde	69.6	11.8
	δ-valerolactol	1.9	20.6
	1,5-pentanediol	0.0	35.6
	5-(tetrahydro-2H-pyran-2-yloxy) pentan-1-ol	0.0	0.1
	benzyl alcohol	28.5	31.9
	benzaldehyde	0.0	70.0
	benzyl alcohol	100.0	29.1
Oil Phase	5-(tetrahydro-2H-pyran-2-yloxy) pentan-1-ol	0.0	0.9

On the other hand, as summarized in Table 4.4, different products were obtained from the hydrogenation of glutaraldehyde. When Pd was present on the hydrophilic side (high conversion of glutaraldehyde), the cyclic hemiacetal, d-valerolactol, was observed as the main product, together with the fully hydrogenated 1,5-pentanediol. Another product observed in lower yields when Pd was present in the hydrophilic side, was the ether 5-(tetrahydro-2H-pyran-2-yloxy)pentan-1-ol. Our group has recently shown that alcohols and aldehydes react on Pd to form ethers. In this case, it seems that d-valerolactol and 5-hydroxypentanal readily form the ether in the aqueous phase, which tends to partition between the organic and aqueous phases ( $\log P = 1.578$ ). By contrast, both d-valerolactol and 1,5-pentanediol remained in the aqueous phase due to their high solubility in water ( $\log P$  values are 0.547 and 0.095, respectively).

#### 4.3.4. Aqueous-Phase Selective Catalysis on Pd/SWCNT/SiO<sub>2</sub> Nanohybrids

We next explored the reactivity of molecules that were exclusively soluble in either the organic or aqueous phase. Octanal and glutaraldehyde were chosen as the model compounds soluble in the decalin and water phases, respectively. In one of them, octanal and glutaraldehyde were partitioned in an equimolar mixture of water and decalin. In the other two, octanal and glutaraldehyde were separately dissolved in pure decalin and pure water, respectively. These molecules were readily hydrogenated over Pd to the corresponding alcohols. However, the nanohybrids that were used in this case had the metal preferentially deposited on the hydrophilic side. Therefore, we anticipated seeing a greater effect on the conversion of glutaraldehyde. Indeed, although only 58% conversion was obtained in the single aqueous phase after 3 hours at 100°C, practically all (98%) of the glutaraldehyde was converted in the emulsion under the same conditions. This enhancement can be ascribed to a combination of selective deposition of Pd on the polar silica as well as the increased exposure of the catalyst at the interface, as compared with the highly aggregated state of the solid catalyst suspended in the one-phase system. Although 5-hydroxypentanal was the expected primary product from the initial hydrogenation of one of the carbonyl groups in glutaraldehyde, this product was not observed. Instead, the cyclic hemiacetal, valerolactol, emerged as a major product. We suspect that the cyclization of the hydroxyaldehyde occurs via attack by the nucleophilic oxygen of the alcohol at the carbonyl carbon, which is analogous to the well-known cyclization of glucose [38].

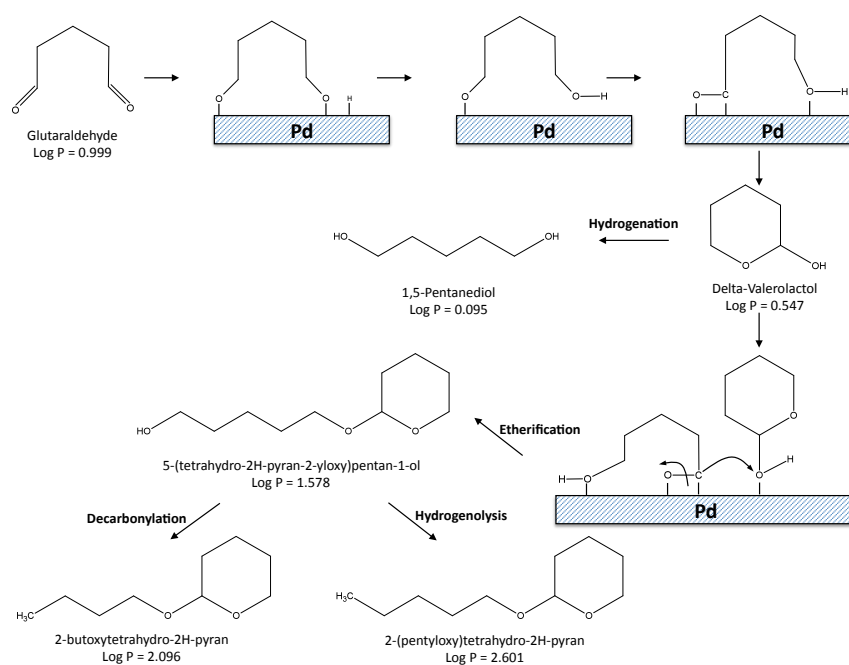
The time evolution of the products (Figure 4.14) indicates that the reaction sequence is glutaraldehyde  $\rightarrow$   $\delta$ -valerolactol  $\rightarrow$  1,5 pentanediol, with the diol dominating at long reaction times. An additional product, 5-hydroxy-1-pentyl tetrahydropyranyl ether, was also observed, but in low yield (< 2%). Whereas glutaraldehyde, octanediol, and valerolactol remained in the aqueous phase, the ether migrated to the decalin phase. This is an example that illustrates the potential of the method by which one can easily separate an intermediate product from the reaction mixture even when it is obtained at low yield before it continues reacting.



**Figure 4.14: Evolution of products and reactant concentration with the reaction time in the experiments performed with glutaraldehyde over 5 wt% of Palladium supported on SWCNT grown on silica oxide at 100°C.**

At higher temperature, the ether underwent decarbonylation or hydrogenolysis before leaving the aqueous phase, producing 2-butoxytetrahydro- 2H-pyran or 2-pentyloxytetrahydro-2H-pyran, respectively (Figure 4.15). In good agreement with the

very high log P values of these two products, they were observed exclusively in the oil phase, once again demonstrating the concept of separation after re- action. This result shows that one could arbitrarily modify selectivity by controlling the relative rates of reaction and migration out of the phase in which the catalyst is located. Analogous to shape-selectivity in zeolites [39] and selectivity affected by mass transfer phenomena [40], we can intro- duce the concept of a phase-transfer selectivity, by which the product distribution resulting from reactions catalyzed at the liquid/liquid interface is modified by the transport to and through the interface, where the catalyst resides. One could design emulsion systems with varying characteristics (such as droplet size, emulsion type, and relative solubilities) that may affect the residence time of intermediate products in one phase before it migrates to the other phase. This controlled migration may in turn affect the extent of reaction of one specific intermediate.



**Figure 4.15: Putative reaction mechanism of glutaraldehyde etherification over the palladium surface.**

Because very little Pd was present on the hydrophobic side, in the case of the octanal reaction we observed the opposing result: an activity enhancement in the pure organic phase relative to the emulsion. The octanol yield on the single phase was 9.1%, whereas that in the emulsion was only 2.3%. We ascribe this outcome to the larger proportion of Pd deposited on the hydrophilic oxide than on the hydrophobic nanotubes, as shown by means of HRTEM. The direct hydrogenation of octanal in the organic phase yielded 1-octanol as the (expected) dominant product, together with a small quantity of the symmetric dioctyl ether derived from alcohol coupling.

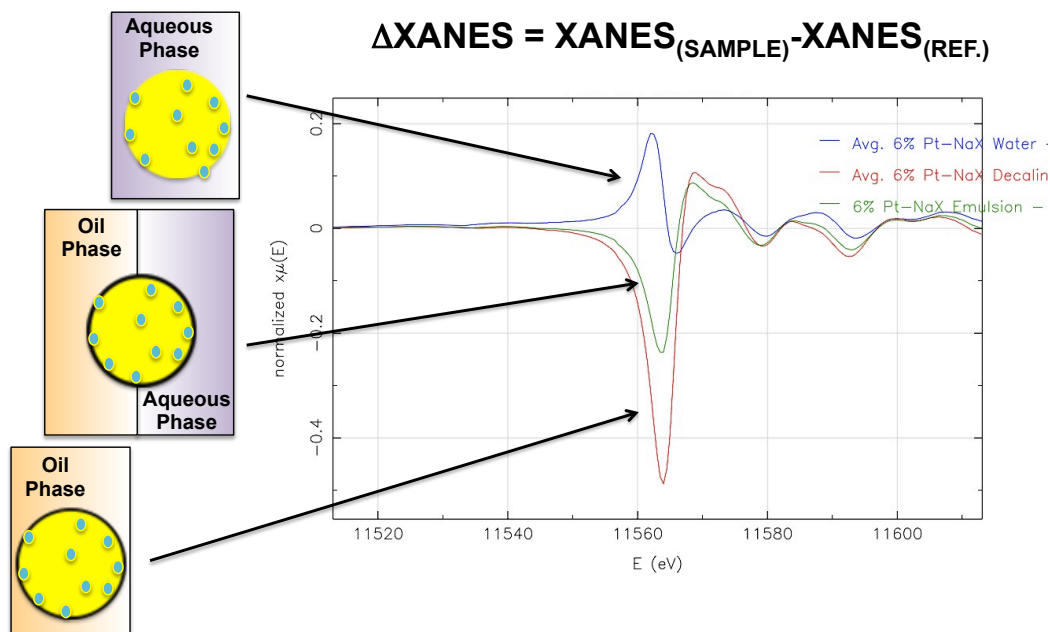
#### *4.3.5. Extended X-ray Fine Structure (EXAFS) Characterization of Pt on hydrophobic NaX zeolite Catalyst*

To our knowledge no-one has done *operando* studies (i.e., *in-situ* with simultaneous monitoring of a reaction) to couple spectroscopic measurements at the liquid-liquid-solid interface during catalytic tests with catalyst synthesis, structure and chemistry in order to understand the fundamental relationships between the catalyst selectivity and activity to its chemical environment.

In-situ XANES were conducted at Argonne National Lab (in collaboration with Dr. Jeff Miller, EXAFS/XANES expert) together with catalytic test of the previous mentioned catalyst in order to monitor molecular interactions of the reacting species at the liquid-liquid-solid interface with the chemistry of the catalyst and its environment. Such strategy has not been previously used to characterize reactive systems in emulsions stabilized by amphiphilic catalyst particles (e.g. Janus particles and



CNT/MeO<sub>x</sub>). As illustrated in the difference XANES spectra of the L<sub>III</sub> Pt edge (Figure 4.16) a dramatic change in difference spectra can be observed depending on the environment surrounding the Pt particle. Such capability allowed us to determine not only whether the catalytic cluster (e.g. Pt, Au, etc.) is in contact with water or oil, but it may even be possible to quantify what fraction each is in each phase under specific conditions. Similar observations were reported by J. Miller et. al [41], which make us believe that these results are an indication that it is possible to perform XAS of Pt nanoclusters supported on Janus catalysts in water-oil emulsions. As shown in Figure 4.16 the DXANES of the Pt L<sub>III</sub> spectra of Pt supported on NaX zeolites dispersed water, as well as Pt on NaX hydrophobized in decalin and emulsion. When the catalyst is aqueous environment the white line shifted towards lower binding energies, while in the case of emulsion and oil phase the shift is to higher binding energies, in clear agreement with previously reported data [41]. This is a clear indication that using XAS it is possible to identify the chemical environment of the catalysts in nanoparticle-stabilized emulsions. Further experiments under reaction conditions are required in order to correlate the catalytic activity and selectivity to the XAS information.



**Figure 4.16: Pt L<sub>III</sub> DXANES spectra from 11.54 to 11.6 keV of 5 % wt. Pt/NaX in Water, decalin and 5 % wt. Pt/NaX-C18 at 25°C.**

#### 4.3.6. Hydrophobic Catalyst Nanoparticles with Polar-Selective Catalytic Activity

In zeolites and microporous catalytic materials the size and shape of molecules is exploit to control the diffusion towards the active site. This property is particular useful in the conversion of small hydrocarbons into high-octane gasoline in crude oil refining. Molecular sieves are also widely used industrially in the selective removal of impurities from gaseous streams (i.e. CO<sub>2</sub>, H<sub>2</sub>O, CH<sub>4</sub>). More recently, application of micro-porous materials has been expanded to the conversion of biomass-derived molecules for the production of renewable chemicals and fuels. In many of these strategies the reactants are molecules with high polarity and low vapor pressure due to the oxygen functionalities. Hereby, polar solvents are required to solvate these species during catalytic conversion, in which zeolites are prone to deactivation by hydrolysis of the Si-OH groups on the microporous structure. Our research has reported recently

reported that in hot condensed water the stability of faujasite HY zeolites is remarkably enhanced by hydrophobization of the external surface with octadecyltrichlorosilane (OTS) functional groups, while untreated zeolites rapidly deactivated.

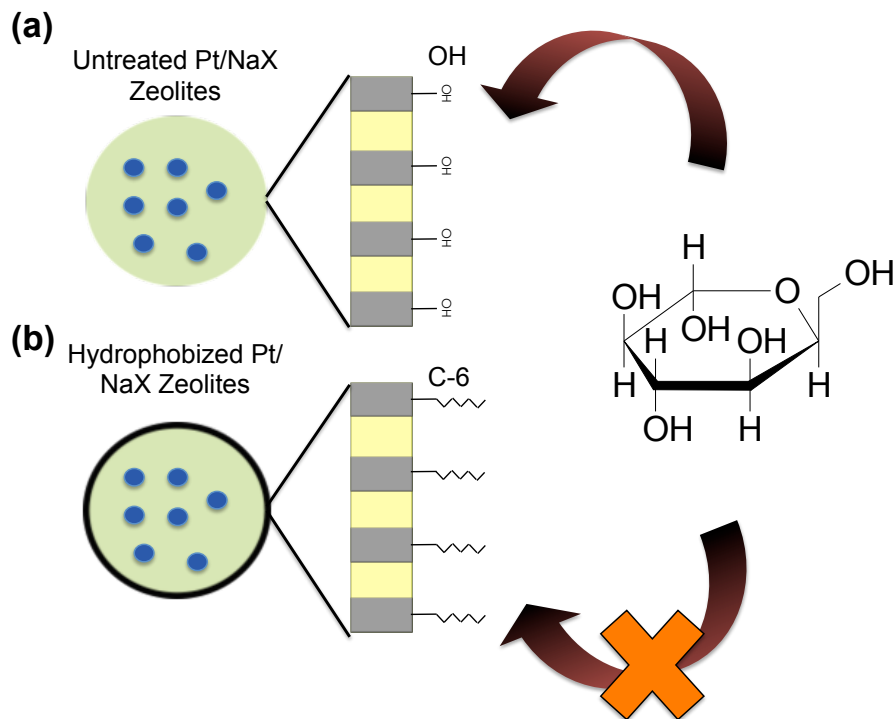
An interesting application of the hydrophobic functionalization is the selective control of the diffusion of molecules towards the catalyst surface based on their polarity. For instance, in the gasification of biomass CO and H<sub>2</sub> are accompanied by a significant amount of impurities. In order to use the bio-syngas Fischer-Tropsch (FT) synthesis an expensive conditioning of the gas phase products is required to remove sulfur-, nitrogen-, and oxygen- containing molecules can poison the transition-metal catalysts used in the FT reaction. Typically, these highly deactivating molecules have elevated polarity or polarizability, hence if the transition metal catalyst nanoparticles are anchored inside a porous material functionalized in the external surface with hydrophobic groups that can limit the diffusion of these polar species, then the catalyst lifetime could be dramatically enhanced.

To test the concept we conduct a series of rigorous experiments in aqueous environments for the isomerization of glucose (highly polar bio-derived molecule) using a NaX and HY zeolites with three different types of surface wettabilities, including: hydrophilic (CsNaX/NaX), amphiphilic Janus (NaX-APTES), and hydrophobic (NaX-C18, HY-APTES, and HY-MAPTMS). As expected the isomerization of glucose to fructose is significantly lower on the hydrophobic and amphiphilic catalysts, with values varying from 2 to 8 % conversion, while in the hydrophilic NaX and CsNaX the conversion was around 15 to 19 %, respectively (Table 4.5).

**Table 4.5: Activity of Hydrophilic/Hydrophobic and Amphiphilic catalysts for the glucose Isomerization in aqueous environment. Mass of catalyst 200 mg and 100 °C. Initial glucose concentration 10 wt. % and 600 rpm of agitation.**

Catalyst Surface Polarity	Catalysts	Glucose Conversion (%)	Fructose Selectivity (%)	Carbon Balance (%)
<b>Hydrophilic</b>	CsNaX	15.2	94.2	93.2
	NaX	19.9	94.2	94.2
<b>Amphiphilic</b>	Janus NaX	7.6	90.3	99.4
	NaX-C18	2.1	52.0	99.0
<b>Hydrophobic</b>	HY-APTES	4.67	79.99	89.9
	HY-MAPTMS	6.61	99.28	88.4

This dramatic drop in the catalytic activity of the hydrophobic and amphiphilic Janus catalysts is a clear indication that the surface functional groups effectively hindered the diffusion of glucose molecules to the active sites (Figure 4.17). Although, further experiments are required to test the concept in more complex systems in which sulfur and nitrogen poisoning is a major cause of catalyst deactivation, these proof-of-concept experiments showed that a reduction in the rate of isomerization is caused upon functionalization of the external surface of the microporous catalyst. The major question that needs to be answered is if this reduction in the molecular diffusion is due to the polar-non-polar repulsion or steric hindrance at the pore entrance caused by these bulky functional groups, i.e. smaller pore size entrance.



**Figure 4.17: Polarity-controlled conversion of polar molecules using a) hydrophilic catalysts and b) hydrophobic functionalized zeolites.**

In summary, proper functionalization on the catalyst surface with these hydrophobic functionalities offers remarkable opportunities for the design of ultra-stable catalysts for reactions in aqueous environments, in which catalyst stability and selectivity can be precisely tailored based on the hydrophobicity/hydrophilicity balance (HHB) of the catalyst surface.

#### 4.4. Conclusions

In the present contribution we have shown that by tailoring the location of the active sites in either the hydrophilic or hydrophobic side of the catalyst it is possible to selectively react molecules at the liquid-liquid interface based on their solubility, a concept that called “phase selectivity”. While it is well known that reaction rates are

only a function of the chemical potential of the reacting molecules, rather than their concentration, in this system we have exploited mass transport limitations to control the rates of reaction at the liquid-liquid interface using the differences in solubility of the reacting molecules. A detailed study of this concept was accomplished by comparing hydrogenation reaction rates of organic-soluble and aqueous soluble aldehydes in water-oil emulsion. For instance, aqueous phase selectivity was accomplished by anchoring Pd clusters on SWCNT/SiO<sub>2</sub> in which the weak interaction of the metal nanoparticles with the pristine SWCNT enabled the preferential distribution of the catalyst in the hydrophilic metal-oxide. In this case only reaction of the aqueous soluble probe molecule (glutaraldehyde) was observed, while the conversion in the organic phase (octanal) was negligible. Meanwhile, organic phase selectivity was achieved by selective deposition of palladium clusters on the hydrophobic side of Janus particles. In this example, only conversion of the organic-soluble molecule (benzaldehyde) was achieved. In contrast, when the metal nanoparticles were deposited on the entire surface of the Janus particles both the organic-soluble (benzaldehyde) and aqueous soluble (Glutaraldehyde) molecules underwent the hydrogenation.

The preliminary studies of polarity-controlled diffusion have been performed using NaX zeolites with different surface wettabilities for the catalytic isomerization of glucose to fructose in aqueous phase. For instance, we have observed that when catalyst surface have been extensively hydrophobized partially hydrophobized Janus NaX the conversion of glucose were rather lower when compared to the values obtained with the untreated NaX. This dramatic drop in the catalytic activity of the hydrophobic and

amphiphilic Janus catalysts is a clear indication that the surface functional groups effectively hindered the diffusion of the highly polar glucose molecules to the active sites

In summary, we have demonstrate that proper functionalization catalyst surface with hydrophobic functionalities offers remarkable opportunities for the design of ultra-stable catalysts for reactions in aqueous environments, in which catalyst stability and selectivity can be tailored based on the hydrophilic/hydrophobic balance (HHB) of the catalyst and the location of the active sites on the surface.

## References

- [1] R.J. Madon and E. Iglesia, *J. Mol. Catal. A Chem.* 163 (2000) 189.
- [2] R.J. Madon, J.P. O'Connell and M. Boudart, *AIChE J.* 24 (1978) 904.
- [3] S. Mukherjee and M.A. Vannice, *J. Catal.* 243 (2006) 108.
- [4] S. Mukherjee and M.A. Vannice, *J. Catal.* 243 (2006) 131.
- [5] J. Struijk, M. d'Angremond, W.J.M. Lucas-de Regt and J.J.F. Scholten, *App. Catal. A* 83 263.
- [6] L. Gilbert and C.I. Mercier, *Stud. Surf. Sci. Catal.* 78 (1993) 51.
- [7] J.T. Wehrli, A. Baiker, D.M. Monti, H.U. Blaser and H.P. Jalett, *J. Mol. Catal.* 57 (1989) 245.
- [8] H.U. Blaser, H.P. Jalett and J. Wiehl, *J. Mol. Catal.* 68 (1991) 215.
- [9] R.L. Augustine, *Adv. Catal.* 25 (1976) 56.
- [10] P.G.J. Koopman, H.M.A. Buurmans, A.P.G. Kieboom and H. Bekkum, *Recl. Trav. Chim. Pays-Bas*, 100 (1981) 156.
- [11] L. Cerveny and V. Ruzicka, *Catal. Rev.-Sci. Eng.* 24 (1982) 503.
- [12] E.E. Gonzo and M. Boudart, *J. Catalysis* 52 (1978) 462.
- [13] M. Shen and D.E. Resasco, *Langmuir* 25 (2009) 10843.
- [14] S. Crossley, J. Faria, M. Shen and D.E. Resasco, *Science* 1 (2010) 68.
- [15] H. Lü, J. Gao, Z. Jiang, F. Jing, Y. Yang, G. Wang and C. Li, *J. Catal.* 239 (2006) 369.
- [16] H. Lü and C. Li, *Chem. Commun.* (2007) 150.
- [17] H. Nur, S. Ikeda and B. Ohtani, *J. Catal.* 204 (2001) 402.



- [18] S. Ungureanu, H. Deleuze, M. I. Popa, C. Sanchez and R. Backov. *Chem. Mater.* 20 (2008) 6494.
- [19] R. Stadler, C. Auschra, J. Beckmann, U. Krappe, I. Voigt and L. Leibler, *Macromolecules* 28 (1995) 3080.
- [20] H. Takei and N. Shimizu, *Langmuir* 13 (1997) 1865.
- [21] S. Forster and M. Antonietti, *Adv. Mater.* 10 (1998) 195.
- [22] Y. Liu, V. Abetz and A.H.E. Muller, *Macromolecules* 36 (2003) 7894.
- [23] A.G. Vanakaras, *Langmuir* 22 (2006) 88.
- [24] O. Cayre, V. Paunov and O.D. Velev, *Chem. Commun.* 18 (2003) 2296.
- [25] B.P. Binks and P.D.I. Fletcher, *Langmuir* 17 (2001) 4708.
- [26] B.P. Binks and S.O. Lumsdon, *Phys. Chem. Chem. Phys.* 1 (1999) 3007.
- [27] T.N. Hunter, R.J. Pugh, G.V. Franks and G.J. Jameson, *Adv. Colloid Interface Sci.* 137 (2008) 57.
- [28] S. Arditty, C.P. Whitby, B.P. Binks, V. Schmitt, and F. Leal-Calderon, *Eur. Phys. J. E* 11 (2003) 273.
- [29] R. Aveyard, J.H. Clint and T.S. Horozov, *Phys. Chem. Chem. Phys.* 5 (2005) 2398.
- [30] P. Kralchevsky, I. Ivanov, K.P. Ananthapadmanabhan and A. Lips, *Langmuir* 21 (2005) 50.
- [31] B.P. Binks, *Curr. Opin. Colloid Interface Sci.* 7 (2002) 21.
- [32] B.P. Binks and J.A. Rodrigues, *Angew. Chem. Int. Ed.* 44 (2005) 441.
- [33] J.N. Chheda, G.W. Huber and J.A. Dumesic, *Angew. Chem. Int. Ed.* 46 (2007) 7164.

- [34] A. Perro, S. Reculosa, S. Ravaine, E. B. Bourgeat-Lami and E. Duguet, *J. Mater. Chem.* 15 (2005) 3745.
- [35] J. Giermanska-Kahn, V. Laine, S. Arditty, V. Schmitt and F. Leal-Calderon, *Langmuir* 21 (2005) 4316.
- [36] T. Prasomsri, D. Shi and D.E. Resasco, *Chem. Phys. Lett.* 497 (2010) 103.
- [37] A. Van Der Burg, J. Doornros, N. J. Kos, W. J. Ultee and V. Ponc, *J. Catal.* 54 (1978) 243.
- [38] R. Brückner, in *Advanced Organic Chemistry: Reaction Mechanisms* (Academic Press, New York, 2002), pp. 283–285.
- [39] N.Y. Chen, W.W. Kaeding and F.G. Dwyer, *J. Am. Chem. Soc.* 101 (1979) 6783.
- [40] E. Iglesia, *Appl. Catal. Gen.* 161 (1997) 59.
- [41] N. Guo, B.R. Fingland, W.D. Williams, V.F. Kispersky, J. Jelic, W.N. Delgass, F.H. Ribeiro, R.J. Meyer and J.T. Miller, *Phys. Chem. Chem. Phys.* 12 (2010) 5678.

## Chapter 5:

### Amphiphilic Nanohybrid Catalysts for Reactions at the Water/Oil

#### Interface in Subsurface Crude Oil Reservoirs

##### 5.1. Introduction

Production from large oil fields is many times stopped when extraction becomes uneconomic, even though a significant fraction of the original oil in place (OOIP) has not yet been recovered [1]. Development of alternative techniques to economically recover higher amounts of oil is an important challenge for engineers and researchers working in the oil industry. The incorporation of chemicals into the oil well as part of Enhanced Oil Recovery (EOR) strategies has been investigated for several decades [2].

Recently, researchers have started to evaluate the potential impact of nanotechnology in subsurface reservoir characterization and oil recovery [3-5]. In addition to the traditional phenomena, involving capillary, viscous, and gravitational forces, researchers are investigating the role of nanoscale interactions (electro-steric effects) in reservoir operations. It is believed that nanotechnology has potential for transforming the modeling and application of chemical EOR. As an example of these activities, researchers have proposed the use of nanoparticles to modify wettability of porous media, which would alter the interaction between the rock and the fluids increasing oil recovery (e. g. by increasing the relative permeability of the oil) [6]. In addition, the use of nanoparticles to reduce the oil-water interfacial tension (IFT) and enhance the recovery of oil was experimentally tested [7]. It has been showed that, by using a combination of nanoparticles and an anionic surfactant the decrease in the IFT was 70% greater than the values obtained using the surfactant alone. Moreover, they

tested the same combination of particles and surfactant in packed beds, obtaining an increase in the oil recovery of 10% OOIP compared to the surfactant flooding without particles. Other authors are investigating nanoparticles as contrast agents for the detection of the water/oil interface in the reservoir and visualization of residual oil [3].

Two major variables that may have a direct impact in the EOR process and can be modified by the addition of different chemicals and particles are the capillary number ( $N_c$ ) and the mobility ratio (MR) [8]. The capillary number  $N_c = v\mu/\sigma$ , where  $v$  is the Darcy velocity (fluid flux per unit of area),  $\mu$  the viscosity of the mobilizing fluid (water), and  $\sigma$  the interfacial tension (IFT) between the oil and the water. Typical values of  $N_c$  are around  $10^{-7}$  after water flooding [1]. The injection of surfactants to reduce oil-water IFT has been practiced for more than 35 years [2,9]. Surfactants formulations based on alcohols dissolved in polyglycoside are generally very effective for enhancing oil recovery. In addition to decreasing the oil-water IFT, emulsifiers act as stabilizers of the interface, leading to a greater interfacial area and a decrease in the capillary forces that act on the oil inside the pores [10]. Both, wettability and entry pressure requirements affect the displacement of oil by water. When the rock is water-wet, spontaneous imbibition of the rock displaces oil from the pores. In addition, if during drainage the pressure gradient exceeds the required entry pressure (proportional to oil-water IFT) for the water, the displacement of oil from larger pores can be achieved at lower pressure gradients by decreasing the IFT [11].

The mobility ratio ( $MR = (k_w/k_o)/(m_w/m_o)$ ) is a function of the relative permeability ( $k_i$ ) of the porous media towards oil and water, respectively, and the viscosity ( $m_i$ ) of the oil and the mobilizing fluid (water), respectively. To achieve

displacement of the oil by the water, MR must be lower than unity [12]. This condition can be obtained by increasing the sweeping fluid's viscosity relative to that of the oil, since a high  $\mu_w/\mu_o$  is favorable for oil displacement [13]. The effectiveness of different polymers depends on their chemical structure, their interaction with the surfactants and alkalis used for IFT reduction, as well as their impact on apparent viscosity. Hydrolyzed polyacrylamide and Xanthan gum are examples of polymers that have been widely studied for EOR applications. The rheology of the aqueous solutions of these polymers when combined with anionic surfactants and alkali was investigated, and the authors found that by using adequate concentrations viscosities as high as 210 cP could be reached [14].

Oil-in-water (O-in-W) emulsions can be produced by addition of surfactants, which can improve the mobility of the oil by increasing the sweep efficiency. By changing the oil/water ratio and the salinity of the water, different emulsion types (either O-in-W or W-in-O) can be obtained. The rheological and interfacial properties are affected by these changes, which may result in enhanced oil recovery and variations in pressure drop, as measured in sand pack flood studies [15]. Effect of pore blocking and diversion of injection fluids caused by addition of silica nanoparticles have been investigated in multi-phase flow experiments in core floods. It has been observed that even though particles may propagate through sandstone cores, an addition of polymers usually is required to effectively mobilize residual oil [16].

Silica nanoparticles have been widely studied as stabilizers of Pickering emulsions for different applications. In a series of articles, Binks et al. [17-25] have described systematic studies of the formation, stability, and structure of this type of

emulsions. They represent a novel alternative to conventional emulsions and may prove to be advantageous in subsurface oil reservoir applications due to their higher thermal and mechanical stability. By functionalizing the surface of the silica particles with silanol groups, the hydrophilic–lipophilic balance (HLB) of the particles can be adjusted, so the type of resulting emulsion (O-in-W or W-in-O) can be systematically changed. In contrast to regular emulsions stabilized by surfactant molecules, the stability of Pickering emulsions is greatly affected by a set of different parameters. They include composition of the organic and aqueous phases, contact angle among the water-solid-oil phases, particle size, particle concentration, and particle-particle interaction at the interface [17-25].

According to theoretical calculations, confirmed by experimental results, stable emulsions are formed when the particle size is within the range of 0.01 to 1.0  $\mu\text{m}$ . Outside this range, stability is hindered by either flocculation (when particles are too large) or Brownian motion (when particles are too small) [17,26,27].

The effectiveness of particles in stabilizing emulsion droplets is strongly dependent on the extent of particle-particle interactions. For example, water-wetted particles tend to stabilize oil-in-water emulsions, while oil-wetted particles stabilize water-in-oil emulsions. When they are mixed their stabilizing action is neutralized, leading to a rapid coalescence of the emulsion droplets. Such observation suggests that the strength of the rigid film of particles at the water/oil interface depends significantly on the particle-particle interaction, which ultimately affects the emulsion stability [28].

The composition of the oil and aqueous phases is also important in determining the type of emulsion because the surface of the particles is sensitive to the adsorption of

surface-active molecules that can change the hydrophilic-lipophilic balance or wettability of the particle, as well as the concentration of ionic species in the aqueous phase that can modify the electrostatic interaction between particles and, in consequence, their state of aggregation.

The particle concentration is another important parameter in Pickering emulsions, because it directly affects the volume fraction of emulsion, its stability, and droplet size [29-31]. Droplet size decreases with increasing particle concentration not only due to an increased interfacial area that accommodates more particles, but also due to the modification of rheological properties [32]. At low concentration of particles at the fluid-fluid interface the viscosity coefficients dominate the rheological parameters. However, at high concentrations, elastic contributions become significant due to particle-particle interaction. As a result, the fluid at the colloid-laden interface develops a viscoelastic or pseudoplastic behavior.

In a recent study, our research group demonstrated the stabilization of Pickering emulsions by nanohybrid particles composed of Single-Walled Carbon Nanotubes (SWCNT) and silica [33]. It was found that we could control the effective volume fraction of emulsion and the droplet size by adjusting the water/oil (W/O) ratio and the amount of nanohybrids. More recently, we further investigated the application of the concept to catalysis by incorporating active species on the surface of nanohybrids, which catalyze reactions at the oil-water interface [34]. Some of the reactions used to demonstrate the concept include metal-catalyzed hydrodeoxygenation and base-catalyzed aldol condensation of molecules with different solubilities, some water-soluble and some oil-soluble. The concept of “phase-selectivity” was put forward by

conducting hydrogenation on only one of the phases, while avoiding reaction in the other phase [35,36].

Among the different applications of these nanohybrids our research group have focused in subsurface reactions at the crude-oil-water interface for in-situ crude oil upgrading and catalytic EOR. In addition to the SWCNT/silica originally synthesized, different types of nanohybrids were compared. Multi-Walled Carbon Nanotubes (MWCNT) grown on alumina, onion-like carbon (OC) on silica, and Janus amphiphilic particles were found to be very effective in acting as emulsion stabilizers and catalyst supports. The Janus particles are di-symmetrically functionalized silica nanohybrids that present a structure containing a hydrophobic and a hydrophilic side [37]. We have recently investigated in detail the mobility of aqueous dispersions of these nanohybrids in porous media [38]. Mobility studies on glass beads and crushed Berea sand columns demonstrated that the synthesized nanohybrids successfully flow through porous media, particularly with the aid of small amounts of polymer (e.g. 500 ppm polyacrylamide, PAM). When the column was pre-saturated with oil, about half of the particles passed through the column while the other half remained trapped by the oil/water interface due to their amphiphilic properties. The effect of pH, salt, polymer and surfactant concentration was also studied and it was concluded that neither salinity nor pH have a significant effect on the stability or mobility of the dispersions. In contrast, the addition of surfactants improved the stability of the dispersions, but decreased the surface activity of the particles and the stability of the emulsions. Therefore, we can envision that this type of nanohybrids could travel in water flow through the porous media and reach the oil phase. At that point, they will preferentially locate at the oil/water interface



where, if properly loaded with an appropriate active species, they could act as catalyst for a given reaction.

## **5.2. Experimental Section**

### *5.2.1. Materials*

Nanohybrids of various characteristics were synthesized and used as supports for catalytically active species. Among the various nanohybrids investigated, SWCNT were grown on Co-Mo/SiO<sub>2</sub> catalysts using the CoMoCAT method developed by our group [39-41] and commercialized by Southwest Nanotechnologies Inc. (SWeNT). The as-produced SWCNT/silica are the original nanohybrids described in our previous work as novel emulsifiers and catalyst supports [33]. Variations of the same method resulted in nanohybrids with different characteristics. For example, MWCNT synthesized on an alumina support provided nanohybrids with a higher fraction of hydrophilic moieties. Moreover, a treatment with nitric acid was carried out on the MWCNT on alumina in order to increase the hydrophilic defects on the carbon nanotubes surface. Other carbon structures such as onion carbon were also deposited on silica supports. Finally, Janus-type amphiphilic particles were prepared by a method described by Perro et al. [37]. All of these nanohybrids have been previously used as support for catalytic species in recent studies of our group [34-36].

Different catalytic species (Pd, Cu, Cr, Co, and Fe) were impregnated on the various nanohybrids, using the corresponding nitrate salts (from Sigma Aldrich) as promoters of the metal catalysts. All the catalysts were produced by incipient wetness impregnation of the different supports (i.e., the different types of nanohybrids) with

aqueous solutions of the specific metal precursors (Cu, Pd and other nitrates). The samples were dried overnight at a temperature of 80 °C and then calcined in air at 250 °C for 3 hours.

Tetralin, decalin, and phenanthrene (from Sigma Aldrich) were used as both the oil phase in the oil-in-water (O-in-W) emulsions and as the reactant in the various reactions investigated. The water used in the study was purified by means of two Cole Parmer ion exchangers in series. Emulsions were prepared by ultra-sonicating the two liquid phases in the presence of the nanohybrids with a Fisher Scientific, 600 W, 20 kHz horn-sonicator, operated at an amplitude of 25%, as previously described [33].

#### *5.2.2. Reaction Studies*

Partial oxidation and hydrogenation reactions were carried out in a 50 cc stirred reactor (model Parr 4590), operating in semi-batch mode, with constant flow of gas (air and hydrogen, respectively) while the liquid was kept stirred in the reactor vessel. In each run, the selected amounts of oil, water, and nanohybrid catalysts were placed in the vessel. Then, the emulsion was formed as stated above and the reactor assembled. After this, the system was pressurized with N<sub>2</sub> and heated while stirring at 225 rpm. For the partial oxidation reactions, once the desired pressure and temperature were reached, the reaction time was measured from the start of the reactant gas (air) flow. For the hydrogenation reactions, a water/decalin emulsion stabilized by the catalytic nanohybrid was first formed in the vessel. After purging the lines with N<sub>2</sub>, the reduction of the catalyst was achieved by flowing 110 sccm of H<sub>2</sub> for 3 h at 200 psi and 100°C. Then,

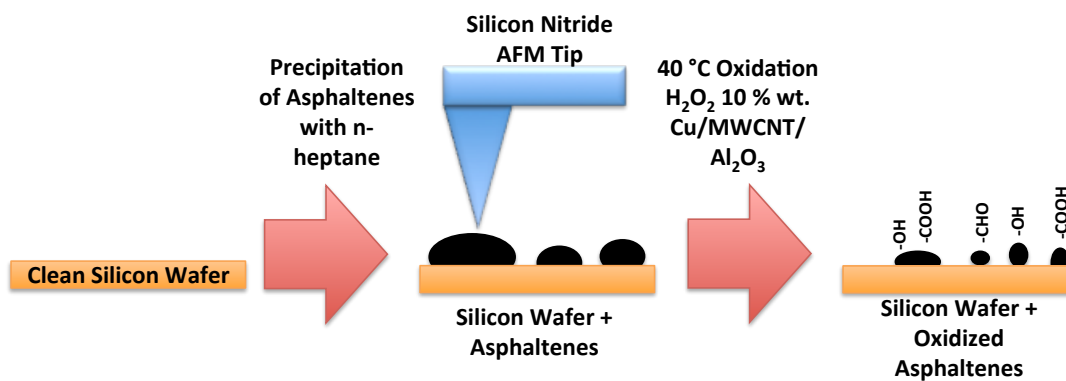
the pressure was adjusted to 900 psi and 200°C and the reaction time was measured from the injection of the substrate molecule (e.g., phenanthrene).

In both cases, after completing the desired reaction period, the system was cooled down, depressurized, and the product liquid filtered. Samples were taken from each phase for product quantification. Reaction products were analyzed in a gas chromatograph (Agilent 6890A series) with a Flame Ionization Detector (FID) using a capillary column (HP-Innowax with a length of 60 m) and a gas chromatograph-mass spectrometer (Shimadzu QP2010S). The interfacial tension between mixtures and pure compounds and water was measured on a drop shape analyzer (Minitec).

### *5.2.3 Catalytic Surface Wettability Modification*

Atomic force microscopy was used to characterize the surface topography as a result of catalytic modification of the surface wettability. First, a silicon wafer was cleaned with isopropanol and dried overnight at 80°C in a vacuum oven. After this the wafer was spin-coated with a thin film of heavy crude oil from the Panhandle oil and gas field (Texas, USA), which then was wash several times with n-hexane (> 98 wt. %, Sigma-Aldrich) to remove the light fractions of oil and leave a film of asphaltenes on the surface. Then, topography and surface wettability of the wafer-asphaltene was characterized by AFM and optical imaging before and after reaction of hydrogen peroxide (30 wt.%, Sigma-Aldrich) in the presence of 10 mg of nanohybrid catalyst 10 wt.% Cu/MWCNT/Al<sub>2</sub>O<sub>3</sub> at 40°C for 3 hours (Figure 5.1). The AFM images were recorded by an Agilent 5420 SPM/AFM equipped with a liquid-phase cell operating in acoustic mode using a silicon nitride tips with forces ~ 1 nN. The solid-gas-liquid

contact angles were measured from the solid-water interface to the water-air interface using Image J to process the pictures accurately.



**Figure 5.1: Experimental procedure for the surface topography characterization before and after catalytic oxidation of physisorbed asphaltenes.**

### 5.3. Results and Discussion

#### 5.3.1. Interfacially Active Nanohybrids

As previously shown [34-36], the use of nanohybrid particles as emulsion stabilizers and catalyst supports leads to several advantages:

(a) Higher activity is obtained for reactions occurring at the water/oil interface in biphasic systems due to the enhanced interfacial area;

(b) Reaction selectivity can be modified according to the solubility of the reactants in each phase;

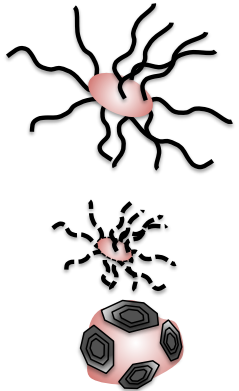

(c) Product separation is facilitated due to differences in solubility; and

(d) Catalyst recovery can be readily accomplished by filtration.

The present chapter deals with the partial oxidation and hydrogenation of probe molecules using nanohybrid catalysts. To this end, several nanohybrids have been used in the partial oxidation of tetralin: SWCNT/SiO<sub>2</sub>, MWCNT/Al<sub>2</sub>O<sub>3</sub>, Onion carbon/SiO<sub>2</sub>

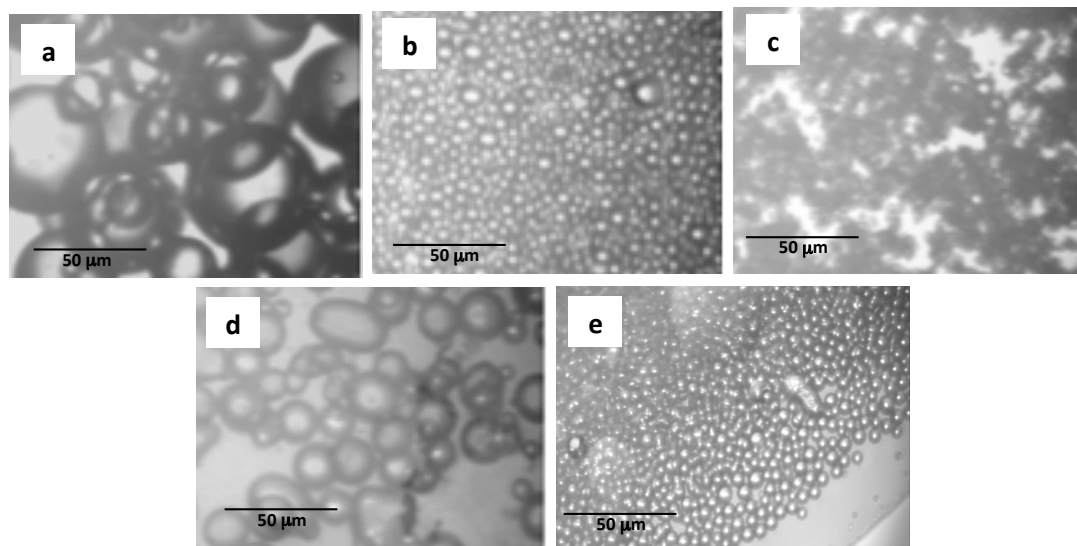
and Janus silica nanoparticles. For hydrogenation studies, Pd catalysts supported on nitric acid-functionalized MWCNT/Al<sub>2</sub>O<sub>3</sub> has been employed. Table 5.1 summarizes the characteristic features of the different nanohybrids, which have been tested for their ability to stabilize water/decalin emulsions. Figure 5.2 shows optical microscopy images of the emulsions produced with each one of the different nanohybrids at the same nanoparticle concentration of 3 mg/ml and a water/oil volume ratio of 1.

**Table 5.1: Schematic description of the different nanohybrids used as emulsion stabilizer and support of metal clusters.**

Type	Description	Schematic
Carbon / Oxide Nanoparticle Nanohybrids	(a) SWCNT/silica	
	(b) MWCNT/alumina	
	(c) Functionalized MWCNT/alumina	
	(d) Onion carbon/silica	
Janus Particles	(e) Partially-hydrophobized silica	

As it can be observed, there are clear differences in the emulsions; under the conditions studied, the emulsions stabilized with SWCNT/SiO<sub>2</sub> and onion carbon/SiO<sub>2</sub> present bigger droplets (35 and 15 mm of average size, respectively) than the ones stabilized with MWCNT/Al<sub>2</sub>O<sub>3</sub>, functionalized MWCNT/Al<sub>2</sub>O<sub>3</sub> and Janus silica particles (8, 2 and 4 mm, respectively). The emulsion fraction also varies, being lower for SWCNT/SiO<sub>2</sub> and onion carbon/SiO<sub>2</sub> (10 and 30 %, respectively) and reaching

values of 50, 85 and 90 % for MWCNT/Al<sub>2</sub>O<sub>3</sub>, functionalized MWCNT/Al<sub>2</sub>O<sub>3</sub> and Janus silica particles, respectively. Thus, among all the nanohybrids investigated, functionalized MWCNT/Al<sub>2</sub>O<sub>3</sub> are the most effective nanohybrids for stabilizing emulsions, with high emulsion fractions and the smallest droplet sizes.



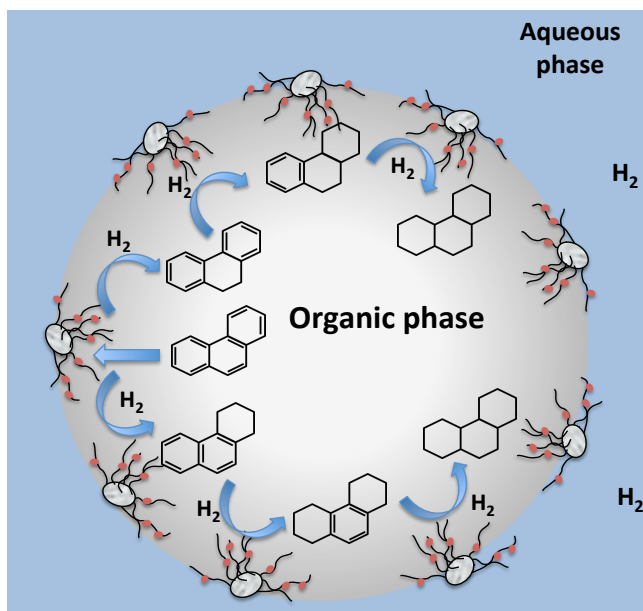
**Figure 5.2: Optical microscopy images of the water/decalin emulsions stabilized by different nanohybrids (see Table 1): (a) SWCNT/SiO<sub>2</sub>, (b) MWCNT/Al<sub>2</sub>O<sub>3</sub>, (c) Functionalized MWCNT/Al<sub>2</sub>O<sub>3</sub>, (d) Onion carbon/SiO<sub>2</sub> and (e) Janus silica nanoparticles.**

The type of emulsion formed also depends on which nanohybrid is used, i.e., water-in-oil for the SWCNT/SiO<sub>2</sub> and MWCNT/Al<sub>2</sub>O<sub>3</sub> emulsions, and oil-in-water for the other three nanohybrids. This dependence of the type of emulsion with the nanohybrid used is directly related to the hydrophilic/lipophilic balance in the nanohybrids. It is well-known that more hydrophilic particles are preferentially wetted by water, which makes the interface bend concavely towards the oil, producing oil-in-water emulsions, and viceversa [18,43,44]. Therefore, onion carbon/SiO<sub>2</sub> and Janus silica particles are more hydrophilic, while SWCNT/SiO<sub>2</sub> and MWCNT/Al<sub>2</sub>O<sub>3</sub> are more

hydrophobic due to their lower density of oxidized defects. The nitric acid treatment to the MWCNT/Al<sub>2</sub>O<sub>3</sub> creates hydrophilic defects on the carbon nanotubes surface, which makes the functionalized nanohybrids more hydrophilic and stabilizes oil-in-water emulsions under the conditions studied.

In summary, comparing the behavior of the different nanohybrids (emulsion fraction and droplet size), it can be concluded that the resulting interfacial area follows the sequence: functionalized MWCNT/Al<sub>2</sub>O<sub>3</sub> > Janus silica particles > MWCNT/Al<sub>2</sub>O<sub>3</sub> > onion carbon/SiO<sub>2</sub> > SWCNT/SiO<sub>2</sub>.

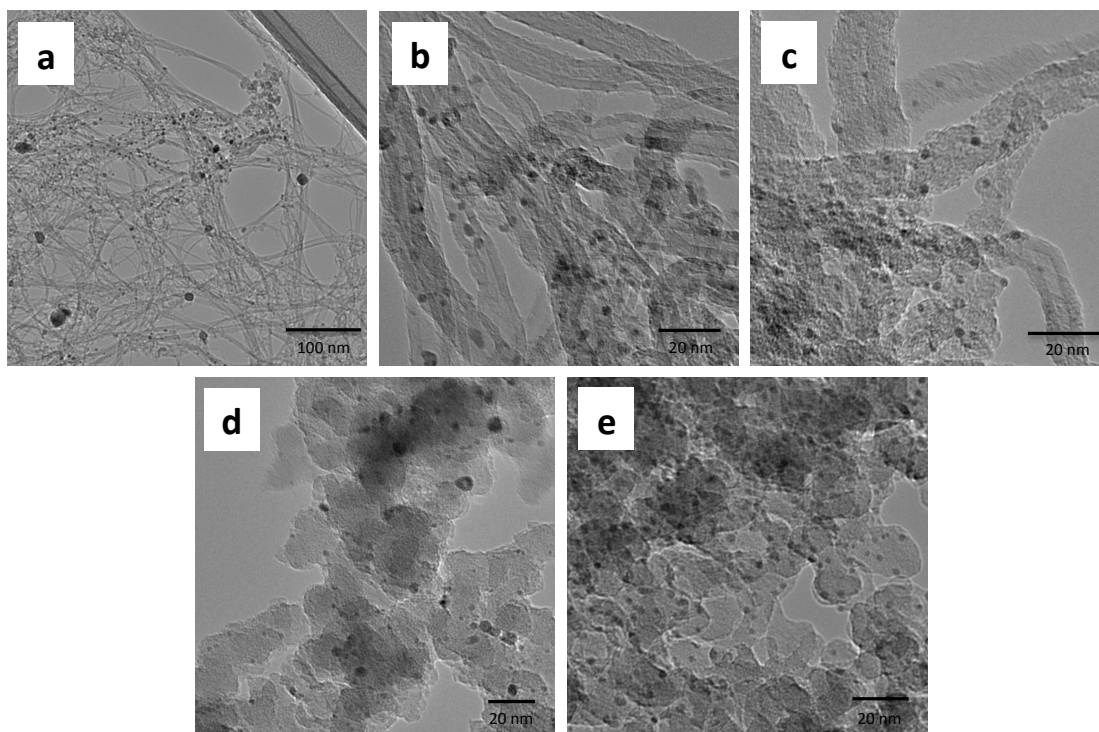
Once the effectiveness of the nanohybrids for stabilizing emulsions was demonstrated, metal particles were deposited on their surface to use them as catalysts for the partial oxidation of tetralin and the hydrogenation of polynuclear aromatics in emulsion systems. Figure 5.3 shows a schematic illustration of the hydrogenation of polynuclear aromatics at the water-oil interface in the nanohybrid-stabilized emulsions. In the case of carbon nanotube based-nanohybrids, we have shown in a previous study that the carbon nanotubes are oriented towards the organic phase, while the metal oxide nanoparticles remain closer to the aqueous phase [34].



**Figure 5.3: Schematic representation of the hydrogenation of phenanthrene at the water-oil interface in the nanohybrid-stabilized emulsions. The reactants and intermediate products are only soluble in the organic phase, while the hydrophobic part of the nanohybrids (CNT) contains most of the catalytically active species (Pd clusters).**

The type of nanohybrids used also affects the dispersion of the metal particles. Figure 5.4 shows TEM images of the different nanohybrid-supported Pd catalysts in this work. Although the catalyst preparation conditions were identical in all cases (incipient wetness impregnation of the aqueous solution of the metal precursor), the size of the metal cluster varied with the type of nanohybrids used as support. That is, the average sizes of the Pd cluster were 4.9, 4.6, 3, 2.5 and 2.1 nm, for SWCNT/SiO<sub>2</sub>, onion carbon/SiO<sub>2</sub>, MWCNT/Al<sub>2</sub>O<sub>3</sub>, Janus silica particles, and functionalized MWCNT/Al<sub>2</sub>O<sub>3</sub>, respectively. That is, the higher the density of anchoring sites on the support, the higher the metal dispersion is.

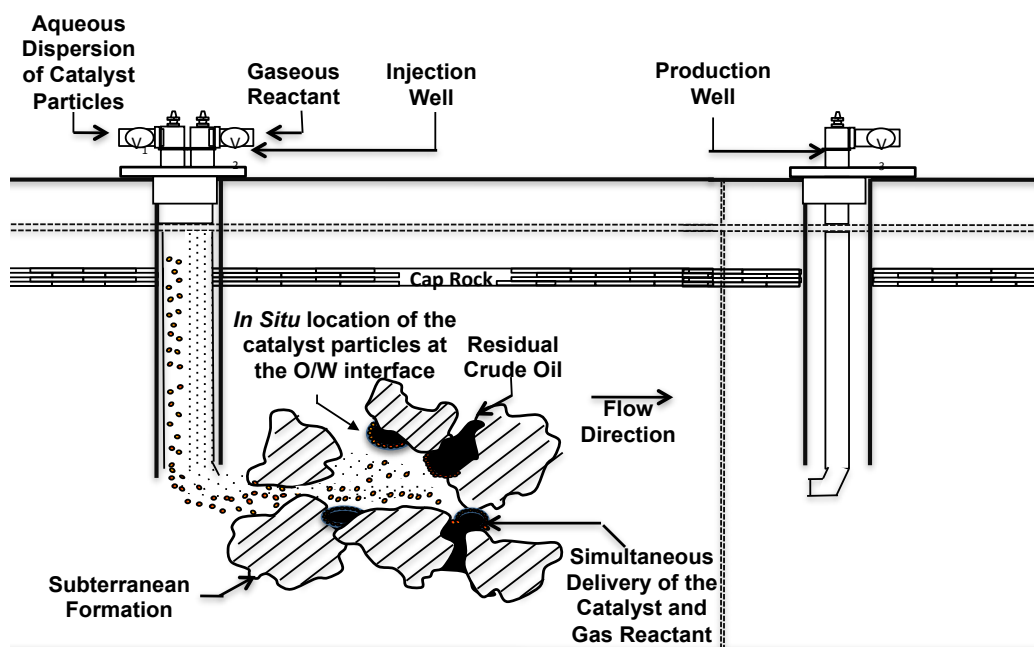




**Figure 5.4: High-resolution TEM images of the catalysts prepared with 5 %wt. Pd supported on different nanohybrids (see Table 1): (a) SWCNT/SiO<sub>2</sub>, (b) MWCNT/Al<sub>2</sub>O<sub>3</sub>(c) Functionalized MWCNT/Al<sub>2</sub>O<sub>3</sub>, (d) Onion carbon/SiO<sub>2</sub> and (e) Janus silica nanoparticles.**

Having in mind a potential application in subsurface reservoirs, we studied the catalytic activity of several nanohybrids for oxidation and hydrogenation reactions of interest in subsurface conversion. Figure 5.5 illustrates the concept of simultaneous injection of the aqueous dispersion of the nanoparticles and the gaseous reactant to react in-situ for subsurface applications. As an example of a possible in-situ reaction, the partial oxidation of hydrocarbons appears as a desirable conversion to increase the polarity of the oil molecules located at the interface. This conversion might significantly reduce the oil/water IFT, enhancing the capillary number. At the same time, if the oxidized molecules migrate to the water phase due to their enhanced water affinity, the

viscosity of the mobilizing fluid will increase and consequently, the sweeping efficiency of this fluid would improve.



**Figure 5.5: Representation of the introduction of the catalyst nanoparticles and the gaseous reactant in the wellbore for application in subsurface reservoirs.**

### 5.3.2. Partial Oxidation of Oil Constituents

#### 5.3.2.1. Catalyst Activity

Tetralin oxidation was carried out at 80 °C and 200 psi under a constant 200 sccm flow rate of air. The water/oil volume ratio in the liquid phase was 0.5 and the total volume was 30 ml. The total nanohybrid catalyst mass was 60 mg with a metal loading of 10 wt. %. Different nanohybrid supports and different metals were used for this reaction. Table 5.2 summarizes the characteristics of the catalysts tested in the partial oxidation reactions.

**Table 5.2: Catalysts tested on tetralin partial oxidation.**

Support	Metal	Metal Loading (wt. %)
(a) SWNT on silica	Pd	6, 10
	Cu	6, 10
	Fe	10
	Cr	10
(b) MWNT on alumina	Pd	10
	Cu	10
(d) Onion carbon/silica	Pd	10
(e) Janus silica nanoparticles.	Pd	10

The activity of different metal catalysts loaded on the SWCNT/SiO<sub>2</sub> nanohybrids was tested under the same reaction conditions. A sample of bare nanohybrids without any metal was used as a blank for comparison. The tetralin conversion, product yields, and selectivities obtained over the various samples after a reaction period of 24 h are summarized in Table 5.3. The main products of the reaction are 1-tetralone and 1-tetralol, as previously reported [45-50], with traces of naphthalene and dihydronaphthalene. The results clearly show that Pd and Cu lead to much higher conversions than the other metals. Regarding the selectivity towards the two possible products, it is clear that Cu displays the highest selectivity towards the ketone (84.5%). For this specific application, tetralone is the desired product since it is more stable than the alcohol, which undergoes dehydration, losing its polarity.

**Table 5.3: Results for the catalyst screening for tetralin oxidation at 80 °C 200 psi. Reaction time: 24 h. O/W ratio 0.5. Total volume: 30 ml. Catalyst weight: 60 mg. Metal loading: 10 wt. %. Air flow 200 sccm. Y is the products yield and S the selectivity. Support: nanohybrid (a) SWNT/silica.**

Metal	Tetralin Conversion	Y (tetralone)	Y (tetralol)	S (tetralone)	S (tetralol)
<b>Pd</b>	6.0%	4.0%	2.0%	64%	36%
<b>Cu</b>	4.8%	4.0%	0.74%	84%	16%
<b>Fe</b>	1.3%	0.85%	0.42%	67%	33%
<b>Cr</b>	1.0%	0.69%	0.33%	68%	32%
<b>Blank</b>	0.49%	0.35%	0.14%	71%	29%

With the two most active metals (Pd and Cu), different metal loadings (6 wt. % and 10 wt. %) were compared and the results are presented in Table 5.4. For the Pd catalysts, an increase in conversion with the metal loading is observed. In contrast, the Cu catalysts showed the opposite behavior, since it is probable that high metal loading in Cu catalysts leads to metal aggregation and consequently, lower activity. Thus, runs at varying reaction times were evaluated on the two most active materials, i.e. 10 wt. % Pd and 6 wt. % Cu supported on the SWCNT/SiO<sub>2</sub> nanohybrids.

**Table 5.4: Comparison of metal loadings for the Cu, Pd on catalysts on nanohybrid (a) SWNT/silica for tetralin oxidation at 80 °C 200 psi.**

Metal	Metal loading	Tetralin Conversion	S (tetralone)	S (tetralol)	Y (tetralone)	Y (tetralol)
<b>Pd</b>	6%	3.0%	68%	32%	2.0%	0.96%
	10%	6.0%	64%	36%	4.0%	2.0%
<b>Cu</b>	6%	8.2%	89%	11%	7.3%	0.94%
	10%	4.8%	84%	16%	4.0%	0.74%

Several nanohybrid supports were tested using Pd as the active metal with a loading of 10 wt. %. The results on the different nanohybrids are compared in Table

5.5. It can be observed that the silica Janus particles and the MWCNT/alumina hybrids showed a five-fold increase in activity compared to the first generation of nanohybrids based on SWCNT on silica.

**Table 5.5: Result of the reaction using 10 wt.% Pd catalysts on different supports for tetralin oxidation at 80 °C 200 psi. Reaction time: 24 h. O/W ratio 0.5. Total volume: 30 ml. Catalyst weight: 60 mg. Air flow 200 sccm. S represents the products selectivity.**

Nanohybrid Support	Tetralin Conversion	S (tetralone)	S (tetralol)
(a) SWNT on Silica	6.0 %	64 %	36 %
(b) MWNT on alumina	27.9 %	65 %	35 %
(d) Onion Carbon on Silica	6.7 %	63 %	37 %
(e) Silica Janus particles	30.2 %	59 %	41 %

This activity enhancement is mainly attributed to the better capability of these particles of forming emulsions with smaller droplet sizes, resulting in a higher interfacial area than the ones obtained with the SWCNT on silica (see Figure 5.2). In addition, when comparing MWCNT to SWCNT and OC, the former has a better capability of anchoring Pd particles due to the higher number of defects on their surface, which as illustrated in Figure 5.3, provides active sites for metal deposition. The series of reactions over time using the MWCNT on alumina catalyst were carried out, and the results are shown in Figure 5.6. As stated before, the values of tetralin conversion and products yield are higher than the ones observed in Table 5.5 for the SWCNT/silica catalysts. However, the activity induction period was still evident since

the conversion grew non-linearly, e.g. 10% after the first 18 h of reaction, but 30% after 24 h.

#### 5.3.2.2. Density Functional Theory (DFT) Calculations of the Metal-Nanohybrid Catalysts

To understand the ability of wall defects in stabilizing Pd nanoclusters DFT calculations have been conducted to compare the strength of the metal-carbon interaction on an oxidized defect site compared to that on a pristine carbon wall. In a recent study [51], we used ONIOM (DFT:MM) calculations to show that the binding energy of Pd clusters was significantly enhanced when the SWCNT surface was oxygen-functionalized, compared to the case of a pristine SWCNT surface. The electronic interaction of Pd atoms with oxygen at the defect sites resulted in a stronger bonding (4.6 eV in comparison with 2.6 eV).

In this work, the adsorption of Pd nanoclusters on MWCNT has been also investigated theoretically. Three layers of graphene sheets were used as a representative for MWCNT surface, as shown in Figure 5.6. The interlayer distance and a typical C–C bond length are  $\sim 3.4$  Å and  $\sim 1.41$  Å, respectively [52]. Each C-dangling bond at the edges of the steps sites was terminated with –COOH functional group. Adsorption energies of Pd nanoclusters on terrace sites and step sites were examined to elucidate a role of defects containing the functional group.

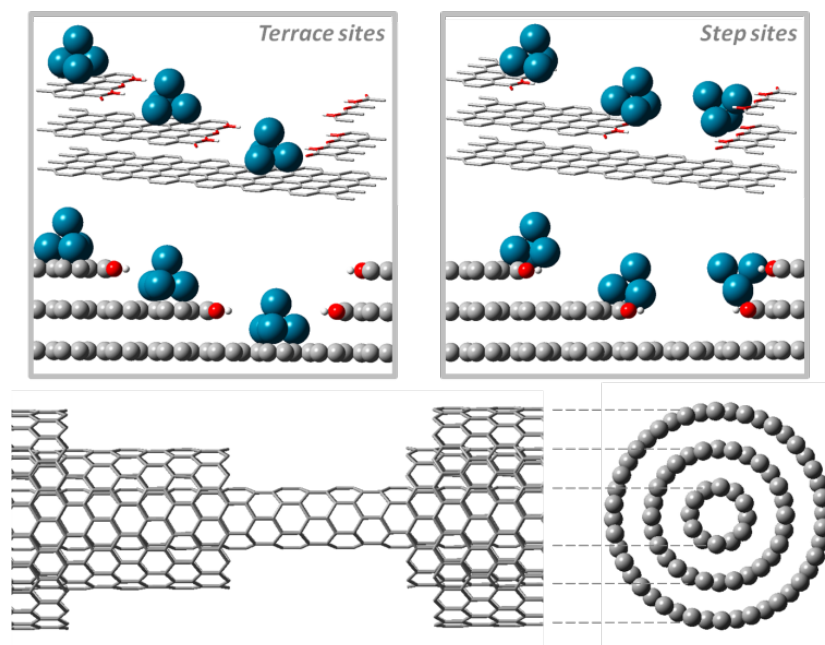
Spin-polarized periodic DFT calculations were performed using the Vienna ab initio simulation package (VASP) [53-57], in which the Kohn-Sham equations are solved by self-consistent algorithms. The dimensions of the unit cells are:  $a = 9.769$

$\text{\AA}$ ,  $b = 29.160 \text{ \AA}$ ,  $c = 30.00 \text{ \AA}$ , and  $\alpha = \beta = \gamma = 90^\circ$ . A cutoff energy of 300 eV was used. Brillouin zone sampling was restricted to the  $\Gamma$ -point. Pd nanoclusters were freely optimized and a quasi-Newton forces-minimization algorithm was employed for the forces-minimization algorithm. The convergence was achieved when forces were below  $0.05 \text{ eV/\AA}$ . The adsorption energy,  $E_{\text{ads}}$ , is given by the following equation:

$$E_{\text{ads}} = E_{\text{Pd/MWCNT}} - E_{\text{MWCNT}} - E_{\text{Pd}} \quad (\text{Eq. 5.1})$$

Where  $E_{\text{Pd/MWCNT}}$  is the total energy of the MWCNT with Pd clusters,  $E_{\text{MWCNT}}$  is the energy of the MWCNT, and  $E_{\text{Pd}}$  is the energy of the Pd clusters in gas phase.

Based on the calculation, the binding energy on the steps is 1.36 eV higher than that on the terrace sites of MWCNT. This demonstrates the preferential adsorption of Pd nanoclusters on oxidized defects of MWCNT, which is consistent with our previous study on SWCNT [51] and the experimental results of this study.

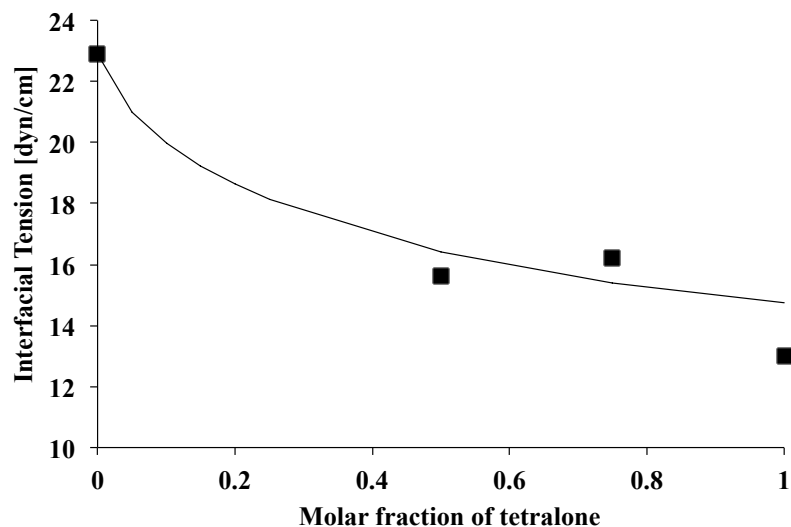


**Figure 5.6: The models for Pd clusters adsorption on terrace sites (left); and steps sites (right) of MWCNT.**

### 5.3.2.3 Changes in Interfacial Tension After Reaction

The interfacial tension of several mixtures of tetralin/tetralone and water was measured to verify that it decreases when oxidized polar groups (tetralone) are generated from the non-polar phase (tetralin), which occurs under oxidation reaction. The measurements were compared to a model [58] that predicts an exponential decay with the concentration of polar species added to a non-polar phase. As shown in Figure 5.7 the fitting is very good (obtaining an average absolute error of 0,5 dyn/cm and an average percentage error of 3 %) and demonstrates that indeed, the addition of small amounts of tetralone generates a considerable decrease in interfacial tension. This decrease is caused by the enrichment of the polar compound at the oil-water interface, due to a higher affinity of the polar compound to water compared to the non-polar bulk phase.





**Figure 5.7: Interfacial tension between mixtures of tetralin/tetralone and water determined experimentally (symbols) and using the exponential model proposed by Kim and Burgess (solid line).**

Although the reduction of IFT showed in Figure 5.7 does not reach the typical desired values for EOR techniques, it serves as an initial proof of concept for this application. If the oxidation reaction was carried out to convert molecules with lower polarity than that of tetralin, such as a long-chain olefin, the impact on the IFT reduction would be increased. In addition, another advantage of this reaction in oil-wet reservoirs could be the modification of the wettability of the porous medium when the particles migrate nearby the rock and generate polar compounds in this region.

Tetralin has been selected as a model compound representing the complex mixtures typically found in crude oil to simplify the experimental procedures required to analyze the results of the oxidation reactions. However, the catalysts used in this study have been tested in our group for different oil compositions including olefins, paraffinic and aromatic compounds showing no change in the activity observed. Thus, it

is expected that the results obtained will not show significant changes when extrapolated to reactions including fluids containing composition similar to that of crude oil.

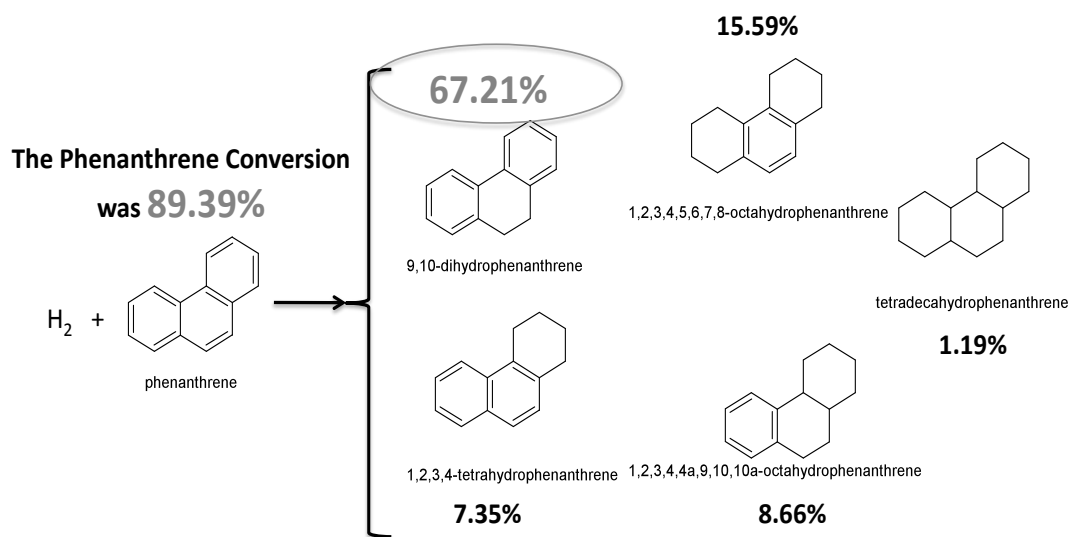
### *5.3.3. Hydrogenation of Polynuclear Aromatics*

#### 5.3.3.1. Catalyst Activity

For the study of hydrogenation reactions, MWCNT on alumina nanohybrids were pre-treated with nitric acid (16 M) at 100°C for 6 h to create anchoring sites at the MWCNT walls. With this particular pre-treatment the Pd nanoparticles become preferentially coordinated at the oxidized MWCNT sites [51] since the density of defects on the MWCNT increases upon oxidation with nitric acid. This enhancement in the metal-support interaction improves the metal dispersion over the hydrophobic carbon nanotubes, which is responsible for the conversion of the hydrocarbons present in the organic phase. Additionally, this oxidation treatment of the MWCNT/ alumina also enhances the repulsive forces between MWCNT, due to higher density of charge caused by the carboxylic acid groups. This repulsion results in a better dispersion of the nanoparticles in the liquid phase, increasing the emulsification efficiency of the nanohybrid.

The hydrogenation reactions were run for 24 h at 200°C and 900 psi under a constant 110 sccm flow of hydrogen. The water/oil volume ratio in the mixture was kept equal to 1 and the total mass of catalytic nanohybrid of MWCNT(ox)/alumina was 30 mg. The active metal employed was Pd (5 wt. %).

Figure 5.8 shows the different products obtained in the hydrogenation of phenanthrene over the 5 wt. % Pd on MWCNT(ox)/alumina after a 24 h reaction period under 900 psi of H<sub>2</sub> and 200°C, including the individual yields obtained at a total conversion of 89.39 %. The main product was 9,10-dihydrophenanthrene (67.2 % yield), followed by 1,2,3,4,5,6,7,8-octahydrophenanthrene (15.6 % yield), 1,2,3,4,4a-octahydrophenanthrene (8.7 % yield), and 1,2,3,4-tetrahydrophenanthrene (1.2 % yield).



**Figure 5.8: Conversion and yields of the different products in the hydrogenation of phenanthrene over 5 % wt. Pd on oxidized MWNT/alumina after 24 h of reaction under 900 psi of H<sub>2</sub> and 200 °C.**

One of the possible effects of hydrogenation on rheological properties could be associated with the increased flexibility of the polyaromatic molecules when the aromaticity is broken. This interesting effect could explain the change of the state of matter observed when the phenanthrene (a solid at room temperature) is selectively hydrogenated towards the 9,10-dihydrophenanthrene (a liquid at room temperature).

Hence, based on this observation, we decided to study the effect of the extent of hydrogenation of the polyaromatic molecules on the dynamic viscosity ( $\mu$ ).

For this analysis, we employed the known approach of combining experimental data with a Quantitative Structure-Property Relationship (QSPR) software [59,60]. This method allowed us to predict the dynamic viscosity of molecules that are not commercially available. The QSPR software used for this purpose was MDL® QSAR provided by MDL Information Systems, Inc. In this approach, experimental measurements of a given property, such as viscosity, become related to the molecular structure using linear models in terms of molecular descriptors (MD), which are readily calculated from the structure of the molecule.

The first step in this method is the construction of a database of the property of interest for molecules with similar structure to those of the unknown (e.g. aromatics, naphthenics, etc.). For building this database, we used viscosity data from the work of Ivanciuc et al. [61] for 27 polyaromatics and polynaphthenics. A model was generated with this set of molecules and tested by the cross-validation method, which confirmed that the training set was statistically reliable and, as demonstrated in Figure 5.9, it was described very well by the regression equation shown below. The square correlation coefficient and standard deviation of the resulting model (Equation 5.2) were 0.9817 and 0.3594 cP, respectively.

$$\mu_{(cP)} = -20.23 * H_{max\ pos} - 11.05 * Q_v + 2.07 * x_2 - 8.61 * xp_9 + 6.48 * xvp_6 + 0.66 SsCH_3 + 32.34 \quad (\text{Eq. 5.2})$$

Where:

$H_{\max\text{pos}}$ : Largest E-state in a hydrogen atom in the molecule.

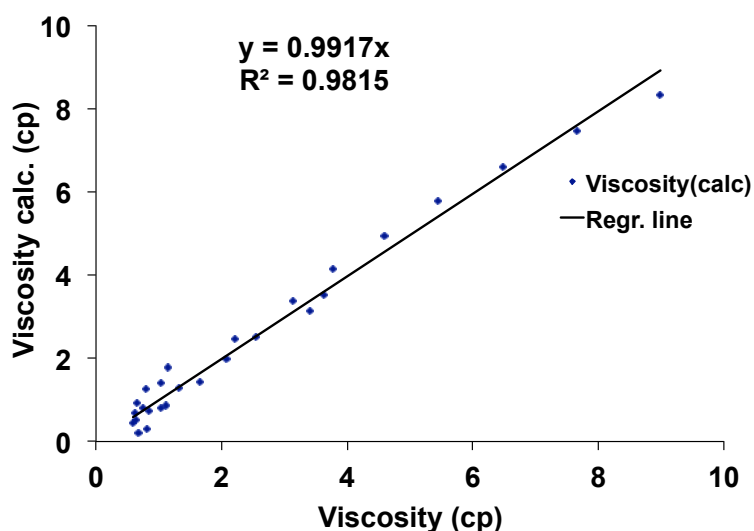
$Q_v$ : Molecular and group polarity index.

$x_2$ : Connectivity Simple 2<sup>nd</sup> order Chi Index.

$x_{p9}$ : Connectivity Simple 9<sup>th</sup> order path Chi Index.

$x_{vp6}$ : Connectivity Valence 6<sup>th</sup> order path Chi Index.

$SsCH_3$ : Count of all the  $-CH_3$  groups in the molecules.



**Figure 5.9: Validation of the QSPR model for the prediction of the viscosity of polyaromatic molecules ( $r^2=0.9817$ ) and mean absolute error (MAE) was 0.26 cp.**

This model was used to predict the dynamic viscosity of the 9,10-dihydrophenanthrene, 1,2,3,4-tetrahydrophenanthrene, 1,2,3,4,4a-octahydrophenanthrene, 1,2,3,4,5,6,7,8-octahydrophenanthrene and tetradecanohydrophenanthrene, and the results are shown in Table 5.6. Initially, the reduction of the side or central ring of the phenanthrene is enough to change the state of matter of the bulk phenanthrene from solid to liquid. This could be attributed to the

change in the shape of the molecule, that in the case of the phenanthrene is completely flat allowing the arrangement of the molecules in a crystal structure, while in the case of the 9,10-dihydrophenanthrene and 1,2,3,4-tetrahydrophenanthrene is less planar, with a viscosity of 3.457 cP and 3.549 cP, respectively. Then, further hydrogenation of the phenanthrene yields to the 1,2,3,4,4a-octahydrophenanthrene (6.123 cP) and 1,2,3,4,5,6,7,8-octahydrophenanthrene (4.285 cP), with higher viscosities than those obtained during the first hydrogenation. This reverse effect in the dynamic viscosity could be ascribed to the increase of the dispersion forces between molecules and the larger molecular volume obtained upon hydrogenation. Finally, the complete hydrogenation of the phenanthrene to tetradecanohydrophenanthrene increases the viscosity up to 19.82 cP.

**Table 5.6: Change in the QSPR molecular descriptors and the viscosity of phenanthrene upon hydrogenation reaction of phenanthrene.**

Compound	Descriptors						Property Viscosity (cp)
	Hmaxpos	Qv	X2	Xp9	Xvp6	SsCH3	
9,10-dihydrophenanthrene	1.2284	1.372	5.9941	0.8958	0.9319	0.0	3.54
1,2,3,4-tetrahydrophenanthrene	1.2114	1.4370	5.9941	0.8958	1.0521	0.0	4.28
1,2,3,4,4a,9,10,10a-octahydrophenanthrene	1.1424	1.6528	5.9941	0.8958	1.6164	0.0	6.12
tetrahydrophenanthrene	0.5191	2.1147	5.9941	0.8958	2.577	0.0	19.85

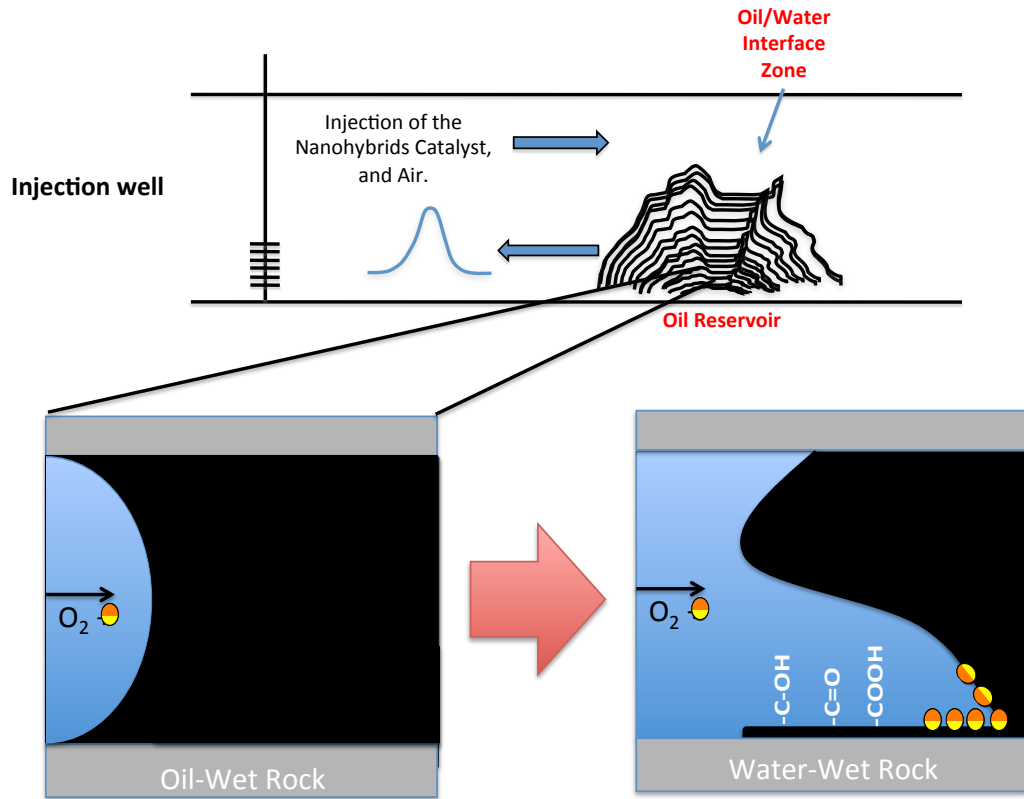
In addition to the impact on the oil viscosity, partial hydrogenation is an effective treatment previous to the partial oxidation of the aromatic compounds. This is demonstrated by the capability of being oxidized showed by partially hydrogenated aromatic compounds compared to their saturated and completely aromatic counterparts. For example, while tetralin is readily oxidized at mild conditions (as showed in this

work), decalin and naphthalene cannot be partially oxidized in such conditions. The main reason for this is the existence of an alpha carbon in the 1 position in tetralin which has two hydrogen atoms weakly bounded to it due to the resonance stabilization of the aromatic ring. An evidence for this is that in the present work tetralin is only oxidized at the 1 position, and no products of partial oxidation at a different carbon are observed.

Furthermore, selective hydrogenation to target products could also be used to convert components in the oil phase of the emulsions to increase the viscosity of the sweeping fluid. As a result, this decrease in mobility ratio will result in enhancement of the oil recovery.

#### *5.3.4. Catalytic Surface Wettability Modification*

The high capillary pressures inside the small pores of the rock are the responsible for the low the recovery of crude oil in subsurface reservoirs. These elevated pressures are due to the hydrophobic nature of the rock-oil interface, detouring the sweeping fluid towards lower resistance paths. An attractive strategy to reduce the surface free energy of the water-oil-rock interface is catalytic oxidation of the oil-wetted rock employing amphiphilic nanohybrid catalysts that selectively adsorb at the liquid-oil-rock interface. By introducing hydrophilic functional groups at the rock-oil surface the interfacial tension is decreased, which in turns lowers the capillary pressure and improves the disjoining efficiency of the sweeping fluid (Figure 5.10).

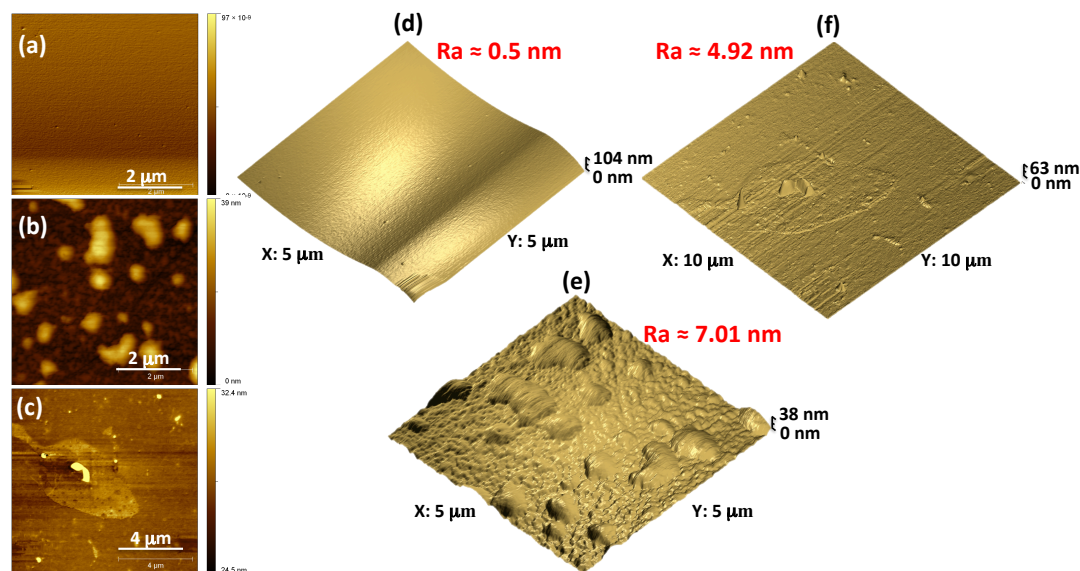


**Figure 5.10: Schematic representation of the surface wettability modification via catalytic oxidation of the surface physisorbed hydrocarbon molecules.**

A proof-of-concept study was performed using atomic force microscopy and water-air-surface contact angle measurements of precipitated asphaltenes on a silicon wafer before and after catalytic oxidation using a nanohybrid catalyst. The oxidation reaction was accomplished using hydrogen peroxide aqueous solutions as the oxidant and 10 wt. % Cu/MWCNT/Al<sub>2</sub>O<sub>3</sub> as the catalyst at 40 °C for 3 hours. It can be found in Figure 5.11 the AFM images, 3D surface topography, and the average surface roughness of the clean silicon wafer (a-d), asphaltenes physisorbed before reaction (b and e), and after catalytic surface oxidation (c-f). It is worth to note that the silicon surface roughness dramatically increases from 0.5 nm (bare silicon wafer) to 7.0 nm upon the precipitation of the asphaltenes, which tend to form aggregates of ~ 0.5 μm in



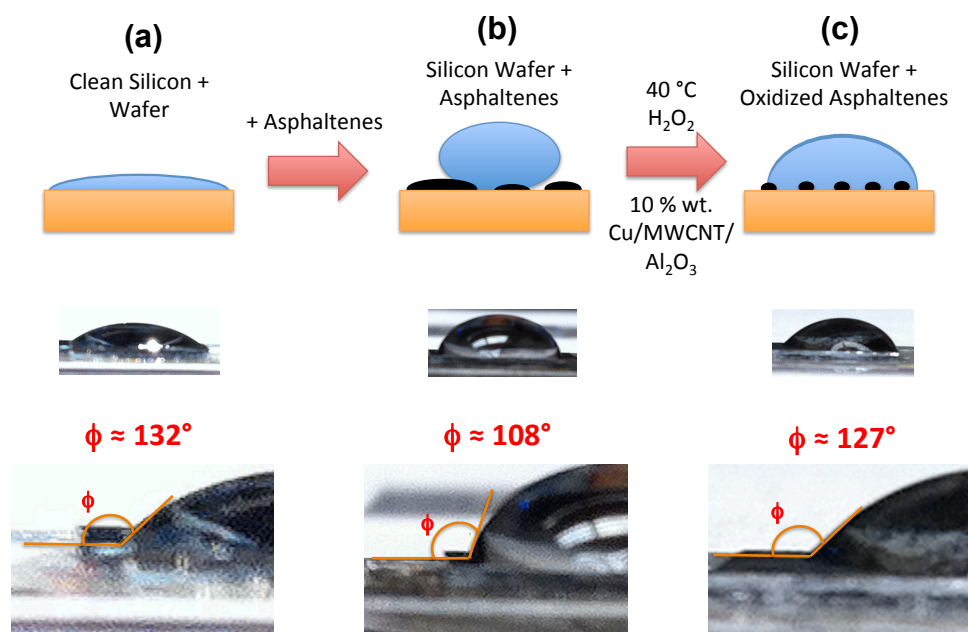
size resulting. Surprisingly, the surface roughness is reduced dramatically after the catalytic oxidation of the asphaltenes physisorbed on the silicon surface.



**Figure 5.11: AFM images and 3D surface topography of the clean silicon wafers (a and d), asphaltenes physisorbed before reaction (b and e), and after oxidation (c-f) in hydrogen peroxide (30 wt. %) using 10mg of 10 wt. % Cu/MWCNT/Al<sub>2</sub>O<sub>3</sub> nanohybrids catalyst. The average surface roughness (Ra) of the samples is presented in red color.**

The contact angle at the liquid-solid-air interface is a technique widely used to determine the wettability of solid surfaces. Figure 5.12 shows the contact angle results for the three different surfaces studied. First, it is clear that in the bare silicon wafer the contact angle was around 132° indicative of hydrophilic character, in the asphaltene-coated surface the values were around 108°. This decrease in the contact angle is due to the elevated hydrophobicity of the asphaltenes even at low surface coverage. As expected in the surface catalytically oxidized the contact angle increase as a result of the formation of hydrophilic moieties on the surface of the asphaltenes aggregates. In these

experiments it was possible to demonstrate that using amphiphilic catalytic nanoparticles it is possible to selectively modify the surface chemistry of physisorbed hydrocarbons, which in turns decreased the interfacial contact angel of the water-surface boundary. It is anticipated that similar results in subsurface could lead to a significant reduction in the capillary pressure inside the porous, improving the recovery of the crude oil.



**Figure 5.12: Schematic illustration of the water-air-silicon wafer contact angle measured on the clean silicon surface (a), asphaltenes physisorbed before reaction (b), and after oxidation (c) in hydrogen peroxide (30 wt. %) using 10mg of 10 wt. % Cu/MWCNT/Al<sub>2</sub>O<sub>3</sub> nano hybrids catalyst.**

#### 5.4. Conclusions

In addition to be able to stabilize emulsions, the catalysts resulting from the deposition of metals on nano hybrid supports are active for both oxidation and hydrogenation of organic compounds at the oil–water interface.

The oxidation of aromatic compounds and hydrocarbons at the interface reduces the oil-water IFT since the species with higher dipole moment (oxygenates) dominate the interface. The reduction of the IFT improves the capillary number, which should enhance the oil recovery.

The complete hydrogenation of the polyaromatic molecules increases the viscosity of the resulting products. The selective hydrogenation could be an appropriate strategy to increase the viscosity of the sweeping fluid (emulsion), improving the mobility ratio.

As a result, the combination of oxidation and hydrogenation reactions would enhance the oil recovery by simultaneously increasing the capillary number (decreasing the interfacial tension) and enhancing the mobility ratio (increasing the viscosity of the sweeping phase), with the same effect as the currently used injections of surfactant and polymer water solutions.

The results from the surface wettability modification showed promising results using the amphiphilic nanohybrid catalyst based on Cu supported on MWCNT/Al<sub>2</sub>O<sub>3</sub> nanohybrids. These proof-of-concept experiments showed that upon catalytic oxidation is possible to increase the hydrophilicity of the physisorbed asphaltenes by introducing oxygen-containing functional groups on the structure of the hydrocarbons. It is expected that in a real application the reduction in the rock-water-oil interfacial tension could dramatically decrease the disjoining pressure required to recover the crude oil located in the small pores.

## References

- [1] D.C. Standnes and T. Austad, *J. Pet. Sci. Eng.* 28 (2000) 123.
- [2] S. Iglauer, Y. Wu, P. Shuler, Y. Tang and W.A. III Goddard, *J. Pet. Sci. Eng.* 71 (2010) 23.
- [3] D.R. Ingram, C. Kotsmar, K.Y. Yoon, S. Shao, C. Huh, S.L. Bryant, T.E. Milner and K.P. Johnston, *J. Colloid Interface Sci.* 351 (2010) 225.
- [4] H. Yu, C. Kotsmar, K.Y. Yoon, D.R. Ingram, K.P. Johnston, S.L. Bryant and C. Huh, 17<sup>th</sup> SPE Improved Oil Recovery Symposium; Tulsa, OK 2010, SPE 129887.
- [5] A.J. P. Fletcher and J.P. Davis, 17<sup>th</sup> SPE Improved Oil Recovery Symposium, Tulsa, OK 2010, SPE 129531.
- [6] B. Ju, T. Fan and M. Ma, *China Particuol.* 4 (1996) 41.
- [7] B.A. Suleimanov, F.S. Ismailov and E.F. Veliyev, *J. Pet. Sci. Eng.* 78 (2011) 431.
- [8] E.C. Donaldson, G.V. Chilingarian and T.F. Yen, *Enhanced oil recovery, I: fundamentals and analyses*; Elsevier Science Publishing Company Inc.: New York, NY, 1985, pp 47-63.
- [9] A. Abrams, *SPEJ* 15 (1975) 437.
- [10] S. Thomas and S.M. Farouq Ali, *J. Pet. Sci. Eng.* 3 (1989) 121.
- [11] R. Simon, *Phys. Chem. Earth* 13/14 (1981) 447.
- [12] A. Satter, G.M. Iqbal and J.L. Buchwalter, *Practical enhanced reservoir engineering: assisted with simulation software*; PennWell Corporation: Tulsa, OK, 2007, pp 235-238.

- [13] M.R. Islam and S.M. Farouq Ali, *J. Pet. Sci. Eng.* 8 (1993) 303.
- [14] H.A. Nasr-El-Din and K.C. Taylor, In *Advances in Engineering Fluid Mechanics: Multiphase Reactor and Polymerization System Hydrodynamics* (ed. Cheremisinoff, N. P.); Gulf Publishing Company: Houston, TX, 1996, pp 615-668.
- [15] R. Kumar, E. Dao and K.K. Mohanty, 17<sup>th</sup> SPE Improved Oil Recovery Symposium, Tulsa, OK 2010, SPE 129914;
- [16] T. Skauge, K. Spildo and A. Skauge, 17<sup>th</sup> SPE Improved Oil Recovery Symposium, Tulsa, OK 2010, SPE 129933
- [17] B.P. Binks and S.O. Lumsdon, *Langmuir* 17 (2001) 4540.
- [18] B.P. Binks and S.O. Lumsdon, *Phys. Chem. Chem. Phys.* 1 (1999) 3007.
- [19] B.P. Binks and S.O. Lumsdon, *Langmuir* 16 (2000) 2539.
- [20] B.P. Binks and S.O. Lumsdon, *Phys. Chem. Chem. Phys.* 2 (2000) 2959.
- [21] N.P. Ashby and B.P. Binks, *Phys. Chem. Chem. Phys.* 2 (2000) 5640.
- [22] B.P. Binks and J.H. Clint, *Langmuir* 18 (2002) 1270.
- [23] J. Giermanska-Kahn, V. Schmitt, B.P. Binks and F. Leal-Calderon, *Langmuir* 18 (2002) 2515.
- [24] B.P. Binks and M. Kirkland, *Phys. Chem. Chem. Phys.* 4 (2002) 3727.
- [25] V.N. Paunov, B.P. Binks and N.P. Ashby, *Langmuir* 18 (2002) 6946.
- [26] C.W. Bowman, *Proc. 7<sup>th</sup> World Petroleum Congress, Mexico City, Mexico*, 2-8 April 1967, 3, 583-604.
- [27] J.H. Schulman and J. Leja, *J. Trans. Faraday Soc.* 50 (1954) 598.

- [28] E.H. Lucassen-Reynders and M. Van den Tempel, *J. Phys. Chem.* 67 (1962) 731.
- [29] D.E. Tambe and M.M. Sharma, *J. Colloid Interf. Sci.* 157 (1993) 244.
- [30] R. Aveyard, B.P. Binks and J.H. Clint, *Adv. Colloid Interface Sci.* 100 (2003) 503.
- [31] S. Arditty, C.P. Whitby, B.P. Binks, V. Schmitt and F. Leal-Calderon, *Eur. Phys. J.* 11 (2003) 273.
- [32] D.E. Tambe and M.M. Sharma, *J. Colloid Interf. Sci.* 52 (1994) 1.
- [33] M. Shen and D.E. Resasco, *Langmuir* 25 (2009) 10843.
- [34] S. Crossley, J. Faria, M. Shen and D.E. Resasco, *Science* 327 (2010) 68.
- [35] J. Faria, M.P. Ruiz and D.E. Resasco, *Adv. Synth. Catal.* 352 (2010) 2359.
- [36] M.P. Ruiz, J. Faria, M. Shen, S. Drexler, T. Prasomsri and D.E. Resasco, *ChemSusChem* 4 (2011) 964.
- [37] A. Perro, F. Meunier, V. Schmitt and S. Ravaine, *Colloids Surf., A* 332 (2009) 57.
- [38] L. Villamizar, P. Lohateeraparp, J. Harwell, D.E. Resasco and B. Shiau, 17<sup>th</sup> SPE Improved Oil Recovery Symposium, Tulsa, OK 2010 SPE 129901.
- [39] B. Kitiyanan, W.E. Alvarez, J.H. Harwell and D.E. Resasco, *Chem. Phys. Lett.* 317 (2000) 497.
- [40] W.E. Alvarez, B. Kitiyanan, A. Borgna and D.E. Resasco, *Carbon* 39 (2001) 547.
- [41] D.E. Resasco, W.E. Alvarez, F. Pompeo, L. Balzano, J.E. Herrera, B. Kitiyanan and A. Borgna, *J. Nanopart. Res.* 4 (2002) 131.

- [42] W.E. Alvarez, F. Pompeo, J.E. Herrera, L. Balzano and D.E. Resasco, *Chem. Mater.* 14 (2002) 1853.
- [43] B.P. Binks, *Curr. Opin. Colloid Interface Sci.* 7 (2002) 21.
- [44] B.P. Binks and P.D.I. Fletcher, *Langmuir* 17 (2001) 4708.
- [45] I.Y. Saratov, V.A. Simanov, B.I. Golovanenko and S.D. Saratova, *Pet. Chem.* 8 (1968) 59.
- [46] M. Martan, J. Manassen and D. Vofsi, *Tetrahedron* 26 (1970) 3815.
- [47] A.I. Kamneva, V.I. Zakharova, L.N. Piperskii, V.A. Seleznev and A.V. Artemov, *Pet. Chem.* 15 (1975) 98.
- [48] F. Mizukami, Y. Horiguchi, M. Tajima and M. Imamura, *J. Bull. Chem. Soc. Jpn.* 53 (1979) 2689.
- [49] Y.M. Chung, K.K. Kang, W.S. Ahn and P.K. Lim, *J. Mol. Catal. A: Chem.* 137 (1999) 23.
- [50] F.X. Llabrés i Xamena, O. Casanova, R. Galiasso Tailleur, H. Garcia and A. Corma, *J. Catal.* 255 (2008) 220.
- [51] T. Prasomsri, D. Shi and D. E. Resasco, *Chem. Phys. Lett.* 497 (2010) 103.
- [52] L. Guan, K. Suenaga and S. Iijima, *Nano Lett.* 8 (2008) 459.
- [53] G. Kresse and J. Furthmüller, *Phys. Rev. B* 54 (1996) 11169.
- [54] G. Kresse and J. Hafner, *Phys. Rev. B* 49 (1994) 14251.
- [55] G. Kresse and J. Hafner, *Phys. Rev. B* 48 (1993) 13115.
- [56] G. Kresse and J. Hafner, *Phys. Rev. B* 47 (1993) 558.
- [57] G. Kresse and J. Furthmüller, *Comp. Mater. Sci.* 6 (1996) 15.
- [58] H. Kim and D. Burgess, *J. Colloid Interf. Sci.* 241 (2001) 509.

- [59] S. Crossley, W.E. Alvarez and D.E. Resasco, *Energy Fuels* 22 (2008) 2455.
- [60] D.E. Resasco and S. Crossley, *AIChE J.* 55 (2009) 1082.
- [61] O. Ivanciuc, T. Ivanciuc, P.A. Filip and D. Cabrol-Bass, *J. Chem. Inf. Comput. Sci.* 39 (1999) 515.



## Chapter 6:

# Catalyst Hydrophobization for Enhanced Hydrothermal Stability in Condensed Hot Water

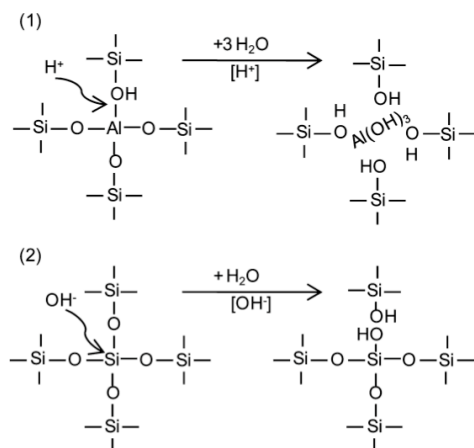
### 6.1. Introduction

The use of heterogeneous catalysts in the conversion of molecules in environmentally friendly solvents such as water is one of the major challenges in the production of fuels and chemicals renewable feedstocks. In the majority of these reactions the polar solvent tends to affect the catalyst performance by either irreversibly absorption (poisoning), dissolution of the active site into the bulk water phase (leaching) or destruction of the crystalline structure.

In particular, zeolites have served as major functional materials in the catalytic transformation of fossil feedstocks towards conventional fuels and chemicals in the petroleum refinery industry. These microporous aluminosilicate minerals are of particular interest due their tunable acid density/strength [1], thermal/mechanical robustness [2], and their large cavities accessible through windows of specific wide that allow the control of the product selectivity based on the molecules shape and size [3,4]. More recently, the use of zeolites is being intensely investigated in the production of renewable fuels and chemical platforms from lignocellulosic biomass. However, in contrast to fossil feedstocks, biomass has a highly oxygenated structure that results in a low vapor pressure for any of its constituents. Therefore, liquid-phase processing is likely to play a decisive role in the development of novel catalytic strategies to economically and competitively produce commodities with added value from biomass, like fuels and chemicals [5,6].

In such processes, polar solvents that can facilitate the solubilization of the lignocellulosic biomass are highly desirable, as high levels of conversion can be achieved. In particular, condensed water has promising applications as it is cheap, environmentally friendly, readily available and can dissolve large quantities of oxygenate molecules from biomass. This solvent has been successfully used in different catalytic strategies, such as hydrolysis of cellulose and isomerization/dehydration of monosaccharides [7,8]. A major drawback, however, is the migration of the aluminum atoms out of the zeolite framework in the presence of hot liquid water (100-250 °C) that greatly disrupts its crystalline structure and consequently affects its stability and catalytic activity [9]. Overcoming this limitation is a key challenge for the development of economical processes for biofuel production [5,10].

In zeolites the Brønsted and Lewis acid sites, resulting from the charge neutralization at the oxygen bridges between aluminum and silicon atoms in the framework, is a function of the Si/Al ratio, the framework configuration, and the type of cation used in the compensation [11,12]. Likewise, their stability in hot liquid water is also related to these properties; for instance, the ZSM-5 is stable at 150-200 °C independent of its Si/Al ratio, whereas the faujasite zeolite is degraded to a level that depends on their Si/Al ratio. In the latter, the degradation pathway by condensed water involves the hydrolysis of Si-O-Si bonds rather than dealumination, which leads to the formation of an amorphous material with no catalytic activity whatsoever (Figure 6.1) [9,13].

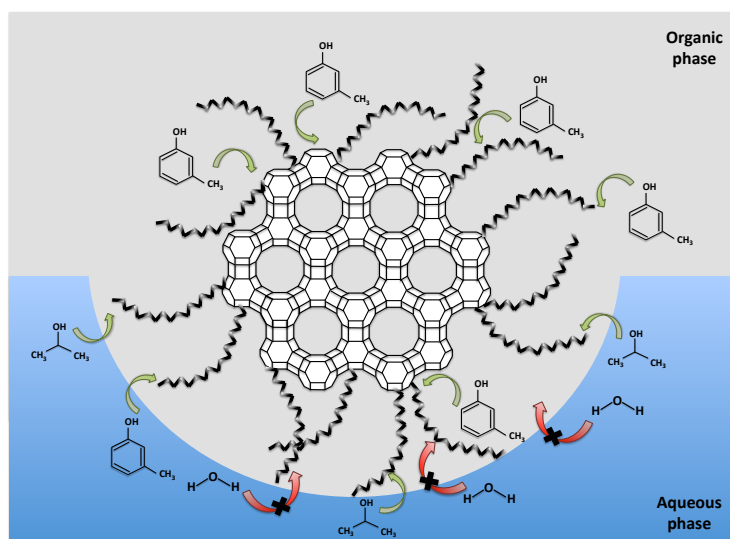


**Figure 6.1: Mechanisms for acid-catalyzed dealumination (1) and base-catalyzed hydrolysis of siloxane bonds (2) [9,13].**

Several authors have reported that increasing the Si/Al ratio on the zeolites has been proved as an effective strategy to improve the catalyst stability in aqueous environments, due to the increase in the hydrophobicity of the zeolite framework [14-16]. Related studies were performed on mesoporous materials by other authors, in which it was observed that incorporation of aluminum into MCM-41 and MCM-48 increased their stability in boiling water [17-20]. Furthermore, A. Corma et al. have developed hydrophobic Sn-beta zeolites that can act as weak Lewis acid sites for the Meerwein-Ponndorf-Verley reduction and Oppenauer oxidation reactions with good stereoselectivity and reasonable enantioselectivity, even in the presence of 10 % condensed water [21,22]. Moreover, M.E. Davis et al. have shown that these dealuminated Sn-beta zeolites are also highly active and stable towards the isomerization of glucose to fructose in acid aqueous environments [23-26]. Nevertheless, these approaches always require the sacrifice of the Brønsted acid sites in order to reduce the surface hydrophilicity, which results in lower catalytic activity for

dehydration, alkylation and oligomerization reactions. In addition, the synthesis method used involves the utilization of non-environmentally friendly fluorated media.

An alternative method to increase the hydrophobicity of the zeolites is the silylation of the zeolite with organosilanes (Figure 6.2). Although several authors have proposed that incorporation of organosilanes functionalities as skeletal of the zeolite structure or inside the porous framework could enhance the catalyst stability in the presence of water, the acid sites density and thermal stability are diminished [27-35]. A more desirable approach would be the selective functionalization of the external surface of the zeolite, in which the acid properties are preserved. In this regard, hydrophobic molecular sieves have been commonly synthesized to adsorb hydrocarbons and volatile organic compounds in the treatment of contaminated liquid water [36-40]. However, the use of these functionalized zeolites for catalytic applications have been proved to be challenging [21,41,42].



**Figure 6.2: Schematic illustration of the alkylation of m-cresol and 2-propanol taking place at the water/oil interface in emulsions stabilized by functionalized zeolites.**

Here it is presented a unique catalytic system recently developed in our research group in which surface-modified faujasites are employed simultaneously as water/oil emulsion stabilizers, as well as catalysts for the alkylation reaction of organic-soluble phenolic probes with aqueous-soluble alcohols in emulsion systems. Such technology could have a major impact in the liquid-phase catalytic upgrading of bio-oil and polysaccharides, where biphasic reaction systems are greatly desirable since they lead to higher product yields, as the rapid separation of the products into the organic phase prevents undesired repolymerization reactions [43,44].

A remarkable property of these functionalized materials is their high liquid/liquid interfacial activity, due to the increase in their surface hydrophobicity [45], which allows them to be preferentially adsorbed at the interface and, subsequently, stabilize water/oil emulsions with small droplet size. In this context, we have recently reported that the use of amphiphilic catalytic particles that simultaneously stabilize water/oil emulsion in biphasic systems and catalyze reactions at the liquid/liquid interface, presents several advantages, such as; 1) enhancement of the liquid/solid/liquid interfacial area, 2) the direct partitioning and separation of molecules due to differences in solubility, and 3) the possibility of converting molecules present only in one of the phases (phase-selectivity) [46-50].

In summary, by a modification of the zeolite surface by silylation with organosilanes, we have developed zeolites highly stable in hot condensed water, which naturally segregate at the liquid/liquid interface of biphasic systems and catalyze C-C bond formation reactions of molecules with different solubilities.

## 6.2. Experimental Section

### 6.2.1. Untreated HY Zeolites

The zeolites used in this work were faujasite HY zeolites, named CBV400 and CVB760, provided by Zeolyst International. CBV400 HY zeolite has a  $\text{SiO}_2/\text{Al}_2\text{O}_3$  molar ratio of 5.1, a surface area of  $730 \text{ m}^2/\text{g}$ , and the unit cell is  $24.50 \text{ \AA}$ . CVB760 HY zeolite has a  $\text{SiO}_2/\text{Al}_2\text{O}_3$  molar ratio of 60, a surface area of  $720 \text{ m}^2/\text{g}$ , and the unit cell is  $24.24 \text{ \AA}$ . In the experiments run with these untreated zeolites, they were used as received.

### 6.2.2. Preparation of Functionalized Zeolites

In order to functionalize the surface of the zeolites, we followed a silylation procedure similar to the one described by other authors [51]. Octadecyltrichlorosilane (OTS) was used as the silylation agent. First, 1 g of the untreated HY zeolite was dispersed in 20 ml of toluene by sonication with a Horn sonicator (Fisher Scientific 600 W, 20kHz) at 25 % of amplitude. Then, the zeolite suspension was added to a 50 ml solution of OTS (0.5 mmol/g zeolite) in toluene. Both OTS and toluene were provided by Sigma Aldrich. The final suspension was stirred for 24 h at 500 rpm at room temperature. After 24 h, the zeolite was collected by filtration with nylon filters of 0.22 mm of pore volume. After washing several times with ethanol, the functionalized zeolite was dried at  $100 \text{ }^\circ\text{C}$  overnight.

### 6.2.3. Characterization Techniques

Several techniques were employed to characterize the properties and structure of both untreated and functionalized zeolites, such as thermogravimetric/differential thermal analysis (TG-DTA), temperature-programmed oxidation (TPO), diffuse reflectance infrared Fourier transformation spectroscopy (DRIFT), X-ray diffraction (XRD), N<sub>2</sub> physisorption, scanning electron microscopy (SEM) and high-resolution transmission electron microscopy (HRTEM).

#### 6.2.3.1. Thermogravimetric/Differential Thermal analysis (TG-DTA)

Thermogravimetric analysis of the functionalized zeolite was conducted in a Netzsch STA 449 F1 Jupiter TG-DTA equipment, under flow of air at 100 °C for 30 min, followed by a heating ramp of 10 °C/min up to 800 °C, and a cooling ramp of 20 °C/min up to 400 °C.

#### 6.2.3.2. Temperature-Programmed Oxidation (TPO)

A temperature-programmed oxidation experiment was conducted on the functionalized zeolite passing a continuous flow of 5 % O<sub>2</sub>/He at a rate of 80 ml/min through the sample (~ 30 mg), which was located in a quartz tube reactor. During this process, the temperature of the oven was then linearly heated to 900 °C at a constant rate of 10 °C/min. The exit gas was sent through a methanator containing a 5 % Ni/Al<sub>2</sub>O<sub>3</sub> catalyst and a side-stream of H<sub>2</sub> to convert all of the CO and CO<sub>2</sub> into CH<sub>4</sub>, which can be detected by the sensitive flame ionization detector (FID). The area of the

C peak was then compared with that of a reference peak resulting from a pulse of 100  $\mu\text{l}$  of  $\text{CO}_2$  in order to quantify the amount of deposited carbon.

#### 6.2.3.3. Diffuse Reflectance Infrared Fourier Transformation Spectroscopy (DRIFT) and Pyridine Chemisorption

DRIFT spectra were recorded on a Perkin-Elmer Spectrum 100 FTIR, equipped with a high temperature DRIFT cell (HVC, Harrick) with  $\text{CaF}_2$  windows. The sample powder (100 mg) was placed in the cell, heated in situ up to 250  $^\circ\text{C}$  under a flow of He (30 mL/min) with a ramp of 10  $^\circ\text{C}/\text{min}$ , and kept at this temperature for 30 min. A background spectrum was recorded in each run followed by 256 scans taken at a resolution of 4  $\text{cm}^{-1}$  to obtain the final average spectrum. For the pyridine adsorption experiments, the samples were outgassed in He at 350  $^\circ\text{C}$  and then cooled in He to 100  $^\circ\text{C}$ ; subsequently, the samples were exposed to a stream of -20  $^\circ\text{C}$  saturated pyridine in He. After pyridine exposure, the sample was purged in He at 100  $^\circ\text{C}$  for 3 h, and the DRIFT spectra were recorded.

#### 6.2.3.4. X-ray Diffraction (XRD)

X-ray powder diffraction patterns (XRD) for the untreated and functionalized zeolites were collected on a D8 Series II X-ray diffractometer (BRUKER AXS), using Cu  $K\alpha$  radiation generated at 40 kV and 35 mA. The scans covered the  $2\theta$  range from 10 $^\circ$  to 35 $^\circ$ .



#### 6.2.3.5. N<sub>2</sub> Physisorption

The pore volume distribution and BET surface area of the zeolites were determined by N<sub>2</sub> physisorption using a Micromeritics ASAP 2010 with micropore option.

#### 6.2.3.6. Electron Microscopy Techniques (SEM and HRTEM)

SEM images were obtained from a JEOL JSM-880 high-resolution scanning electron microscope with a useful magnification of up to x300,000. HRTEM images were obtained on a JEOL 2010-F field emission intermediate voltage (200,000 volt) scanning transmission research electron microscope, with a magnification of up to x 8,000,000.

#### 6.2.4. *Preparation of Particle-Stabilized Emulsions*

In order to check the ability of these zeolites in stabilizing water/oil emulsions, 30 mg of each zeolite were added to a biphasic system of deionized water and decalin (vol. ratio 1:1), with a total volume of 10 ml. The energy necessary to produce the emulsion was applied by sonication with a Horn sonicator at 25 % of amplitude for 30 min. After the sonication, the suspension was kept static for 24 h before measuring the droplet size (by optical microscopy) and the fraction of emulsion formed.

#### 6.2.5. *Reaction System*

The catalytic experiments of alcohols dehydration and alkylation of 2-propanol and m-cresol were carried out in a Parr 4843 reactor of 300 ml in volume. The

temperature inside the reactor was measured with a J-Type thermocouple (OMEGA) and controlled by a temperature controller CAL 9500P from CAL Controls Ltd. An ASHCROFT pressure transducer was used for monitoring pressure inside of reactor. In each reaction, the catalyst (500 mg) was dispersed in a 60 ml mixture of equal volumes of deionized water/decalin and sonicated for 30 min with a horn sonicator at 25 % of amplitude. The mixture was placed in the stainless steel reaction vessel and purged with a 200 ml/min flow of He until the pressure reached 300 psi, while stirring at 80 rpm. Afterwards the reactor was heated up to 200 °C, 25 ml of a solution of the reactants dissolved in a mixture of equal volumes of deionized water and decalin were injected into the feeding cylinder. The cylinder was then pressurized up to 700 psi of He before the reactants were transferred to the reactor vessel. The inert gas was then flown until a pressure of 700 psi was reached in the reactor. At that moment, the gas inlet was closed. After the reaction time was completed, the reactor was cooled to 20 °C and depressurized.

After reaction, the emulsion was broken filtering the nanohybrids in two steps. First, a coarse paper filter (8 mm pore) was used to trap a large fraction of the solid particles since they quickly agglomerate over the surface of the filter. In the second step, a PTFE (0.2 micron pores) filter was used to separate the small fraction of catalyst particles that passed the first filter. The two clear liquid phases obtained after filtration were easily separated and 500 µl samples of each one analyzed by gas chromatography (GC-FID and GC-MS). In all the GC-FID analyses, methanol and 1,2-dichloromethane were used as internal standards to help closing the mass balances. All the aqueous fractions were extracted in methanol before injecting them in the GC, to minimize

column damage. An Agilent GC-FID 6890A equipped with a capillary column of polyethylene glycol (HP-INNOWAX) of 60.0 m x 0.32 mm x 0.25 mm nominal was used for quantitative analysis, while a Shimadzu QP2010S GC-MS equipped with an HP-INNOWAX polyethylene glycol capillary column, 30.0 m long x 0.25 mm nominal, was used for product identification, by using standards for those compounds that are commercially available.

For the alcohol dehydration reactions, the reactant consisted of either 2-propanol or 3-pentanol, with a final alcohol concentration in the system of 1 M. For the alkylation reactions, the reactants were 2-propanol and m-cresol, fed in two different 2-propanol/m-cresol molar ratios, 1 or 3, always with a total molar concentration in the system of 2 M. For these reactions, reagent grade 2-propanol, 3-pentanol and decalin (decahydronaphthalene) from Sigma Aldrich, and m-cresol from SAFC were used as received. Thymol from Sigma Aldrich was used as standard for the GC calibration.

### **6.3. Results and Discussion**

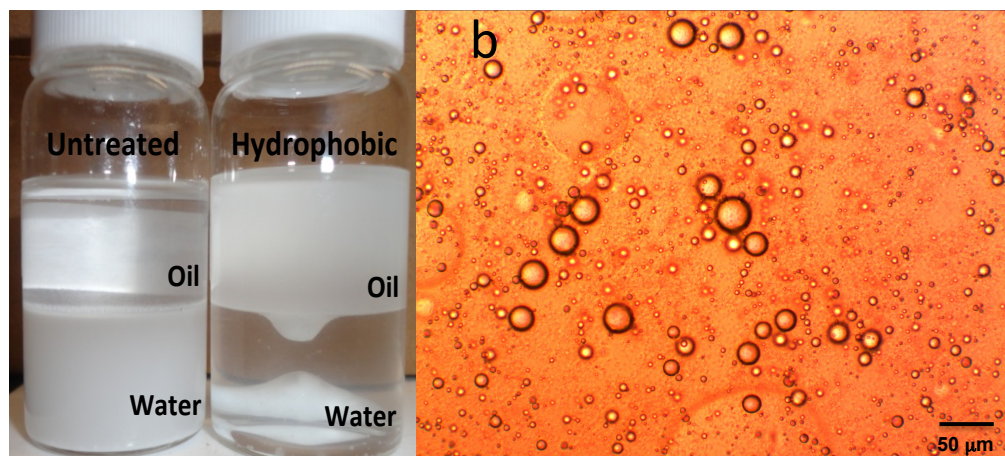
#### *6.3.1. Characterization of Untreated and Functionalized HY Zeolites*

The functionalization of the HY zeolites by a silylation process with a chlorosilanes is commonly used to modify and hydrophobize the surface of zeolites and silicas [37,52-54]. Although the exact mechanism is not clear, it is generally believed that the adsorption of alkyltrichlorosilanes on oxide surfaces proceeds through the hydrolysis of Si-Cl bonds to form silanols (with Si-OH groups) as intermediates. Then, the -OH groups undergo condensation reaction with the -OH groups of the substrate to

form a network polymer that is covalently bound to the surface [55-60]. Due to this functionalization the surface of the silica becomes hydrophobic.

### *6.3.2. Particles Dispersability and Emulsion Characterization of Untreated and Functionalized HY Zeolites*

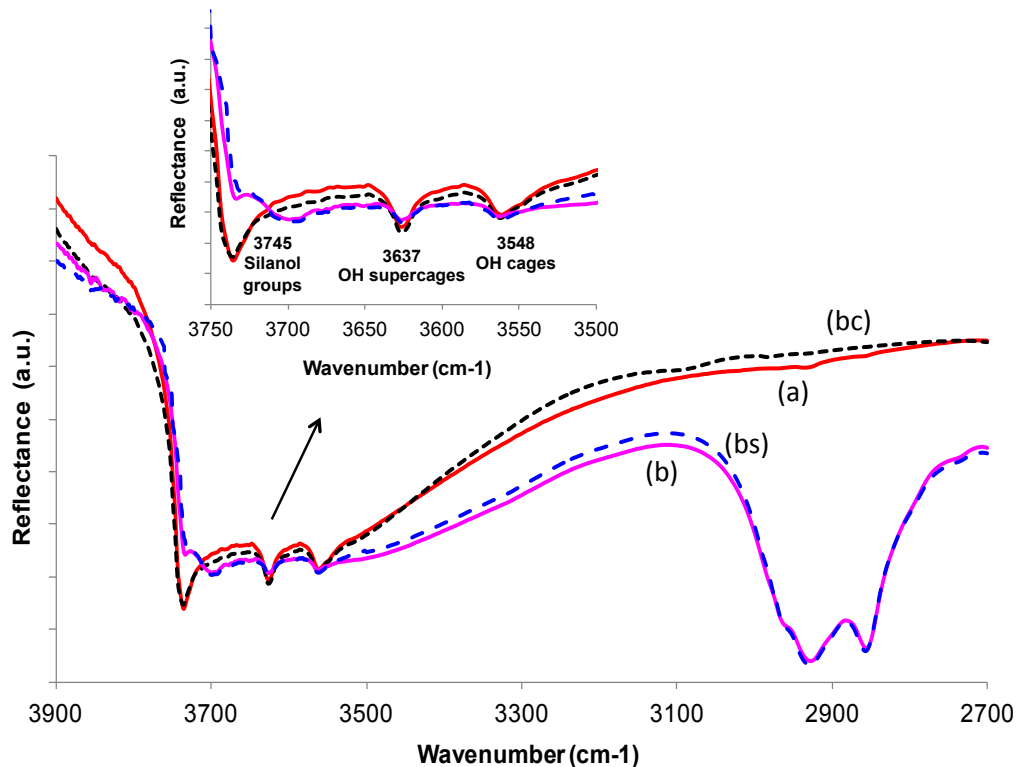
Two HY zeolites with different  $\text{SiO}_2/\text{Al}_2\text{O}_3$  molar ratios were chosen for this study, 5.1 and 60. Both of them were functionalized following the same procedure. After the functionalization of the HY zeolite surface, we compared the properties and catalytic performance of both untreated and functionalized zeolites. When we added the zeolites to a biphasic system of deionized water and decalin (Figure 6.3a left), we observed that the untreated zeolites rapidly migrated to the aqueous phase and precipitated. However, when we poured the functionalized zeolites, they dispersed on the oil phase and naturally segregated to the water/decalin interface. Besides, when energy was applied into the system by sonication, the functionalized zeolites stabilized emulsions of very small droplets of water dispersed in the organic phase (Figure 6.3a right), while the untreated zeolites did not produce a stable emulsion. The functionalized zeolites were able to stabilize water-in-oil emulsions with an average droplet size of  $\sim 5 \text{ nm}$  (Figure 6.3b). Upon the formation of the emulsion, the liquid/liquid interfacial area increased by a factor of  $10^4$  times, reaching a value of  $\sim 10 \text{ m}^2$  per gram of functionalized zeolite. Moreover, the emulsions stabilized by the hydrophobic-zeolites were stable for weeks, while the untreated ones progressively underwent phase-separation due to Ostwald-ripening.



**Figure 6.3: a) Distribution of the untreated and OTS functionalized HY zeolite in a biphasic water/decalin system; b) Optical microscopy image of the water/decalin emulsion stabilized by functionalized HY zeolite (Si/Al = 30).**

### 6.3.3. DRIFT of Untreated and Functionalized HY Zeolites

To further characterize the properties of the zeolites, we conducted DRIFT studies of the untreated and functionalized zeolites with  $\text{SiO}_2/\text{Al}_2\text{O}_3$  molar ratio of 60. Figure 6.4 shows the DRIFT spectra for both zeolites. It can be observed that the functionalized zeolite exhibits several bands in the  $2800\text{-}3000\text{ cm}^{-1}$  region that do not appear in the case of the hydrophilic one. These bands can be attributed to the C-H stretching of the OTS adsorbed on the zeolite surface [37,55]. There can be observed methylene ( $-\text{CH}_2$ ) and methyl ( $-\text{CH}_3$ ) asymmetric and symmetric C-H bonds.  $\text{CH}_2$  asymmetric and symmetric stretching observed for OTS on the zeolite surface appear at  $2935$  and  $2864\text{ cm}^{-1}$ , respectively, while  $\text{CH}_3$  asymmetric stretching is observed at  $2964\text{ cm}^{-1}$  [55,56,59,61].  $\text{CH}_2$  bands can shift to lower frequencies with increasing the OTS concentration on the surface [60].



**Figure 6.4: DRIFT spectra of (a) untreated HY zeolite; (b) OTS functionalized HY zeolite; (bs) functionalized zeolite after 3 h treatment in biphasic solvent (water/decalin) at 200 °C; and (bc) functionalized zeolite after calcination in air at 450 °C for 16 h.**

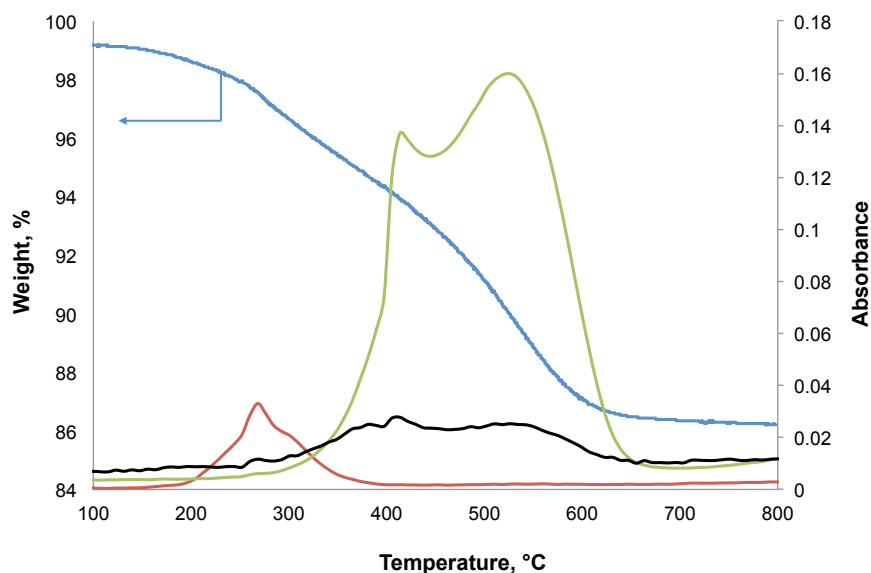
In the untreated zeolite spectrum, the sharp band at 3745 cm<sup>-1</sup> is due to the single and germinal silanol groups [58], which in the case of the functionalized zeolite has much less intensity and shifts to a lower frequency (3700 cm<sup>-1</sup>) due to the bonding to OTS molecules. After calcining in air the functionalized zeolite at 450 °C for 16 h, it can be observed that the DRIFTS spectrum is very similar to the untreated sample one. In the calcined sample, the bands attributed to the C-H stretching of the OTS adsorbed on the zeolite surface disappear, and the ones attributed to the silanol groups appear. This is an indicative of the OTS desorption from the zeolite surface during the calcination treatment.

Also, in all the samples, the bands observed at 3637 and 3548  $\text{cm}^{-1}$  correspond to the high-frequency (HF) and low-frequency (LF) hydroxyl vibrations, which are assigned to the Brönsted sites [62-65]. In HY zeolites, Brönsted hydroxyls are present in both large and small cages. The high-frequency hydroxyl groups are associated with the hydroxyl groups located in the supercages, and the low-frequency hydroxyl groups are attributed to hydroxyls in the small cages [64,66]. It is worth noting that these bands appear at the same frequencies in both untreated and functionalized zeolites, which could mean that the OTS do not adsorb in the cages and supercages due to its size.

#### *6.3.4. TG-DTA and TPO of Functionalized HY Zeolites*

To study the behavior of the functionalized zeolite with temperature and quantify the amount of carbon anchored on the zeolite surface during the silylation process, we conducted TG-DTA and TPO analyses over one of the functionalized zeolites, specifically the one with  $\text{SiO}_2/\text{Al}_2\text{O}_3$  ratio of 60. The TG-DTA analysis results are shown in Figure 6.5, where we can observe the weight loss in the zeolite with time and temperature. From the heating ramp used in this technique, we obtained a total weight loss of 13.8 %. There was observed a loss of weight of 0.8 % in the first 40 min of the analysis (where the temperature was kept constant at 100 °C), followed by a weight loss of 3.4 % in the ramp from 100 to 350 °C, and a final weight loss of 9.6 % in the ramp from 350 to 600 °C. This weight loss in the functionalized zeolite can be attributed to both the water adsorbed on the surface and the carbon chains from the functionalization agent (OTS). It has been reported before that the weight loss corresponding to the OTS mainly occurs in air the range of 230-400 °C [61]. Besides,

the weight loss up to 150 °C can be associated with breakup of hydrogen bonded network and removal of adsorbed water from the zeolite surface, and the one corresponding to 150-600 °C can also be associated with desorption of the adsorbed water, as well as water generated by the condensation of free silanols [61].



**Figure 6.5: Thermogravimetric analysis (TG-DTA) of the untreated and OTS functionalized HY zeolite (Si/Al ratio: 30). Left Axis: Weight (%) Right axis: Absorbance due to water ( $3735\text{ cm}^{-1}$ ), hydrocarbons, C-H stretching ( $2962\text{ cm}^{-1}$ ), and  $\text{CO}_2$  ( $2350\text{ cm}^{-1}$ ).**

Besides, from the TPO experiment conducted on the same zeolite, we observed that the amount of carbon anchored on the surface of the zeolite was around 5.7 %, which corresponds to a mass of OTS of 6.7 wt. %. This means that of the total 13.8% weight loss observed in the TG-DTA analysis about 7.1% could be attributed to water. This result is in agreement with the results obtained by K.A. Northcott et al. [37] and Ouki and Kavannagh [67], who observed that the average weight reduction due to water loss upon heating clinoptilolite to high temperatures was approximately 10 %.

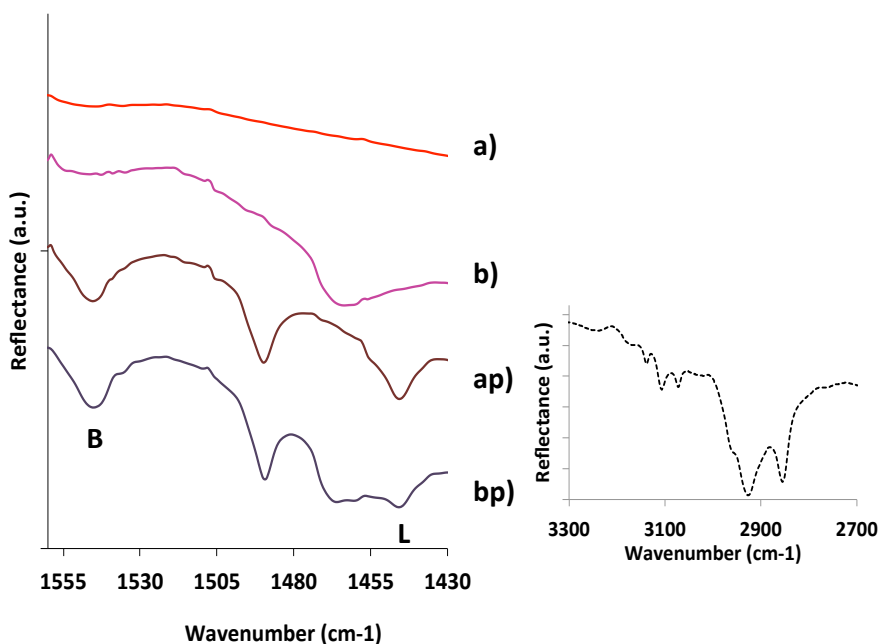


The TG-DTA studies suggest that, under the conditions used for the alcohol dehydration and alkylation reactions (200 °C and in absence of oxygen), the integrity of the OTS functional groups should be preserved. However, to further support this conclusion we conducted an additional experiment. The functionalized zeolite was placed in the reactor in contact with a mixture of water and decalin, the two solvents used in the reaction experiments, and heated to 200 °C for 3 h in 700 psi He. After this period, the sample was recovered by filtration, dried at 100 °C, and analyzed by FTIR to confirm that the intensity of the bands due to OTS do not decrease, nor do the bands due to silyanol OH increase. As compared in Figure 6.4, this is indeed the case. There was practically no change in the entire spectrum of the functionalized zeolite after heating in the biphasic solvent.

#### *6.3.5. Pyridine Chemisorption using in-situ DRIFT of Untreated and Functionalized HY Zeolites*

Another important consideration is whether the functionalization occurs preferentially on the external surface of the zeolite, leaving the Brønsted and Lewis acid sites largely unaltered, or to the contrary, whether the functionalization causes a significant loss in acid density. To answer this question, we have conducted FTIR analysis of adsorbed pyridine on both the untreated and the OTS-functionalized HY zeolites. The corresponding DRIFT spectra on the two zeolites before and after exposure to pyridine at atmospheric pressure and 100 °C are presented in Figure 6.6. Upon chemisorption on acidic zeolites, pyridine exhibits characteristic IR absorption

bands at  $1545\text{ cm}^{-1}$  when adsorbed on Brønsted acid sites (i.e., forming a pyridinium ion), and at  $1450\text{ cm}^{-1}$  when adsorbed in Lewis sites [68,69].



**Figure 6.6: DRIFT spectra of the pyridine chemisorption experiments at 100C and atmospheric pressure for the different HY zeolites ( $\text{SiO}_2/\text{Al}_2\text{O}_3$  molar ratio: 60). untreated and functionalized HY zeolite; a) untreated HY zeolite, b) functionalized HY zeolite, bp) functionalized HY zeolite after pyridine chemisorption, ap) untreated HY zeolite after pyridine chemisorption. Right: DRIFT spectra of the region around  $2900\text{ cm}^{-1}$  of the functionalized HY zeolite after pyridine chemisorption.**

As shown in the spectra, both bands are clearly present on the two zeolites, with very similar intensities, which clearly shows that most of the original Brønsted and Lewis acid sites remain unaffected after the OTS functionalization. Also, as shown in Figure 6.6, the characteristic C-H bands of the functionalization (see Figure 6.4) are present and largely unaffected during the pyridine adsorption experiments. It is not clear why while the density of acid sites is essentially unchanged, the intensity of the HF and

LF hydroxyl bands appears somewhat weaker for the functionalized zeolite. However, as shown below, functionalization does not cause any loss in the catalytic activity of these acid sites, which is the most important outcome.

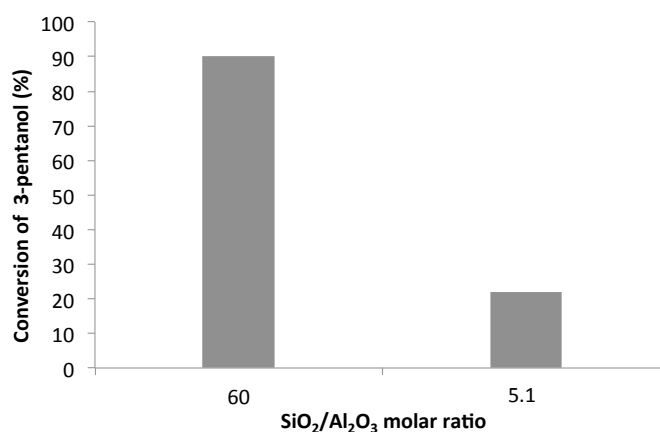
### 6.3.6. Alcohols Dehydration

In order to compare the activity of the untreated and functionalized zeolites, the dehydration of 3-pentanol and 2-propanol to pentenes and propylene, respectively, was studied in an emulsion system (water/decalin ratio 1:1). In this system, we can take advantage of the fact that the alkene products migrate to the oil phase upon formation, due to their low solubility in water, facilitating the product separation. Table 6.1 summarizes the results of alcohol conversion after 3 h reaction at 200 °C and 700 psi of He on the untreated and functionalized zeolites with a SiO<sub>2</sub>/Al<sub>2</sub>O<sub>3</sub> molar ratio of 60. It can be observed that, when 3-pentanol was the reactant, the conversion with the untreated zeolite was 27.3 %, and 85.0 % with the functionalized zeolite. In the case that we used 2-propanol, the conversions were 25.9 and 88.1 %, with the untreated and functionalized zeolites, respectively. Therefore, in both cases we reached much higher conversion of the alcohol (up to 3 times higher) with the functionalized zeolite.

**Table 6.1: Alcohol conversion in the 3 h dehydration reactions of 3-pentanol or 2-propanol at 200 °C and 700 psi of He over both untreated and OTS functionalized HY zeolites. Feed: 3-pentanol or 2-propanol with a total molar concentration of 1 M.**

Conversion (%)	Zeolite	
	Untreated	Functionalized
3-Pentanol	27.3	85.0
2-Propanol	25.9	88.1

It was also considered the behavior of two functionalized zeolites with different  $\text{SiO}_2/\text{Al}_2\text{O}_3$  molar ratios, 5 and 60. The results of 3-pentanol conversion after 3 h reaction (Feed: 3-pentanol 1 M) in emulsion at 200 °C and 700 psi of He, catalyzed by those two functionalized zeolites, are shown in Figure 6.7. As it can be seen, the 3-pentanol conversion with the zeolite with a  $\text{SiO}_2/\text{Al}_2\text{O}_3$  molar ratio of 60 is 90 %, while with the zeolite with a  $\text{SiO}_2/\text{Al}_2\text{O}_3$  molar ratio of 5, the conversion is much lower, 20 %. This decrease in alcohol conversion with the decrease in the  $\text{SiO}_2/\text{Al}_2\text{O}_3$  molar ratio may be attributed to the stronger Brønsted acidity of the zeolite with a higher Si/Al ratio [62].



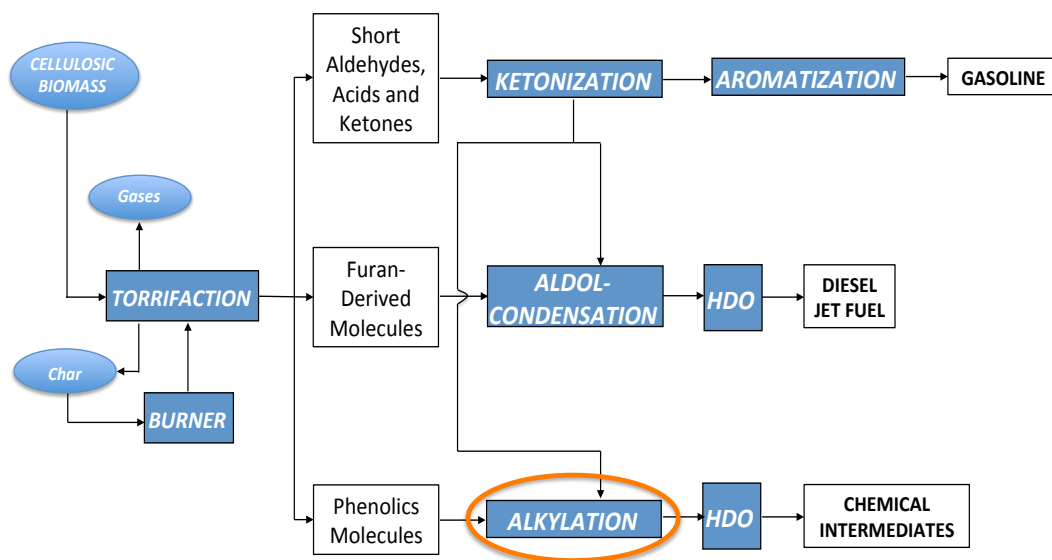
**Figure 6.7: Conversion of 3-pentanol after 3 h reaction at 200 °C and 700 psi of He over functionalized HY zeolites with different  $\text{SiO}_2/\text{Al}_2\text{O}_3$  molar ratios.**

### 6.3.7. Alkylation of 2-propanol and m-cresol

After proving the effectiveness of the functionalized zeolite towards the alcohol dehydration to produce alkenes, we decided to study the alkylation of a phenolic compound, m-cresol, and an alcohol, 2-propanol, in a water/decalin emulsion. Alkylation of m-cresol is an industrially important reaction that produces the precursors

for a number of commercially important antioxidants and light protection agents [70]. More importantly, it have been proposed that such carbon-carbon bond formation reactions will be of crucial importance in the exploitation of the small oxygenated molecules (C<sub>1</sub>-C<sub>3</sub> alcohols, aldehydes, ketones) present in the bio-oil by coupling them with the phenolic fraction towards the production of fuels and chemicals, that otherwise could be lost as light gases in a hydrotreating approach (Figure 6.8).

Among the alkylated products from the reaction of m-cresol and isopropanol, 2-isopropyl-5-methylphenol (thymol) is an important precursor of menthol, which is a compound used widely in the pharmaceutical industry and perfumery [71-73]. In addition, these chemicals could serve as platforms for the production of gasoline upon hydrogenolysis.



**Figure 6.8: Flow diagram for the conversion of biomass into chemical intermediates by alkylation of the phenolic fraction of the bio-oil with the small oxygenates.**

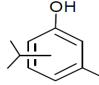
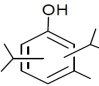
In this emulsion system, isopropanol is mostly water-soluble, while m-cresol partitions in both phases. As it was mentioned before, the alcohol (2-propanol) can dehydrate to form an alkene (propylene), which migrates to the organic phase and further can react with m-cresol to produce mono and dialkylated products. Since the functionalized zeolite is mostly hydrophobic, the adsorption of the alkenes and m-cresol is favored in comparison to the untreated zeolite, in which more water can be adsorbed on its surface.

Table 6.2 summarizes the results of m-cresol conversion and alkylation products yield in the alkylation of m-cresol and 2-propanol (2-propanol/m-cresol molar ratio: 3) at 200 °C and 700 psi of He on both the untreated and functionalized with a SiO<sub>2</sub>/Al<sub>2</sub>O<sub>3</sub> molar ratio of 60. Also, the reactions were run in single aqueous phase and in water/oil emulsion. It can be noted that with both untreated and functionalized zeolites, the m-cresol was also higher in the emulsion system, compared to the single aqueous phase one. As an example, after 3 h of reaction with the functionalized zeolite as catalyst, the m-cresol conversion was ~ 10 % in single aqueous phase, and ~ 20 % in emulsion system, which proves the higher efficacy of the emulsion system due to the increase in the interfacial area upon the emulsion formation [46-50].

In that reaction, the product yields changed from 7.3 and 3 % for the mono and dialkylated products, respectively, in the reaction in single phase, to 13 and 6.5 % in emulsion. Besides, comparing the activity of the untreated and functionalized zeolites for these alkylation reactions, it can be observed that the untreated zeolites is more active, leading to higher m-cresol conversions, and thus, higher alkylated product yields. For example, in the 3 h reaction in emulsion, the conversion of m-cresol was 9.1

% with the untreated zeolite, and 19.5 % for the functionalized one. This is in agreement with the alcohols dehydration results discussed above (Table 6.1), in which we observed how the functionalized zeolite favored the 2-propanol conversion towards the propylene formation. One can expect that the diffusion of water molecules to the interior of the hydrophobic zeolite will be hindered by the presence of the functional groups. By contrast, while 2-propanol mostly resides in the aqueous phase, its transport through the organic functional groups will be less restricted than that of water, a molecular discrimination that does not occur on the untreated zeolite.

**Table 6.2: Conversion of m-cresol and product yield obtained in the alkylation reaction of m-cresol and 2-propanol at 200°C and 700 psi of He over untreated and OTS functionalized HY zeolite (Si/Al = 30), in single aqueous phase and in water/decalin emulsion.**

Product yield (%)	Zeolite							
	Single aqueous phase				Biphasic (Water/Decalin)			
	Untreated		Functionalized		Untreated		Functionalized	
	1.33 h	3 h	1.33 h	3 h	1.33 h	3 h	1.33 h	3 h
	1.8	2.3	2.2	7.3	2.6	6.6	6.9	13.0
	0.2	1.1	0.6	3.0	1.0	2.5	3.0	6.5
M-cresol conversion	2.0	3.3	2.8	10.3	3.6	9.1	9.9	19.5

Also, the uptake rates of 2-propanol and m-cresol have were measured from aqueous and organic solutions into the functionalized and untreated zeolites, directly measured in suspension at room temperature. Table 6.3 summarizes the adsorption rate measurements. In general, the highest adsorption rates for both adsorbates were

observed from the oil phase. However, it is remarkable that the adsorption of cresol on the hydrophobic functionalized zeolite is very high even from the aqueous phase.

**Table 6.3: Adsorption constants [in (g of zeolite)<sup>-1</sup> h<sup>-1</sup>] of m-cresol and 2-propanol on OTS functionalized HY and untreated HY zeolites (Si/Al = 30)\*.**

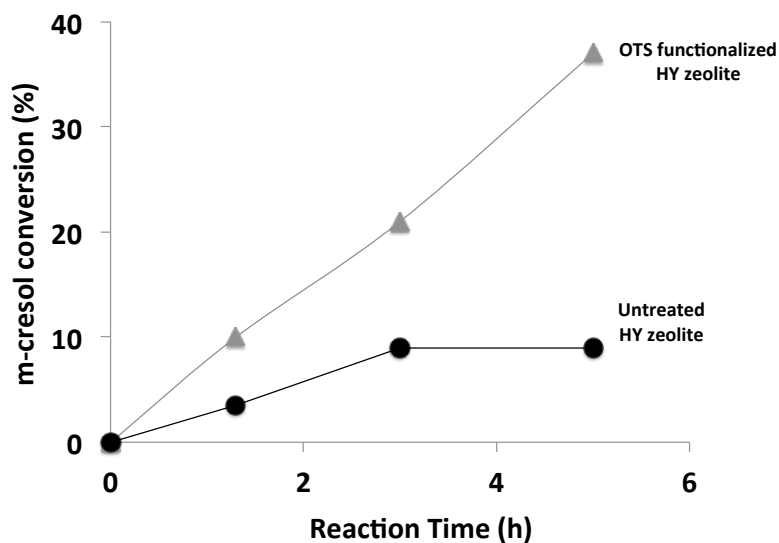
Compound	Aqueous phase		Organic phase	
	Functionalized	Untreated	Functionalized	Untreated
2-propanol (2POL)	0.20	0.29	0.32	0.30
m-cresol (MCR)	0.30	0.12	0.47	0.19
ratio MCR/2POL	1.50	0.41	1.47	0.63
Average	0.25	0.21	0.40	0.25

\*: Uptake measurements as a function of time were conducted in a batch stirred glass system at room temperature and atmospheric pressure.

Even though the kinetics of a surface reaction is governed by chemical potentials rather than concentrations, and solubility is not a crucial parameter for surface kinetics [74], the rate of mass transport is directly affected by solubility. In this case, the hydrophilicity or hydrophobicity of the zeolite seems to play a crucial role in determining the rate of reactions occurring inside the pores.

Figure 6.9 compares the time evolution of conversion for the two zeolites. A clear difference is observed between the hydrophobic and hydrophilic zeolites. While the former (OTS- functionalized) shows a continuous increase in the m-cresol conversion with reaction time, the latter (untreated) seems to lose its activity quite rapidly. For instance, while conversion on the hydrophobic zeolite from 3 to 5 h of reaction goes from 21 to 37%, no change in conversion is observed with the untreated zeolite after 3 h. That is, the hydrophilic catalyst is completely deactivated at this point.





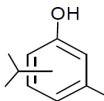
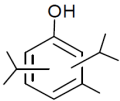
**Figure 6.9: Conversion of m-cresol as a function of reaction time during alkylation with 2-propanol at 200 °C and 700 psi in He over two HY zeolites (Si/Al molar ratio: 30). Circles: Untreated; Triangles: OTS functionalized. Feed: 2-propanol/m-cresol molar ratio: 3; total molar concentration: 2 M.**

#### 6.3.8. Catalyst Regenerability and Reusability

Taking into account the differences observed in the performance of the untreated and functionalized zeolites for the alkylation reactions in the water-decalin emulsion system the catalyst reusability and regenerability were studied. First, the alkylation of m-cresol with 2-propanol was run for 3 h in the batch reactor as described above. After this first reaction period, the resulting liquid was separated from the catalyst by centrifugation at 5000 rpm for 5 min. The solid was washed first with water, then with decalin, and finally centrifuged again to separate it from the liquid. The resulting solids were dried overnight in an oven at 100 °C. To preserve the hydrophobicity of the OTS zeolite, no other high-temperature regeneration method was employed. Since a significant fraction of catalyst is lost during the separation, washing, and drying process, in order to compare the activity of the used (and dried) catalysts with the original catalyst, the catalysts of two runs were combined in order to load the same

amount of catalyst in the reactor for the second reaction run. The comparison of activity between the first run and the second run with the two zeolites is made in Table 6.4. A remarkable difference is observed. While the OTS-functionalized zeolite is seen to retain a large fraction of its original activity (~ 85%) after regeneration and reuse, the untreated zeolite has completely lost its activity.

**Table 6.4: Data for analysis of the untreated and OTS functionalized HY zeolites (SiO<sub>2</sub>/Al<sub>2</sub>O<sub>3</sub> molar ratio: 60) stability. Reaction conditions: 3h, 200 °C, 700 psig He, feed: 2-propanol/m-cresol molar ratio: 3; total molar concentration: 2 M, 500 mg catalyst.**

Products Yield %	Zeolite			
	Untreated		Functionalized	
	First Run	Second Run	First Run	Second Run
	5.8 (+/- 0.2)	< 0.01	13.0 (+/- 0.5)	10.9 (+/- 0.3)
	2.5 (+/- 0.1)	< 0.01	6.4 (+/- 0.2)	5.3 (+/- 0.3)
<b>m-cresol conversion (%)</b>	9.1 (+/- 0.8)	< 0.01	19.5 (+/- 0.4)	16.2 (+/- 0.6)

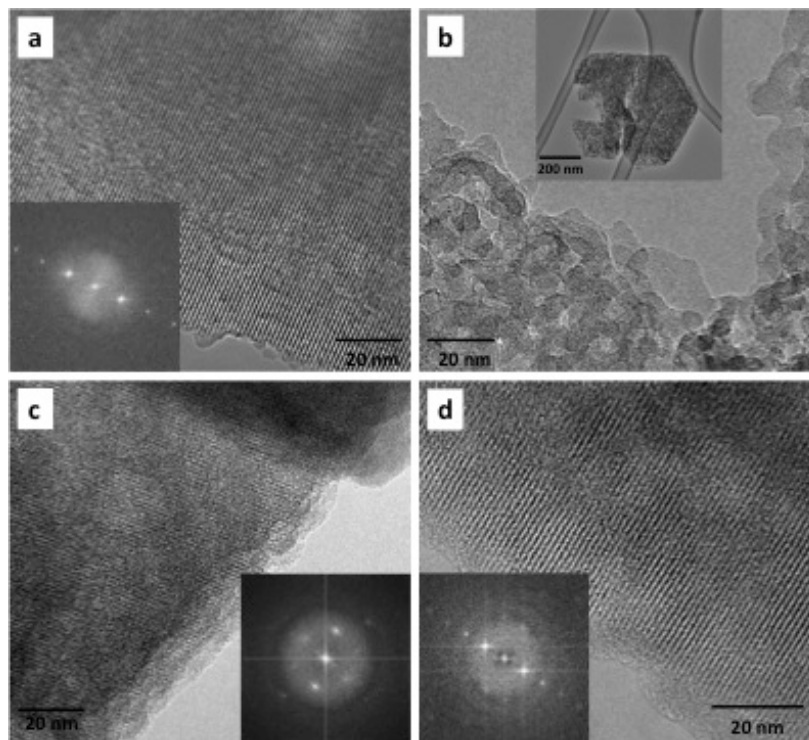
### 6.3.9. Characterization of the Zeolites after Reaction

To explain the differences observed in the performance of the untreated and functionalized zeolites for the alkylation reactions, we characterized the changes occurring in the different zeolites after being used as catalyst for the alkylation changes in the XRD profiles of the hydrophobic zeolite are seen after reaction, which indicates that the structure of the functionalized sample remains largely undisturbed after exposure to the aqueous environment at 200 °C. By contrast, a dramatic drop in

diffraction intensity is observed after reaction on the untreated hydrophilic zeolite, indicating a significant loss of crystallinity. Interestingly, this loss in crystallinity is not accompanied by any shifts in the position of the diffraction peaks, which indicates that the destruction of the untreated zeolite in liquid water is not a selective leaching of cations, which may change the unit cell size, it is rather a drastic collapse of the crystals. As indicated by Ravenelle et al.,<sup>Error! Bookmark not defined.</sup> this process is different from the better-known dealumination by steaming that occurs at much higher temperatures and in the vapor phase.

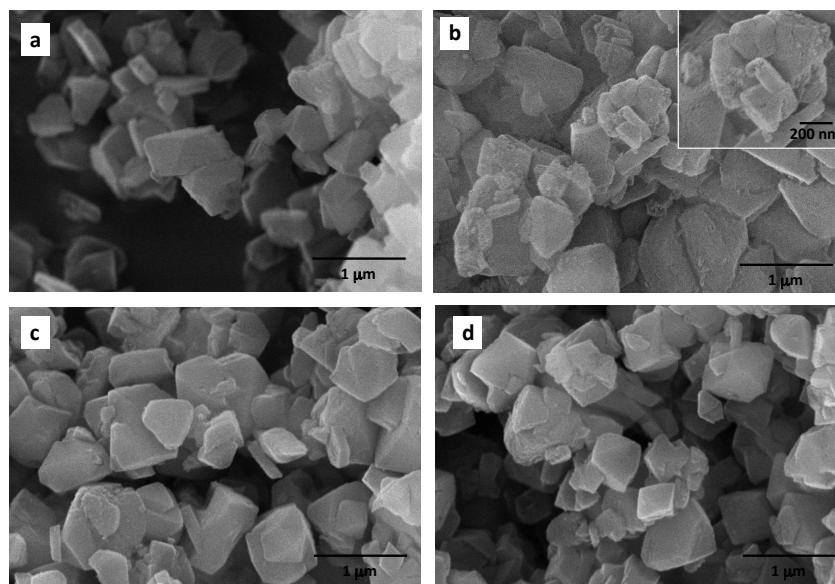
In sharp contrast, the destruction of the crystalline structure does not occur on the OTS-functionalized zeolite. This striking difference clearly shows that the severely deactivating effect of hot liquid water can be minimized by hydrophobic functionalization, which dramatically inhibits the direct interaction and exchange of mass with the bulk liquid water.

The contrasting behavior of the OTS-functionalized zeolite compared to the untreated zeolite was even more clearly evident from the electron microscopy images obtained on the same samples before and after reaction. Both HRTEM (Figure 6.10) and SEM (Figure 6.11) demonstrate that the crystalline structure of the functionalized zeolite remains unchanged after reaction, while that of the hydrophilic zeolite is greatly affected.



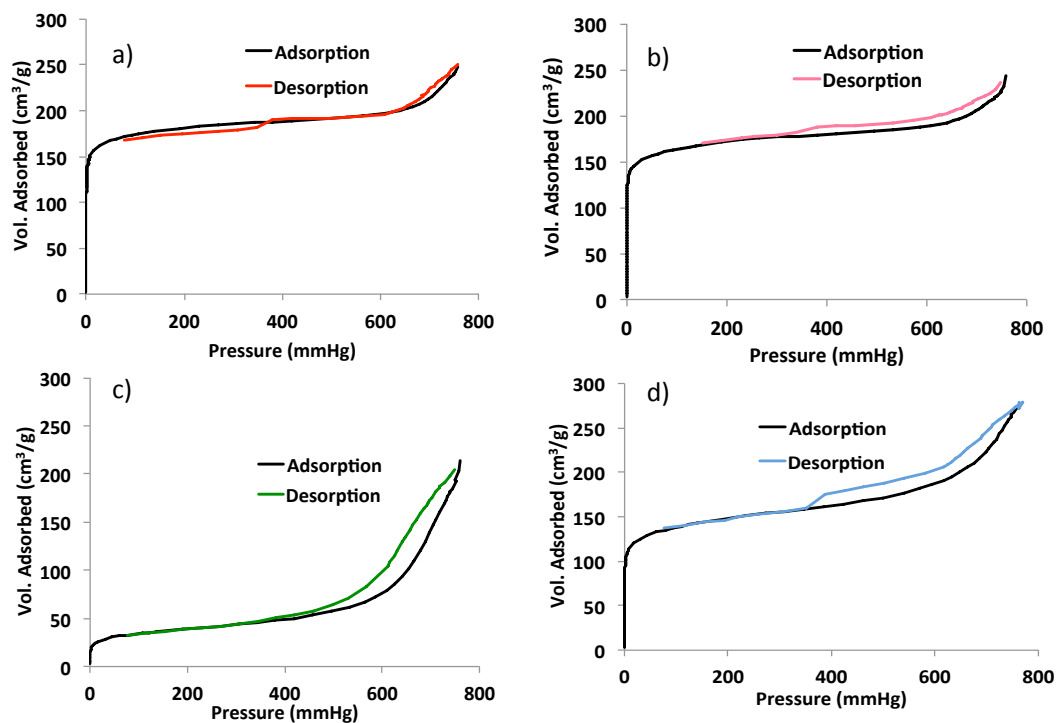
**Figure 6.10: Electron microscopy (HRTEM) of the HY zeolites (Si/Al=30). Untreated zeolite, before (a) and after reaction (c); OTS functionalized zeolite, before (b) and after reaction (d).**

The HRTEM of the used OTS-functionalized zeolite (Figure 6.10d) clearly shows that the ordered patterns of the microporous structure of the zeolite remain practically identical to those of the zeolite before reaction (Figure 6.10c). By contrast, in the untreated zeolite (Figure 6.10b) they disappear after reaction. Similarly, the SEM images indicate that while the external surface of the functionalized zeolite particles does not exhibit a significant change in texture after reaction (see Figure 6.11c,d), a significantly rougher surface is observed on the untreated zeolite after reaction in the hot liquid water (see Figure 6.11b).



**Figure 6.11: Scanning electron microscopy (SEM). Untreated zeolite: before (a) and after reaction (c); OTS functionalized zeolite: before (b) and after reaction (d).**

In perfect agreement with these observations, the BET surface area and pore size distribution measurements on the four samples give further evidence for the remarkable difference in stability upon exposure to an aggressive liquid environment. As shown in Figure 6.12, while the adsorption isotherms of the untreated sample shows a drastic change after reaction (Figure 6.12a,b), the change for the OTS-functionalized sample is relatively minor (Figure 6.12c,d).



**Figure 6.12: N<sub>2</sub> Adsorption-desorption isotherms of the HY zeolites (Si/Al=30). Untreated zeolite, before (a) and after reaction (c); OTS functionalized zeolite, before (b) and after reaction (d).**

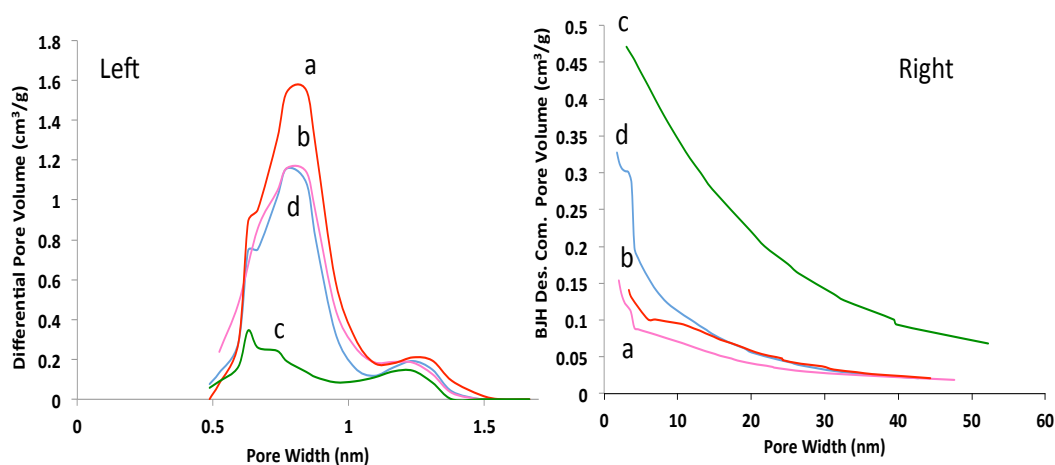
As summarized in Table 6.5, the resulting BET surface areas, pore volumes, and micro/mesopores ratio all reflect this contrasting behavior. Specifically, it should be noted that the surface areas of the functionalized and untreated zeolites are similar, which is in agreement with the conclusion reached above regarding the absence of significant pore plugging due to functionalization. Additionally, the drop in surface area after liquid-phase reaction is only 17% for the hydrophobic zeolite, but almost 70% for the untreated zeolite.

**Table 6.5: Specific area ( $S_{\text{BET}}$ ), and pore volume of the two HY zeolites (untreated and OTS functionalized) before and after reaction. Alkylation reaction conditions: 3 h at 200 °C and 700 psi of He; feed: 2-propanol/m-cresol molar ratio: 3; total molar concentration: 2 M.**

Sample	$S_{\text{BET}}$ ( $\text{m}^2/\text{g}$ )	$V_{\text{total}}$ ( $\text{cm}^3/\text{g}$ )	$V_{\text{micro}}$ ( $\text{cm}^3/\text{g}$ )	$V_{\text{meso}}$ ( $\text{cm}^3/\text{g}$ )	$S_{\text{micro}}$ ( $\text{m}^2/\text{g}$ )	$S_{\text{meso}}$ ( $\text{m}^2/\text{g}$ )	$V_{\text{meso}}/$ $V_{\text{micro}}$
<i>Untreated HY</i>							
Before Reaction	690	0.35	0.27	0.07	660	30	0.26
After Reaction	215	0.41	0.01	0.40	35	180	40
<i>Functionalized HY</i>							
Before Reaction	640	0.33	0.25	0.08	600	40	0.32
After Reaction	530	0.38	0.18	0.20	430	100	1.1

An analysis of the variation in micro- and mesoporosities after reaction in hot liquid is important to further understand the destruction of the zeolite structure and its prevention by enhancing the hydrophobicity. First, one can see that the microporosity of the hydrophilic zeolite practically disappears when it is exposed to the hot liquid medium. That is, as shown in Table 6.5, the ratio meso/microporosity goes from about 0.3 to about 40. It is then no surprise that the catalytic activity of this sample practically vanishes after a few hours in the medium and cannot be restored by drying. As illustrated in Figure 6.13a, the micropore size distributions obtained by DFT analysis of the  $\text{N}_2$  physisorption data show similar behavior. That is, no significant differences in pore distribution between the functionalized and untreated samples before reaction, but a dramatic degradation on the hydrophilic zeolite after reaction. Interestingly, as shown in Figure 6.13b, this degradation of micropores is paralleled by an increase in mesoporosity. The structural conversion of microporosity into mesoporosity is an indication that, as mentioned above, the zeolite degradation process of the untreated

zeolite can be described as a collapse of the crystallites, which give rise to internal mesopores. It is important to point out the critical differences in the extent of zeolite degradation occurring in the presence of hot liquid water compared to steam at comparable temperatures. That is, while steaming at 200 °C would cause little if any change in crystallinity [75], heating in liquid water at the same temperature caused almost a total destruction of the crystallites. Therefore, one may conclude that the hydrophobization of the external surface of the zeolite prevents the contact of the crystallites with liquid water, which readily destroys the hydrophilic zeolite via hydrolysis accelerated by solvation and rapid mobility of the ions into the liquid phase.



**Figure 6.13: Pore size distribution of the HY zeolites (before (a) and after reaction (c); OTS functionalized zeolite, before (b) and after reaction (d)). Left) differential pore volume of the micropores (calculated by the DFT method); and Right) desorption cumulative pore volume of the mesopores (calculated by the BJH method).**

#### 6.4. Conclusions

In the present work our research group have shown that highly stable solid acid catalysts can be synthesized upon the selective hydrophobization of microporous Y type



zeolites. These nanocomposites are able to both stabilize water/oil emulsions and catalyze upgrading reactions of biofuel molecules. We anticipate that the application of this novel technology in the processing of complex biphasic systems, typically encountered in the conversion of lignocellulosic biomass, would have a significant impact in overcoming the technological and economical challenges of the future Biorefinery.

The major differences in catalytic activity between the untreated and functionalized zeolites can be attributed to the increase in the hydrophobicity of the zeolite surface that hinders the adsorption of water molecules inside the catalyst cages. Such exclusion of the water has two major effects; a) increase on the catalyst stability in hot condensed water by preventing the hydrolysis of the Si-O-Si framework, and b) reduction of the competitive adsorption of water molecules with the reacting species.

We have conducted several characterization studies (BET, XRD, SEM and HRTEM) on both untreated and functionalized zeolites, before and after the alkylation reactions, which confirm the results described above; the structure of the untreated zeolite starts to collapse during the reaction, while the structure of the hydrophobized zeolites remain unaltered.

We have also observed that surface functionalization of the zeolite (normally hydrophilic) displays a hydrophobic behavior, which allows the effective stabilization of water/oil emulsions with small droplet size. Due to the increase in the interfacial area upon the formation of the emulsion, we have observed that the reactant conversion both in the alcohols dehydration and in the alkylation of m-cresol and 2-propanol, is higher in emulsion than in single aqueous phase.

Therefore, by combining the interfacial activity of the functionalized zeolite to stabilize emulsions along with its hydrothermal resistance, we have developed catalytic zeolites with enhanced performance compared to untreated zeolites (hydrophilic and non-hydrothermally resistant) for the alcohol dehydration and alkylation reactions.

## References

- [1] M. Elanany, M. Koyama, M. Kubo, E. Broclawlk and A. Miyamoto, *Appl. Surf. Sci.* 246 (2005) 96.
- [2] H. van Bekkum, E.M. Flanigen and J.C. Jansen, *Introduction to zeolite science and practice*, Elsevier, Amsterdam, 1991.
- [3] P.B. Weisz, V.J. Frilette, R.W. Maaatman and E.B. Mower, *J. Catal.* 1 (1962) 307.
- [4] N.Y. Chen, T.F. Degnan Jr. and C.M. Smith, *Transport and reaction in zeolites. Design and application of shape selective catalysts*. Wiley-VCH, New York, 1994.
- [5] A.T. Bell, B.C. Gates and D. Ray, *Catalysis for Energy*. DOW BES report, 2008.
- [6] G.W. Huber, S. Iborra and A. Corma, *Chem. Rev.* 106 (2006) 4044.
- [7] C. Luo, S.A. Wang and H.C. Liu, *Angew. Chem. Int. Ed.* 46 (2007) 7636.
- [8] Y. Román-Leshkov, J.N. Chheda and J.A. Dumesic, *Science* 312 (2006) 1933.
- [9] R.M. Ravenelle, F. Schüàler, A. D'Amico, N. Danilina, J.A. van Bokhoven, J.A. Lercher, C.W. Jones and C. Sievers, *J. Phys. Chem. C* 114 (2010) 19582.
- [10] G.W. Huber, *Breaking the chemical and engineering barriers to lignocellulosic biofuels: next generation hydrocarbon biorefineries*, National Science Foundation, Chemical, Bioengineering, Environmental and Transport Systems Division, Washington DC, 2008.
- [11] J. Cejka, A. Corma and S.I. Zones, *Zeolites and catalysis: Synthesis, reactions and applications*, Wiley, New York, 2010.

- [12] J.A. Lercher and A. Jentys, Catalytic properties of micro and mesoporous nanomaterials. In encyclopedia of nanoscience and nanotechnology, J.A. Schwarz, C.I. Contescu, K. Putyera, Marcel Dekker, Inc.: New York, 2004.
- [13] T. Okuhara, Chem. Rev. 102 (2002) 3641.
- [14] D.H. Olson, W.O. Haag and R.M. Lago, J. Catal. 61 (1980) 390.
- [15] K. Nishimiya and K. Tsutsumi, Zeolite 6 (1989) 14.
- [16] K. Tsutsumi, Zeolite 10 (1993) 179.
- [17] R. Mokaya, J. Phys. Chem. B 104 (2000) 8279.
- [18] S.C. Shen and S. Kawi, J. Phys. Chem. B 103 (1999) 8870.
- [19] J.M. Kim and R. Ryoo, Bull. Korean Chem. Soc. 17 (1996) 66.
- [20] Y.D. Xia and R. Mokaya, J. Phys. Chem B 107 (2003) 6954.
- [21] A. Corma, M.E. Domine and S. Valencia, J. Catal. 215 (2003) 294.
- [22] A. Corma, L.T. Nemeth, M. Renz and S. Valencia, Nature 412 (2001) 423.
- [23] Y. Román-Leshkov and M.E. Davis, ACS Catal. (2011) DOI: 10.1021/cs200411d.
- [24] M. Moliner, Y. Román-Leshkov and M.E. Davis, PNAS 107 (2010) 6164.
- [25] E. Nikolla, Y. Román-Leshkov, M. Moliner and M.E. Davis, ACS Catal. 1 (2011) 408.
- [26] Y. Román-Leshkov, M. Moliner, J.A. Labinger and M.E. Davis, Angew. Chem. Int. Ed. 49 (2010) 8954.
- [27] S. Inagaki, S. Guan, Y. Fukushima, T. Ohsuna and O.S. Terasaki, J. Am. Chem. Soc. 121 (1999) 9611.

- [28] B.J. Melde, B.T. Holland, C.F. Blanford and A. Stein, *Chem. Mater.* 11 (1999) 3302.
- [29] C.Y. Ishii, T. Asefa, N. Cooms, M.J. MacLachlan and G.A. Ozin, *Chem. Commun.* (1999) 2539.
- [30] T. Aefa, M.J. MacLachlan, N. Coombs and G.A. Ozin, *Nature* 402 (1999) 867.
- [31] S. Inagaki, S. Guan, Y. Fukushima, T. Ohsuna and O. Terasaki, *Stud. Surf. Sci. Catal.* 129 (2000) 155.
- [32] S. Collins and Y. Hong, *Tetrahedron Lett.* 28 (1987) 4391.
- [33] S. Inagaki, S. Guan, T. Ohsuna and O. Terasaki, *Nature* 416 (2002) 304.
- [34] I. Diaz, F. Mohino, J. Perez-Pariente and E. Sastre, *Appl. Catal. A-Gen.* 242 (2003) 161.
- [35] J. Perez-Pariente, I. Diaz, F. Mohino and E. Sastre, *Appl. Catal. A-Gen.* 254 (2003) 173.
- [36] A. Giaya, R.W. Thompson and R. Denkwicz Jr., *Microporous Mesoporous Mater.* 40 (2000) 205.
- [37] K.A. Northcott, J. Bacus, N. Taya, Y. Komatsu, J.M. Perera and G.W. Stevens, *J. Hazardous Mater.* 183 (2010) 434.
- [38] C.K.W. Meininghaus and R. Prins, *Microporous Mesoporous Mater.* 35-36 (2000) 349.
- [39] A.E. Senatalar, J.A. Bergengahl, A. Giaya and R.W. Thompson, *Environ. Eng. Sci.*, 21 (2004) 722.
- [40] X.S.G. Zhao and Q. Lu, *J. Phys. Chem. B* 102 (1998) 1556.
- [41] T. Tatsumi, K.A. Koyano and N. Igarashi, *Chem. Commun.* (1998) 325.

- [42] S. Inagaki, H. Ima, S. Tsujiuchi, H. Yakushiji, T. Yokoi and T. Tatsumi, *Microporous Mesoporous Mater.* 142 (2011) 354.
- [43] G.W. Huber, J. N. Chheda, C.J. Barrett and J.A. Dumesic, *Science* 308 (2005) 1446.
- [44] Y. Román-Leshkov, C. J. Barrett, Z.Y. Liu and J.A. Dumesic, *Nature* 447 (2007) 982.
- [45] B.P. Binks and S.O. Lumsdon, *Langmuir* 16 (2000) 2539.
- [46] S. Crossley, J. Faria, M. Shen and D.E. Resasco, *Science* 327 (2010) 68.
- [47] M. Shen and D.E. Resasco, *Langmuir* 25 (2009) 10843.
- [48] J. Faria, M.P. Ruiz and D.E. Resasco, *Adv. Synth. Catal.* 352 (2010) 2359.
- [49] M.P. Ruiz, J. Faria, M. Shen, S. Drexler, T. Prasomsri and D.E. Resasco, *ChemSusChem* 4 (2011) 964.
- [50] P.A. Zapata, J. Faria, M. Pilar Ruiz and D.E. Resasco, *Topic Catal.* 55 (2012) 38.
- [51] R. Singh and P. K. Dutta, *Microporous Mesoporous Mater.* 32 (1999) 29.
- [52] J. Fu, Q. He, R. Wang, B. Liu and B. Hu, *Colloids Surfaces A: Physicochem. Eng. Aspects* 375 (2011) 136.
- [53] X.S. Zhao, G.Q. Lu, A.K. Whittaker, G.J. Millar and H.Y. Zhu, *J. Phys. Chem. B* 101 (1997) 6525.
- [54] B.H. Wouters, T. Chen, M. Dewilde and P.J. Grobet, *Microporous Mesoporous Mater.* 44-45 (2001) 453.
- [55] S.A. Mirji, *Surf. Interface Anal.* 38 (2006) 158.
- [56] N.L. Jeon, K. Finnie, K. Branshaw and R.G. Nuzzo, *Langmuir* 13 (1997) 3382.

- [57] C.P. Tripp and M.L. Hair, *Langmuir* 8 (1992) 1120.
- [58] C.P. Tripp and M.L. Hair, *Langmuir* 11 (1994) 1215.
- [59] H. Hoffmann, U. Mayer and A. Krischanitz, *Langmuir* 11 (1997) 1304.
- [60] D.H. Flinn, D.A. Guzonas and R.H. Yoon, *Colloids Surfaces A: Physicochem. Eng. Aspects* 87 (1994) 163.
- [61] S.A. Mirji, S.B. Halligudi, D.P. Sawant, N.E. Jacob, K.R. Patil, A.B. Gaikwad and S.D. Pradhan, *Appl. Surf. Sci.* 252 (2006) 4097.
- [62] R.A. van Santen, *Stud. Surf. Sci. Catal.* 85 (2004) 273.
- [63] W.P.J.H. Jacobs, H. Jobic, J.H.M.C. van Wolput and R.A. van Santen, *Zeolites* 12 (1992) 315.
- [64] M.A. Makarova, A.F. Ojo, K. Karim, M. Hunger and J. Dwyer, *J. Phys. Chem.* 98 (1994) 3619.
- [65] T.I. Koranyi, F. Moreau, V.V. Rozanov and E.A. Rozanova, *J. Mol. Struct.* 410-411 (1997) 103.
- [66] V.B. Kazansky, A.I. Serykh, V. Semmer-Herdelan and J. Frassissard, *Phys. Chem. Phys. Chem.* 5 (2003) 966.
- [67] S.K. Ouki and M. Kavannagh, *Waste Manag. Res.* 15 (1997) 383.
- [68] J.E. Mapes and R.P. Eischens, *J. Phys. Chem.* 58 (1954) 1059.
- [69] W.E. Farneth and R.J. Gorte, *Chem. Rev.* 95 (1995) 615.
- [70] B. Viswanathan and B. Jacob, *Catal. Rev. Sci. Eng.* 47 (2005) 1.
- [71] A. Vinu, G.S. Kumar, K. Ariga and V. Murugesan, *J. Mol. Catal. A Chem.* 235 (2005) 57.
- [72] J.C. Leffingwell and R.E. Shackelford, *Cosmetics Perfumery* 89 (2000) 69.

- [73] R. Hopp, *Recent Adv. Tobacco Sci.* 19 (1993) 46.
- [74] R.J. Madon, E. Iglesia, *J. Mol. Catal. A: Chem.* 163 (2000) 189.
- [75] C.V. McDaniel and P.K. Maher, *Molecular Sieves; Society of the Chemical Industry: London, 1968; pp 186-195.*